

DEPOSITIONAL AND DIAGENETIC CONTROLS ON RESERVOIR
HETEROGENEITY:
UPPER MORROW SANDSTONE, FARNSWORTH UNIT, OCHILTREE COUNTY,
TEXAS

By
Sara R. Gallagher

Submitted in Partial Fulfillment
of the Requirements for the

Masters of Science in Geology

New Mexico Institute of Mining and Technology
Department of Earth and Environmental Science

Socorro, New Mexico
August, 2014

ABSTRACT

Farnsworth Unit (FWU) is the site of one of the first commercial-scale carbon capture, utilization, and storage (CCUS) projects in the United States. The purpose of this study is to better understand how the depositional environment and diagenesis of the upper Morrow sandstone affect reservoir heterogeneity and the potential for residual CO₂ trapping in FWU. We build upon previous studies of the petroleum geology of the unit using interpretations of the depositional environment that place the unit in a sequence stratigraphic context, and present new core, petrographic, and geochemical data.

Lithofacies in FWU core are consistent with the regional incised valley model of deposition. The coarse-grained reservoir sandstone is interpreted to be fluvial. It is underlain by channel lag conglomerate and marine mudstone and overlain by fine-grained estuarine sandstone and marine mudstone. Reservoir quality does not appear to be controlled by primary depositional features, such as grain size and sorting.

Diagenetic (secondary) processes had a much greater effect on the reservoir quality of the upper Morrow sandstone than depositional processes. Petrography revealed that the diagenetic processes that had the greatest impact on reservoir quality are dissolution of feldspar and lithics; precipitation of authigenic cement, particularly kaolinite, siderite, calcite, ankerite, and quartz overgrowths; and compaction. Porosity facies were created to characterize the pore types and controls on permeability caused by the variable distribution of dissolution, matrix, and compaction.

One question that has yet to be answered is why the reservoir sandstone in the eastern side of the field has a lower permeability than in the western side of the field. There is no evidence to suggest that a change in depositional processes is responsible for the difference in permeability; grain size and degree of sorting do not decrease from west to east. The amount of porosity, matrix, and compaction is not significantly different in samples from the western and eastern sides of the field either. The reason for the difference in permeability may lie in the small-scale spatial distribution of porosity, but that was not sufficiently quantified in this study to provide a definitive answer.

This study also examined pore-to-throat ratios (PTRs) and heterogeneity of the pore network in order to assess the residual trapping potential of the upper Morrow sandstone. Image analysis was used to measure pore body diameters and Mercury Injection Capillary Pressure (MICP) analysis provided pore throat diameters. Calculations of the PTRs of several porosity facies were made by synthesizing this data. Of the four samples analyzed, the porosity facies with the highest residual trapping potential are microporous clay dominated and grain-sized pore dominated.

The upper Morrow sandstone in FWU is a heterogeneous reservoir with variable reservoir quality and residual trapping potential. This study serves as preliminary

geological characterization of the field and can be used as the foundation for further characterization and modeling.

Keywords: Anadarko Basin, incised valley deposits, upper Morrow sandstone, sandstone diagenesis, reservoir quality, residual trapping, CCUS, EOR

ACKNOWLEDGMENTS

This project was completed for the Southwest Regional Partnership on Carbon Sequestration (SWP) and funded by the U.S. Department of Energy National Energy Technology Laboratory. I received support as a research assistant at the Petroleum Recovery Research Center (PRRC) at the New Mexico Institute of Mining and Technology (NMT).

I would like to thank my committee members for all of their time and help with this project. Dr. Peter Mozley, Dr. Dana Ulmer-Scholle, Dr. Jason Heath (Sandia National Laboratories), and Martha Cather served on my committee and helped with different aspects of my research. I am especially grateful to Dr. Peter Mozley, who served as both my academic and research advisor. Throughout my time at NMT, he has been an excellent teacher and mentor, and provided valuable feedback on my thesis. I am grateful for the petrographic knowledge I received from Dr. Dana Ulmer-Scholle. Dr. Jason Heath helped with the core descriptions and oversaw the collection and analysis of several samples used in this study. Martha Cather guided my research to ensure it met the goals of the SWP and acted as my mentor at the PRRC.

I would like to thank the others who worked on the Farnsworth project from the PRRC, the NM Bureau of Geology (NMBGR), Sandia National Laboratories (SNL), and Chaparral Energy. Dr. Reid Grigg and Dr. Bob Balch at the PRRC were valuable collaborators. Dr. Thomas Dewers (SNL) and Dr. Steven Cather (NMBGR) assisted with the core descriptions. Lynn Heizler (NMBGR) oversaw the electron microprobe analysis. Chaparral Energy, the operator of Farnsworth Unit, was very cooperative and provided some of the data for this project.

I would like to thank the companies who provided services for this project. TerraTek, a Schlumberger Company, assisted with core handling and sampling and provided XRD analysis. Wagner Petrographic made several of the thin sections. Poro-Technology provided Mercury Injection Capillary Pressure analysis.

Tim Munson graciously allowed me to use his thin sections, which were invaluable to the petrography aspect of this project.

I would not have made it this far in my education if it wasn't for the support of my friends and family. I am especially grateful to my parents, Peter Gallagher and Vicki Strickler for encouraging me to pursue my interest in science. A special thanks Nic Barth, who is my role model and partner, for his emotional support and guidance throughout my time in graduate school.

TABLE OF CONTENTS

	Page
LIST OF TABLES	vi
LIST OF FIGURES	viii
CHAPTER 1. INTRODUCTION	1
Significance of Research.....	1
Production History	1
Background	2
Carbon Capture, Utilization, and Storage.....	2
Residual Trapping.....	3
Previous work.....	5
Anadarko Geology.....	5
Farnsworth Field.....	5
Munson 1988 and 1989.....	5
McKay and Noah 1996	6
CHAPTER 2. GEOLOGICAL SETTING	7
Regional Stratigraphic Framework	7
Tectonic Setting.....	7
Sequence stratigraphy and depositional environment.....	9
CHAPTER 3: METHODS.....	13
Core Descriptions and Data Analysis	13
Petrography	13
X-ray Diffraction Analysis.....	14
Electron Microprobe Analysis	14
Mercury Injection Capillary Pressure	14
Image Analysis.....	15
CHAPTER 4: RESULTS	16
Core Description and Lithofacies.....	16
Fine-grained Sandstone Facies	23
Coarse-grained Sandstone Facies	23

Conglomerate Facies	29
Paraconglomerate.....	29
Basal Lag Conglomerate.....	29
Mudstone Facies	32
Mudstone with Brachiopod Fossils.....	32
Dark Gray Mudstone.....	32
Bioturbated Mudstone.....	33
Porosity and Permeability	37
Composition	45
Fine-grained Sandstone Facies	45
Coarse-grained Sandstone Facies	50
Bioturbated Mudstone Facies	52
Diagenesis	60
Siderite cement	62
Quartz Overgrowths	66
Feldspar Overgrowths.....	68
Calcite Cement	70
Ankerite	73
Compaction.....	75
Feldspar Dissolution.....	77
Authigenic Clay.....	80
Kaolinite.....	83
Hydrocarbon Emplacement	84
Pore Types.....	85
Intergranular Macroporosity.....	85
Intragranular Macroporosity.....	85
Grain-Sized Macroporosity	89
Macro- and microporosity in Carbonate Cement	91
Microporosity in grains	93
Microporosity in completely dissolved grains.....	94
Microporosity in Clay Matrix and Authigenic Clay.....	96
Fracture Porosity.....	96
Porosity Facies	98

Intergranular Macroporosity Dominated	100
A. "Clean" macroporosity	100
B. Macroporosity dominated, with authigenic and detrital clay	101
Grain-sized Pore Dominated	102
C. Grain-sized pore dominated	102
Microporous Authigenic Clay Dominated	103
D. Microporous Authigenic Clay Dominated	103
E. Low-IGV Microporous Authigenic Clay Dominated.....	104
Carbonate Cement Dominated.....	105
F. Dissolution porosity in poikilotopic calcite.....	105
G. Intergranular porosity in siderite cement	106
Intragranular Porosity dominated	107
H. Low-IGV Intragranular Porosity Dominated	107
Mercury Injection Capillary Pressure (MICP).....	109
Image Analysis	113
CHAPTER 4: DISCUSSION.....	116
Depositional Environment.....	116
Controls on reservoir quality and heterogeneity	121
Implications for residual trapping of CO ₂	127
CHAPTER 5. CONCLUSIONS	129
SUGGESTIONS FOR FUTURE WORK.....	130
REFERENCES	131
APPENDIX A. STRATIGRAPHIC COLUMNS.....	135
APPENDIX B. INVENTORY OF THIN SECTIONS AND SAMPLE ANALYSES....	159
APPENDIX C. X-RAY DIFFRACTION (XRD) METHODS.....	161
APPENDIX D. ELECTRON MICROPROBE DATA.....	163
APPENDIX E. IMAGEJ METHODS	168
APPENDIX F. PHOTOS OF CORE FROM WELL 13-10A	172
APPENDIX G. MICP DATA.....	184
APPENDIX H. PHOTOMICROGRAPHS ANALYZED WITH IMAGEJ.....	206

LIST OF TABLES

Table	Page
Table 1. Lithofacies descriptions for FWU core.....	16
Table 2. Comparison of grain size and sorting for western and eastern sides of FWU.....	38
Table 3. Mineralogy of the Fine-grained Sandstone facies. Results of the 300-point count. IGV= intergranular volume.....	48
Table 4. Whole rock mineralogy of samples from well 13-10A, in weight percent, from XRD analysis. Samples E1- E4 are from the Coarse-grained Sandstone facies, E5 is from the Bioturbated Mudstone facies, and E6 is from the Fine-grained Sandstone facies.....	49
Table 5. Clay mineralogy of samples from well 13-10A, in weight percent, from XRD analysis. Samples E1- E4 are from the Coarse-grained Sandstone facies, E5 is from the Bioturbated Mudstone facies, and E6 is from the Fine-grained Sandstone facies.....	50
Table 6. Mineralogy of the Coarse-grained Sandstone. Results of 300-point counts. TR= trace, <1%.....	53
Table 7. Porosity of the Coarse-grained Sandstone. Results of 100-point counts for porosity. Thin sections with low porosity were visually estimated.....	55
Table 8. Elemental composition of carbonate cement in the Coarse-grained Sandstone from well 13-10A. Results of microprobe analysis, in mol%. All weight % totals were 100%, plus or minus 0.5%, which is an acceptable range of error. See Appendix D for raw data.....	56
Table 9. Elemental composition of clay in the Coarse-grained Sandstone from well 13-10A, in weight %. Results have been normalized to 100%. The “totals” column shows the pre-normalized totals, all of which are below 100%. Totals below 100% are less accurate. See Appendix D for raw data.	57
Table 10. Summary of porosity types observed in the Morrow B sandstone.....	87
Table 11. Porosity facies of the Morrow B sandstone.....	98
Table 12. Number of samples from the western and eastern sides of FWU that are dominated by each porosity facies.....	100
Table 13. Porosity facies, plug porosity and permeability, grain size, and pore-throat size for samples E1 – E4 from the Coarse-grained Sandstone facies from well 13-10A.	109

Table 14. Summary of ImageJ data. Porosity and permeability values are from routine core (plug) analysis. Image porosity, areas, and feret diameters were calculated with ImageJ and averaged for each sample.	113
Table 15. Comparison of the lithofacies in FWU with lithofacies described in Puckette et al. (2008) and Wheeler et al. (1990).....	120
Table 16. Pore size-to-throat ratios of pore diameters and pore-throat diameters.....	128

LIST OF FIGURES

Figure	Page
Figure 1. Paleogeography of the Morrow in the mid-continent. Modified from Swanson (1979) by R. Andrews, Oklahoma Geological Survey.....	2
Figure 2. Time versus trapping contribution of the four main trapping mechanisms. From IPCC (2005).	4
Figure 3. Illustration of residual trapping of CO ₂ . When a plume of CO ₂ moves through a pore network, residual trapping occurs when small amounts of CO ₂ “snaps off” of the plume and become isolated within pores. Figure source: The Cooperative Research Centre for Greenhouse Gas Technologies (CO2CRC).	4
Figure 4. Stratigraphic chart showing divisions of the Upper Morrowan and Lower Atokan-aged strata in the Farnsworth Unit. Wireline log is from well 32-2. Modified from Munson (1989) and Puckette et al. (2008) by Dylan Rose-Coss and Sara Gallagher.	8
Figure 5. Structural features during Morrowan time. Modified from Sonnenburg et al. (1990) in DeVries (2005).	9
Figure 6. Sediment- dispersal systems for late Morrowan deposition. From Puckette et al. (2008), after Puckette et al. (1996), Blakeney et al. (1990), Bowen et al. (1990), and Sonnenberg et al. (1990).	10
Figure 7. System tracts that controlled upper Morrowan deposition. Modified from Wheeler et al. (1990) by Al-Shaieb and Puckette (2001). (a) Lowstand systems tract (b) Transgressive systems tract.	11
Figure 8. General depositional sequence of Morrowan strata in the Northwest shelf of the Anadarko Basin. MFS= Maximum Flooding Surface, TSE= Transgressive Surface of Erosion. HST= High Stand Systems Tract, LST= Lowstand Systems Tract, TST= Transgressive Systems Tract. Modified from Wheeler and others (1990) by Devries (2005).	12
Figure 9. Map of Farnsworth Unit showing wells with core, thin sections, or both, that were observed for this study.	17
Figure 10. Summary stratigraphic column for well 8-5.	18
Figure 11. Summary stratigraphic column for well 9-8.	19
Figure 12. Summary stratigraphic column for well 13-10. Due to close proximity and similar lithology, a separate summary stratigraphic column was not made for well 13-10A. See Appendix A for a detailed stratigraphic column for well 13-10A.	20

Figure 13. Summary stratigraphic column for well 32-2.....	21
Figure 14. Summary stratigraphic column for well 32-6.....	22
Figure 15. Fine-grained Sandstone facies. (a) Well 13-10A, 7668 ft. (b) Well 13-10, 7667.6 ft to 7667.7 ft. Note soft sediment deformation and/or burrow.	23
Figure 16. Well 32-6, 7967 ft to 7977 ft. In well 32-6, the Coarse-grained Sandstone facies exhibits considerable variation in grain size at the centimeter scale, alternating in size between coarse sand and conglomerate. Note hematite staining, clay seams, and mudstone interbed.	25
Figure 17. Well 13-10A, 7677 ft to 7689 ft. Scale on left in in tenths of feet. Coarse-grained Sandstone facies. Sedimentary structures include cross bedding, clay seams, and stylolites.....	26
Figure 18. Coarse-grained Sandstone facies. (a) Well 8-5, 7653 ft. Carbonaceous stylolite (b) Well 32-2, 7940 ft. High-amplitude carbonaceous stylolite.	27
Figure 19. Coarse-grained Sandstone facies, Well 9-8. (a) Rounded mudstone intraclasts with desiccation cracks. (b) Clay seams and stylolites. (c) Low-angle cross bedding.....	27
Figure 20. Well 32-6, 7977 ft to 7782 ft. Coarse-grained Sandstone facies. Hematite stained, over-steepened cross beds exhibiting possible rhythmites sets. Note mudstone interbed in upper left corner. This bed contained very small shell fragments.....	28
Figure 21. Well 13-10A, 7704.9 ft to 7705.4 ft. The Paraconglomerate facies has a gradational upper contact with the Coarse-grained Sandstone facies and an erosional lower contact with the Basal Lag Conglomerate facies.	29
Figure 22. Basal Lag Conglomerate facies. (a) Well 13-10, 7696.3 ft to 7697.7 ft. (b) Well 32-6, 7999 ft to 7999.5 ft.	30
Figure 23. Well 13-10A, 7705.4 ft to 7706.2 ft. Basal Lag Conglomerate facies.	31
Figure 24. Well 8-5, 7644 ft. Brachiopod shell fragments in the Mudstone with Brachiopod Fossils subfacies. Small tick marks on ruler are millimeters.	32
Figure 25. Well 8-5, 7664.9 ft. Siderite concretion. Ruler is cm scale.	33
Figure 26. Well 8-5, Dark Gray Mudstone facies. (a) 7668.5 ft. Yellow mineral might be sulfur or jarosite. (b) 7667 ft. Plant fragment.....	34
Figure 27. Well 13-10A lower mudstone interval. Note: last 0.4 ft not pictured. Scale is in tenths of feet.....	34
Figure 28. Well 13-10A, 7629 ft to 7641 ft. Fissile dark gray mudstone with lighter gray, silty lenses. Scale on left is in tenths of feet.	35
Figure 29. Well 13-10A. 7610 ft, 7612 ft, 7614 ft, and 7612 ft. Calcareous upper mudstone with bioturbation. Note fossil hash layer (E6 sample location), burrows below, and coal.	36

Figure 30. Plot of porosity versus permeability for plugs obtained from conventional core of the upper Morrow sandstone. Note considerable inter-well variation in reservoir quality. Porosity and permeability data provided by Chaparral Energy.	39
Figure 31. Bar graphs showing grain sizes from samples on the western and eastern sides of FWU, data from Table 2. g.c. = granular conglomerate, vcU = very coarse upper sand, vcL = very coarse lower sand, cU = coarse upper sand, cL = coarse lower sand, mL = medium lower sand, fU = fine upper sand.	40
Figure 32. Plot of porosity versus permeability for plugs obtained from conventional core of the upper Morrow sandstone. Symbols indicate mean grain size (from visual estimate of rock near plug location). Gran. Congl. = granular conglomerate, vcU = very coarse upper sand, vcL = very coarse lower sand, cU = coarse upper sand, cL = coarse lower sand, mL = medium lower sand, fU = fine upper sand. Porosity and permeability data provided by Chaparral Energy.	41
Figure 33. Plot of porosity versus permeability for plugs obtained from conventional core of the upper Morrow sandstone. Symbols indicate degree of sorting (from visual estimate of rock near plug location). Porosity and permeability data provided by Chaparral Energy.	42
Figure 34. Porosity versus permeability of the western side and eastern side of FWU. Whereas both sides exhibit a wide range of reservoir quality, the eastern side does not achieve as high of permeability values as the west side. Porosity and permeability data provided by Chaparral Energy.	43
Figure 35. Box plots of plug porosity and permeability values for the western and eastern sides of FWU. (a) Porosity box plot. The median porosity is 1.6% higher in the western side of the field than the eastern side of the field. (b) Permeability box plot. The median permeability of the western side of the field is 14.8 md higher than the median permeability of the eastern side of the field. The maximum permeability of samples from the eastern side of the field is 28 md, but the maximum permeability of samples from the western side of the field is 290 md, which is an order of magnitude greater.	44
Figure 36. Sample E6, well 13-10A, 7668.10 ft. Photomicrograph of the Fine-grained Sandstone facies. Pink epoxy is not visible in the sample, which indicates that porosity is negligible. (a) xpl (b) ppl.	46
Figure 37. (a) Ternary plot based on the Folk (1968) classification showing the abundances of quartz (Q), lithics (R), and feldspar, including GRF's (F). The Fine-grained Sandstone can be classified as a lithic arkose. (b) Ternary diagram showing the abundance of grains, porosity, and cement. Porosity is negligible in this facies.	47
Figure 38. (a) Ternary plot based on the Folk (1968) classification showing the abundances of quartz (Q), lithics (R), and feldspar (including GRF's) (F). (b) Abundance of grains, porosity, and cement. (c) Abundance of Intergranular	

Macroporosity, Dissolution Porosity (Intragranular Macroporosity), and Microporosity (Inter- and Intragranular).	54
Figure 39. Carbonate cement ternary diagrams for samples E1- E4, from well 13- 10A. Values are in mol% oxide. Fresh and marine domains are from Mozley (1989). Note that composition of ankerite is fairly consistent in all samples, but siderite composition varies. (a) $\text{FeCO}_3\text{-MgCO}_3\text{-CaCO}_3$ diagram. (b) $\text{MnCO}_3\text{-MgCO}_3\text{-CaCO}_3$ diagram.....	58
Figure 40. Sample E5, well 13-10A, 7610.40 ft. Photomicrograph of a sample from the bioturbated mudstone facies. Many fossil fragments are composed of calcite. Some fossils, such as the crinoid pictured, have been replaced by silica. (a) xpl (b) ppl.....	59
Figure 41. Paragenetic sequence of the Morrow B sandstone.	61
Figure 42. Well 42-1, 8005 ft, xpl. A siderite crystal formed on the surface of a quartz grain, and a quartz overgrowth formed around the siderite, indicating that siderite precipitated before quartz cement.	62
Figure 43. Well 13-10A, 7675.9 ft. Siderite formed on a quartz grain and a quartz overgrowth grew next to and around the siderite. This suggests that the overgrowth came later and only grew on the grain surface that did not have siderite cement already. (a) Siderite cement fills the IGV between quartz grains, ppl. (b) A close-up of the area in the blue box in figure (a), ppl. (c) A backscattered electron (BSE) image of the same location.....	63
Figure 44. Well 42-1, 8015.5 ft, ppl. Calcite precipitated on a siderite crystal, indicating that siderite precipitated before the calcite.	64
Figure 45. Well 42-1, 8005 ft, ppl. A carbonaceous stylolite with abundant siderite. Siderite was probably concentrated around this stylolite during pressure solution.....	65
Figure 46. Sample E1, well 13-10A, 7675.90 ft. A BSE image labeled with FeCO_3 concentrations from microprobe analysis, in mol%. The inner siderite has a greater Fe concentration than the outer siderite, which indicates two stages of siderite cementation. The inner siderite likely precipitated before the outer siderite.....	66
Figure 47. Well 32-2, 7957 ft, ppl. Calcite and kaolinite surround quartz overgrowths, which indicate that the quartz overgrowths formed before the calcite or kaolinite.....	67
Figure 48. Well 32-3, 7987 ft, xpl. Poikilotopic calcite surrounds a quartz overgrowth, which suggests that calcite precipitated after quartz overgrowths. Floating feldspar relicts in poikilotopic calcite suggest that calcite replaced feldspar.....	67
Figure 49. Well 42-1, 8022 ft, xpl. (a) Quartz overgrowth in contact with a feldspar overgrowth. Quartz precipitation was restricted by the feldspar overgrowth and feldspar precipitation by the quartz overgrowth, suggesting they formed at the same time. (b) Quartz and feldspar overgrowths on a GRF. The boundary	

between the two overgrowths suggests that they precipitated at the same time because neither overgrowth is encroaching on the other.	69
Figure 50. (a) Well 42-1, 8015.5 ft, xpl. Grains floating in poikilotopic calcite cement suggest that poikilotopic calcite may have prevented compaction. (b) Well 9-8, 7709 ft, xpl. The presence of calcite adjacent to an area with a high degree of grain packing suggests that calcite precipitation overlapped with compaction, or a second stage of calcite cementation occurred after compaction.	71
Figure 51. (a) Well 32-1, 7994.5 ft, xpl. Poikilotopic calcite replaced the feldspar crystals in this VRF. The calcite in the VRF goes extinct at same time as the poikilotopic calcite surrounding the grain, suggesting that calcite replaced feldspar and precipitated around the grain at the same time. (b) Well 42-1, 8015.5 ft, xpl. Dissolution porosity within the feldspar grain suggests that poikilotopic calcite replaced some feldspar, and later the feldspar partially dissolved, leaving intragranular porosity.	72
Figure 52. Well 13-10A, 7696.25 ft. A BSE image showing ankerite that formed on the outside of a euhedral quartz overgrowth, which indicates that ankerite precipitated after quartz cement.	73
Figure 53. Sample E2, well 13-10A, 7684.75 ft. Ankerite replaced feldspar. Note that there are some micropores within the feldspar grain, and they are not filled with ankerite. This suggests that ankerite replaced feldspar, and some feldspar dissolution occurred later. (a) A photomicrograph, xpl. (b) A BSE image of the same feldspar grain.	74
Figure 54. Well 13-10A, 7684.75 ft, xpl. Different types of grain contacts within the same sample indicate varying degrees of compaction. (a) Convo-convex grain contacts and (b) sutured grain contacts indicate high levels of compaction.	76
Figure 55. Well 9-8, 7693 ft, ppl. Stylolites are the result of pressure solution, which indicate significant chemical compaction.	77
Figure 56. (a) Well 32-2, 7957 ft, ppl. Intragranular porosity in a feldspar grain from dissolution. Some intragranular porosity is filled with kaolinite. (b) Well 42-1, 8015.5 ft, ppl. Dissolution of feldspar in a GRF created intragranular porosity. Some intragranular porosity is filled with kaolinite. (c) xpl.	78
Figure 57. (a) Well 32-2, 7936 ft, ppl. Kaolinite “ghost grain.” (b) Well 32-1, 7970 ft, ppl. Kaolinite “ghost grains,” some with feldspar relicts. This suggests that other ghost grains may have originally been feldspar.	79
Figure 58. Well 9-8, 7693 ft, xpl. This sample is highly compacted, yet a delicate skeletal feldspar grain is preserved, which indicates that feldspar dissolution occurred after compaction. If the feldspar had dissolved before compaction occurred, it would have been crushed and the intragranular porosity would have been destroyed.	80

Figure 59. BSE images from sample E1, well 13-10A, 7675.90 ft. (a, b) Siderite, chlorite, and kaolinite filling a pore. (c) Siderite and chlorite blocking a pore throat. (d) Chlorite blocking a pore throat.	81
Figure 60. BSE images from well 13-10A. (a) Sample E2, 7684.75 ft. Siderite, chlorite, and kaolinite filling a pore. (b) Sample E3, 7686.4 ft. Kaolinite and chlorite filling a pore. The delicate booklets displayed by this kaolinite is indicative of authigenic clay.	82
Figure 61. Well 32-3, 7983 ft, ppl. This partially dissolved feldspar grain is surrounded by kaolinite, but kaolinite is not present within the intragranular porosity. This suggests that some feldspar dissolution may have occurred after kaolinite precipitation.	83
Figure 62. Well 13-10A, 7675.90 ft. This oil-stained kaolinite indicates that oil emplacement occurred after the precipitation of kaolinite. This kaolinite also displays authigenic textures in the form of delicate booklets.	84
Figure 63. Well 9-8, 7704 ft, ppl. Photomicrograph showing abundant intergranular macroporosity. The feldspar grain in the middle contains feldspar cement and some quartz grains have quartz overgrowths.	86
Figure 64. Well 32-2, 7936 ft, ppl. Macroporosity surrounded by authigenic clay and cement.	86
Figure 65. Well 32-1, 7980 ft, ppl. Intragranular macroporosity in a feldspar grain (center) appears to be connected to the surrounding intergranular macroporosity. In this example, the intragranular pores are effective. Elsewhere in the photo, the porosity has been reduced by quartz overgrowths and kaolinite.	88
Figure 66. Well 42-1, 8015.5 ft, ppl. Feldspar dissolution in a GRF created intragranular macroporosity. Note that some porosity has been filled with kaolinite. This grain is encased in poikilotopic calcite, so the porosity is not effective.	88
Figure 67. Well 13-10A, 7696.25 ft, ppl. These grain-sized pores are most likely the result of grain dissolution and appear to be interconnected. The high permeability of the sample is likely due to the presence of these grain-sized pores because most of intergranular porosity in this sample is filled with authigenic clay.	89
Figure 68. Well 32-2, 7957 ft, ppl. Kaolinite and quartz overgrowths blocking the throats of grain-sized pores. These pores are less effective because of the kaolinite.	90
Figure 69. Well 42-1, 8015.5 ft, ppl. Grain-sized pores in poikilotopic calcite from the dissolution of feldspar or rock fragments. These pores are not effective because they are isolated in the cement.	90
Figure 70. Well 13-10A, 7675.9 ft. Photomicrograph showing siderite and clay that fill an enlarged pore. The siderite is either partially cemented or partially dissolved, which created micro- and macroporosity. (a) xpl (b) ppl.	92

Figure 71. Well 42-1, 8028 ft, ppl. Microporosity and dissolution porosity in a feldspar grain. Some micropores are isolated within the grain, whereas others are connected to surrounding intergranular porosity.	93
Figure 72. Well 42-1, 8028 ft, ppl. Photomicrograph showing dissolution porosity in a feldspar grain that is partially filled with kaolinite.	94
Figure 73. Well 32-1, 7970 ft, ppl. Photomicrograph showing microporous kaolinite ghost grains, some of which have feldspar relicts.	95
Figure 74. Well 9-8, 7694 ft, ppl. Kaolinite ghost grains and kaolinite filling pores. In some places, the outlines of the ghost grain are well defined; in other places they are indistinguishable.	95
Figure 75. Photomicrographs showing fractures in the Morrow B sandstone. They are filled with epoxy so it is unlikely that they were caused by thin section preparation. The fractures may have been generated during differential compaction. (a) Well 32-3, 7983 ft, ppl. Microfractures in quartz grains. (b) Well 42-1, 8022 ft, ppl. Microfracture in a lithic fragment. The fracture is small and does not extend past the grain, so it probably does not contribute much to the permeability of the sample.	97
Figure 76. Porosity versus permeability by porosity facies. Porosity and permeability values are from thin sections that are dominated by a single porosity facies.	99
Figure 77. Representative thin sections from the “A” porosity facies. (a) Well 32-1, 7980 ft, ppl. Abundant intergranular macroporosity with very little authigenic clay. Quartz overgrowths have reduced porosity in some areas. (b) Well 32-1, 7983 ft, ppl. Abundant intergranular macroporosity with no authigenic clay.	101
Figure 78. Representative thin sections from the “B” porosity facies. Intergranular macroporosity is abundant, but trace amounts of clay, particularly in pore throats, makes it less effective. (a) Well 9-8, 7704 ft, ppl. (b) Well 32-2, 7936 ft, ppl.	102
Figure 79. Well 13-10A, 7679.25 ft, ppl. Representative thin section from the “C” porosity facies. (a) Several grain-sized pores are interconnected, making them effective. (b) Two grain-sized pores are interconnected, but also surrounded by clay, which may make them less effective.	103
Figure 80. Representative thin sections from the “D” porosity facies. Most porosity is filled with authigenic clay and cement. (a) Well 42-1, 8005 ft, ppl. (b) Well 13-10A, 7684.74 ft, ppl.	104
Figure 81. Representative thin sections from the “E” porosity facies. (a) Well 32-2, 7936 ft, ppl. Long grain contacts indicate significant compaction. (b) Well 9-8, 7694 ft, ppl. Abundant ghost grains.	105
Figure 82. Well 42-1, 8015.5 ft, ppl. Representative thin section from the “F” porosity facies. (a) Two large pores are surrounded by poikilotopic calcite, and therefore are not effective. (b) Dissolution pores are filled with kaolinite and surrounded by poikilotopic calcite.	106

Figure 83. Well 13-10A, 7675.9 ft, ppl. Representative thin section from the “G” porosity facies. Siderite is abundant and occludes porosity.	107
Figure 84. Well 13-10A, 7689.4 ft, ppl. Representative thin section from the “H” porosity facies. This facies is found in a sample that is highly compacted, with very little IGv. Most porosity is found within partially dissolved rock fragments. (a) Stylolites in this VRF indicate significant compaction. All porosity pictured is intragranular. (b) Intragranular porosity from dissolution of a rock fragment.	108
Figure 85. Comparison of pore throat diameter vs. mercury saturation for samples E1 – E4, well 13-10A. Mercury saturation is expressed in incremental percent of the pore volume.....	110
Figure 86. MICP data for samples E1 – E4 from well 13-10A. Mercury saturation is expressed in incremental percent of the pore volume. (a) Sample E1 (b) Sample E2 (c) Sample E3 (d) Sample E4.	111
Figure 87. (a) Dominant pore-throat size versus plug permeability. There is a strong positive correlation, $R^2 = 0.986$. (b) Secondary pore-throat size versus plug permeability. There is a negative correlation. Note that sample E2 is not bimodal, and therefore does not have a secondary pore-throat size.	112
Figure 88. Average image porosity versus plug porosity. There is a correlation between average image porosity and plug porosity, $R^2 = 0.871$	114
Figure 89. Pore size versus permeability. (a) Average pore area, $R^2 = 0.617$ (b) Average pore diameter, $R^2 = 0.843$ (c) Largest pore area, $R^2 = 0.852$ (d) Largest pore diameter, $R^2 = 0.257$	115
Figure 90. Depositional model for the Farnsworth Unit. Modified from Wheeler et al. (1990) and Puckette et al. (2008). MFS= Maximum Flooding Surface. LSE= Lowstand Surface of Erosion. TSE= Transgressive surface of Erosion.	119
Figure 91. Box plots of XRD data from Munson (1988) and this study. (a) Total clay, in percent of whole rock. (b) Smectite clay fractionation, weight% (c) Chlorite clay fractionation, weight% (d) Kaolinite clay fractionation, weight%.	123
Figure 92. Box plots of select point counting data. (a) Total matrix, (b) Total clay, (c) Total cement, and (d) IGv.	124
Figure 93. Box plots of porosity point count data. (a) Total macroporosity and (b) Total microporosity.....	125

(Signature Page)

CHAPTER 1. INTRODUCTION

Significance of Research

Farnsworth Unit (FWU) is the site of one of the first commercial-scale carbon capture, utilization, and storage (CCUS) projects in the United States (NATCARB Atlas, 2012). It was selected as a CCUS pilot site by the Southwest Regional Partnership on Carbon Sequestration (SWP), one of seven regional partnerships established by the Department of Energy (DOE)'s Office of Fossil Energy. Each regional partnership has developed a regional carbon management plan to identify suitable storage strategies and technologies, aid in regulatory development, and propose appropriate infrastructure for CCUS commercialization (DOE, 2012). The National Energy Technology Laboratory (NETL) manages the partnerships.

Currently, FWU is in the injection phase of the CCUS project. A major goal of this project is to inject 1 million tonnes of anthropogenic CO₂ into the upper Morrow sandstone reservoir in FWU over a 5 year period. Other general goals include supporting industry's ability to assess CO₂ storage capacity, develop and validate technologies to ensure storage permanence, develop technologies to improve reservoir storage efficiency while ensuring containment effectiveness. Techniques developed at FWU will help in the creation of Best Practice manuals and workflows for monitoring, verification, accounting, and assessment; site screening, selection, and initial characterization; public outreach; well management activities; and risk analysis and simulation (SWP 2014 annual meeting). This study is part of the geological characterization aspect of the project.

The purpose of this study is to better understand how the depositional environment and diagenesis of the upper Morrow sandstone affects reservoir heterogeneity and how it relates to CO₂ storage in FWU. This study aims to (1) determine the depositional environment of the upper Morrow sandstone and (2) assess the principle micro-scale controls on porosity and permeability. Understanding reservoir heterogeneity at different scales is important to predict the behavior of injected CO₂ and estimate the volume of CO₂ that can be stored.

Production History

Farnsworth Unit (FWU) is located in Ochiltree County, Texas and is currently operated by Chaparral Energy, L.L.C. (Chaparral). The field is geologically located on the northwest shelf of the Anadarko Basin (Figure 1), and is the largest upper Morrowan oil field in the western part of the basin (McKay and Noah, 1996). FWU was discovered in 1955 and unitized in 1964, which is when waterflooding was implemented (Munson, 1988; McKay and Noah, 1996). Before the implementation of waterflooding, the eastern side of the unit produced more oil than the western side (Munson, 1988). Since the implementation of waterflooding, the western side of the field has produced more

(Munson, 1988). Peak production during the water-flooding stage was 7,967 BOPD in 1972 (McKay and Noah, 1996). The upper Morrow sandstone, or “Morrow B,” is the primary target for oil production and CCUS and is locally and informally referred to as the “Buckhaults” (Munson, 1988). The sandstone ranges in thickness from 0 to 54 feet within the field, with an average thickness of 29 feet (Munson, 1989). The trapping mechanism is stratigraphic (Munson, 1989).

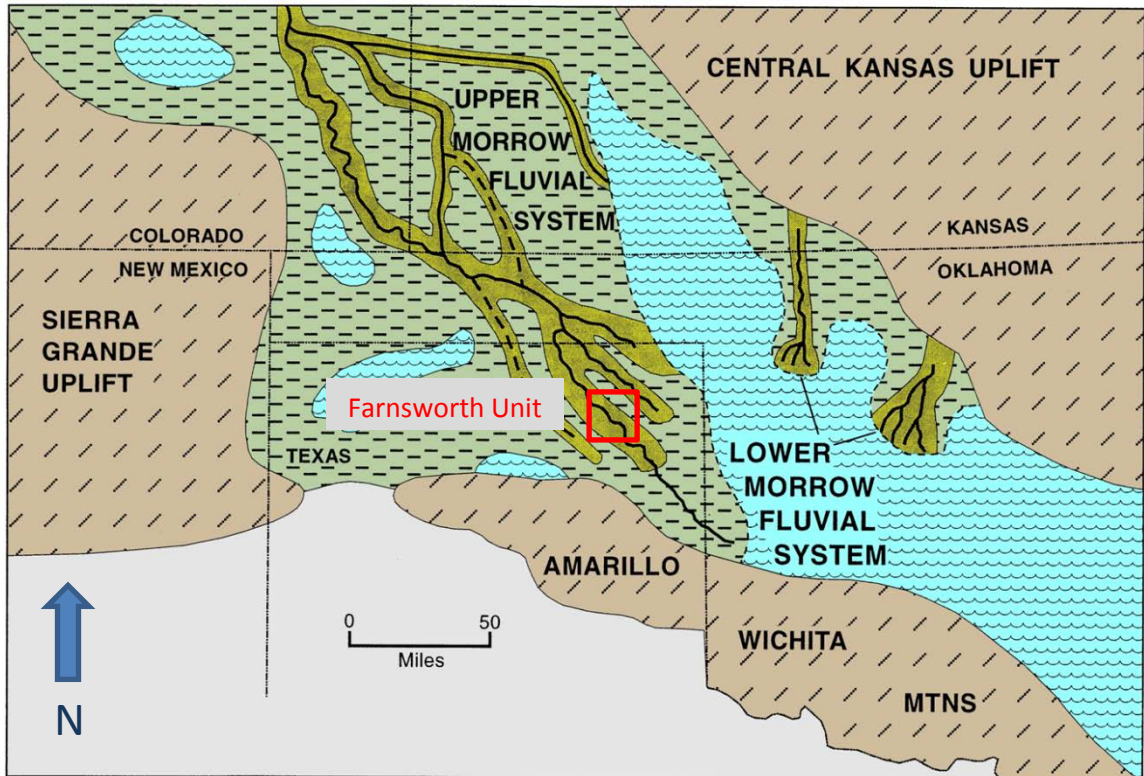


Figure 1. Paleogeography of the Morrow in the mid-continent. Modified from Swanson (1979) by R. Andrews, Oklahoma Geological Survey.

Background

Carbon Capture, Utilization, and Storage

The purpose of carbon capture, utilization, and storage is to reduce the amount of CO₂ released into the atmosphere to help mitigate the effects of anthropogenic climate change. The “Utilization” part of CCUS is using the CO₂ for economic gain, such as Enhanced Oil Recovery (EOR), before permanently storing it. Using CO₂ for EOR is common in the oil industry, but most of the CO₂ is usually produced from natural, geological sources (Bachu, 2008). CCUS uses anthropogenic sources of CO₂ for EOR. After the CO₂ is injected, some is produced along with the oil, but a significant volume CO₂ remains trapped within the pore space of the reservoir (Bachu, 2008). The produced CO₂ is separated from the produced oil and water, re-injected, and the process repeats.

The four main CO₂ trapping mechanisms are structural and stratigraphic trapping, residual trapping, solubility trapping, and mineral trapping (Figure 2). Structural and stratigraphic trapping play a major role immediately after initial CO₂ injection; however,

they are the least secure types of trapping because they are more susceptible to leaks (IPCC, 2005).

When a plume of CO₂ moves through a pore network, residual trapping occurs when small amounts of CO₂ “snap off” of the plume and become isolated within pores (Figure 3). The CO₂ is immobilized due to the interfacial tension between the CO₂ and the formation water (Bachu, 2008). The CO₂ begins to dissolve into the oil and water, which is known as solubility trapping. Mineral trapping occurs when the CO₂ reacts with the rock and pore waters and precipitates as a solid mineral within the reservoir. Mineral trapping is the most secure form of CO₂ storage, but it can take hundreds or thousands of years before it occurs.

Residual Trapping

Residual trapping of CO₂ is essentially the opposite of recovery efficiency, which is mobilizing trapped oil. Oil and CO₂ are both the non-wetting phase of a water-wet system. The two main properties that affect recovery efficiency/residual trapping are the pore system and the fluid properties. According to Wardlaw and Cassan (1978), the pore-network properties that control recovery efficiency (inverse of residual trapping potential) are: the pore-to-throat size ratio, the throat-to-pore coordination number, and the type and degree of nonrandom heterogeneity. As the pore-to-throat diameter and volume ratios increase, the residual trapping potential increases (Wardlaw and Cassan, 1978). The coordination number is the number of throats connected to each pore, and recovery efficiency increases (residual trapping decreases) as coordination number increases.

This study will in part evaluate properties of the pore system that affect the residual trapping potential of the Morrow B sandstone. When evaluating porosity and permeability, the term “reservoir quality” is used from the standpoint of oil production: high porosity and permeability are generally favorable. However, high porosity and permeability do not necessarily indicate a higher potential for residual trapping. Factors that cause low “reservoir quality” by decreasing porosity and permeability, such as poor sorting or large amounts of matrix, may increase the residual trapping potential (Holtz, 2002).

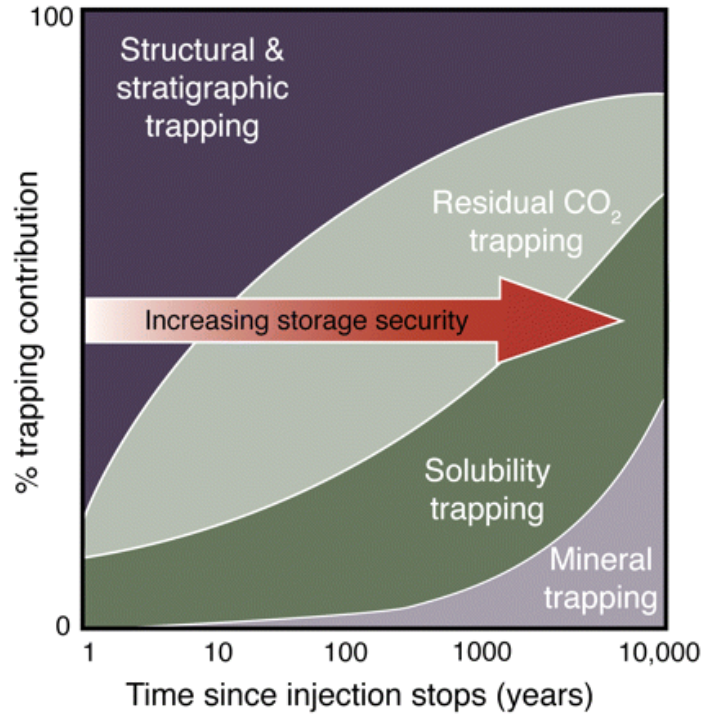


Figure 2. Time versus trapping contribution of the four main trapping mechanisms. From IPCC (2005).

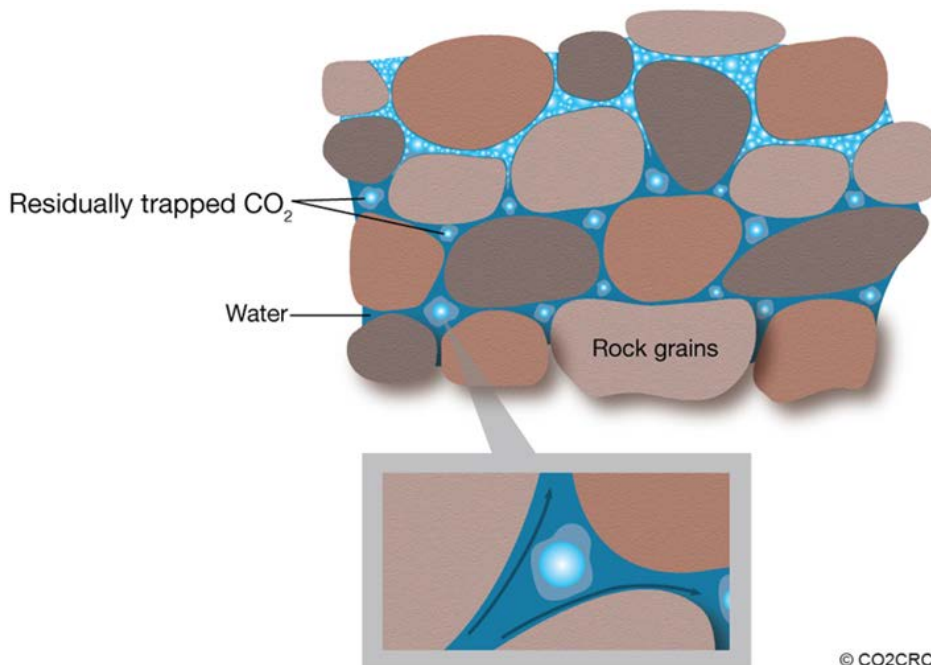


Figure 3. Illustration of residual trapping of CO₂. When a plume of CO₂ moves through a pore network, residual trapping occurs when small amounts of CO₂ “snaps off” of the plume and become isolated within pores. Figure source: The Cooperative Research Centre for Greenhouse Gas Technologies (CO2CRC).

Previous work

Anadarko Geology

The Morrowan sandstones of the Anadarko Basin have been extensively studied because they were, and continue to be, targets for oil production. The tectonic setting, stratigraphy, and depositional history of the region have been described by Forgotson et al. (1966), Swanson (1979), Rascoe and Adler (1983), Sonnenberg et al. (1990), and Wheeler et al. (1990).

The understanding of the depositional environment of the Morrow Formation has evolved over the decades. Early workers believed that the upper Morrow sandstone was deposited in fluvial-deltaic environments (Swanson, 1979). These studies had limited data and relied heavily on log-signatures for depositional environment interpretations (Puckette et al., 1996). As more fields were developed and studied, the understanding of the geology improved. In particular, applying sequence stratigraphic concepts significantly improved the depositional model for the upper Morrowan sandstones (Al-Shaieb et al., 1995). This incised valley-fill model of the Anadarko basin was developed by Krystinik and Blakeney (1990), Sonnenberg (1990), and Wheeler et al. (1990) based on studies of Morrow reservoirs in eastern Colorado and western Kansas.

Krystinik and Blakeney (1990) describe fluvial and estuarine lithofacies and discuss depositional and diagenetic controls on reservoir quality. Sonnenburg et al. (1990) described the regional structure and sequence stratigraphy of the Anadarko Basin. Wheeler et al. (1990) observed 72 cores and described the main lithofacies and depositional environments of the Morrow Formation.

Farnsworth Field

There is very little literature focusing specifically on the Farnsworth Unit. Relevant studies include Munson (1988 and 1989) and McKay and Noah (1996).

Munson 1988 and 1989

By far the most comprehensive geological study of Farnsworth Unit is an excellent unpublished master's thesis of Munson (1988), and a summary of the thesis in the Oklahoma Geological Society's circular, "Shale Shaker" (Munson, 1989). Munson used the available well logs and core data to map the thickness and structure of the Buckhaults (Morrow B) Sandstone across the field. He analyzed the sedimentary structures and textures of core and performed grain size analysis to determine the depositional environment of the Buckhaults Sandstone. He also analyzed the mineralogy and abundance of clay in the field. Finally, he performed petrographic work to classify the rock types, speculate on the sediment source area, and describe the diagenetic history of the Buckhaults Sandstone.

Munson (1988) concluded that the upper Morrow sandstone in FWU was deposited as distributary channels and distributary mouth bars in a fluvial-deltaic environment. He indicated that higher authigenic clay content in the sandstone from the eastern side of the field could be the reason for the lower permeability. He also speculated that an engineering issue due to well spacing and development could be the reason why wells on the eastern side of the field did not respond as well to waterflooding as wells on the western side.

Certain aspects of the work in Munson (1988) can be improved and expanded upon using more modern approaches. The depositional model in particular should be reevaluated because the utility of using grain size analysis, such as skewness and kurtosis, to determine depositional environment has been called into question (e.g., Ehrlich, 1983). Also, many studies of the upper Morrow sandstone have been published since Munson (1989) was published, allowing Farnsworth Unit to be placed within a wider depositional framework of the Anadarko Basin.

Munson (1988) serves as the foundation of this study. The present study builds upon and improves upon his analysis in several ways: (1) The interpretation of depositional environment using modern sequence stratigraphic techniques. (2) The petrographic characteristics of the porosity are described in greater detail and directly related to permeability data. (3) The diagenesis is described in greater detail, including the addition of microprobe data for carbonate cements. (4) The potential for residual trapping of CO₂ is considered.

McKay and Noah 1996

McKay and Noah (1996) used the findings from Munson (1989) and other unpublished theses, internal Unocal reports, along with new data from the field to reinterpret reservoir geometry and redefine the depositional environment model. They found three types of sandstone deposits in Farnsworth core: point-bar, mixed-load sinuosity channel-fill, and overbank splay and sheet flood-plain. They note that the upper Morrowan sandstones in Colorado are incised valley deposits, but that in the Oklahoma and Texas Panhandles, the valleys are less incised, and that they are the result of point-bar deposition. They concluded that the upper Morrow sandstone in FWU was deposited by a fluvial-deltaic system. There are at least two shortcomings to their interpretation: (1) their depositional model shows the fluvial process changing from meandering to braided in a down-stream direction, which is very unusual, and (2) they do not cite any of the literature that was published a few years prior which created an integrated depositional history of the Anadarko Basin based on sequence stratigraphy.

CHAPTER 2. GEOLOGICAL SETTING

Regional Stratigraphic Framework

The Farnsworth Unit is one of many oil fields on the northwest shelf of the Anadarko Basin, which spans the Texas and Oklahoma panhandles, southeastern Colorado, and western Kansas (Figure 1). In the study area, Morrowan-aged strata underlie the Akotan-aged “Thirteen Finger Limestone” and unconformably rest on Mississippian Chesterian strata (Figure 4; Cunningham, 1961). The “Morrow Formation” (which is an operational name) is broken into the upper Morrow and lower Morrow, the boundary of which is generally defined by a limestone marker bed (Puckette et al. 1996, 2008). The upper Morrow generally contains multiple sandstone units separated by mudstone intervals. FWU contains five upper Morrow sandstones and produces from the upper-most sandstone unit, locally known as the “Morrow B” and “Buckhaults” (Figure 4; Munson, 1988).

Tectonic Setting

The Wichita orogeny was the result of the collision between the North American and South American plates from the late Morrowan into early Desmoinesian time (Roscoe and Adler, 1983). The tectonic events that comprise the Wichita orogeny are the folding and faulting of the Ouachita foldbelt; the subsidence of the Arkoma basin; the emergence of Amarillo-Wichita, Apishapa, and Nemaha uplifts; and the uplift of the Cimarron arch and small structures along the Las Animas arch (Roscoe and Adler, 1983).

Positive features that were present during the deposition of upper Morrowan rocks and are possible sediment-source areas include: Sierra Grande Uplift to the west, Cimarron arch and Keyes Dome to the west and northwest, Central Kansas Uplift to the northeast, Bravo Dome to the west-southwest, Dalhart Basin to the west, and Plainview Basin and Nemaha Ridge to the south and east (Figure 5; Munson, 1988; Sonnenburg et al., 1990).

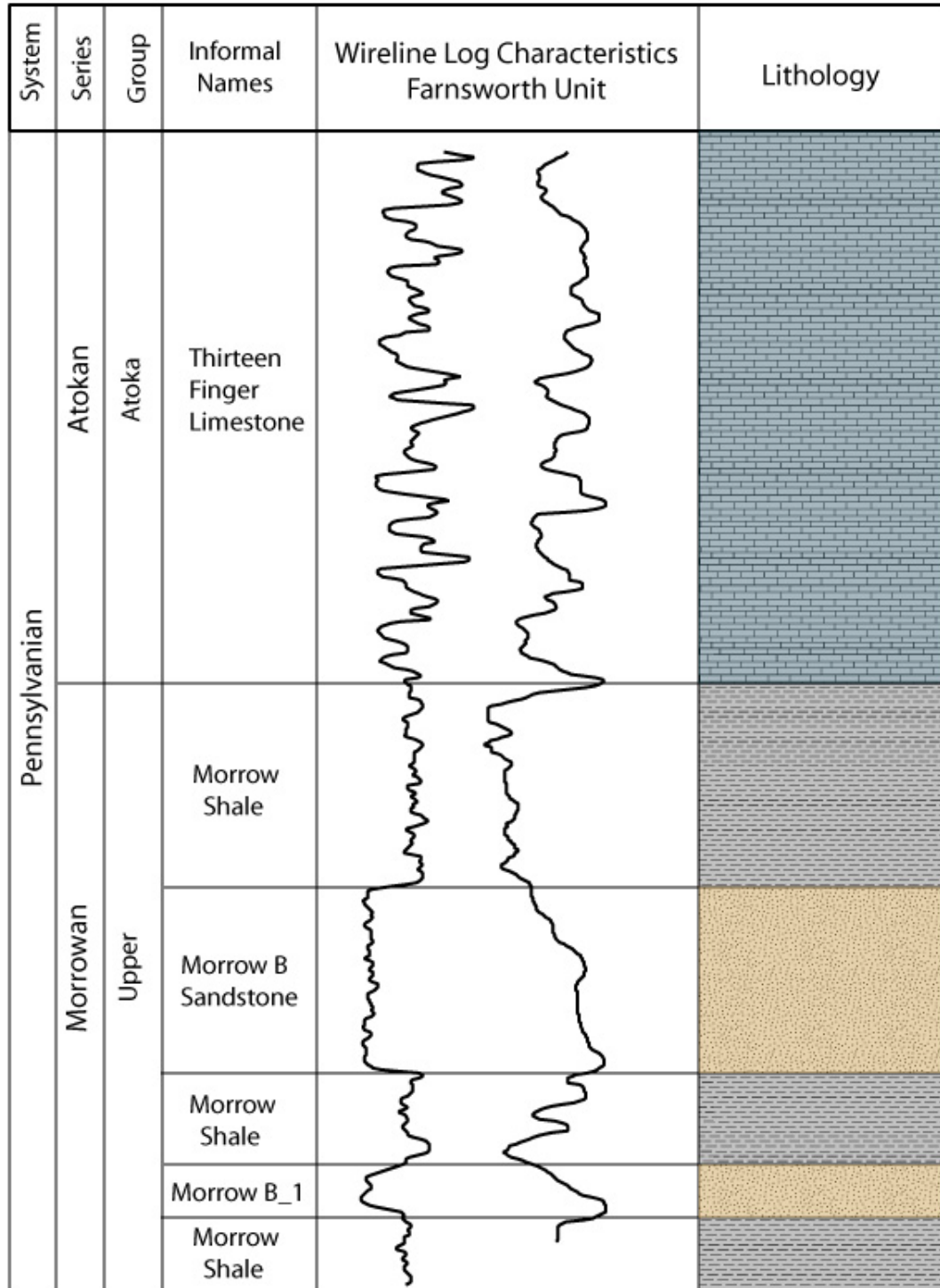


Figure 4. Stratigraphic chart showing divisions of the Upper Morrowan and Lower Atokan-aged strata in the Farnsworth Unit. Wireline log is from well 32-2. Modified from Munson (1989) and Puckette et al. (2008) by Dylan Rose-Coss and Sara Gallagher.

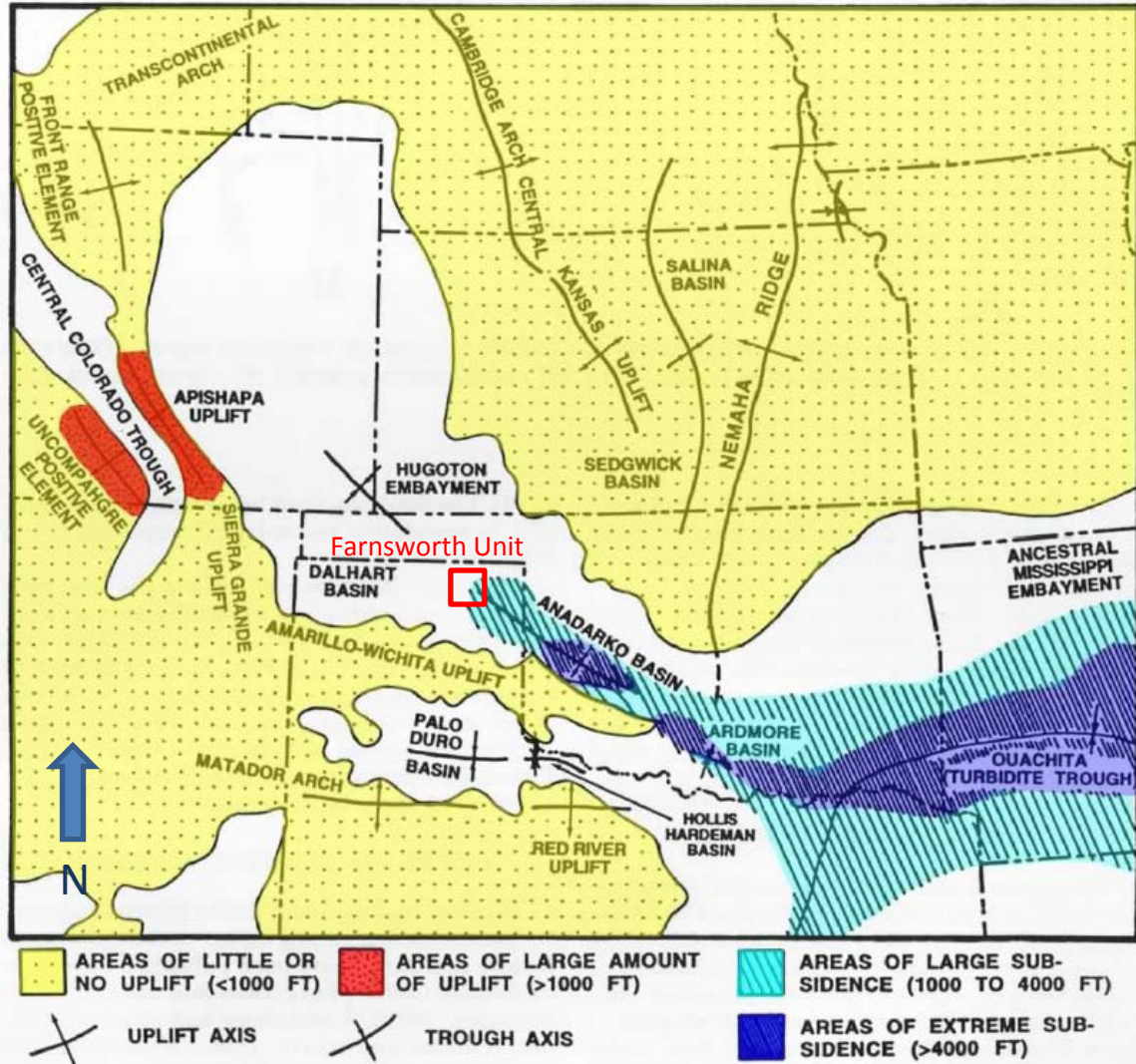


Figure 5. Structural features during Morrowan time. Modified from Sonnenburg et al. (1990) in DeVries (2005).

Sequence stratigraphy and depositional environment

Glaciation is thought to be the main cause of the rapid sea level fluctuations during Pennsylvanian time (Sonnenburg et al., 1990), which controlled the deposition of Morrowan rocks (Sonnenburg et al., 1990; Krystinik and Blakeney, 1990; Wheeler et al., 1990; Al-Shaieb et al., 1995). Upper Morrowan deposits represent two processes: valley incision during episodes of regression and infilling of valleys during subsequent transgression (Wheeler et al., 1990; Al-Shaieb et al., 1995). When sea level was low, fluvial systems were dominated by erosion and sediment was transported towards the southeast (Figures 6 and 7a; Wheeler et al., 1990). Channel lag deposits represent the lowstand systems tract (Figure 8; Wheeler et al., 1990). When sea level rose initially, these valleys were filled with fluvial sediments (Figure 8). During continued transgression, the valleys flooded and estuarine and floodplain sediments were deposited (Figure 7b and 8). The final phase of deposition covered these deposits with nearshore to offshore marine mud (Figure 7b and 8; Wheeler et al., 1990).

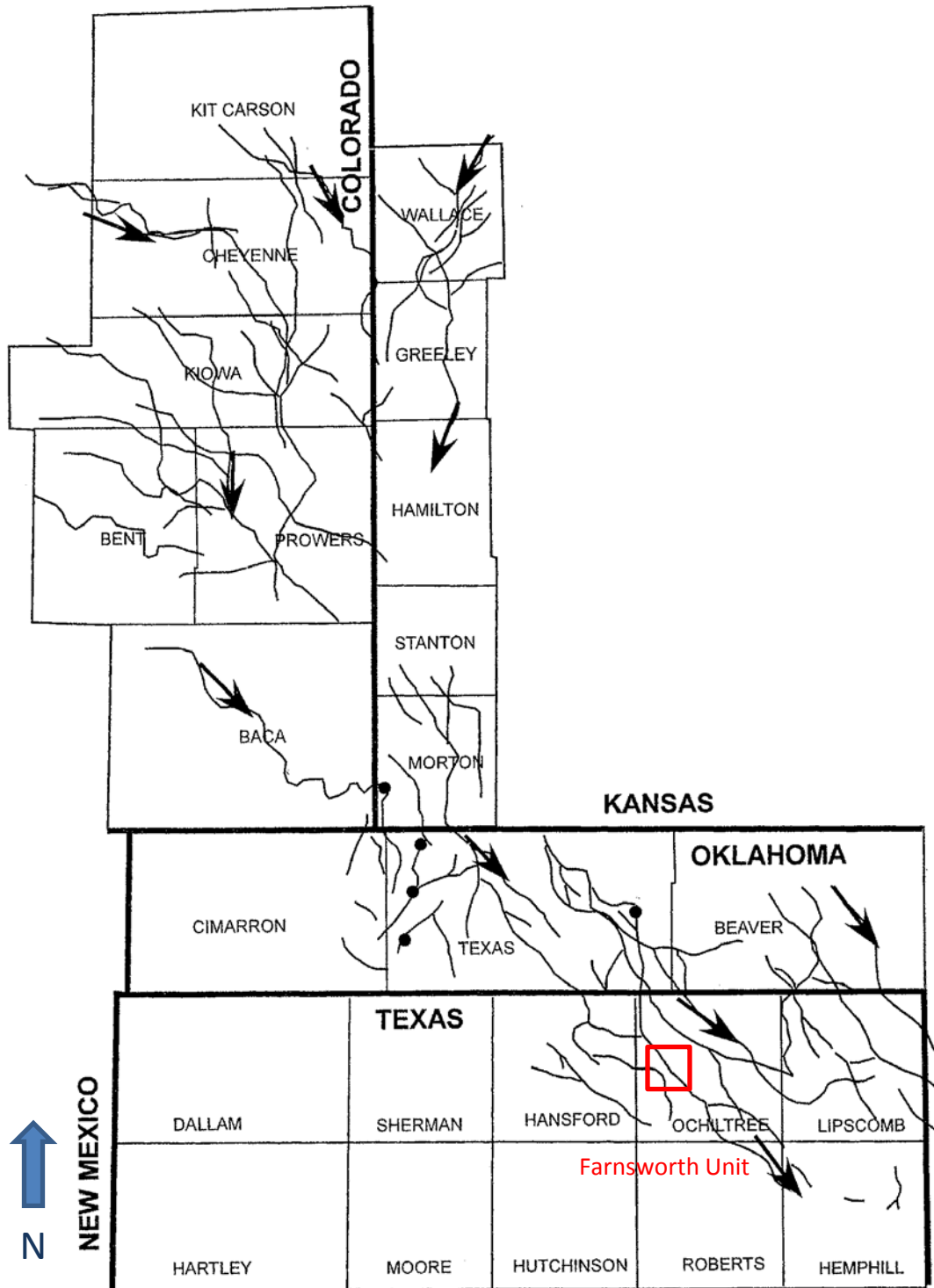


Figure 6. Sediment- dispersal systems for late Morrowan deposition. From Puckette et al. (2008), after Puckette et al. (1996), Blakeney et al. (1990), Bowen et al. (1990), and Sonnenberg et al. (1990).

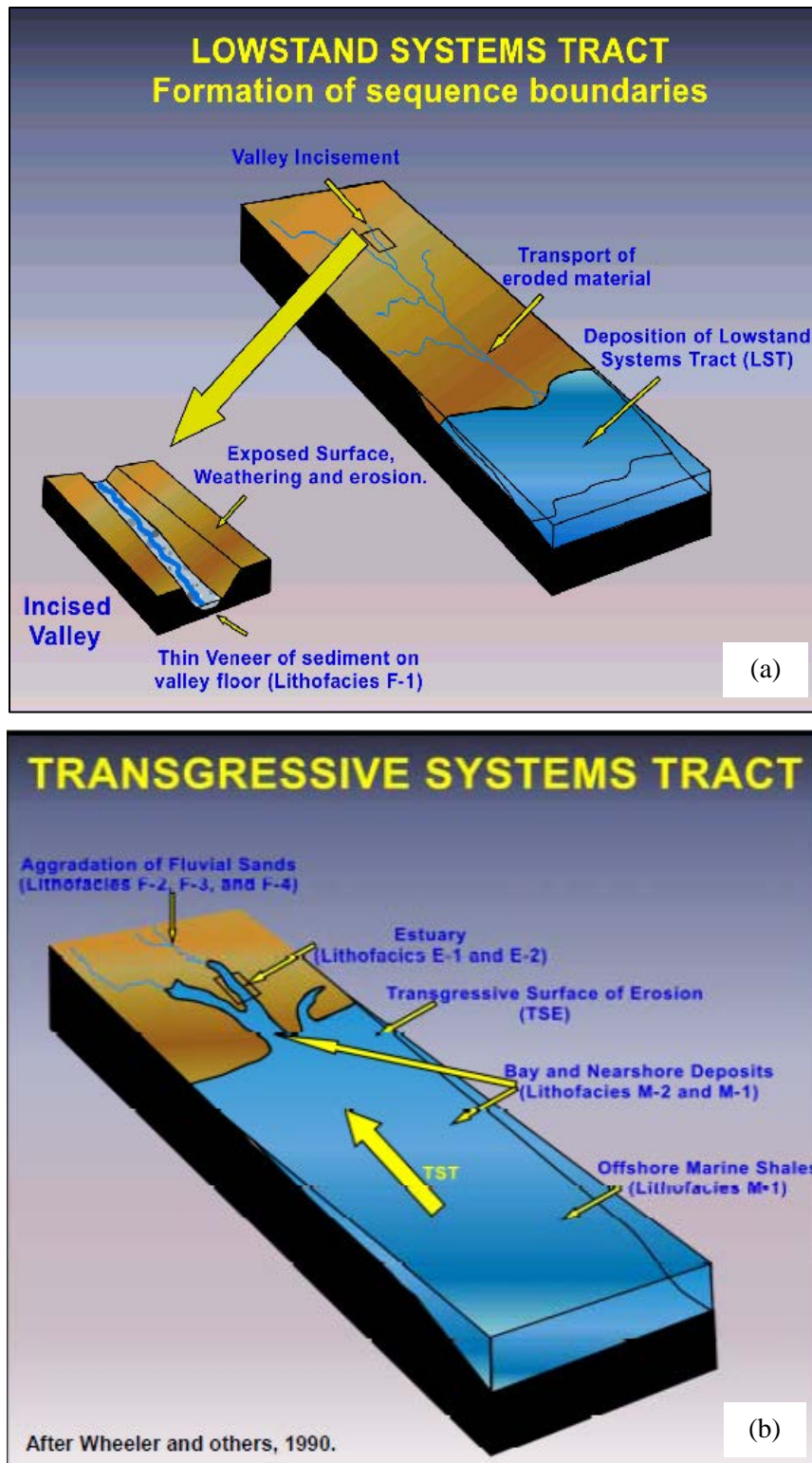


Figure 7. System tracts that controlled upper Morrowan deposition. Modified from Wheeler et al. (1990) by Al-Shaieb and Puckette (2001). (a) Lowstand systems tract (b) Transgressive systems tract.

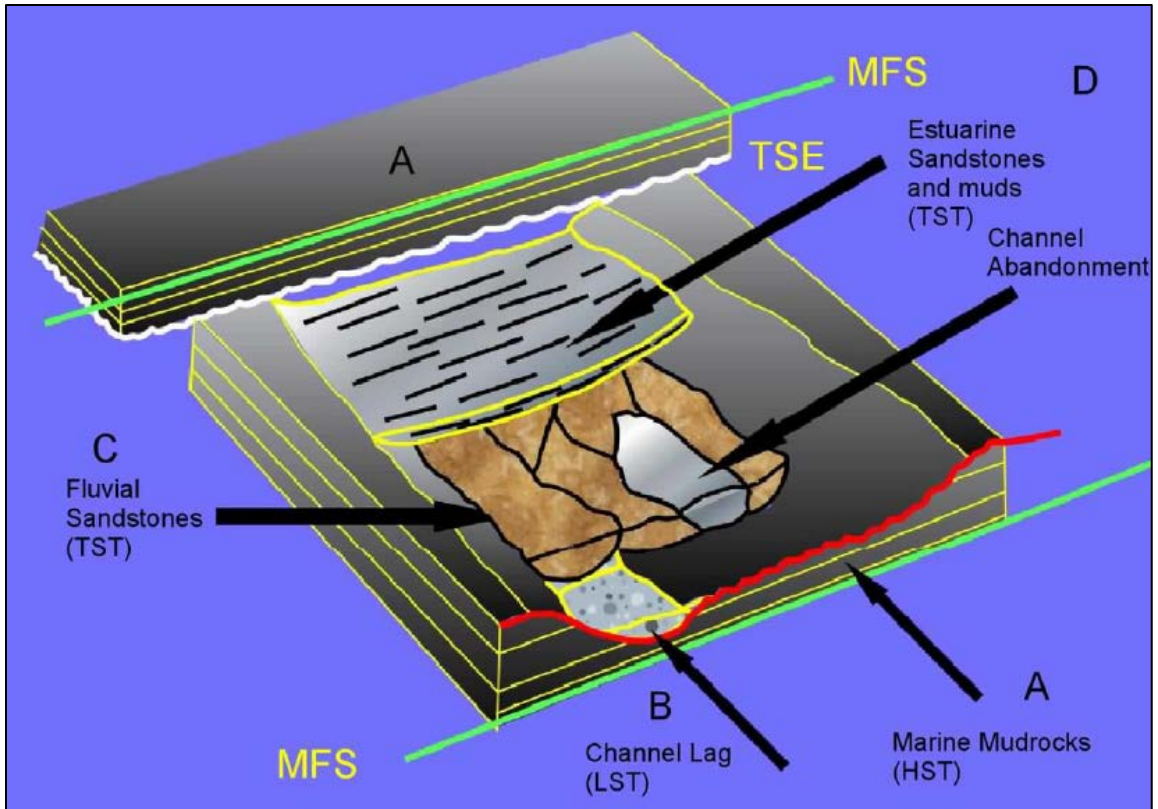


Figure 8. General depositional sequence of Morrowan strata in the Northwest shelf of the Anadarko Basin. MFS= Maximum Flooding Surface, TSE= Transgressive Surface of Erosion. HST= High Stand Systems Tract, LST= Lowstand Systems Tract, TST= Transgressive Systems Tract. Modified from Wheeler and others (1990) by Devries (2005).

CHAPTER 3: METHODS

Core Descriptions and Data Analysis

Cored intervals from six wells, four from the western side of the field (8-5, 9-8, 13-10, and 13-10A) and two from the eastern side of the field (32-2 and 32-6), were described (Figure 9). All wells besides 13-10A were drilled previously, and well 13-10A was drilled during this study. No destructive sampling was permitted for any core except 13-10A, so for the other cores, observations were limited to visual inspection aided by hand lenses and grain size cards. Texture, including grain size and sorting, and sedimentary structures, such as bedding and siderite concretions, were described. The descriptions were used to divide the core into seven lithofacies. These descriptions and lithofacies are represented in stratigraphic columns (Appendix A). These data were used to determine the depositional environment of the upper Morrow sandstone in Farnsworth Unit and the relationship between primary texture and porosity and permeability.

Porosity and permeability (P&P) data from laboratory analysis of core-plug samples for wells 8-5, 9-8, 13-10, 32-2 and 32-6 was provided by Chaparral Energy. Routine plug analysis for well 13-10A was performed by TerraTek in Salt Lake City, Utah. When observing the older cores, the location where the plug sample was taken was sometimes visible. The grain size and sorting at the sample location was recorded, and for these locations the P&P data was plotted against the textural data to analyze textural control on reservoir quality. If the location of the P&P plug was not apparent, but a thin section was available, the grain size and sorting of the thin section was noted.

Petrography

Petrography was performed using an Olympus CX31 petrographic microscope equipped with a Canon EOS Rebel T2i camera. Thirty-one thin sections, from various intervals from seven different cored wells, were observed. Six thin sections were created by Wagner Petrographic from the new 13-10A core. The other 25 thin sections were provided by Timothy Munson and were the same thin sections described in Munson 1988 and 1989. Twenty-nine of the thin sections were taken from the coarse-grained (reservoir) sandstone, one from the fine-grained sandstone just above the reservoir sandstone, and one from a fossil hash layer in the upper mudstone interval. The thin sections were impregnated with blue or pink epoxy to aid in porosity determination. See Appendix B for an inventory of thin sections and analyses performed.

Three hundred-point counts were performed on each of the coarse-grained sandstone thin sections and one fine-grained sandstone sample to quantify the abundance

of grain types, matrix, and porosity. The amount of quartz, feldspar (plus granitic rock fragments), and lithic fragments (including chert) were recalculated to 100% and plotted on a ternary diagram after Folk (1968) to classify the rock type. Additional 100-point porosity counts were performed on each coarse-grained sandstone thin section to quantify the porosity types. For thin sections that did not have sufficient porosity to complete a 100-point count, a visual estimate of porosity types was made. These data were plotted on a ternary diagram showing the percentages of intergranular macroporosity, dissolution porosity, and microporosity.

Photomicrographs were taken with a digital camera to document porosity distribution, texture, and sedimentary structures. These data were used to determine the diagenetic history of the upper Morrow sandstone and interpret the porosity and permeability data.

Porosity facies were determined based on the pore types controlling permeability. Each thin section was assigned a dominant porosity facies, and a representative thin section was selected for each facies. Porosity versus permeability was plotted by facies to determine the ranking of reservoir quality for each facies.

X-ray Diffraction Analysis

X-ray Diffraction Analysis (XRD) was performed by TerraTek in Salt Lake City, UT. Six samples from well 13-10A were analyzed for whole-rock mineralogy, including < 4 μm grain size (i.e., clay size fractionation), as well as relative clay abundance including percent expandability of illite and smectite. See Appendix C for detailed XRD methods.

Electron Microprobe Analysis

Four thin sections from the reservoir sandstone of Well 13-10A were analyzed at the New Mexico Bureau of Geology and Mineral Resources (on the New Mexico Institute of Mining and Technology campus) using a CAMECA SX-100 electron microprobe with three wavelength dispersive (WD) spectrometers. Samples were carbon coated then examined using backscattered electron (BSE) imaging, and the elemental composition of selected cement and clay were analyzed quantitatively. Analytical standards included the following minerals: albite, anorthite, apatite, barite, calcite, dolomite, fluorophlogopite, forsterite, ilmenite, magnesium oxide, magnetite, manganese oxide, orthoclase, pyrite, scapolite, siderite, and strontium titanate. An accelerating voltage of 15 kV and probe current of 20 nA was used with the exception of analyses using a general glass label which utilized a 10 nA probe current. A beam diameter of 20 μm was used for most sample locations, but a 10 μm beam was used when necessary, particularly for very small accumulations of clay. Results were given in weight percent of oxide. Totals of 100%, plus or minus 2%, are considered within the acceptable range of error. For carbonate cements, the data was recalculated for carbonate and normalized to 100%, then converted to mol%. See Appendix D for raw microprobe data.

Mercury Injection Capillary Pressure

Four samples from well 13-10A were selected for Mercury Injection Capillary Pressure (MICP) analysis. Sample plugs were cleaned by TerraTek then sent to PoroTechnology for MICP analysis. Samples were trimmed to one inch by one inch and

analyzed using a Micromeritics AutoPore IV 9500 series machine. Mercury was incrementally injected into the plugs under increasing pressure up to 6,000 psi and the volume of mercury entering the sample was recorded. The size distribution of the pore throats was calculated by PoroTechnology using the Washburn equation (Washburn, 1921; Li et al., 2005).

Image Analysis

ImageJ was used to analyze the pore size distribution and porosity of photomicrographs from thin sections. A total of 23 photomicrographs from the samples that underwent MICP analysis were analyzed with ImageJ. Photos were pre-processed in Adobe Photoshop. The jPOR plug-in was used to threshold photos in ImageJ. See Appendix E for detailed methods.

CHAPTER 4: RESULTS

Core Description and Lithofacies

Cores from six wells were described (Figures 9 to 14). Five of the wells were drilled early in the field's history and the core primarily consists of the reservoir sandstone. Well 13-10A was drilled during this study and the entire interval of the upper Morrow formation was cored, including the mudstone above and below the reservoir sandstone. The cores were subdivided into four principal lithofacies and seven subfacies based on lithology and sedimentary structures (Table 1). The four principle lithofacies are: Fine-grained Sandstone, Coarse-grained Sandstone, Conglomerate, and Mudstone. The conglomerate lithofacies is subdivided into the Paraconglomerate and Basal Lag Conglomerate subfacies. The Mudstone lithofacies is subdivided into the Mudstone with Brachiopod Fossils, the Dark Gray Mudstone, and Bioturbated Mudstone subfacies. See Appendix A for detailed stratigraphic columns and Appendix F for photos of core from well 13-10A.

Table 1. Lithofacies descriptions for FWU core.

Lithofacies	Subfacies	Found in wells	Description
Fine-grained Sandstone		13-10, 13-10A	Light gray, very fine sandstone interbedded with mudstone. Fines upward. Clay drapes, lenticular bedding. Low-angle cross beds. Burrows or soft sediment deformation.
		8-5, 9-8, 13-10, 13-10A, 32-2, 32-6	Coarse - very coarse sandstone and conglomerate. Moderate - poorly sorted. Cross bedding, laminar bedding, or massive bedding. Stylolites and clay seams.
Conglomerate	Paraconglomerate	13-10A	Paraconglomerate with a light gray, fine-grained sandstone matrix. Intraclasts are subrounded, 2 mm to 3 cm long, consisting of mudstone and sandstone rip-up clasts and pyrite.
	Basal Lag Conglomerate	13-10, 13-10A, 32-6	Clast-supported conglomerate with clay matrix. Subrounded clasts. Maximum grain size 5 cm. Mudstone and siderite rip-up clasts.
Mudstone	Mudstone with Brachiopod Fossils	8-5	Dark gray mudstone with brachiopod fossils
	Dark Gray Mudstone	8-5, 9-8, 32-6	Gray to dark gray, massive to fissile mudstone. Top half of 8-5 mudstone carbonaceous material. 8-5 and 9-8 have coal and sulfur. Siderite concretions in 8-5 and 32-6. No fossils observed.
	Bioturbated Mudstone	13-10A	Dark gray, fissile mudstone, olive gray bioturbated mudstone, pyrite, and coal. The intervals of dark gray, fissile mudstone contain light gray siltstone lenses. The upper mudstone contains some fossil hash intervals and burrows, and becomes increasingly calcareous upward.

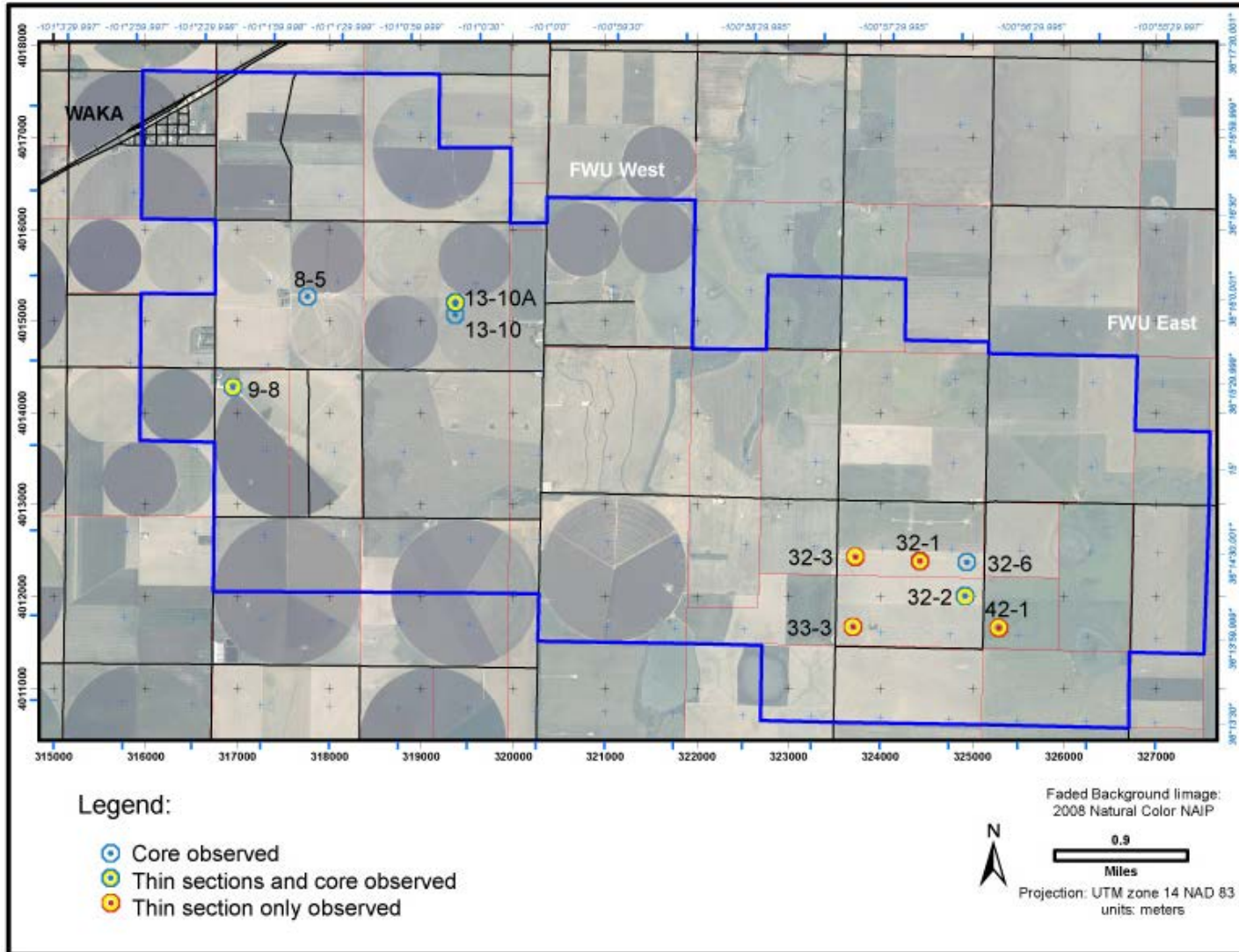


Figure 9. Map of Farnsworth Unit showing wells with core, thin sections, or both, that were observed for this study.

Well #8-5

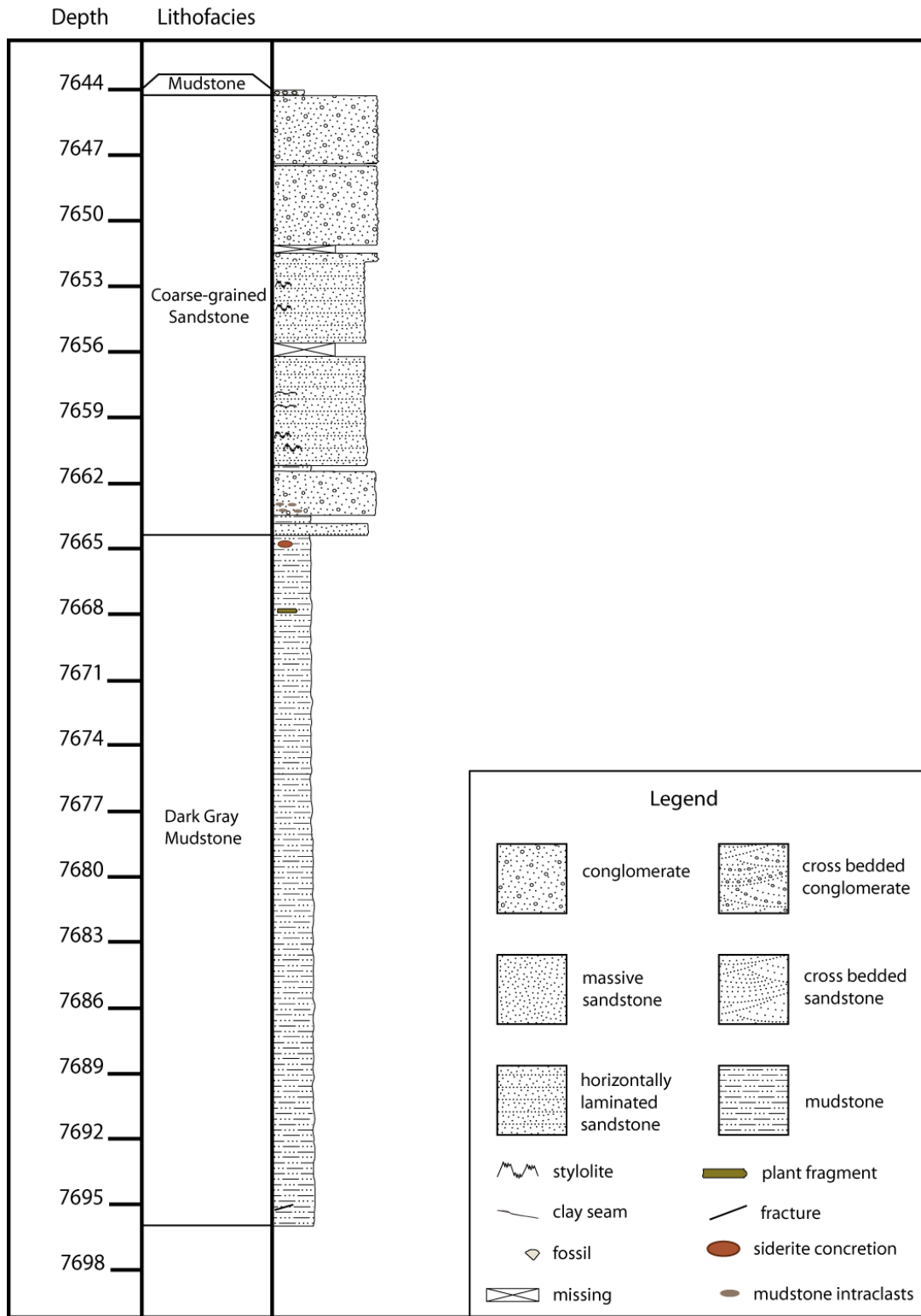


Figure 10. Summary stratigraphic column for well 8-5.

Well #9-8

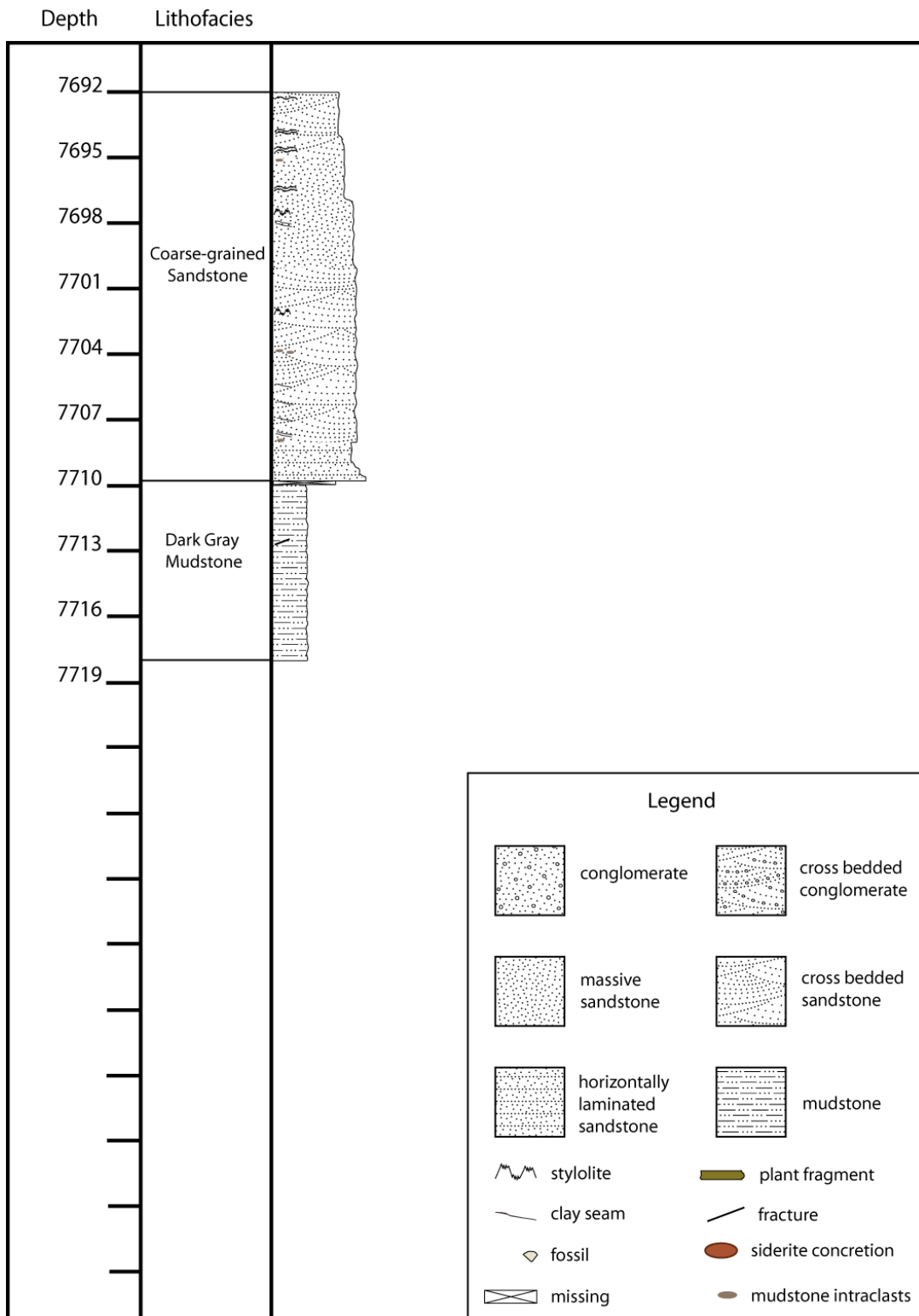


Figure 11. Summary stratigraphic column for well 9-8.

Well #13-10

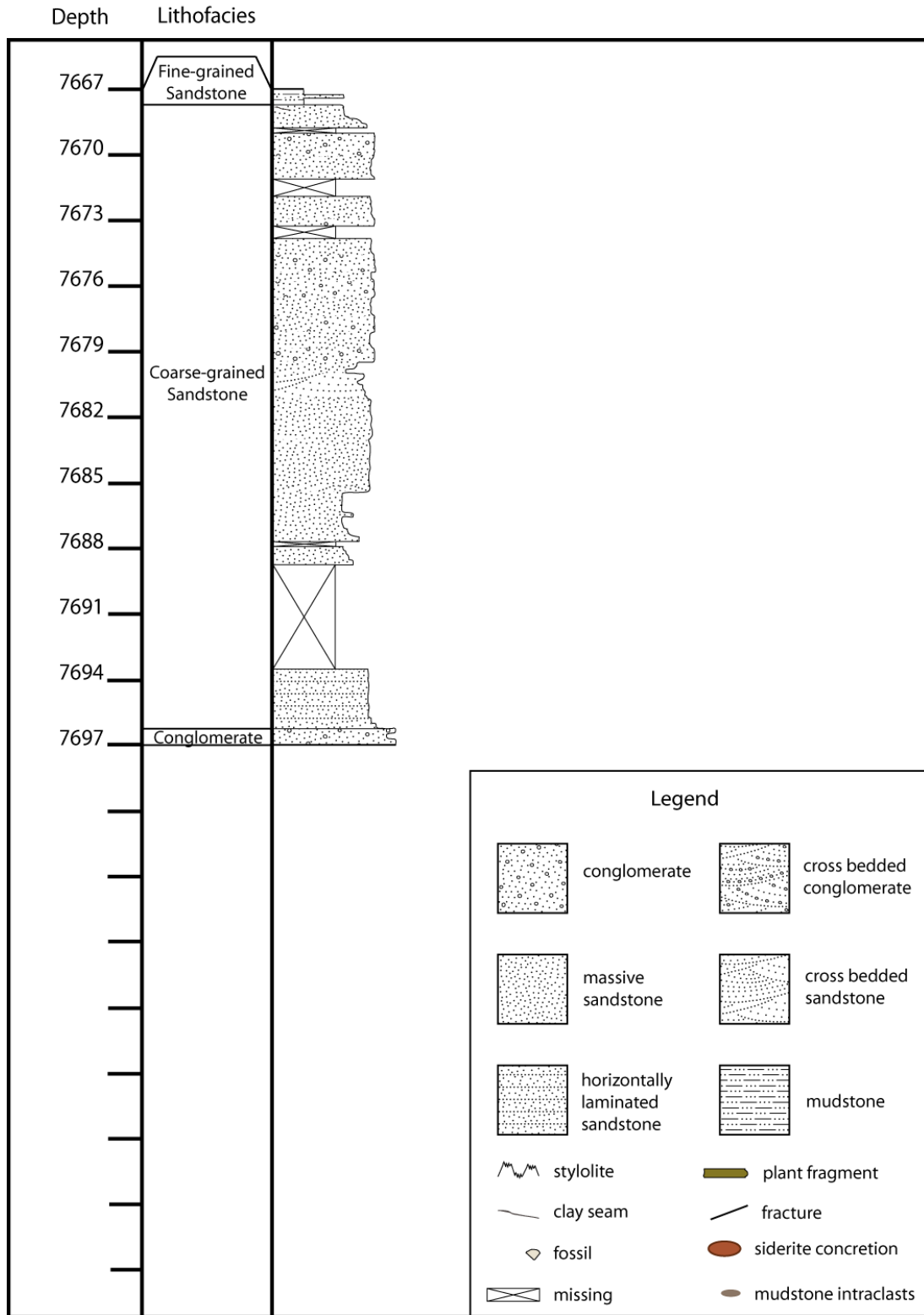


Figure 12. Summary stratigraphic column for well 13-10. Due to close proximity and similar lithology, a separate summary stratigraphic column was not made for well 13-10A. See Appendix A for a detailed stratigraphic column for well 13-10A.

Well #32-2

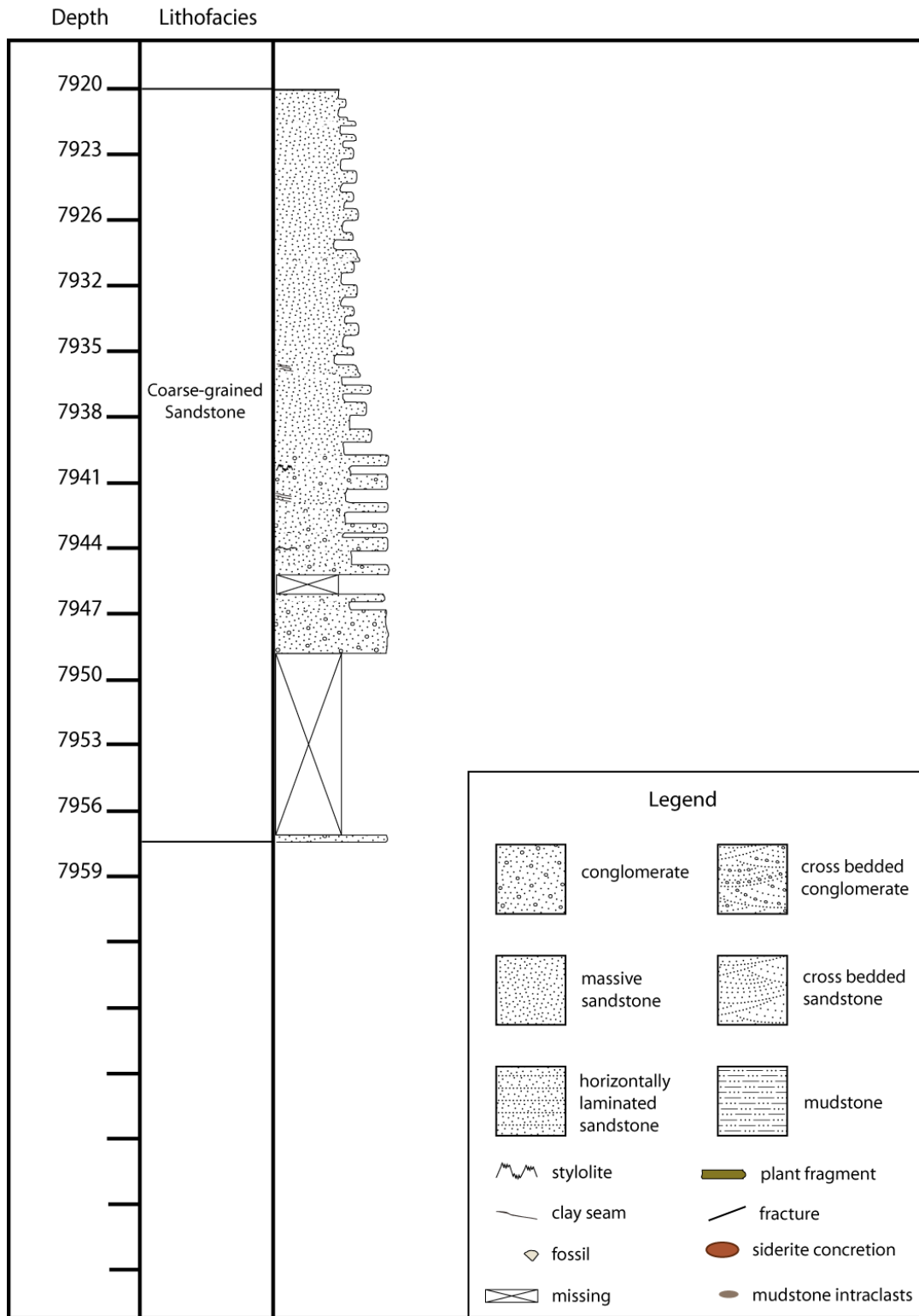


Figure 13. Summary stratigraphic column for well 32-2.

Well #32-6

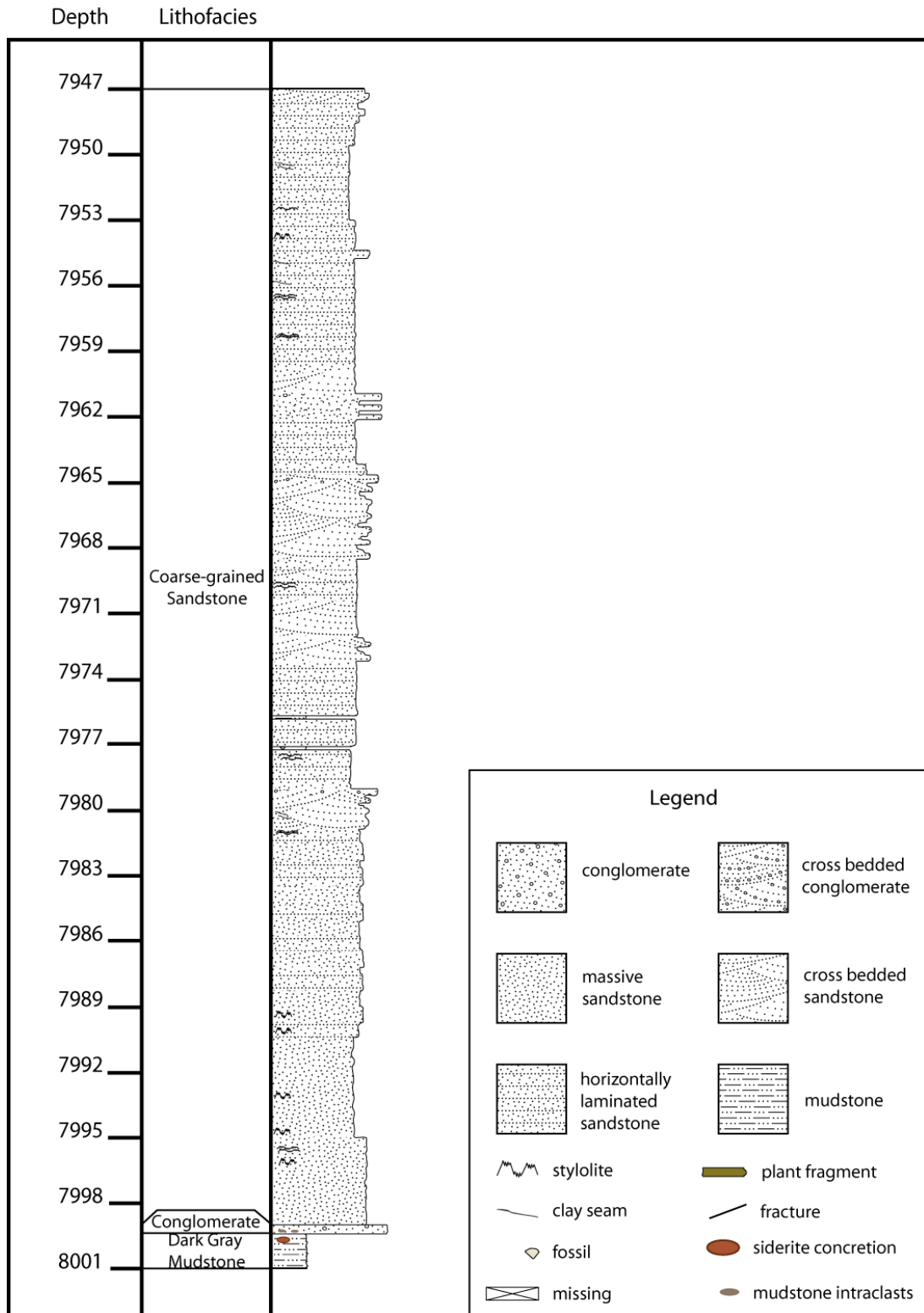


Figure 14. Summary stratigraphic column for well 32-6.

Fine-grained Sandstone Facies

The Fine-grained Sandstone facies was observed in wells 13-10 and 13-10A, above the Coarse-grained Sandstone facies (Figure 12). It consists of light gray, very fine-grained sandstone interbedded with mudstone (Figure 15). The grain size fines upward. This facies displays low-angle cross bedding. Clay drapes and lenticular bedding are present locally. Structures possibly formed by soft sediment deformation and/or burrowing are present in well 13-10. Both upper and lower contacts are gradational.

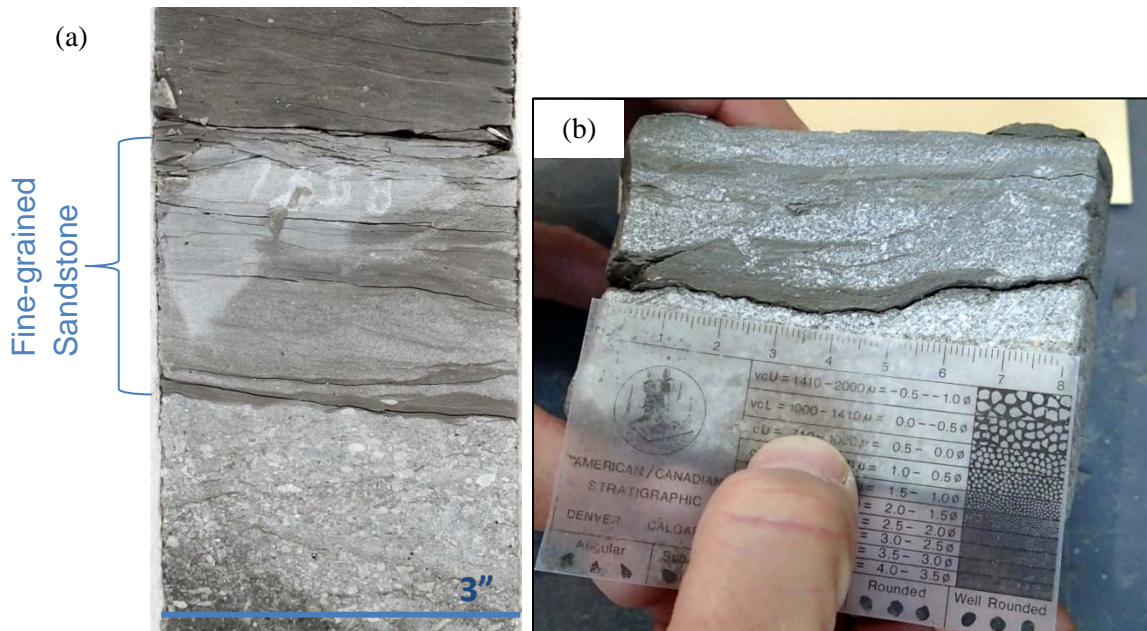


Figure 15. Fine-grained Sandstone facies. (a) Well 13-10A, 7668 ft. (b) Well 13-10, 7667.6 ft to 7667.7 ft. Note soft sediment deformation and/or burrow.

Coarse-grained Sandstone Facies

This lithofacies is the main reservoir (oil-producing/CCUS target) of the Farnsworth Unit. It is known locally as the Morrow B (formerly Buckhaults) sandstone and regionally as the upper Morrow sandstone (Munson, 1989).

This lithofacies consists of coarse- to very coarse-grained, moderately- to poorly-sorted sandstone and granule conglomerate (Figure 16). Bedding types include cross bedding, planar bedding, and massive bedding (Figures 16 and 17). Clay seams and stylolites are common (Figure 18), except in well 13-10, in which no stylolites were observed. The Coarse-grained Sandstone facies is directly underlain by the Conglomerate and/or Mudstone facies.

This facies in well 9-8 is finer grained than observed in other wells. It is mostly fine- to coarse-grained sandstone and exhibits fining upward sequences (Figure 11). Rounded mudstone intraclasts occur locally, some with desiccation cracks (Figure 19a). Clay seams and stylolites are abundant in well 9-8 (Figure 19b).

Well 32-6 contains cross bedding that exhibits considerable variation in grain size at the centimeter scale, alternating in size between coarse sand and conglomerate (Figure

16). In a one-foot section containing these textures, over-steepened cross beds are present (Figure 20). This section is also characterized by orange-brown staining, possibly hematite, which is mostly in the finer-grained layers. Hematite staining is observed in other locations in the reservoir facies of 32-6, but not in distinct sets. Dark reddish-brown staining was observed in well 13-10A, and petrography and microprobe analysis confirmed that it is siderite cement. Because sampling was not permitted for the 32-6 core, the chemical composition of the orange-brown cement could not be confirmed. In wells 8-5 and 32-6, a few thin, cm-scale mudstone interbeds are present within the reservoir facies (Figure 20). One mudstone interbed in well 32-6 contains shell fragments, ~1 mm in diameter. They were too small to identify, but they could possibly be ostracod fossils.



Figure 16. Well 32-6, 7967 ft to 7977 ft. In well 32-6, the Coarse-grained Sandstone facies exhibits considerable variation in grain size at the centimeter scale, alternating in size between coarse sand and conglomerate. Note hematite staining, clay seams, and mudstone interbed.

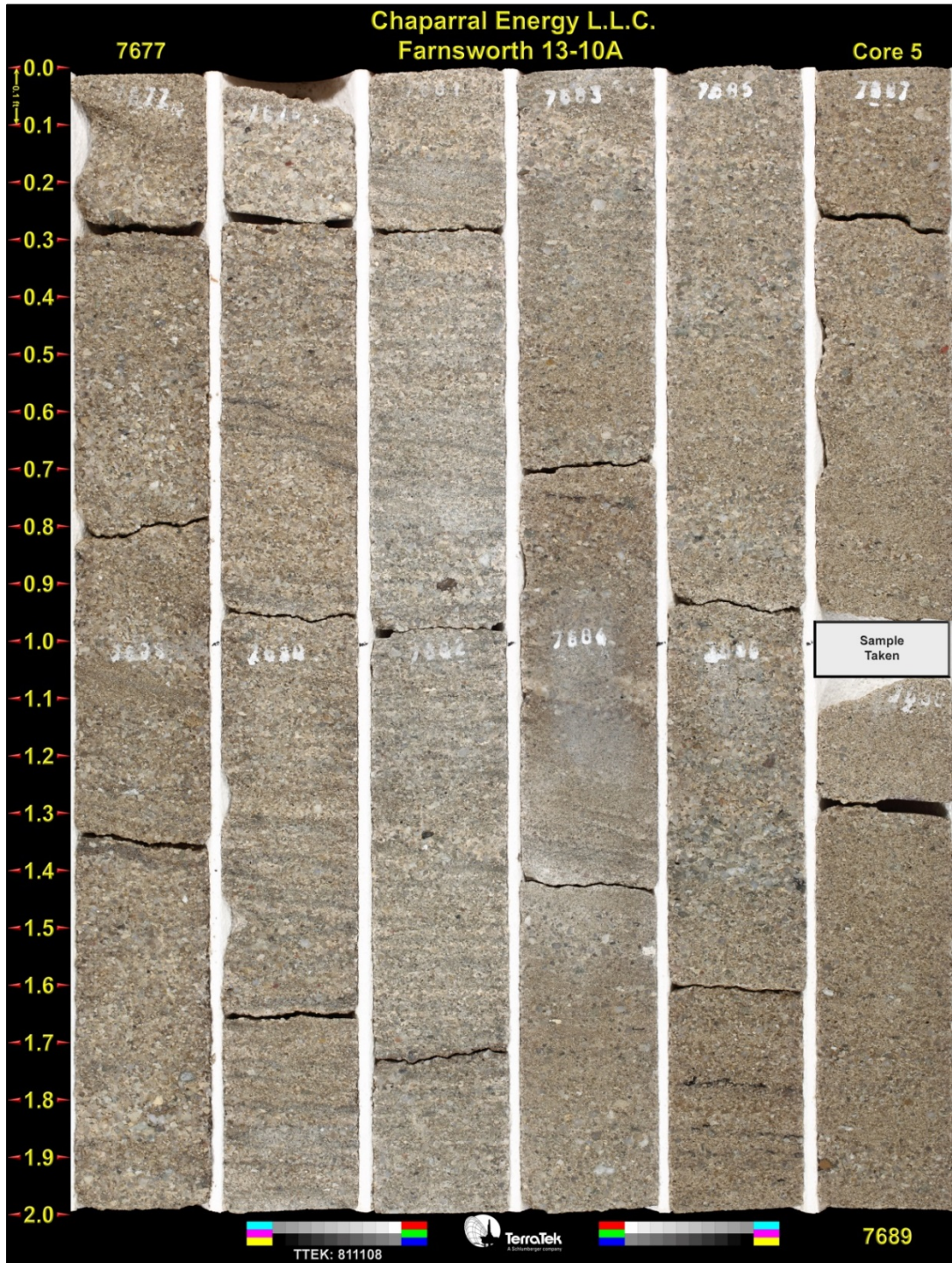


Figure 17. Well 13-10A, 7677 ft to 7689 ft. Scale on left in in tenths of feet. Coarse-grained Sandstone facies. Sedimentary structures include cross bedding, clay seams, and stylolites.

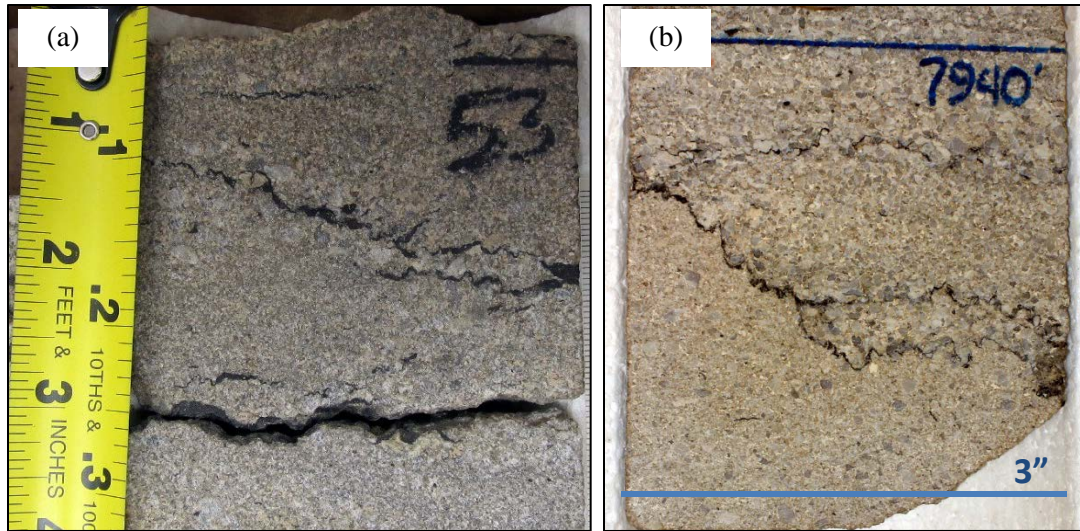


Figure 18. Coarse-grained Sandstone facies. (a) Well 8-5, 7653 ft. Carbonaceous stylolite (b) Well 32-2, 7940 ft. High-amplitude carbonaceous stylolite.

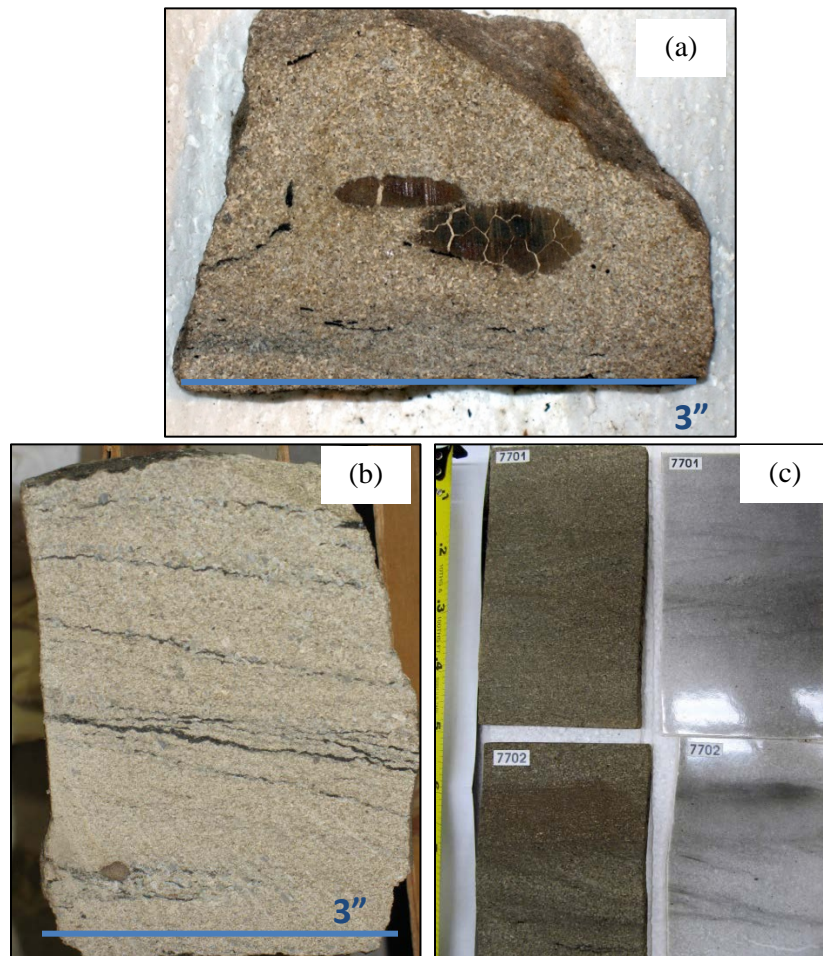


Figure 19. Coarse-grained Sandstone facies, Well 9-8. (a) Rounded mudstone intraclasts with desiccation cracks. (b) Clay seams and stylolites. (c) Low-angle cross bedding.



Figure 20. Well 32-6, 7977 ft to 7782 ft. Coarse-grained Sandstone facies. Hematite stained, over-steepened cross beds exhibiting possible rhythmite sets. Note mudstone interbed in upper left corner. This bed contained very small shell fragments.

Conglomerate Facies

Paraconglomerate

Well 13-10A contains ~0.5 ft of paraconglomerate (Figure 21). It has a light gray, sandstone matrix with a coarse-lower (cL) grain size. Intraclasts are subrounded, 2 mm to 3 cm long, consisting of mudstone, sandstone, and pyrite rip-up clasts. Some are elongate. It has a gradational upper contact with the Coarse-grained Sandstone facies and an erosional lower contact with the basal lag conglomerate.

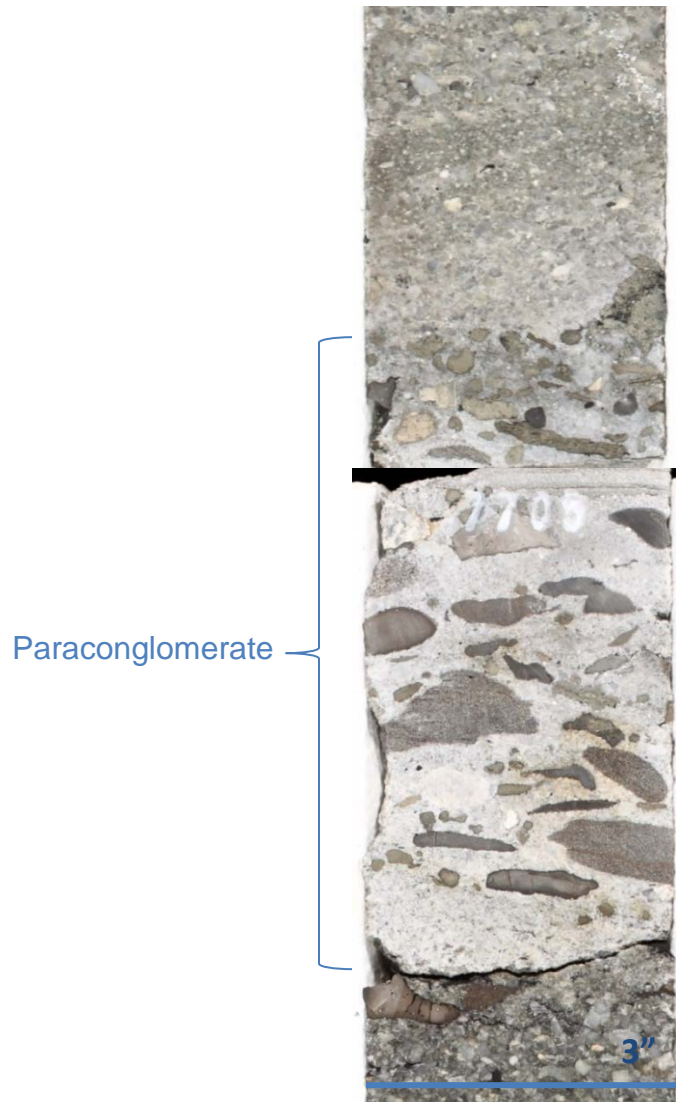


Figure 21. Well 13-10A, 7704.9 ft to 7705.4 ft. The Paraconglomerate facies has a gradational upper contact with the Coarse-grained Sandstone facies and an erosional lower contact with the Basal Lag Conglomerate facies.

Basal Lag Conglomerate

This facies is found in well 13-10, 13-10A, and 32-6 (Figures 12 and 14). The conglomerate is clast supported with subrounded clasts. The maximum clast size is 5 cm.

Well 13-10 has ~1 foot of the Basal Lag Conglomerate and well 32-6 has ~0.5 feet. The conglomerate in these two wells contains mudstone and siderite rip-up clasts, most likely derived from the underlying mudstone and siderite concretions (Figure 22a, b). The conglomerate in the 13-10 core is stained by iron oxides (Figure 22a). In wells 13-10 and 32-6, this facies has a gradational upper contact with the Coarse-grained Sandstone facies. In well 32-6, it has an erosional lower contact with the siderite concretion in the Dark Gray Mudstone facies. The core of 13-10 ends at the base of the conglomerate, so the nature of the lower contact is unknown.

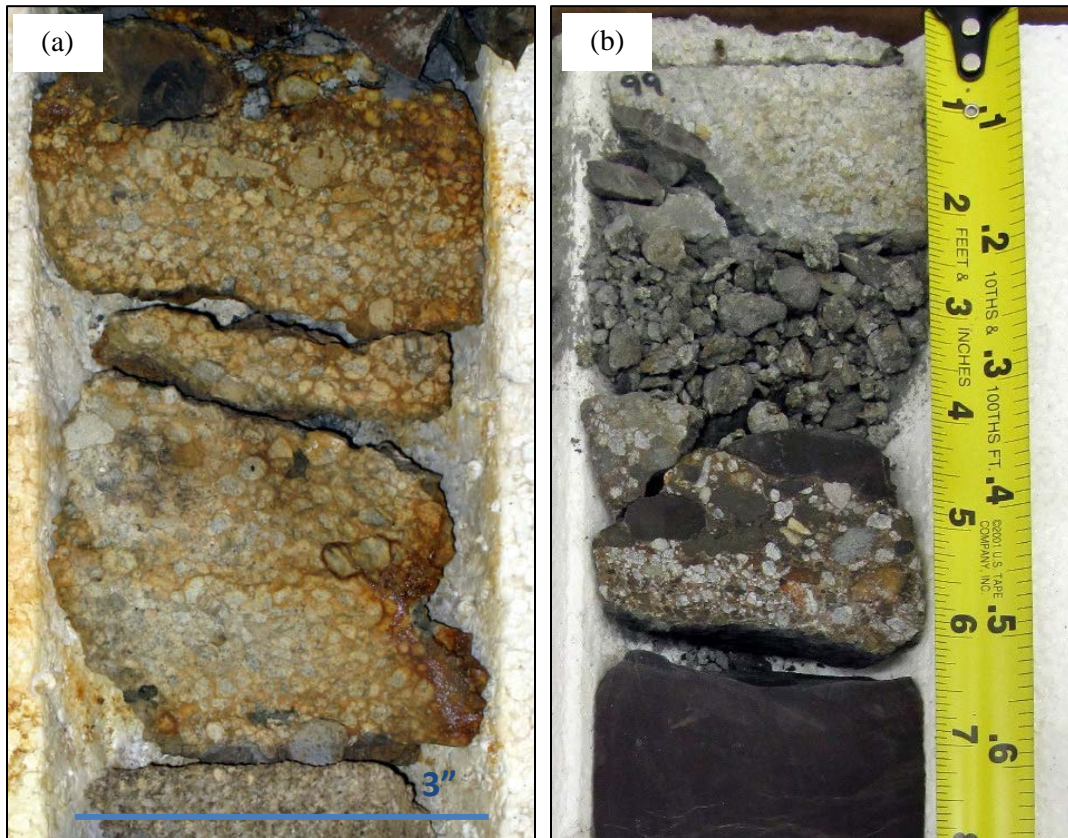


Figure 22. Basal Lag Conglomerate facies. (a) Well 13-10, 7696.3 ft to 7697.7 ft. (b) Well 32-6, 7999 ft to 7999.5 ft.

There is 0.8 feet of granule conglomerate in well 13-10A (Figure 23). The clasts are very similar to those in the Coarse-grained Sandstone, but the grain size is predominantly granule conglomerate. It does not contain rip-up clasts. It has an erosional upper contact with the Paraconglomerate facies and an erosional lower contact with the Bioturbated Mudstone facies.



Figure 23. Well 13-10A, 7705.4 ft to 7706.2 ft. Basal Lag Conglomerate facies.

Mudstone Facies

From log and core observations, it is apparent that there is mudstone below the Conglomerate and/or Coarse-grained Sandstone facies and above the Fine-grained Sandstone and/or Coarse-grained Sandstone facies. These will be referred to as “lower” and “upper” mudstone. Cores from wells 8-5, 9-8, and 32-6 have variable amounts of mudstone preserved. Of these wells, only the core from well 8-5 has upper mudstone preserved, and it is only 0.3 feet thick. The lower mudstone in core from these wells ranges from 1.5 ft (well 32-6) to 32 ft (well 8-5). Core from wells 13-10 and 32-2 have no mudstone preserved. Because of this, it is difficult to correlate the mudstone facies across the wells. The core from well 13-10A, on the other hand, has much more mudstone intact: 19.4 feet of lower mudstone and 62 feet of upper mudstone were observed.

Mudstone with Brachiopod Fossils

This lithofacies was only observed at the top of the core from well 8-5, above the Coarse-grained Sandstone facies (Figure 10). This mudstone is dark gray and contains several brachiopod shell fragments, which are 5 - 10 mm in diameter (Figure 24). It has an erosional lower contact with the Coarse-grained Sandstone facies.

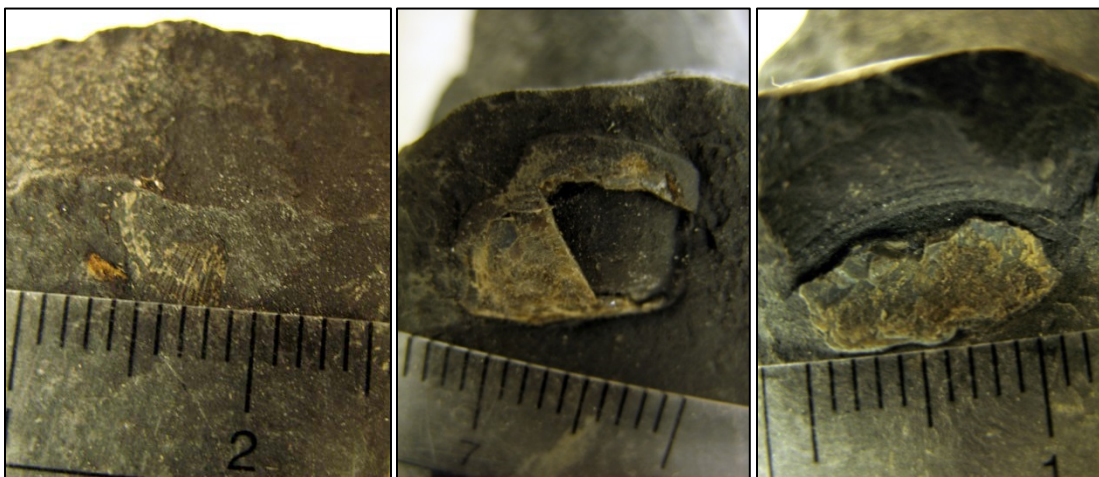


Figure 24. Well 8-5, 7644 ft. Brachiopod shell fragments in the Mudstone with Brachiopod Fossils subfacies. Small tick marks on ruler are millimeters.

Dark Gray Mudstone

This lithofacies is found beneath the Conglomerate and/or Coarse-grained Sandstone facies in wells 8-5, 9-8, and 32-6 (Figures 10, 11, and 14). It consists of a gray to dark gray, massive to fissile mudstone. It can be distinguished from the other mudstone facies by the absence of fossils, trace fossils, or bioturbation. Siderite concretions are present at the top of this lithofacies in well 8-5 and 32-6 (Figure 25). Slickensided fractures are also present in this lithofacies.

Well 8-5 and 9-8 have intervals of a dark gray, fissile mudstone containing carbonaceous material. Coal and sulfur or jarosite were observed (Figure 26a). Wood fragments and a 5 cm-long plant fragment were observed in well 8-5 (Figure 26b). It has

an erosional upper contact with the Conglomerate and/or Coarse-grained Sandstone facies.

Bioturbated Mudstone

The mudstone observed in well 13-10A differs from the mudstone observed in other wells. It does not contain large brachiopod shells, siderite concretions, or plant material. Both the upper and lower mudstone of 13-10A is characterized by intervals of dark gray, fissile mudstone, olive gray bioturbated mudstone, pyrite, and coal (Figures 27, 28, and 29). The lower mudstone contains no fossils or burrows, and is not calcareous (does not react with HCl; Figure 27). The intervals of dark gray, fissile mudstone contain light gray lenses of silty mudstone (Figure 28). The upper mudstone contains some fossil hash intervals and burrows, and becomes increasingly calcareous upward (Figure 29). The upper mudstone has a gradational lower contact with the Fine-grained Sandstone facies. The lower mudstone has an erosional upper contact with the Basal Lag Conglomerate facies (Figure 27).



Figure 25. Well 8-5, 7664.9 ft. Siderite concretion. Ruler is cm scale.



Figure 26. Well 8-5, Dark Gray Mudstone facies. (a) 7668.5 ft. Yellow mineral might be sulfur or jarosite. (b) 7667 ft. Plant fragment.

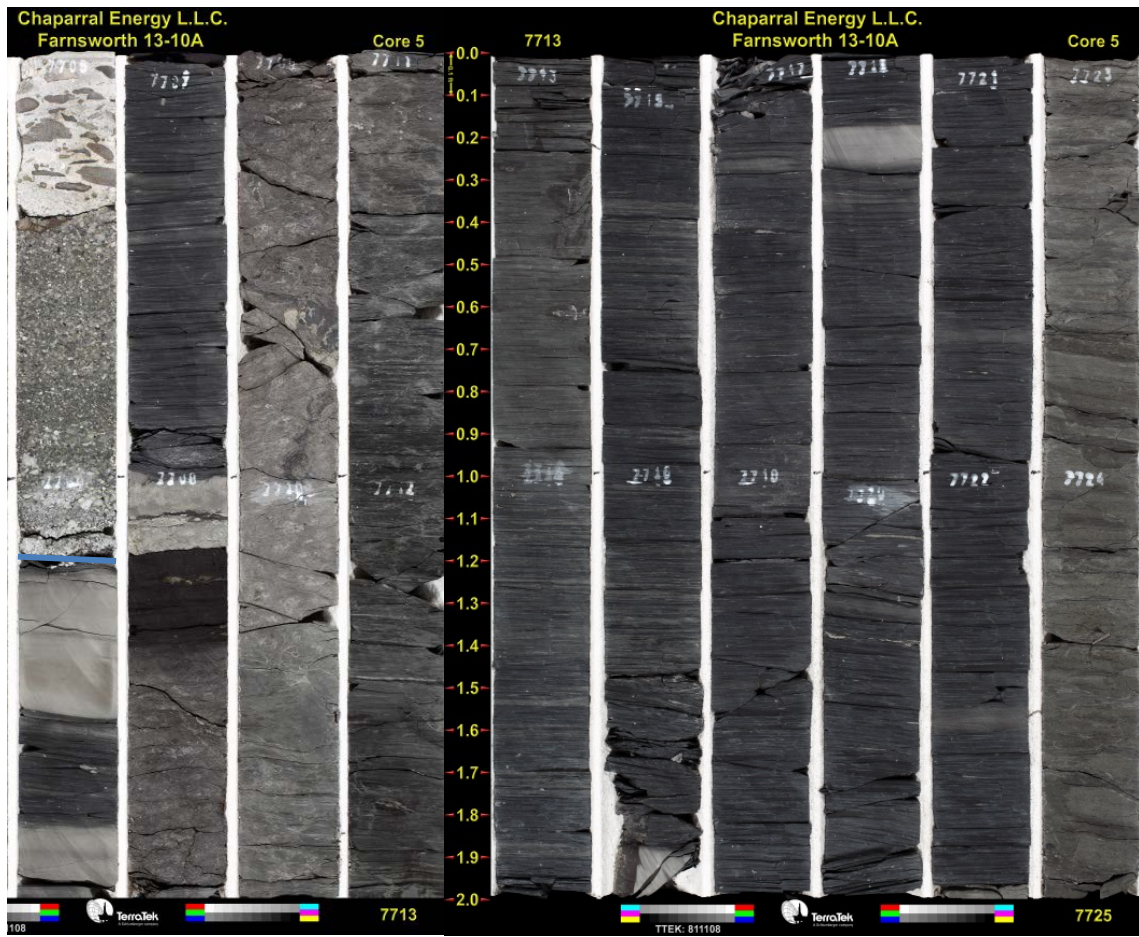


Figure 27. Well 13-10A lower mudstone interval. Note: last 0.4 ft not pictured. Scale is in tenths of feet.

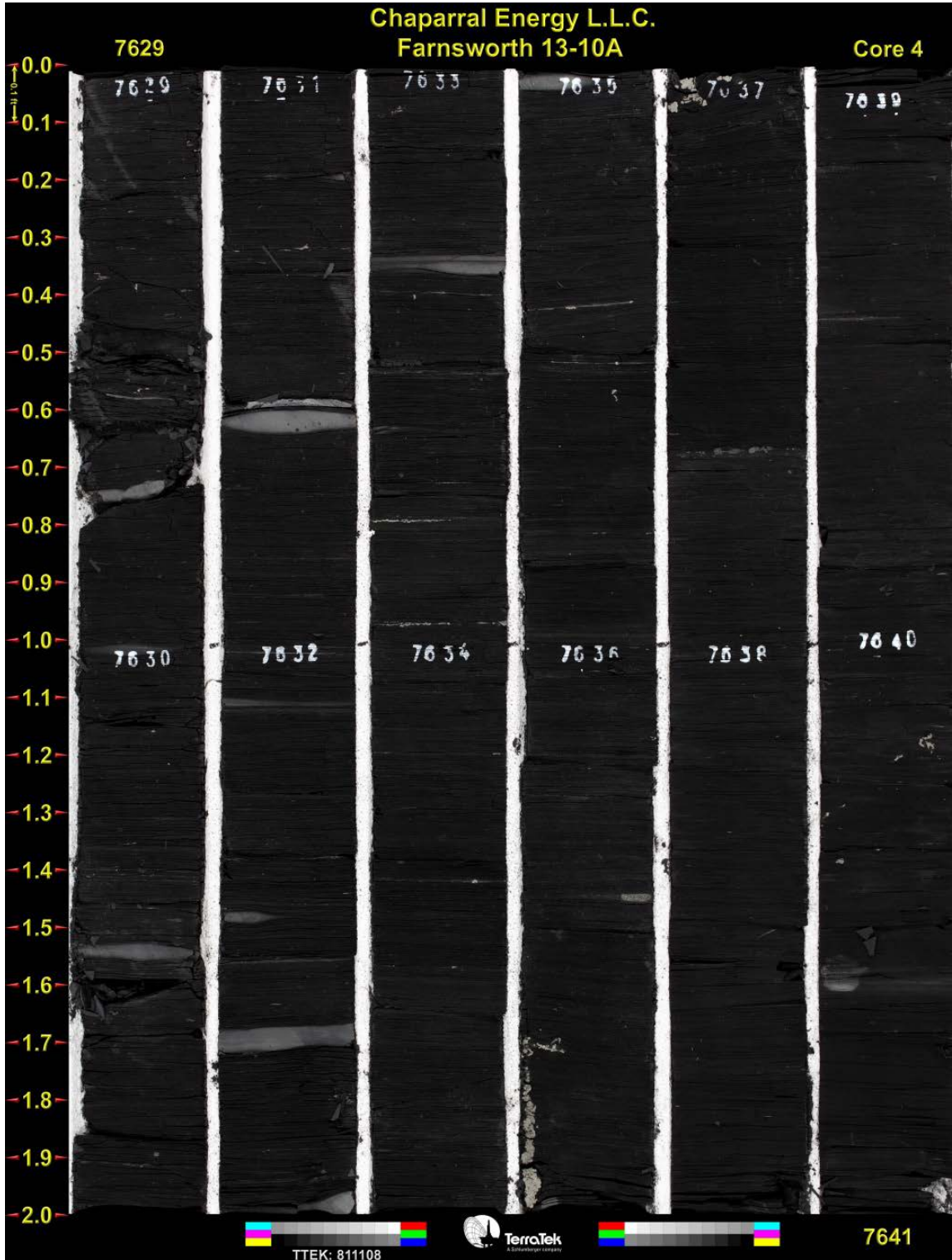


Figure 28. Well 13-10A, 7629 ft to 7641 ft. Fissile dark gray mudstone with lighter gray, silty lenses. Scale on left is in tenths of feet.

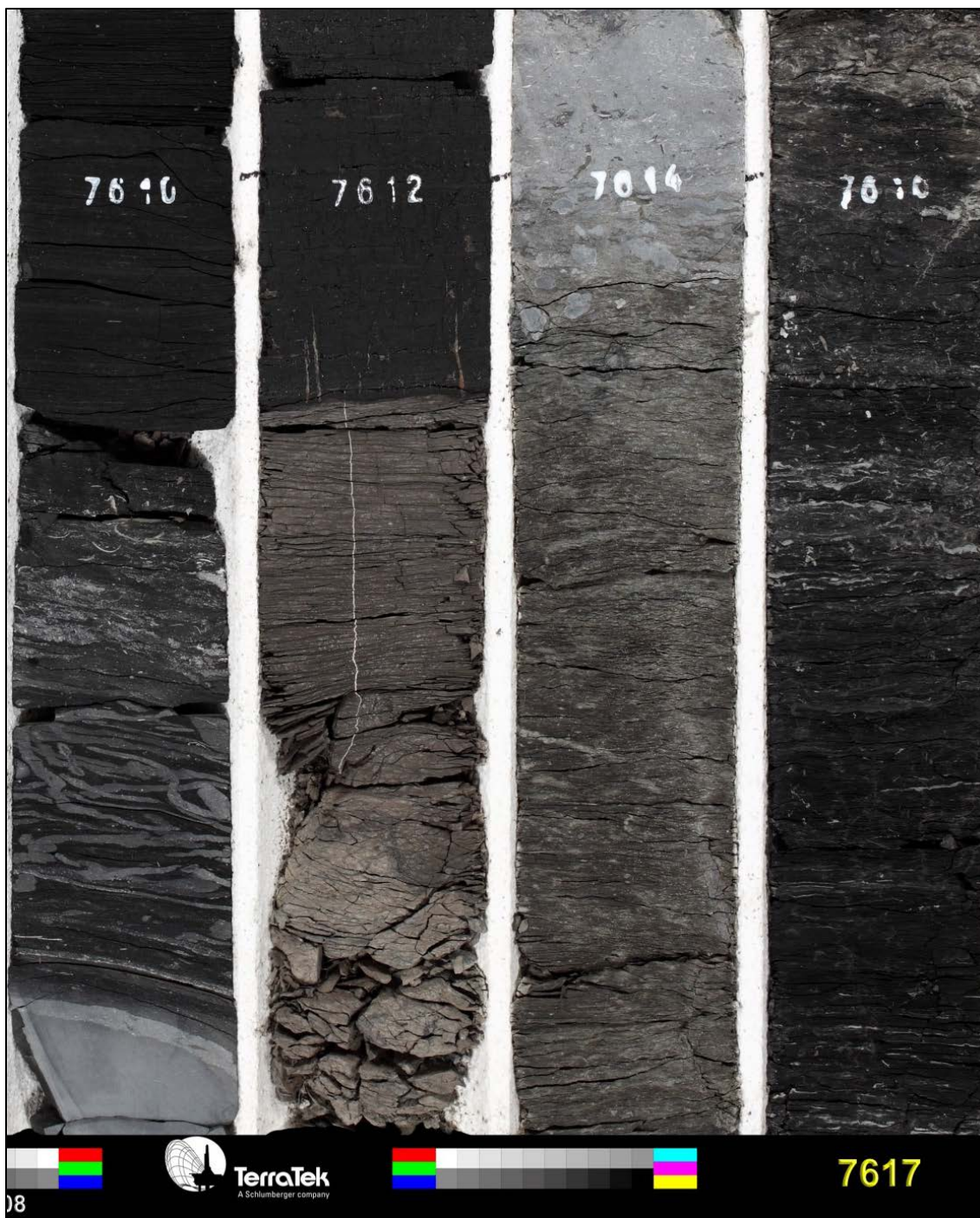


Figure 29. Well 13-10A. 7610 ft, 7612 ft, 7614 ft, and 7612 ft. Calcareous upper mudstone with bioturbation. Note fossil hash layer (E6 sample location), burrows below, and coal.

Porosity and Permeability

Porosity and permeability data from the Coarse-grained Sandstone facies are available for the six cores that were observed for this study (Figure 30). Locations of porosity and permeability (P&P) plugs were noted while describing the core, as well as visual estimates of grain size and sorting (Table 2). For well 13-10A, grain size and sorting were determined from thin sections. Grain size and sorting data were compared to porosity and permeability data to evaluate primary textural controls on reservoir quality (Figures 31 and 32).

There does not appear to be a relationship between grain size and sorting and reservoir quality. The eastern side of the field has a higher percentage of samples with grain sizes greater than 1 mm (Table 2, Figure 32). Samples from the eastern side of FWU also generally have better sorting than the western side of the field (Table 2). It should be noted that there were significantly more samples available from the eastern side of the field than from the western side. Consequently, porosity, permeability, grain size, and sorting data were available for 55 samples from the eastern side, but only for 13 samples from the western side.

Porosity versus permeability was plotted by western and eastern sides of FWU, and it is apparent both sides have similar porosity values and a wide range of permeability values, but the western side achieves higher permeability values than the eastern side (Figure 34). Box plots were created for porosity and permeability to understand the differences in reservoir quality for the two sides of the field (Figure 35). The average porosities are very similar in both sides of the field (Figure 35a). The median porosity of the western side of the field is only 1.6% higher than the eastern side of the field. The difference in average permeability, however, is much greater. The median permeability of the western side of the field is 14.8 millidarcies (md) higher than the median permeability of the eastern side of the field (Figure 35b). The maximum permeability of samples from the eastern side of the field is 28 md, but the maximum permeability of samples from the western side of the field is 290 md, which is an order of magnitude greater.

Table 2. Comparison of grain size and sorting for western and eastern sides of FWU.

West	Grain size	Count	Percent of samples						Sorting	Count	Percent of samples
		g.c.	0						0%	> 1 mm diameter:	38%
	vcU	1	8%	Moderate	4	31%					
	vcL/vcU	3	23%	Poor	9	69%					
	vcL	1	8%	Total	13						
	cU	0	0%	< 1 mm diameter:	62%						
	cU/cL	2	15%								
	cL	5	38%								
	mL/fU	1	8%								
	Total	13									

East	Grain size	Count	Percent of samples						Sorting	Count	Percent of samples
		g.c.	4						7%	> 1 mm diameter:	75%
	vcU	14	25%	Moderate	19	35%					
	vcL/vcU	0	0%	Poor	31	56%					
	vcL	23	42%	Total	55						
	cU	10	18%	< 1 mm diameter:	25%						
	cU/cL	0	0%								
	cL	4	7%								
	mL/fU	0	0%								
	Total	55									

g.c. = granular conglomerate, vcU = very coarse upper sand, vcL = very coarse lower sand, cU = coarse upper sand, cL = coarse lower sand, mL = medium lower sand, fU = fine upper sand.

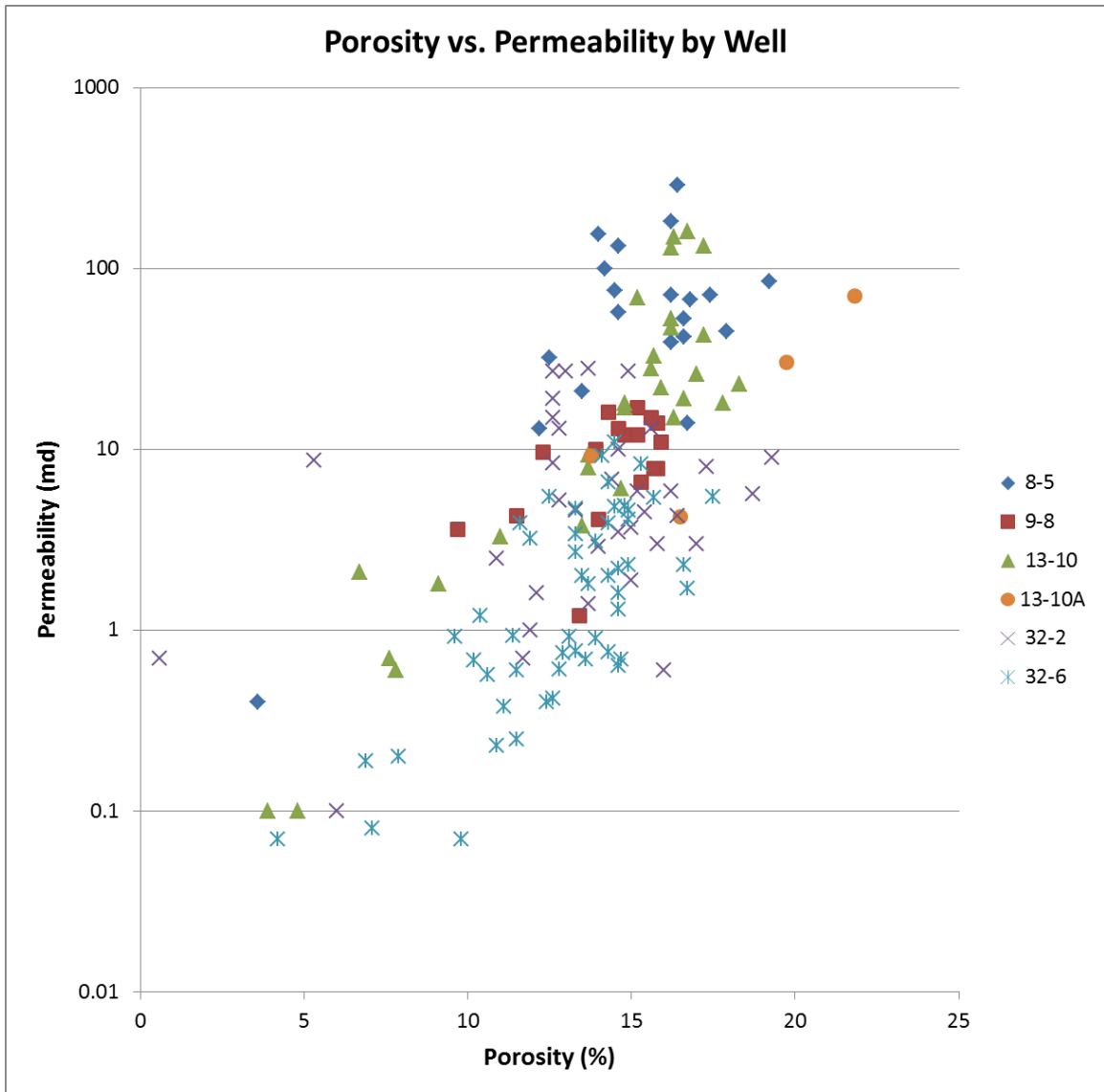


Figure 30. Plot of porosity versus permeability for plugs obtained from conventional core of the upper Morrow sandstone. Note considerable inter-well variation in reservoir quality. Porosity and permeability data provided by Chaparral Energy.

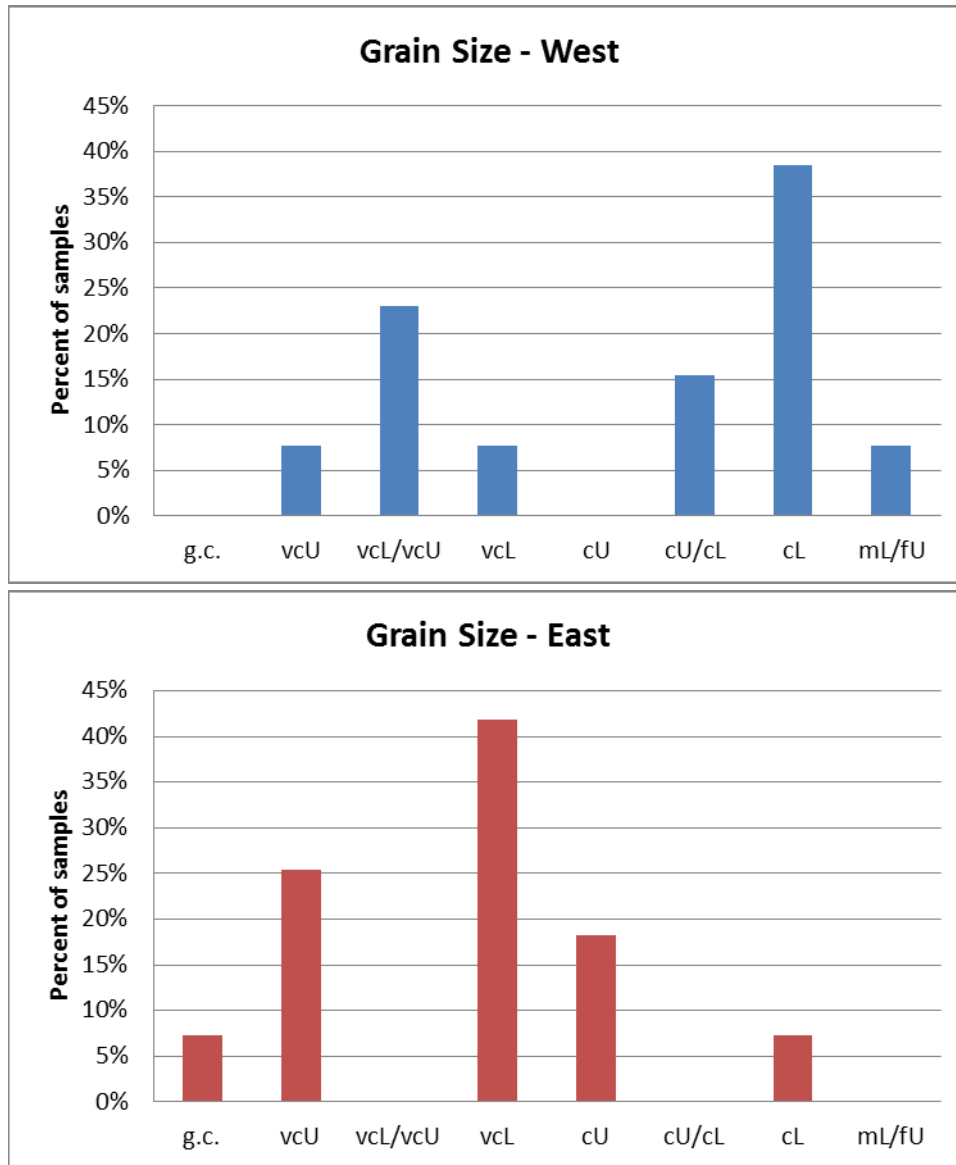


Figure 31. Bar graphs showing grain sizes from samples on the western and eastern sides of FWU, data from Table 2. g.c. = granular conglomerate, vcU = very coarse upper sand, vcL = very coarse lower sand, cU = coarse upper sand, cL = coarse lower sand, mL = medium lower sand, fU = fine upper sand.

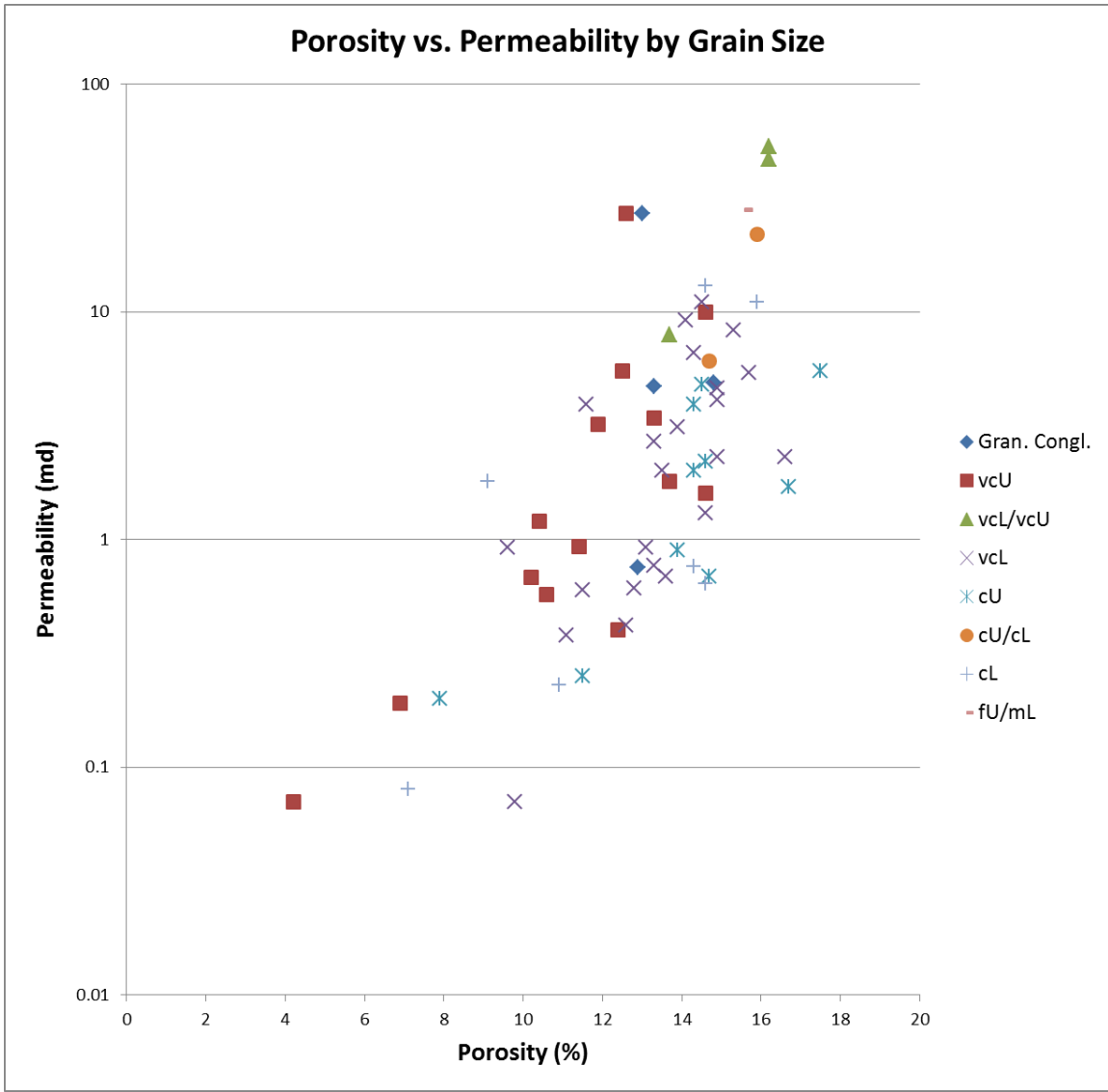


Figure 32. Plot of porosity versus permeability for plugs obtained from conventional core of the upper Morrow sandstone. Symbols indicate mean grain size (from visual estimate of rock near plug location). Gran. Congl. = granular conglomerate, vcU = very coarse upper sand, vcL = very coarse lower sand, cU = coarse upper sand, cL = coarse lower sand, mL = medium lower sand, fU = fine upper sand. Porosity and permeability data provided by Chaparral Energy.

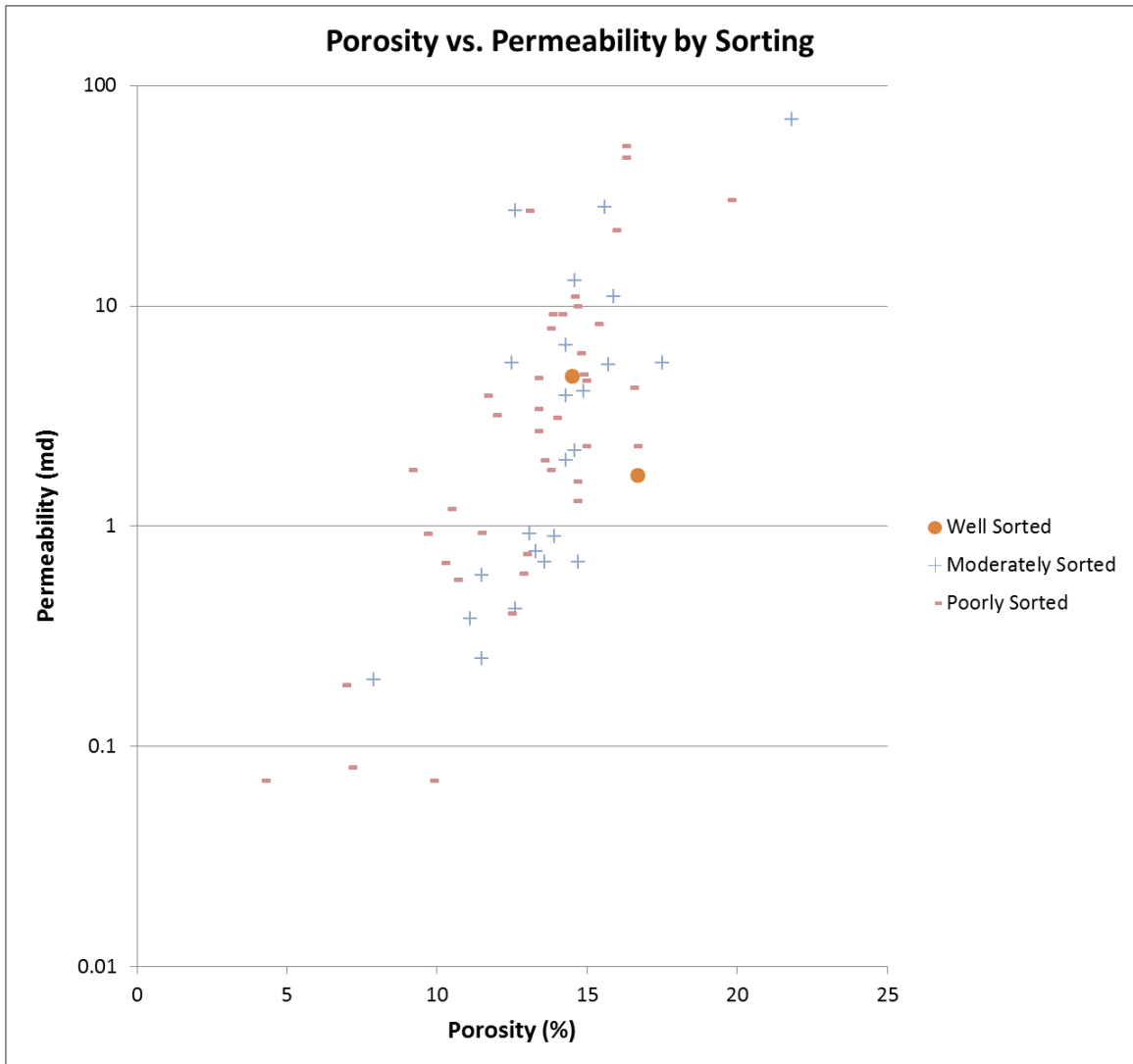


Figure 33. Plot of porosity versus permeability for plugs obtained from conventional core of the upper Morrow sandstone. Symbols indicate degree of sorting (from visual estimate of rock near plug location). Porosity and permeability data provided by Chaparral Energy.

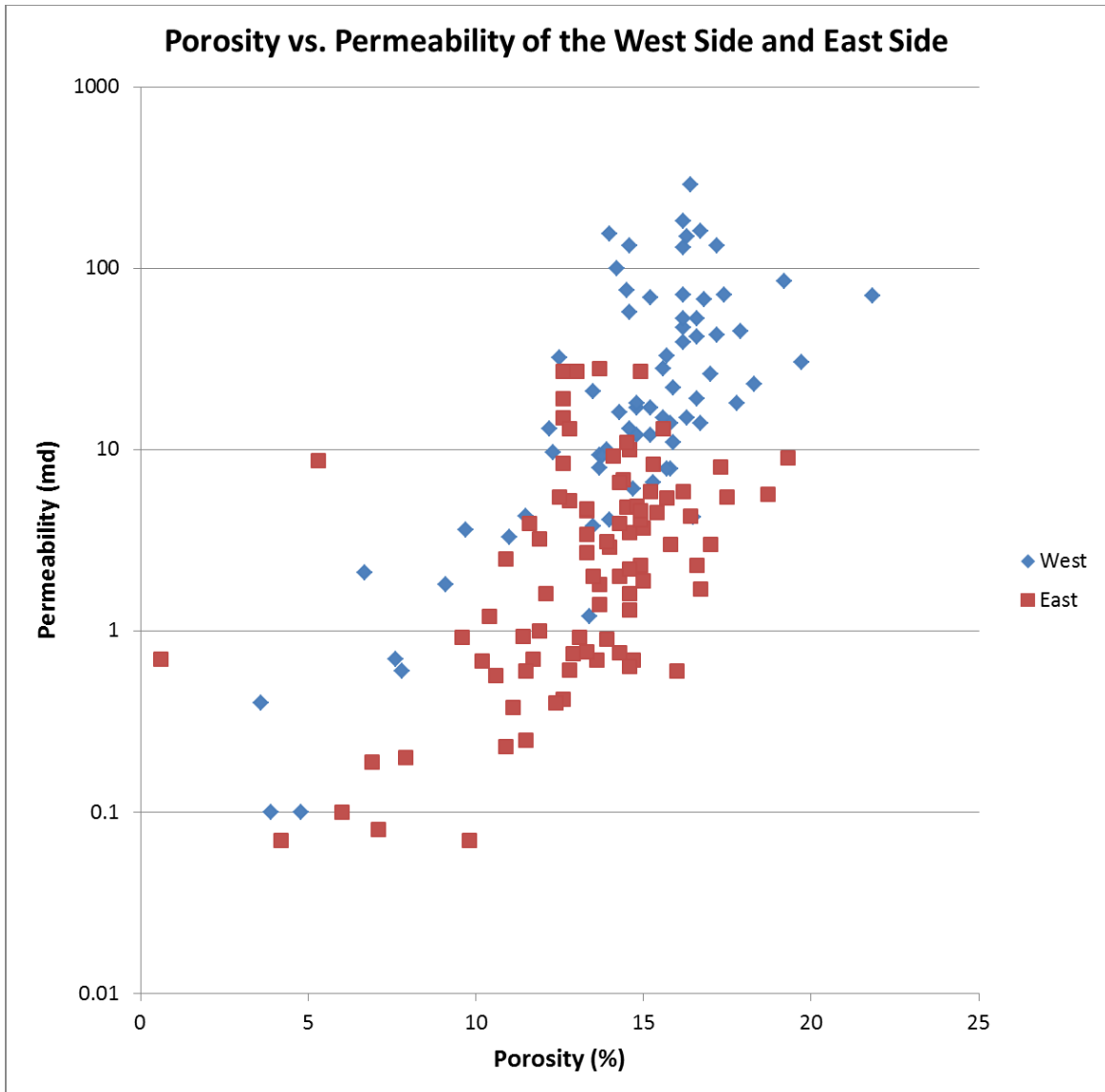


Figure 34. Porosity versus permeability of the western side and eastern side of FWU. Whereas both sides exhibit a wide range of reservoir quality, the eastern side does not achieve as high of permeability values as the west side. Porosity and permeability data provided by Chaparral Energy.

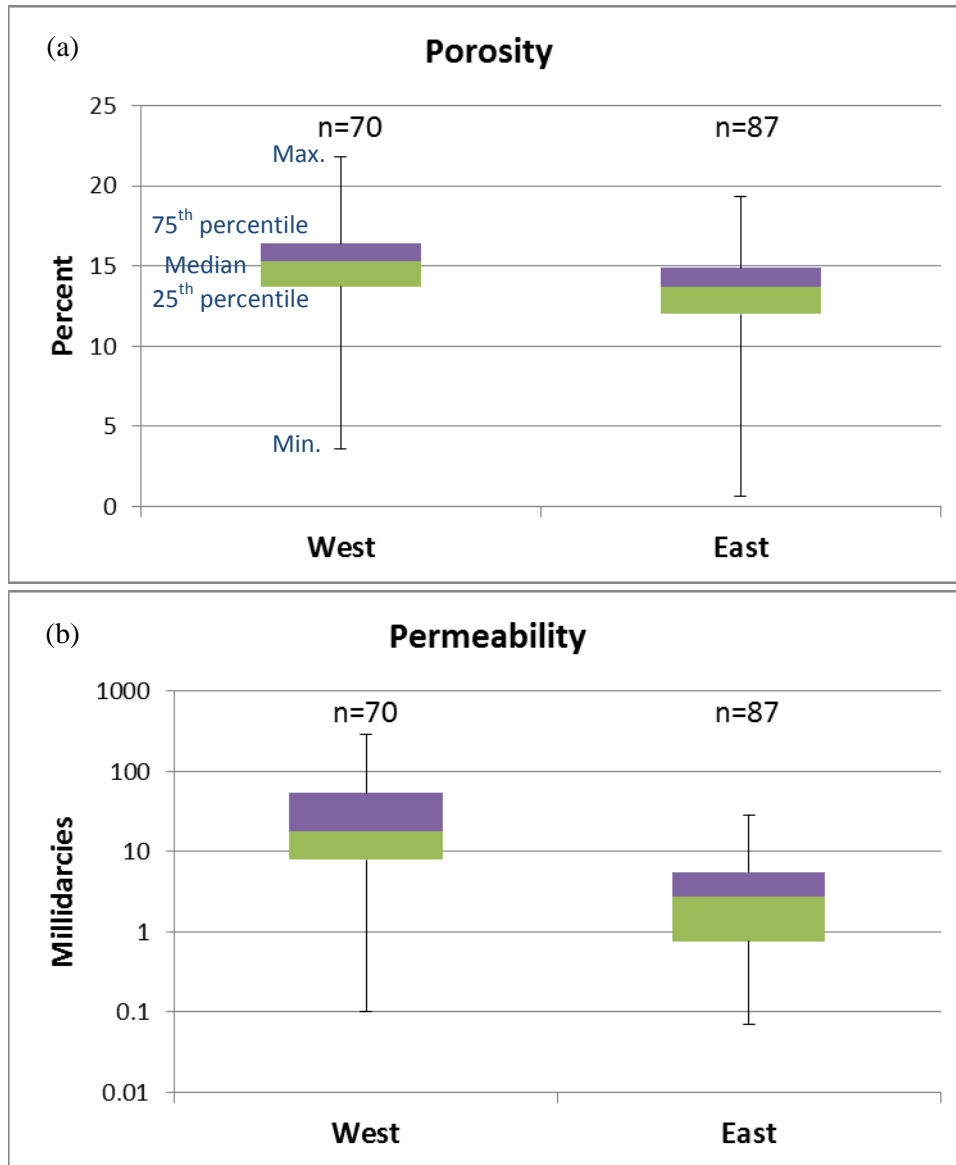


Figure 35. Box plots of plug porosity and permeability values for the western and eastern sides of FWU. (a) Porosity box plot. The median porosity is 1.6% higher in the western side of the field than the eastern side of the field. (b) Permeability box plot. The median permeability of the western side of the field is 14.8 md higher than the median permeability of the eastern side of the field. The maximum permeability of samples from the eastern side of the field is 28 md, but the maximum permeability of samples from the western side of the field is 290 md, which is an order of magnitude greater.

Composition

Fine-grained Sandstone Facies

One thin section from the Fine-grained Sandstone facies of well 13-10A was point-counted to determine modal composition (Table 3). The porosity of the sample is negligible, so a separate point count for porosity was not performed (Figure 36). One sample from this facies (E6, well 13-10A, 7668.10 ft) was analyzed using XRD to determine whole-rock composition and clay type and abundance (Tables 4 and 5).

From the results of the 300-point count, the Fine-grained Sandstone facies can be classified as a lithic arkose using the Folk (1968) classification (Figure 37a). The framework grains are primarily monocrystalline quartz, with lesser amounts of feldspar, chert, mica, and trace amounts of glauconite. Pyrite is present in the sample, but it appears to be authigenic, so it was counted as cement. The results of the XRD analysis (Table 4) show that sample E6 consists of 35% non-clay minerals and 66% clay minerals. It contains 24% quartz and 7% feldspar. Three percent of the feldspar is K-feldspar, and the other four percent is plagioclase feldspar. It also contains ankerite/Fe-dolomite (2%), pyrite (1%), and barite (1%). The most abundant type of clay in this sample is mixed layer illite-smectite, with lesser amounts of kaolinite, illite, chlorite, and smectite (Table 5).

Porosity is negligible in this sample (Figure 36b and 37b). The intergranular volume (IGV) of the Fine-grained Sandstone is high; it accounts for 45% of the sample. IGV includes cement, matrix, and intergranular porosity. Because the porosity of this sample is negligible, the IGV is mostly filled with matrix.

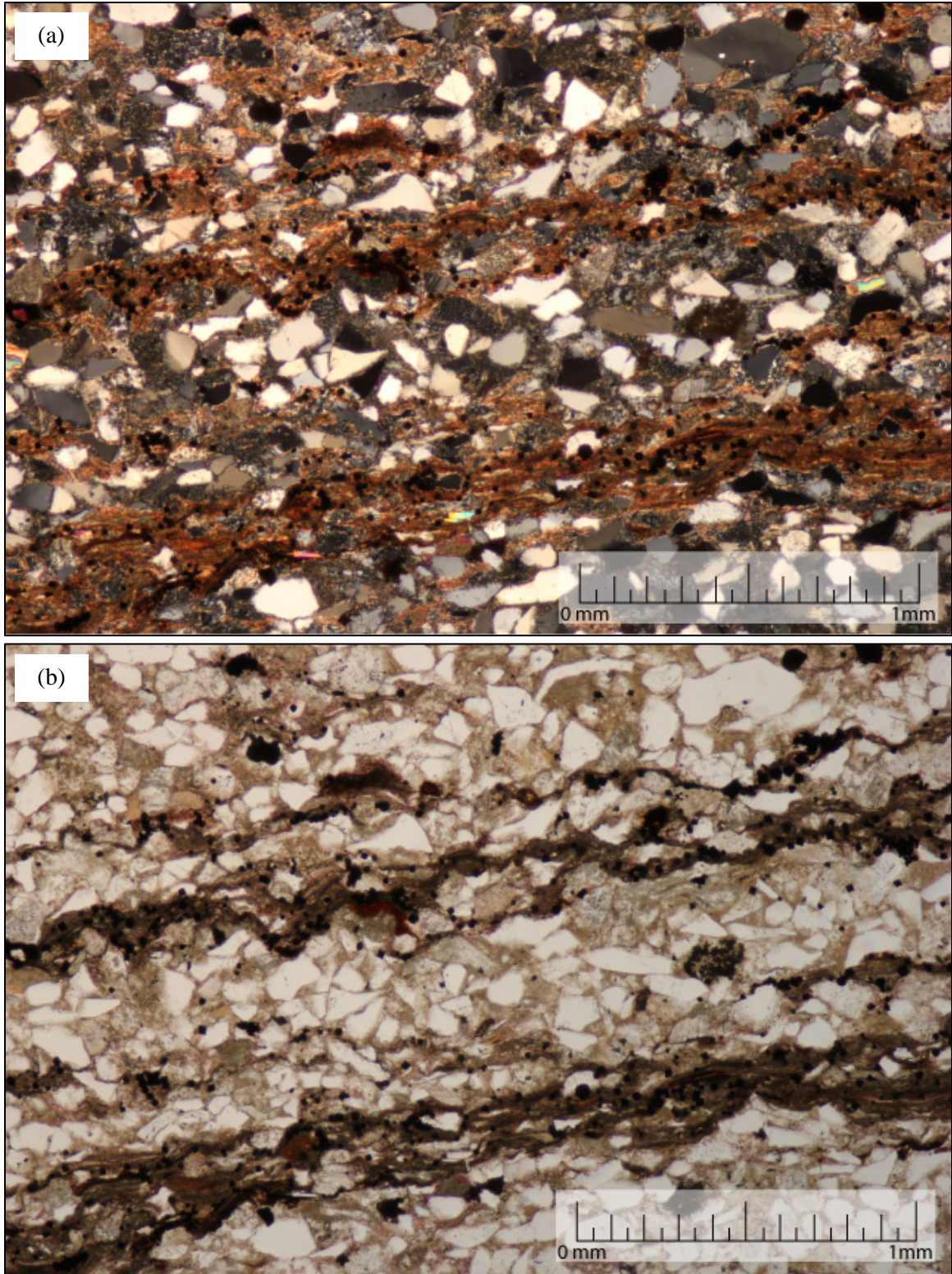


Figure 36. Sample E6, well 13-10A, 7668.10 ft. Photomicrograph of the Fine-grained Sandstone facies. Pink epoxy is not visible in the sample, which indicates that porosity is negligible. (a) xpl (b) ppl.

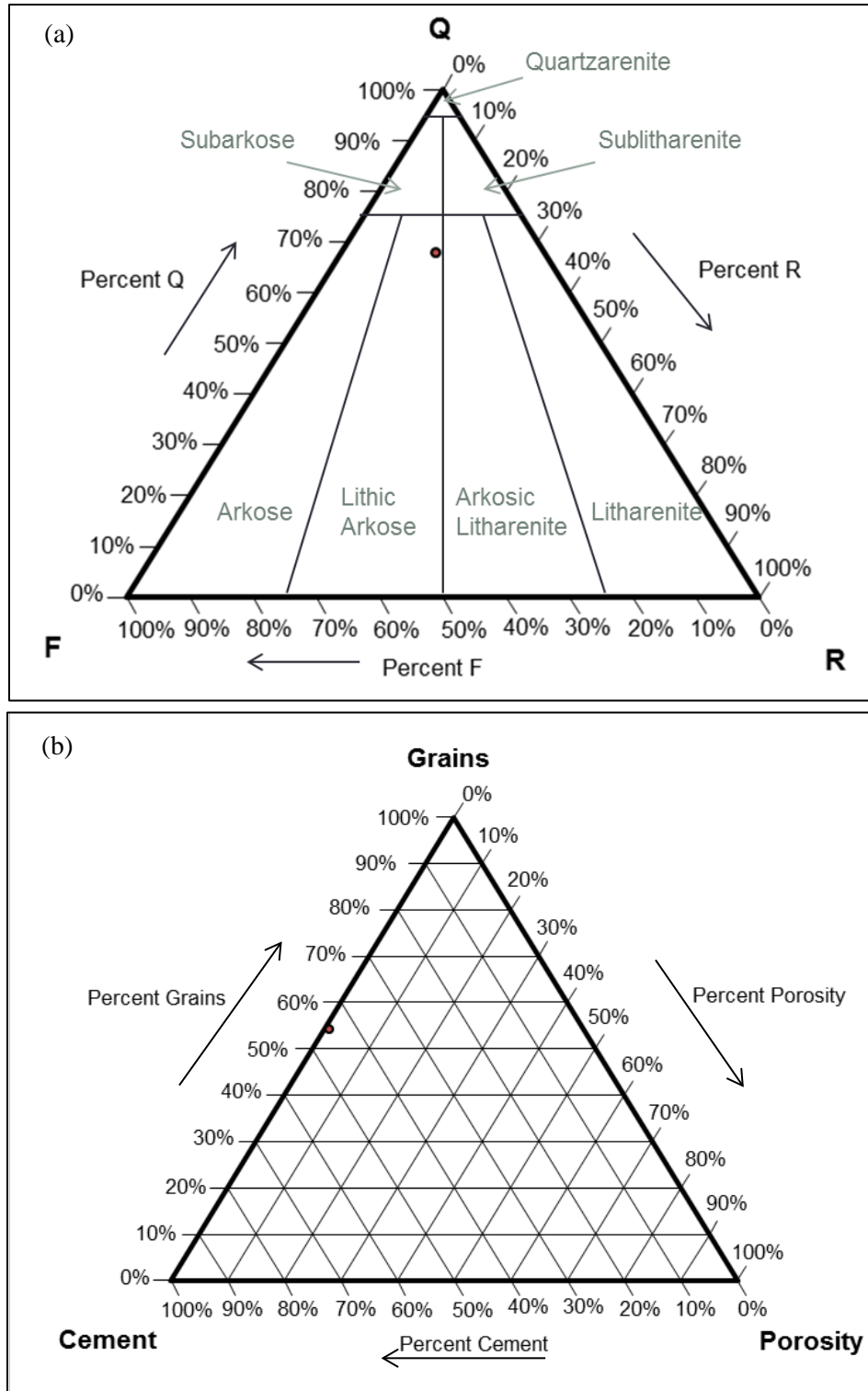


Figure 37. (a) Ternary plot based on the Folk (1968) classification showing the abundances of quartz (Q), lithics (R), and feldspar, including GRF's (F). The Fine-grained Sandstone can be classified as a lithic arkose. (b) Ternary diagram showing the abundance of grains, porosity, and cement. Porosity is negligible in this facies.

Well	Thin Section	Depth (ft)	Framework Grains									Cement / Matrix					Porosity			
			Mono Quartz	Poly Quartz	Feldspar	Glauconite	Chert	Mica	Pyrite	MRF	Other/ Unidentified Grains	Kaolinite	Quartz Overgrowth	Calcite/ Ankerite	Siderite	Other Authigenic and Detrital Clay	Intergranular Porosity	Intragranular Porosity	Total Porosity	IGV
13-10A	E6	7668.10	34%	0%	9%	TR	7%	1%	2%	0%	1%	0%	0%	0%	0%	44%	1%	0%	1%	45%

Table 3. Mineralogy of the Fine-grained Sandstone facies. Results of the 300-point count. IGV= intergranular volume.

Whole Rock Mineralogy																									
Sample	Depth (ft)																Relative Clay Abundance in Bulk Sample								
		Quartz	K-Feldspar	Plagioclase	Calcite	Siderite	Ankerite/ Fe-Dolomite	Dolomite	Pyrite	Fluorapatite	Barite	Total Non-Clay	Smectite	Illite/ Smectite (I/S)	Illite+Mica	Kaolinite	Chlorite	Total Clay	% I/S Expandability	Smectite	Illite/ Smectite (I/S)	Illite+Mica	Kaolinite	Chlorite	Total Expandable Clay
E1	7675.9	84	0	8	0	2	1	0	0	0	0	95	0	0	1	2	2	5	25	7	9	17	38	29	0
E2	7684.8	85	0	8	2	0	0	0	0	0	0	95	0	0	1	3	2	6	25	0	0	20	53	27	0
E3	7686.4	82	0	14	0	0	1	0	0	0	0	97	0	0	0	1	2	3	25	0	0	12	30	58	0
E4	7696.3	86	0	8	0	0	0	0	0	0	0	94	0	0	2	3	1	6	20	0	0	30	47	23	0
E5	7610.4	20	7	2	32	0	1	2	3	1	0	68	1	11	12	5	4	33	50	3	34	38	14	11	7
E6	7668.1	24	3	4	0	0	2	0	1	0	1	35	1	21	17	17	9	66	50	2	33	27	25	14	12

Table 4. Whole rock mineralogy of samples from well 13-10A, in weight percent, from XRD analysis. Samples E1- E4 are from the Coarse-grained Sandstone facies, E5 is from the Bioturbated Mudstone facies, and E6 is from the Fine-grained Sandstone facies.

Table 5. Clay mineralogy of samples from well 13-10A, in weight percent, from XRD analysis. Samples E1- E4 are from the Coarse-grained Sandstone facies, E5 is from the Bioturbated Mudstone facies, and E6 is from the Fine-grained Sandstone facies.

Clay Mineralogy								
		Relative Clay Abundance (< 4 Microns)						
Sample	Depth (ft)	% I/S Expandability	Smectite	Illite/ Smectite (I/S)	Illite	Kaolinite	Chlorite	Total Clay
E1	7675.9	25	18	22	8	28	25	100
E2	7684.8	25	0	15	7	40	38	100
E3	7686.4	25	0	15	6	50	29	100
E4	7696.3	20	0	16	7	58	19	100
E5	7610.4	50	5	58	14	17	6	100
E6	7668.1	50	3	46	15	25	12	100

Coarse-grained Sandstone Facies

Twenty-nine thin sections from seven wells were point counted to determine the modal composition and quantify pore types. Three hundred-point counts included grains, matrix, and porosity (Table 6, Figure 38a, b). One hundred-point counts only included porosity (Table 7, Figure 38c). For thin sections that had a small sample area or low porosity, visual estimates of porosity types were made in lieu of 100-point counts. Four samples from this facies, E1-E4 from well 13-10A, were also analyzed using XRD and Microprobe. XRD analysis was used to determine whole-rock composition and clay type and abundance (Tables 4 and 5). Microprobe analysis was used to determine elemental composition of selected cement and clay (Tables 8 and 9).

From the results of the 300-point counts, the Morrow B can be classified as subarkose sandstone using the Folk (1968) classification (Figure 38a). However, two samples from well 9-8 have slightly different compositions. Sample 3-9-8 (well 9-8, 7698 ft) has a higher percentage of feldspar than the other slides and can be classified as a sublitharenite. Sample 4-9-8 (well 9-8, 7704 ft) has a higher percentage of lithic fragments and can be classified as a lithic arkose.

The framework grains, which comprise 64 to 86% of the sandstone (Figure 38b), are primarily monocrystalline quartz, with lesser amounts of polycrystalline quartz, feldspar, granitic rock fragments (GRF), volcanic rock fragments (VRF), and chert. Other sedimentary rock fragments (SRF) and metamorphic rock fragments were observed in trace amounts. XRD analysis shows that the only variety of feldspar found in the Coarse-grained Sandstone is plagioclase (Table 4).

Matrix comprises 3 to 32% of the sandstone (Figure 38b). The most abundant type of cement is calcite, with lesser amounts of ankerite, and silica in the form of quartz overgrowths. Quartz overgrowths are quite common and may have been under-counted during point counting because dust rims are usually not present, and therefore the boundary between the grain and the overgrowth is not always clear. Other minor types of cement include feldspar overgrowths and siderite. XRD and microprobe analysis indicate that the carbonate cements in well 13-10A include siderite (sample E1), calcite (sample E2), and ankerite (sample E1 and E3). Thin sections from other wells did not undergo such analysis, so the chemical composition of the carbonate cement is unknown, but it appears to be calcite based on its petrographic characteristics. Microprobe analysis shows that ankerite composition is pretty consistent in all samples from well 13-10A, but siderite has a wide range of Fe values (Figure 40). Elemental composition of early authigenic siderite cement can give clues to whether it formed in fresh or marine water (Mozley, 1989). In general, siderite that formed in a fresh-water environment will be relatively pure (> 90 mol% FeCO_3), and siderite that formed in marine environments is extremely impure and has greater Mg substitution (Mozley, 1989). Siderite samples from well 13-10A have a broad range of FeCO_3 values that fall within fresh and marine domains (Figure 40).

Authigenic clay is abundant in the thin sections (Table 6). Kaolinite is the most common clay, and the only clay type recognized during point counting. Based on XRD analysis, total clay ranges from 3 to 6% in samples from well 13-10A (Table 4). The most abundant type of clay in those samples is kaolinite, followed by chlorite, with lesser amounts of illite, smectite, and mixed layer illite-smectite (Tables 4 and 5). Smectite and mixed layer illite-smectite were only detected in sample E1. Sample E1 had a large mudstone clast which might be the source of some or all of that clay. Illite and smectite can reduce reservoir quality if they are found within pores and pore throats. However, a mudstone grain with these types of clay probably does not have any adverse effects on reservoir quality. Various locations with different kinds of clay underwent microprobe analysis. Due to the low density of clay, the sample results came back with low totals, which can affect the accuracy of the data (Table 9). It was not possible to determine the mineralogy of many of the clay samples based on microprobe analysis alone. Some locations may contain detrital clay, which is typically composed of more than one type of clay, or have a mixture of authigenic and detrital clay. Microprobe analysis did confirm that the clay with euhedral booklets is kaolinite.

Porosity comprises 4 to 23% of the sandstone (Figure 38b). Porosity of the Coarse-grained Sandstone is predominately microporosity (both inter- and intragranular) and intergranular macroporosity (Figure 38c, Table 7). Dissolution porosity is less abundant and is only dominant in one sample, E4 from well 13-10A. Fractures are not a significant source of porosity in the Morrow B sandstone.

The IGV of the samples ranges from 10 to 35%, with an average of 22% (Table 6). IGV is influenced by compaction; lower IGV generally indicates a higher degree of compaction. In the Coarse-grained Sandstone, some of the samples with the highest IGVs have some of the lowest point-count porosity values, a reflection of large volumes of matrix.

Bioturbated Mudstone Facies

XRD analysis was performed on one sample (E5, well 13-10A, 7610 ft) from a fossil hash layer in the Bioturbated Mudstone facies (Tables 4 and 5). It consists of 68% non-clay minerals and 33% clay minerals. It consists of calcite (32%) and quartz (20%), with lesser amounts of k-feldspar (7%), pyrite (3%), plagioclase (2%), dolomite (2%), ankerite/Fe-dolomite (1%), and fluorapatite (1%). Much of the calcite and dolomite is from fossil fragments. Some fossils have been replaced by silica (Figure 39), which accounts for the presence of quartz. The most abundant type of clay in this sample is mixed layer illite-smectite, with lesser amounts of kaolinite, illite, chlorite, and smectite (Table 4 and 5).

Well	Thin Section	Depth (ft)	Framework Grains									Cement/Matrix					Porosity			
			Mono Quartz	Poly Quartz	Feldspar	GRF	Chert	Other SRF	VRF	MRF	Other/Unidentified Grains	Kaolinite	Quartz Overgrowth	Calcite/ Ankerite	Siderite	Other Authigenic and Detrital Clay	Intergranular Porosity	Intragranular Porosity	Total Porosity	IGV
32-3	2-3-32	7987	57%	4%	11%	0%	3%	TR	4%	1%	1%	2%	TR	2%	0%	8%	6%	2%	7%	18%
32-3	1-3-32	7983	49%	14%	10%	TR	3%	TR	0%	0%	TR	6%	1%	0%	0%	3%	10%	2%	12%	21%
32-2	4-B-2-3	7957	34%	34%	11%	0%	0%	0%	0%	0%	TR	TR	TR	TR	0%	2%	15%	2%	17%	19%
32-2	3-B-2-3	7948	48%	30%	5%	0%	1%	0%	0%	0%	1%	TR	0%	0%	0%	4%	11%	0%	12%	16%
32-2	2-B-2-3	7936	48%	13%	7%	1%	4%	TR	TR	TR	TR	4%	TR	0%	0%	7%	13%	2%	15%	25%
32-2	1-B-2-3	7930	38%	23%	6%	2%	1%	0%	0%	0%	1%	5%	TR	0%	TR	5%	16%	1%	18%	27%
42-1	5-1-56	8022	42%	25%	6%	6%	1%	0%	3%	0%	0%	1%	0%	0%	0%	4%	10%	2%	12%	15%
42-1	4-1-56	8028	46%	17%	5%	9%	3%	1%	2%	0%	0%	1%	0%	0%	0%	2%	12%	2%	14%	15%
42-1	3-1-56	8015.5	52%	5%	8%	1%	1%	0%	1%	0%	TR	2%	0%	24%	1%	2%	3%	1%	4%	31%
42-1	2-1-56	8010	53%	9%	7%	1%	3%	0%	3%	TR	TR	4%	1%	3%	0%	2%	13%	1%	14%	22%
42-1	1-1-56	8005	47%	5%	8%	TR	7%	0%	0%	TR	TR	3%	TR	1%	4%	12%	10%	1%	12%	31%
32-1	4-C-1-32	7983	60%	4%	7%	TR	2%	TR	TR	0%	0%	TR	1%	0%	0%	3%	21%	2%	23%	26%
32-1	3-C-1-32	7945.5	60%	6%	7%	TR	4%	0%	0%	0%	1%	0%	0%	12%	0%	2%	8%	TR	8%	21%
32-1	2-C-1-32	7980	66%	4%	7%	6%	2%	0%	1%	0%	0%	2%	1%	0%	0%	3%	6%	2%	8%	12%
32-1	1-C-1-32	7970	64%	5%	5%	1%	2%	1%	1%	0%	TR	5%	0%	0%	0%	6%	12%	TR	12%	22%
9-8	6-9-8	7700	57%	6%	9%	2%	4%	0%	3%	0%	1%	3%	TR	TR	TR	7%	8%	TR	9%	19%
9-8	5-9-8	7709	58%	3%	4%	1%	1%	1%	3%	3%	1%	0%	1%	13%	0%	9%	2%	TR	3%	25%
9-8	4-9-8	7704	50%	4%	8%	4%	2%	TR	3%	3%	0%	3%	1%	TR	0%	7%	15%	TR	15%	25%
9-8	3-9-8	7698	59%	2%	4%	2%	1%	1%	6%	2%	0%	3%	1%	0%	0%	5%	13%	1%	14%	22%
9-8	2-9-8	7694	47%	6%	6%	3%	1%	TR	4%	TR	1%	6%	0%	0%	TR	18%	8%	0%	8%	32%
9-8	1-9-8	7693	48%	7%	6%	3%	3%	1%	4%	TR	1%	5%	0%	TR	1%	15%	6%	TR	7%	27%
33-3	4-B-3-3	7943.2	57%	7%	3%	3%	1%	0%	2%	1%	TR	5%	2%	0%	0%	1%	17%	1%	18%	24%
33-3	3-B-3-3	7958	51%	5%	3%	2%	1%	0%	1%	1%	0%	1%	0%	29%	0%	2%	3%	TR	4%	35%
33-3	2-B-3-3	7948.5	49%	6%	5%	7%	TR	1%	4%	TR	TR	1%	1%	0%	0%	3%	20%	1%	22%	26%
33-3	1-B-3-3	7934	58%	3%	4%	7%	1%	0%	2%	TR	0%	0%	0%	0%	TR	6%	18%	1%	19%	24%
13-10A	E1	7675.9	53%	9%	6%	5%	3%	1%	1%	0%	0%	2%	1%	1%	5%	3%	7%	3%	10%	18%
13-10A	E2	7684.75	65%	4%	7%	6%	0%	0%	3%	0%	0%	2%	2%	2%	1%	3%	4%	2%	6%	14%
13-10A	E3	7689.4	59%	6%	7%	5%	1%	0%	9%	0%	0%	1%	TR	TR	0%	5%	3%	5%	8%	10%
13-10A	E4	7696.25	63%	1%	7%	1%	TR	0%	5%	1%	0%	4%	1%	TR	0%	3%	9%	7%	16%	17%

Table 6. Mineralogy of the Coarse-grained Sandstone. Results of 300-point counts. TR= trace, <1%.

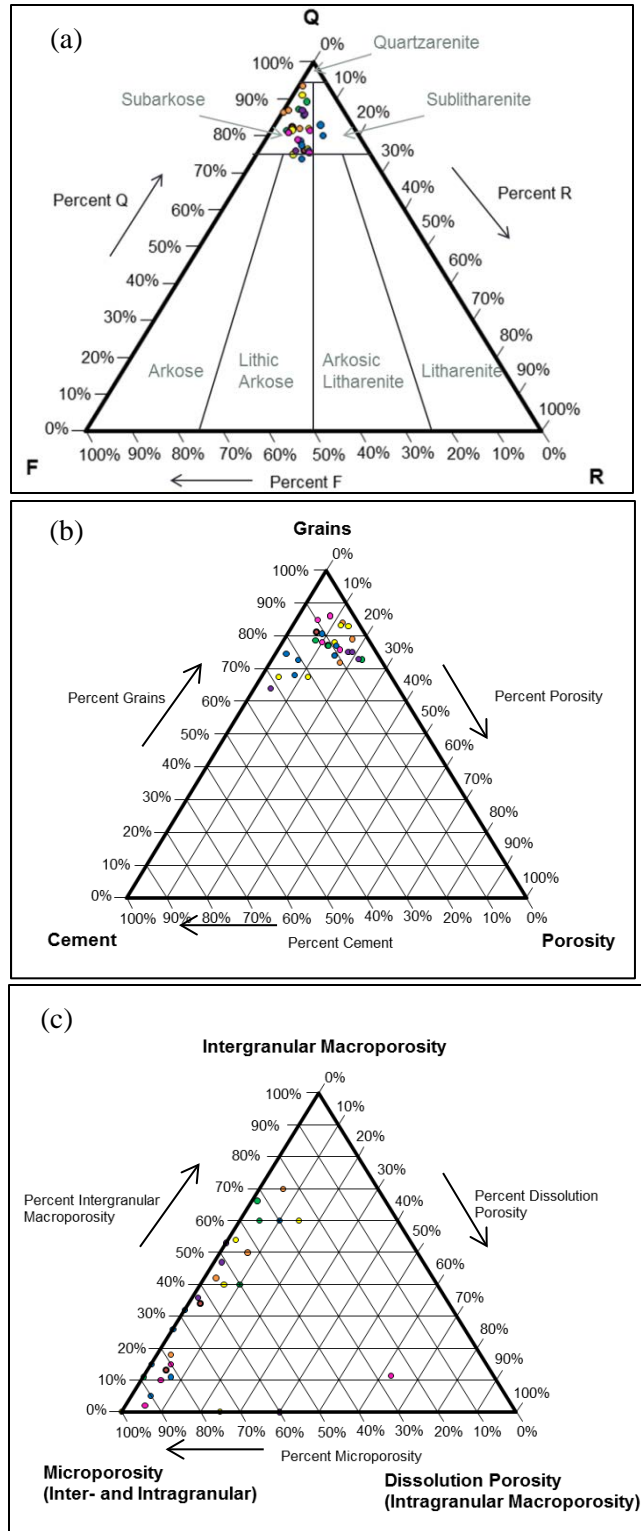


Figure 38. (a) Ternary plot based on the Folk (1968) classification showing the abundances of quartz (Q), lithics (R), and feldspar (including GRF's) (F). (b) Abundance of grains, porosity, and cement. (c) Abundance of Intergranular Macroporosity, Dissolution Porosity (Intragranular Macroporosity), and Microporosity (Inter- and Intragranular).

Table 7. Porosity of the Coarse-grained Sandstone. Results of 100-point counts for porosity. Thin sections with low porosity were visually estimated.

Well	Thin Section	Depth (ft)	Visual Estimate?	Porosity			
				Intergranular Macroporosity	Intragranular Macroporosity	Intergranular Microporosity	Intragranular Microporosity
32-3	2-3-32	7987	X	34%	3%	53%	10%
32-3	1-3-32	7983		13%	5%	75%	6%
32-2	4-B-2-3	7957		50%	7%	25%	18%
32-2	3-B-2-3	7948		70%	6%	14%	9%
32-2	2-B-2-3	7936		18%	4%	65%	13%
32-2	1-B-2-3	7930		42%	3%	47%	8%
42-1	5-1-56	8022		54%	2%	26%	18%
42-1	4-1-56	8028	X	60%	15%	15%	10%
42-1	3-1-56	8015.5	X	0%	25%	0%	75%
42-1	2-1-56	8010		40%	6%	40%	15%
42-1	1-1-56	8005		0%	0%	89%	11%
32-1	4-C-1-32	7983		66%	1%	21%	12%
32-1	3-C-1-32	7945.5	X	60%	5%	25%	10%
32-1	2-C-1-32	7980	X	40%	10%	30%	20%
32-1	1-C-1-32	7970		11%	0%	75%	14%
9-8	6-9-8	7700		11%	7%	66%	15%
9-8	5-9-8	7709	X	60%	10%	20%	10%
9-8	4-9-8	7704		32%	0%	56%	13%
9-8	3-9-8	7698		26%	0%	57%	17%
9-8	2-9-8	7694	X	15%	0%	40%	45%
9-8	1-9-8	7693	X	5%	5%	45%	45%
33-3	4-B-3-3	7943.2		47%	2%	34%	17%
33-3	3-B-3-3	7958	X	0%	40%	5%	55%
33-3	2-B-3-3	7948.5		53%	0%	36%	11%
33-3	1-B-3-3	7934		36%	2%	48%	15%
13-10A	E1	7675.9	X	15%	5%	60%	20%
13-10A	E2	7684.75	X	10%	5%	65%	20%
13-10A	E3	7689.4	X	2%	5%	33%	60%
13-10A	E4	7696.25		11%	26%	32%	31%

Table 8. Elemental composition of carbonate cement in the Coarse-grained Sandstone from well 13-10A. Results of microprobe analysis, in mol%. All weight % totals were 100%, plus or minus 0.5%, which is an acceptable range of error. See Appendix D for raw data.

Sample	MgCO ₃	CaCO ₃	MnCO ₃	FeCO ₃	Na ₂ O
E1-01	27%	47%	2%	24%	0%
E1-02	31%	48%	1%	19%	0%
E1-03	24%	1%	2%	72%	0%
E1-04	25%	1%	2%	72%	0%
E1-05	25%	1%	2%	72%	0%
E1-06	17%	4%	1%	78%	0%
E1-08	26%	47%	2%	25%	0%
E1-09	26%	1%	1%	72%	0%
E1-10	19%	1%	1%	79%	0%
E1-11	30%	3%	3%	63%	0%
E1-15	21%	1%	1%	77%	0%
E1-17	23%	1%	1%	75%	0%
E1-19	25%	1%	2%	72%	0%
E1-20	24%	2%	1%	72%	0%
E1-23	26%	1%	2%	71%	0%
E1-24	25%	1%	2%	72%	0%
E1-25	23%	1%	1%	75%	0%
E1-26	16%	2%	2%	80%	0%
E1-29	6%	3%	2%	89%	0%
E1-30	8%	3%	2%	87%	0%
E1-31	24%	1%	2%	73%	0%
E1-32	31%	49%	1%	19%	0%
E1-33	17%	3%	1%	79%	0%
E1-34	24%	1%	2%	73%	0%
E1-35	24%	1%	2%	74%	0%
E1-37	4%	2%	2%	92%	0%
E1-38	24%	1%	1%	74%	0%
E1-39	24%	1%	1%	74%	0%
E1-40	26%	2%	2%	70%	0%
E1-42	28%	46%	1%	25%	0%
E1-43	24%	1%	2%	73%	0%
E1-44	25%	1%	2%	73%	0%
E1-45	24%	1%	2%	72%	1%
E1-46	24%	1%	1%	73%	0%
E2-01	26%	1%	2%	71%	0%
E2-02	27%	1%	4%	68%	0%
E2-05	28%	1%	4%	67%	0%
E2-07	29%	1%	2%	67%	0%
E2-08	24%	1%	3%	72%	0%
E2-09	22%	2%	3%	74%	0%
E2-10	32%	45%	2%	21%	0%
E2-12	29%	44%	1%	26%	0%
E3-03	30%	45%	2%	23%	0%
E3-04	23%	2%	2%	73%	0%
E3-05	28%	47%	2%	23%	0%
E4-01	29%	47%	2%	22%	0%
E4-02	27%	46%	2%	24%	0%
E4-03	1%	2%	7%	90%	0%
E4-04	27%	2%	3%	67%	0%
E4-06	27%	46%	2%	24%	0%
E4-07	26%	3%	3%	68%	0%
E4-08	29%	1%	3%	67%	0%
E4-10	22%	2%	4%	72%	0%
E4-11	1%	2%	7%	90%	0%
E4-13	23%	1%	3%	73%	0%
E4-15	29%	2%	3%	67%	0%
E4-16	1%	3%	9%	87%	0%

Table 9. Elemental composition of clay in the Coarse-grained Sandstone from well 13-10A, in weight %. Results have been normalized to 100%. The “totals” column shows the pre-normalized totals, all of which are below 100%. Totals below 100% are less accurate. See Appendix D for raw data.

Sample	SiO ₂	TiO ₂	Al ₂ O ₃	FeO	MgO	CaO	Na ₂ O	K ₂ O	P ₂ O ₅	MnO	SO ₂	F	Cl	Totals
E1-07	52.1	0.5	26.8	6.3	2.2	1.1	1.8	6.0	0.1	0.0	0.1	0.5	2.5	76.11
E1-12	34.1	0.8	26.4	30.0	5.7	0.6	0.1	1.1	0.1	0.0	0.0	0.2	0.9	66.63
E1-13	54.4	0.0	44.8	0.0	0.0	0.1	0.1	0.0	0.0	0.0	0.0	0.1	0.6	75.95
E1-14	37.3	0.5	27.4	25.7	5.0	0.4	0.2	1.7	0.1	0.0	0.0	0.2	1.5	63.35
E1-18	30.5	0.0	26.5	34.9	6.7	0.2	0.2	0.2	0.0	0.1	0.1	0.1	0.5	78.17
E1-21	37.1	0.2	28.1	22.2	4.9	1.6	0.1	2.4	1.6	0.0	0.1	0.0	1.7	62.40
E1-22	55.0	0.0	43.9	0.1	0.0	0.1	0.1	0.0	0.0	0.0	0.0	0.0	0.8	72.12
E1-27	39.5	0.1	26.6	24.2	5.0	0.9	0.2	1.9	0.0	0.0	0.1	0.0	1.4	63.07
E1-28	31.9	1.3	20.8	31.9	10.2	1.3	0.2	0.2	1.1	0.1	0.0	0.7	0.2	84.89
E1-36	48.2	0.7	29.0	12.1	3.2	0.5	0.4	5.0	0.1	0.0	0.1	0.0	0.8	76.05
E1-41	54.4	0.0	44.6	0.0	0.0	0.1	0.1	0.0	0.0	0.0	0.1	0.1	0.6	75.51
E2-03	54.4	0.0	45.1	0.1	0.0	0.0	0.1	0.0	0.0	0.0	0.0	0.0	0.1	81.82
E2-04	36.8	0.1	28.0	25.5	5.1	0.4	0.4	1.5	0.1	0.0	0.1	0.2	2.1	52.00
E2-06	33.3	0.3	26.5	30.0	6.8	0.3	0.3	0.7	0.8	0.0	0.0	0.2	0.7	71.13
E2-11	38.2	0.0	28.1	23.2	4.7	0.7	0.4	2.0	0.3	0.1	0.1	0.0	2.1	54.43
E3-01	53.6	0.0	45.9	0.0	0.0	0.1	0.1	0.0	0.0	0.0	0.0	0.0	0.4	79.67
E3-02	31.7	0.1	27.5	31.2	6.3	0.4	0.3	0.6	0.1	0.0	0.1	0.0	1.6	57.26
E3-06	35.0	0.1	27.1	29.2	6.3	0.2	0.3	0.9	0.1	0.0	0.1	0.1	0.5	61.58
E3-07	29.6	0.1	24.5	29.2	5.8	0.2	0.4	0.8	0.1	0.0	8.6	0.1	0.5	73.60
E3-08	31.1	0.0	26.0	36.8	4.5	0.1	0.2	0.2	0.0	0.9	0.0	0.0	0.1	84.05
E4-09	52.5	0.0	44.7	1.1	0.2	0.2	0.1	0.5	0.1	0.0	0.0	0.2	0.4	79.54
E4-12	32.5	0.0	27.5	30.1	6.1	0.5	0.5	0.7	0.0	0.0	0.1	0.0	2.0	59.03
E4-14	29.5	0.1	27.7	34.4	6.8	0.4	0.0	0.1	0.1	0.1	0.0	0.0	0.8	71.56
E4-17	40.6	0.2	27.1	22.6	4.8	0.4	0.7	2.4	0.0	0.0	0.0	0.1	1.0	67.08

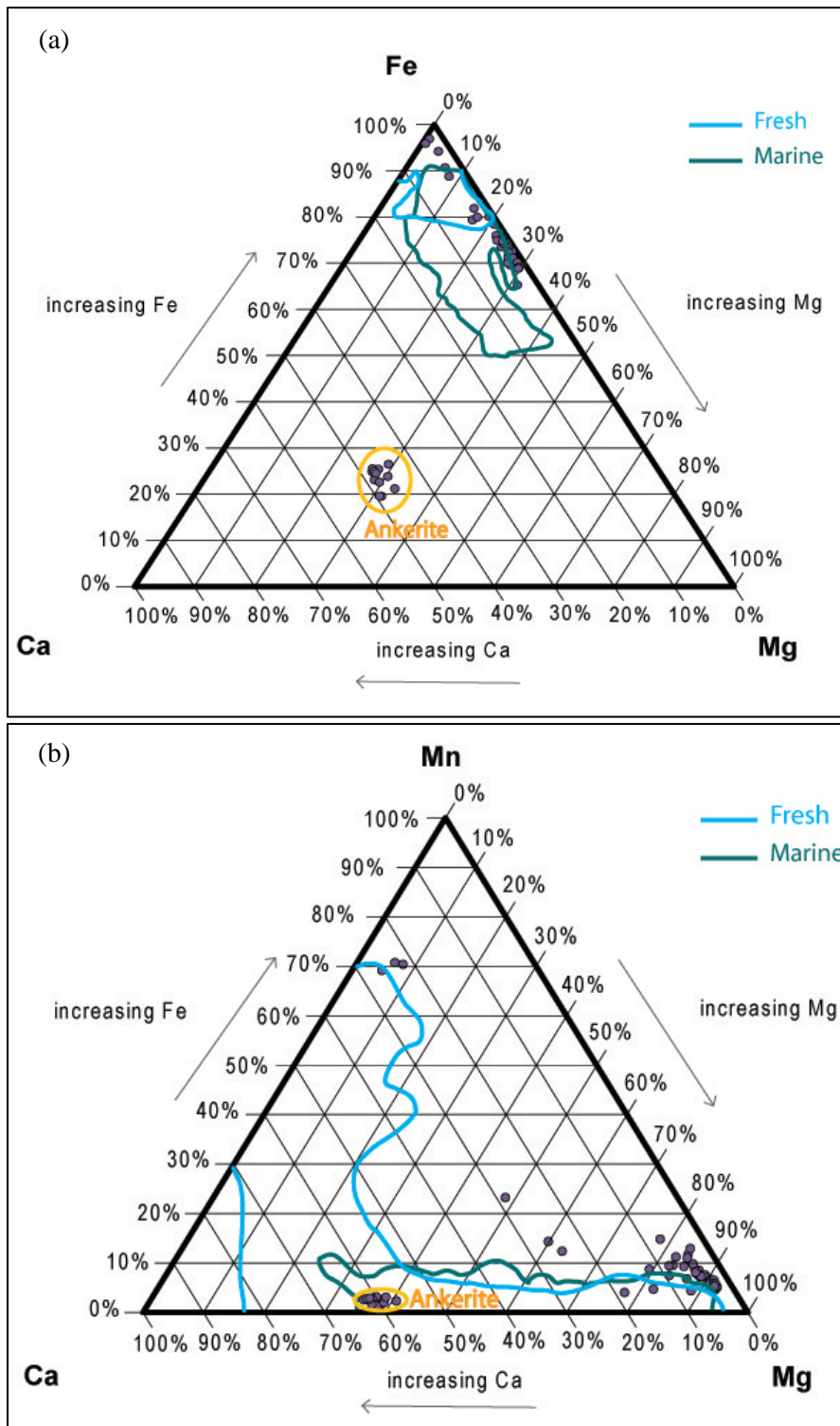


Figure 39. Carbonate cement ternary diagrams for samples E1- E4, from well 13-10A. Values are in mol% oxide. Fresh and marine domains are from Mozley (1989). Note that composition of ankerite is fairly consistent in all samples, but siderite composition varies. (a) FeCO₃-MgCO₃-CaCO₃ diagram. (b) MnCO₃-MgCO₃-CaCO₃ diagram.

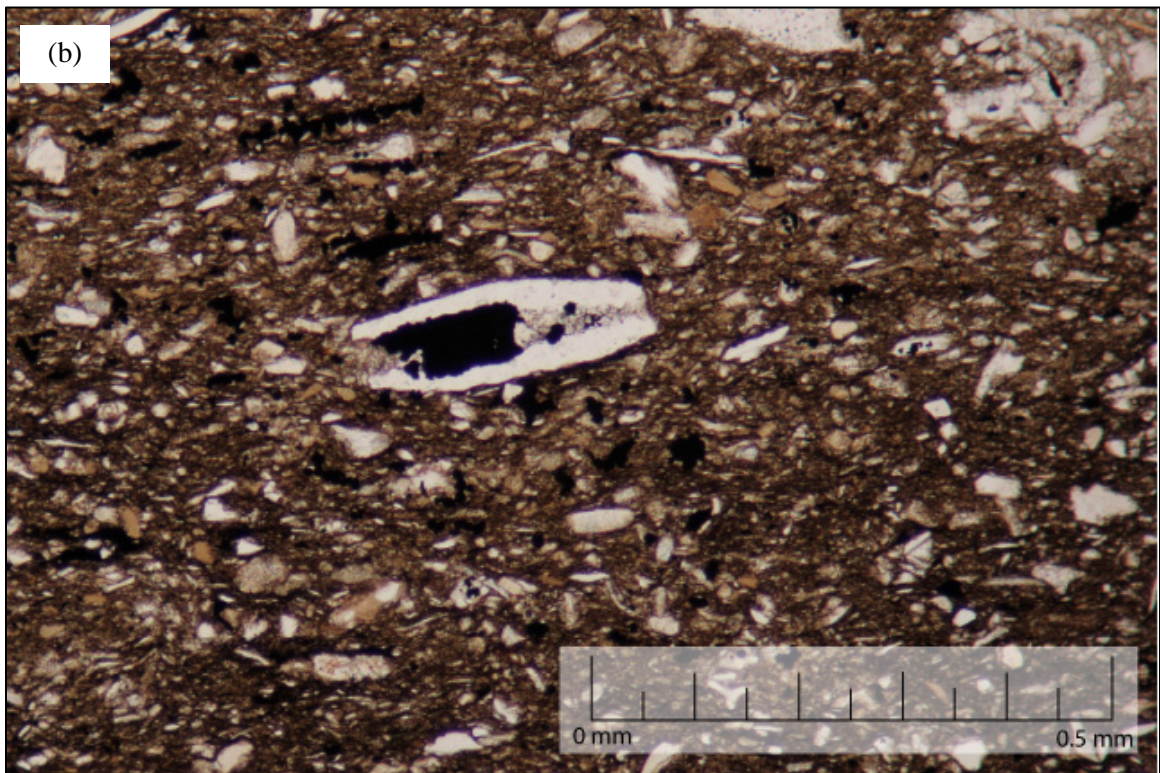
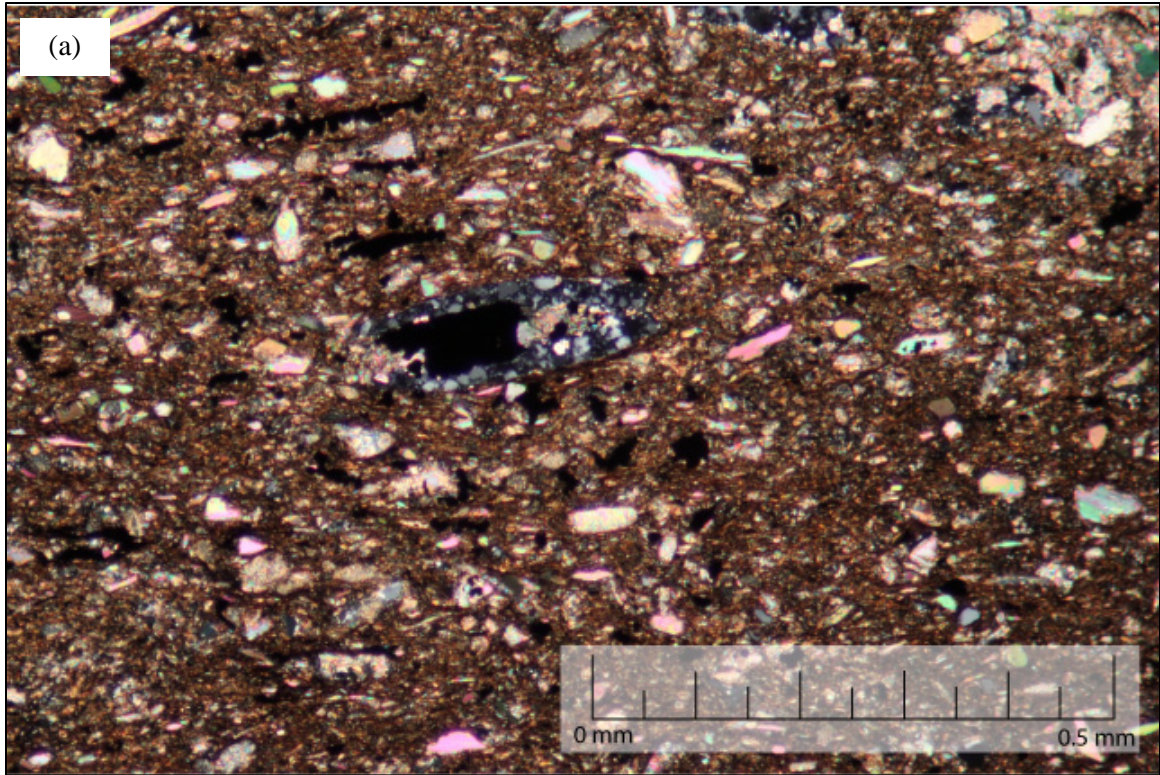


Figure 40. Sample E5, well 13-10A, 7610.40 ft. Photomicrograph of a sample from the bioturbated mudstone facies. Many fossil fragments are composed of calcite. Some fossils, such as the crinoid pictured, have been replaced by silica. (a) xpl (b) ppl.

Diagenesis

Based on petrographic observations, the diagenetic events that occurred in the Morrow B sandstone are, in order from earliest to latest: siderite cementation, quartz overgrowths, feldspar overgrowths, calcite cementation, ankerite cementation, replacement of feldspar by calcite and ankerite, compaction (mechanical and chemical), feldspar dissolution, precipitation of authigenic clay, and hydrocarbon emplacement (Figure 41).

From the results of the microprobe analysis, it was determined that the carbonate cement in the four samples from 13-10A is ankerite (Figure 40). However, the other twenty-five thin sections observed did not undergo microprobe analysis, so the chemical composition of the cement could not be determined. The ankerite cement in samples from well 13-10A displays sweeping extinction. The carbonate cement in the other thin sections does not display sweeping extinction, and in many samples it is poikilotopic, so it is probably calcite. Therefore, the cement is referred to as ankerite where the chemical composition is known to be ankerite, and referred to as calcite where it appears to be calcite.

Event	Early								Late
Siderite Cement	—————								
Quartz Overgrowths		—————							
Feldspar Overgrowths		? ——— ?							
Calcite Cement			—————	-----					
Ankerite Cement			? ——— ?						
Calcite and Ankerite Replace Feldspar			—————						
Significant Compaction- Mechanical				—————					
Significant Compaction- Chemical				—————					
Feldspar Dissolution					—————	-----	-----	-----	?
Authigenic Kaolinite						-----	-----		
Authigenic Chlorite						-----	-----		
Hydrocarbon emplacement									-----

Figure 41. Paragenetic sequence of the Morrow B sandstone.

Siderite cement

Siderite cement formed early in the Morrow B sandstone. There is evidence that it formed before quartz overgrowths and calcite cement. The presence of a siderite on the surface of quartz grains that are surrounded by quartz overgrowths (Figure 42 and 43) demonstrates that siderite precipitation preceded quartz. Sample E1 has abundant siderite cement that fills much of the intergranular volume (IGV), and in some locations has a different texture than was observed in thin sections from other wells (Figure 43a). Siderite formed on grains, and not on quartz overgrowths. In some places, siderite formed on a grain and a quartz overgrowth grew right next to the siderite, suggesting that the overgrowth came later and only grew on the grain surface that did not have siderite cement already (Figure 43b, c). Quartz overgrowths seem to have formed in areas where siderite was absent. Calcite cement surrounds a siderite crystal (Figure 44b), which indicates that siderite cement also preceded calcite cementation.

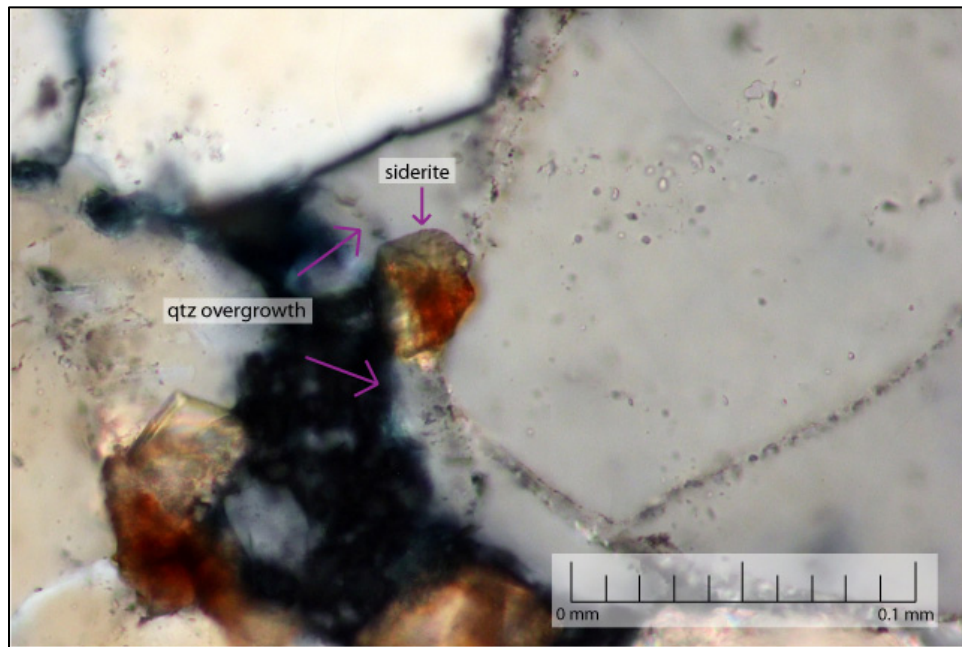


Figure 42. Well 42-1, 8005 ft, xpl. A siderite crystal formed on the surface of a quartz grain, and a quartz overgrowth formed around the siderite, indicating that siderite precipitated before quartz cement.

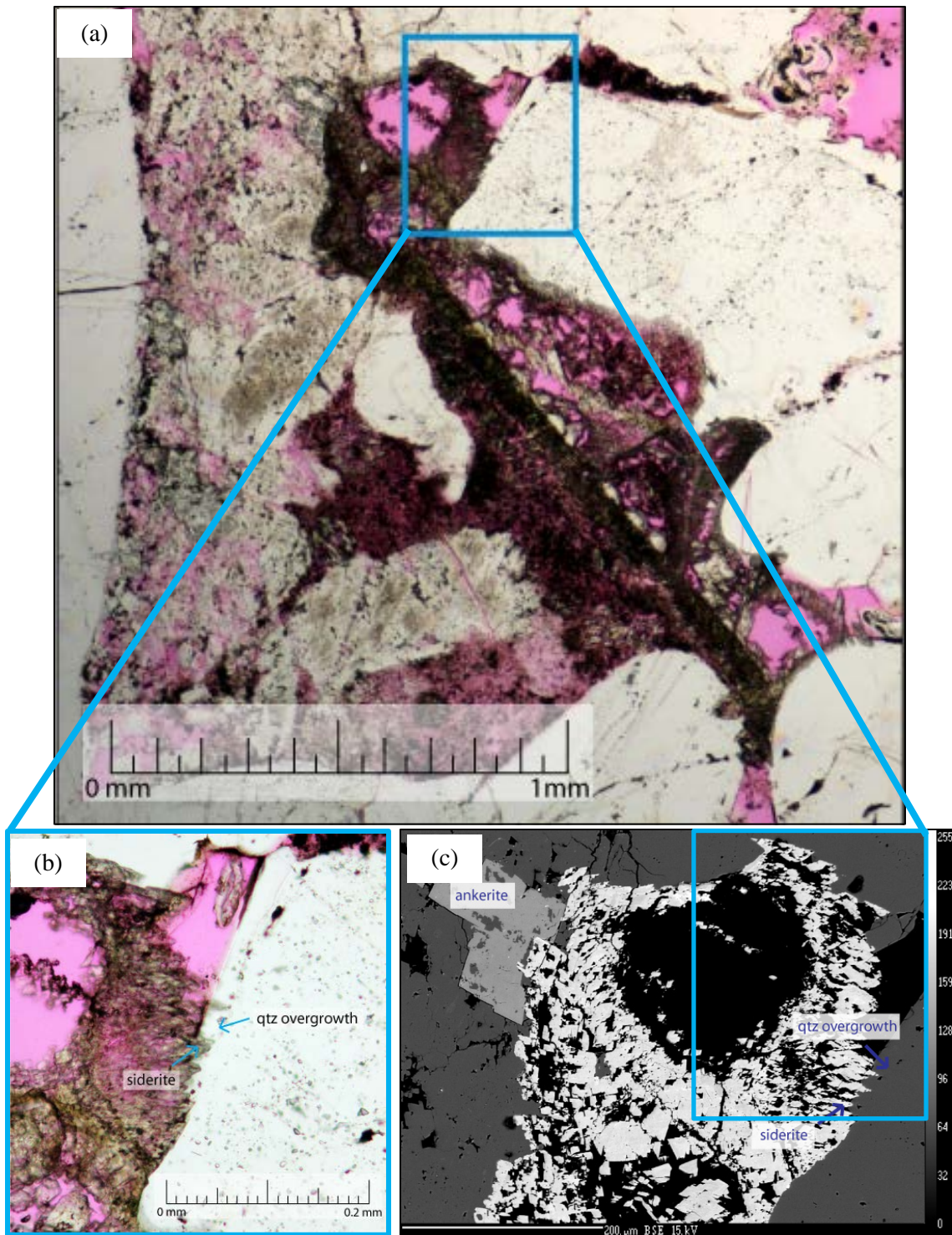


Figure 43. Well 13-10A, 7675.9 ft. Siderite formed on a quartz grain and a quartz overgrowth grew next to and around the siderite. This suggests that the overgrowth came later and only grew on the grain surface that did not have siderite cement already. (a) Siderite cement fills the IGV between quartz grains, ppl. (b) A close-up of the area in the blue box in figure (a), ppl. (c) A backscattered electron (BSE) image of the same location.



Figure 44. Well 42-1, 8015.5 ft, ppl. Calcite precipitated on a siderite crystal, indicating that siderite precipitated before the calcite.

There is evidence to suggest that siderite formed before significant mechanical and chemical compaction. Sample E1 has a high IGV and also has abundant siderite cement (2% of the whole rock, Table 4). Sample E3 is very compacted and contains negligible amounts siderite (not detected by XRD, Table 4). It is likely that early siderite cement prevented compaction in sample E1, and because sample E3 was not cemented by siderite, it underwent more compaction. A few stylolites have siderite crystals concentrated around them (Figure 45). The concentration of siderite is the highest along these stylolites and decreases away from them. The siderite near the stylolites probably formed before pressure solution, then was concentrated around the stylolites because it is stable and did not dissolve. Alternatively, some siderite might have precipitated during pressure solution. However, many stylolites do not have siderite cement, which suggests that siderite did not precipitate during pressure solution.

Microprobe analysis showed that the siderite in well 13-10A has a range of Fe values. BSE images revealed that in some locations, two stages of siderite cementation occurred (Figures 46).

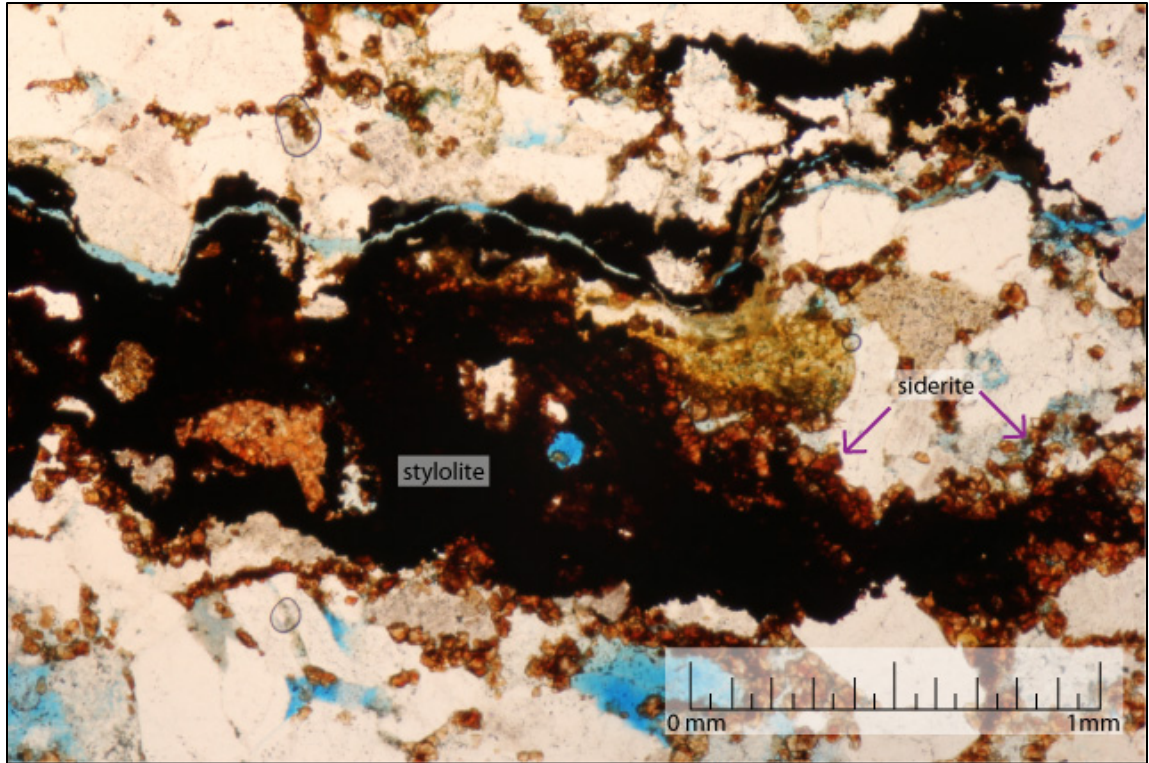


Figure 45. Well 42-1, 8005 ft, ppl. A carbonaceous stylolite with abundant siderite. Siderite was probably concentrated around this stylolite during pressure solution.

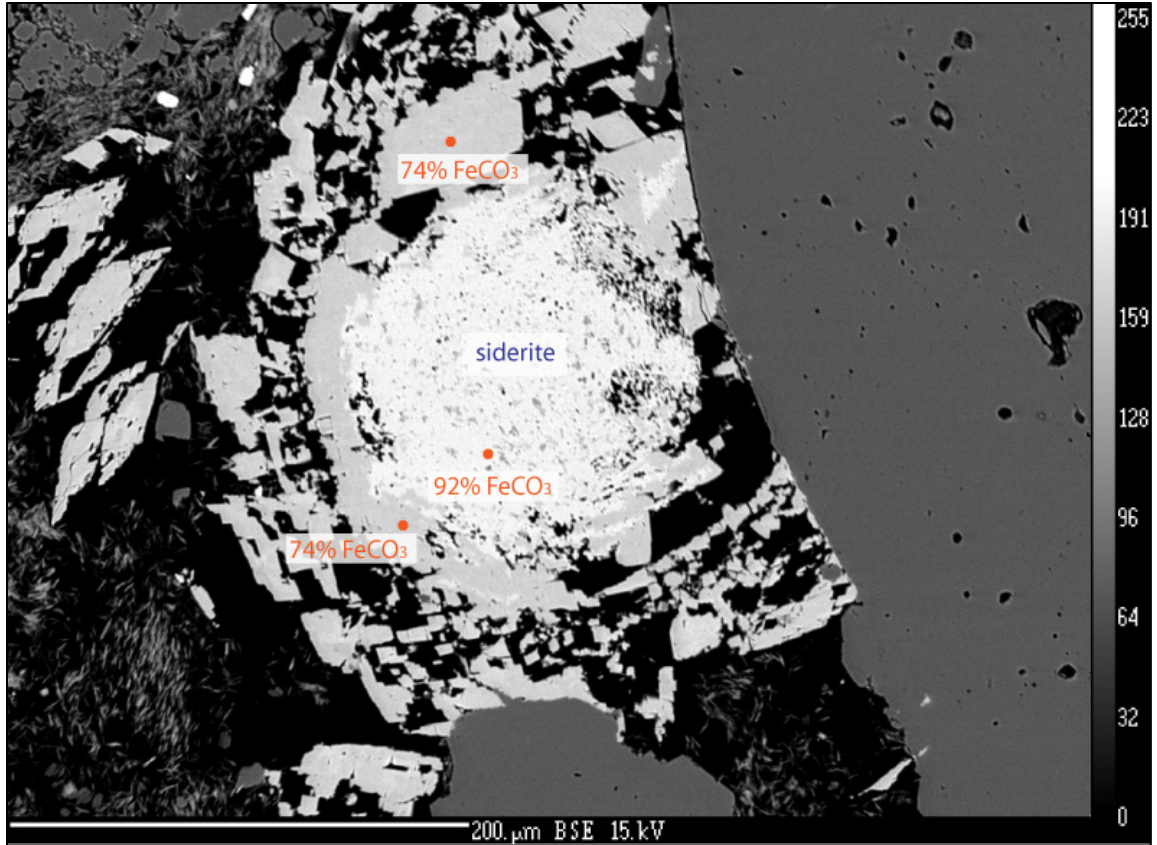


Figure 46. Sample E1, well 13-10A, 7675.90 ft. A BSE image labeled with FeCO_3 concentrations from microprobe analysis, in mol%. The inner siderite has a greater Fe concentration than the outer siderite, which indicates two stages of siderite cementation. The inner siderite likely precipitated before the outer siderite.

Quartz Overgrowths

Quartz overgrowths formed after siderite cement and before calcite, ankerite, and kaolinite. Euhedral quartz overgrowths formed early when there was sufficient primary porosity for them to grow (Figure 47). The presence of quartz overgrowths surrounded by poikilotopic calcite indicates that they precipitated before calcite (Figures 47 and 48). Kaolinite fills pores around quartz overgrowths, indicating that it precipitated later (Figure 47).

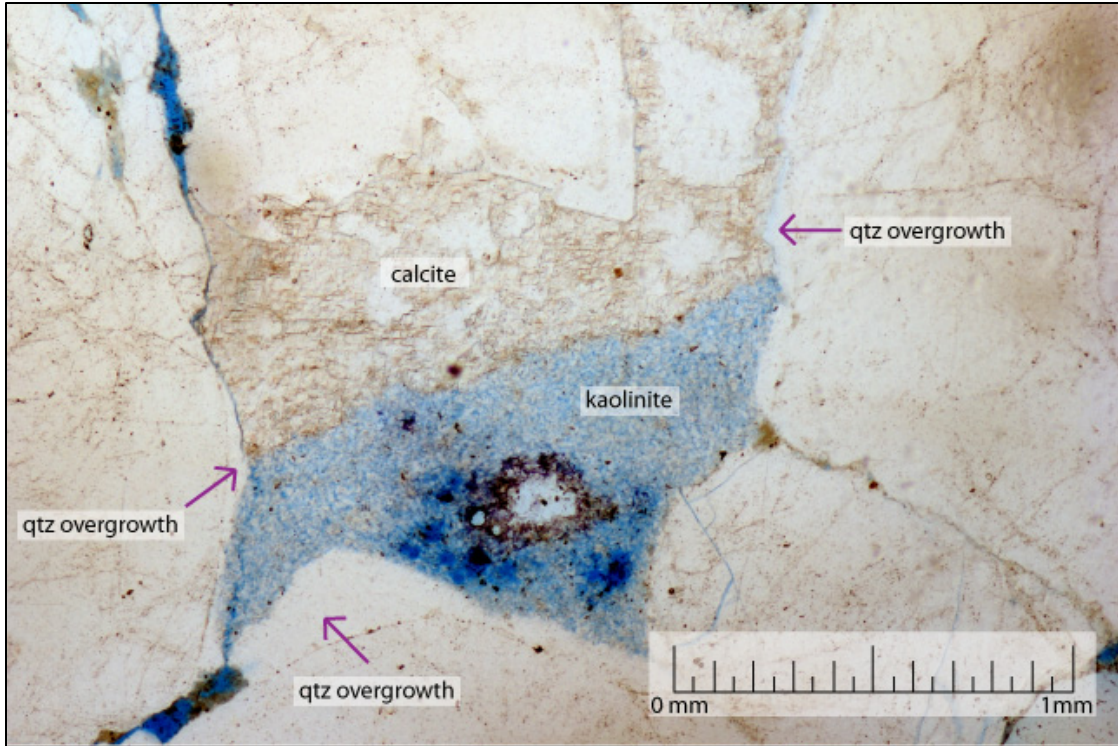


Figure 47. Well 32-2, 7957 ft, ppl. Calcite and kaolinite surround quartz overgrowths, which indicate that the quartz overgrowths formed before the calcite or kaolinite.

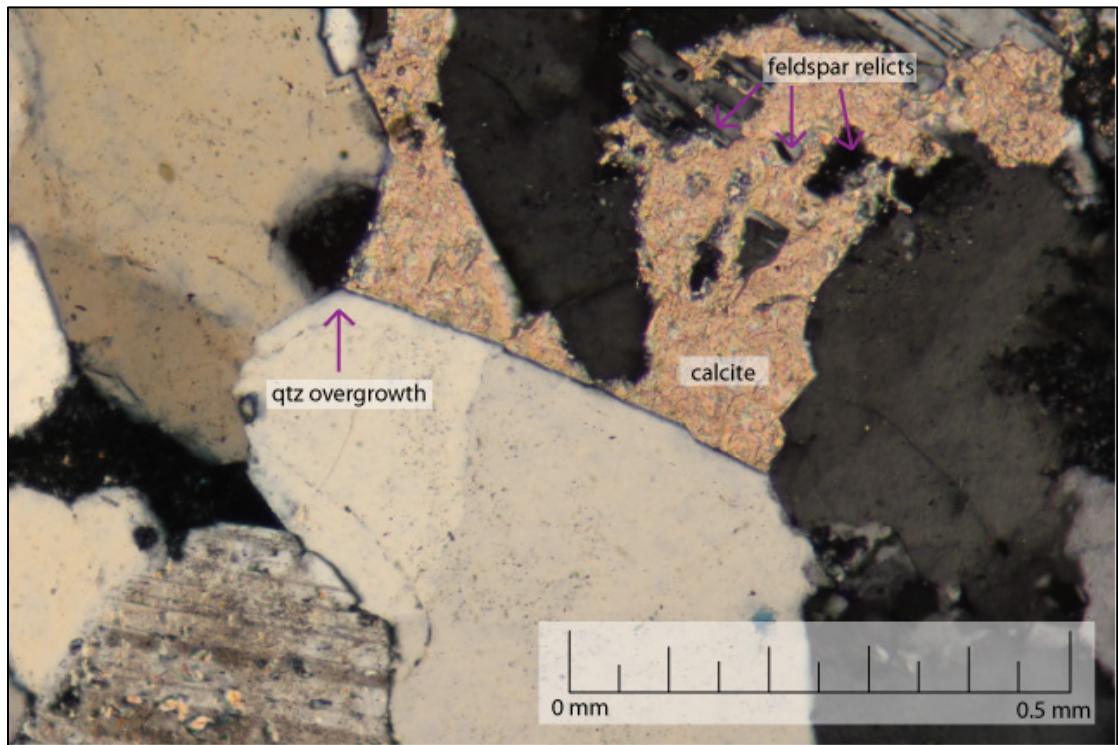


Figure 48. Well 32-3, 7987 ft, xpl. Poikilotopic calcite surrounds a quartz overgrowth, which suggests that calcite precipitated after quartz overgrowths. Floating feldspar relicts in poikilotopic calcite suggest that calcite replaced feldspar.

Feldspar Overgrowths

Feldspar overgrowths are not abundant, so it was not possible to determine their relationship to most other events in the paragenetic sequence. However, there is some evidence indicating that they formed around the same time as quartz overgrowths. The principal evidence for this is contacts between feldspar overgrowths and quartz overgrowths for which it appears that quartz precipitation was restricted by the feldspar overgrowth and feldspar precipitation by the quartz overgrowth (Figure 49a). Thus, if quartz overgrowths had developed before the feldspar overgrowth, it should be in contact with the feldspar grain, but instead it terminates at the edge of the feldspar overgrowth. One GRF has both a quartz overgrowth and a feldspar overgrowth (Figure 49b). The boundary between the two overgrowths also suggests that they precipitated at the same time because neither overgrowth is encroaching on the other.

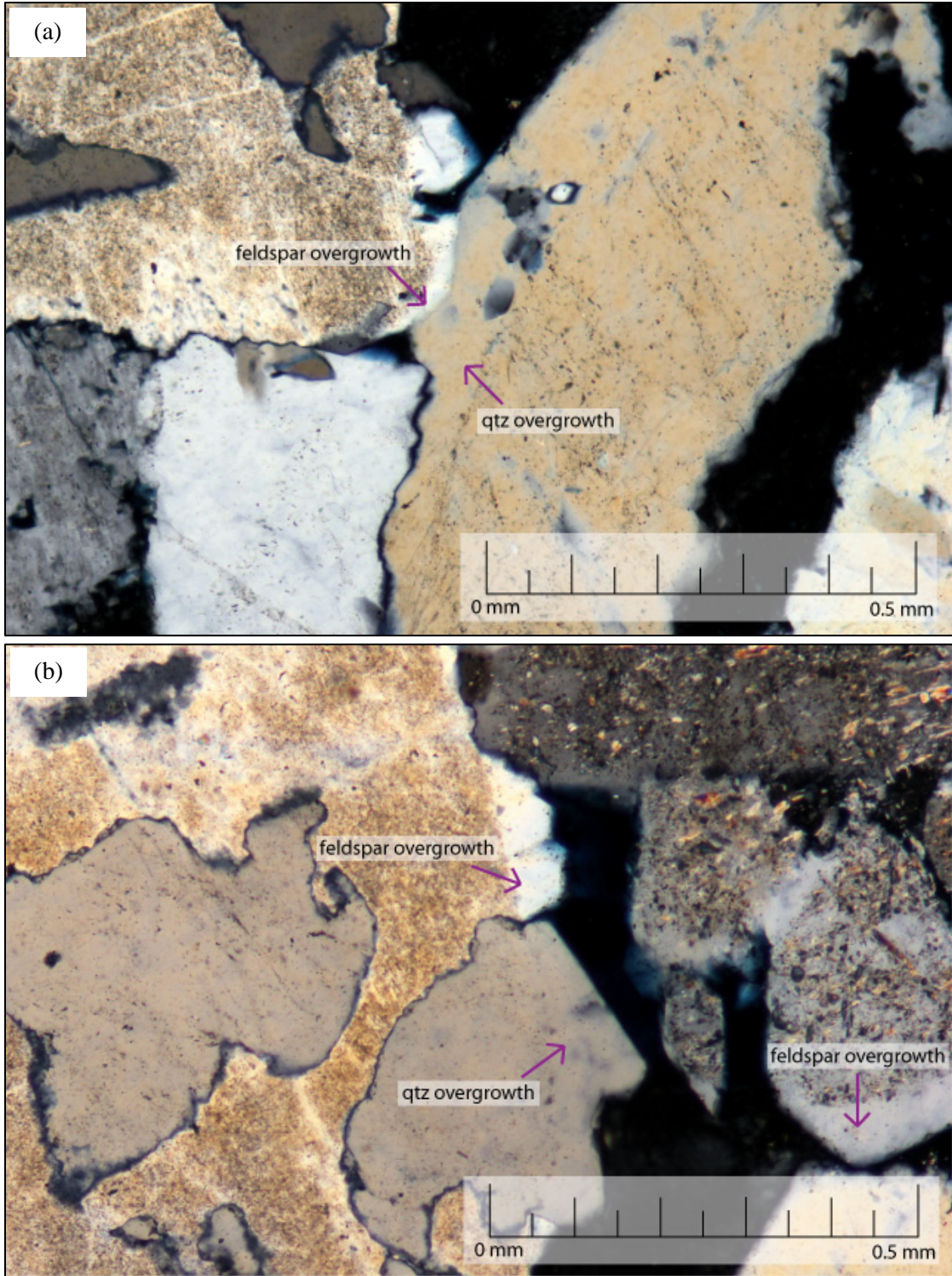


Figure 49. Well 42-1, 8022 ft, xpl. (a) Quartz overgrowth in contact with a feldspar overgrowth. Quartz precipitation was restricted by the feldspar overgrowth and feldspar precipitation by the quartz overgrowth, suggesting they formed at the same time. (b) Quartz and feldspar overgrowths on a GRF. The boundary between the two overgrowths suggests that they precipitated at the same time because neither overgrowth is encroaching on the other.

Calcite Cement

Calcite cement formed after siderite and quartz overgrowths and before authigenic clay (Figures 47). The paragenetic relationship between calcite and compaction is variable. In some slides, poikilotopic calcite fills almost all primary porosity (Figure 50a), whereas many slides have no calcite/ankerite at all. Poikilotopic calcite appears to have prevented compaction in some slides, which is evident from the high IGV of those slides. There are some slides where calcite is adjacent to low-IGV areas that have a high degree of grain packing (Figure 50b). This suggests that calcite precipitation overlapped with compaction, or a second stage of calcite cementation occurred after compaction.

In some places, calcite cements replaced feldspar grains (Figures 48 and 51). In one VRF, feldspar crystals are replaced by calcite that goes extinct at the same time as the poikilotopic calcite surrounding the grain (Figure 51a). Feldspar relicts within poikilotopic calcite suggest that calcite replaced feldspar, rather than filling in after feldspar dissolution (Figure 48 and 51b).

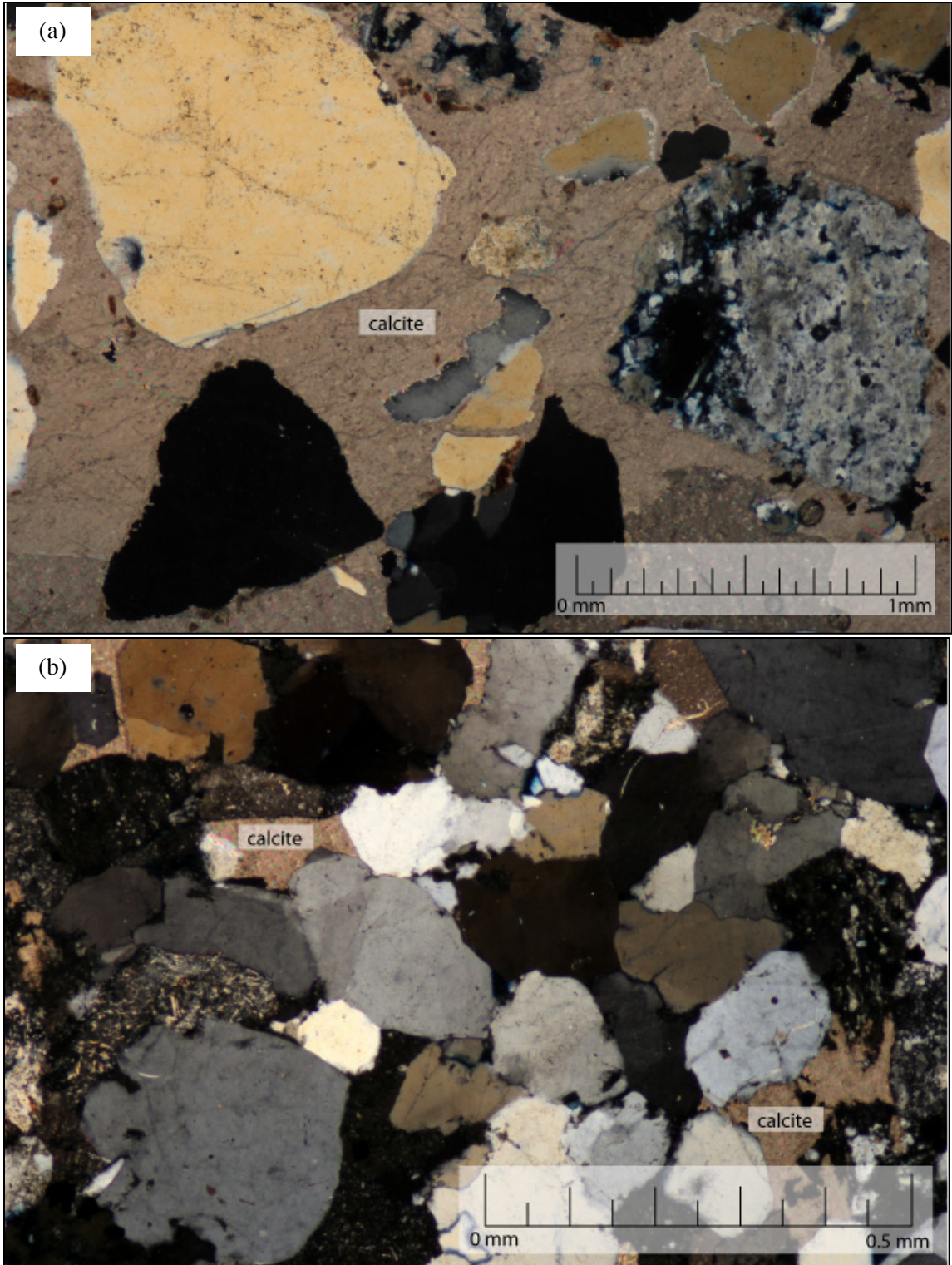


Figure 50. (a) Well 42-1, 8015.5 ft, xpl. Grains floating in poikilotopic calcite cement suggest that poikilotopic calcite may have prevented compaction. (b) Well 9-8, 7709 ft, xpl. The presence of calcite adjacent to an area with a high degree of grain packing suggests that calcite precipitation overlapped with compaction, or a second stage of calcite cementation occurred after compaction.

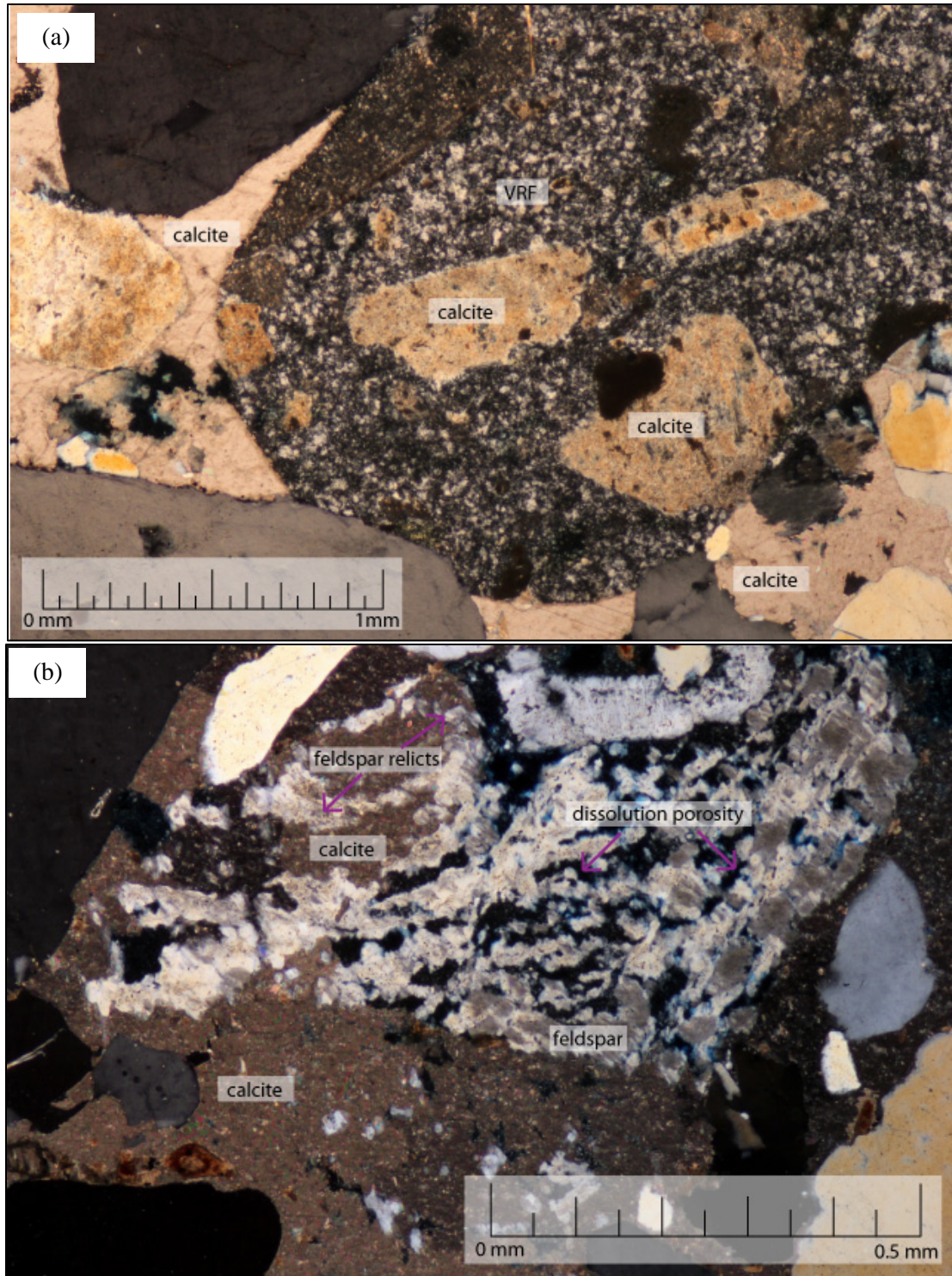


Figure 51. (a) Well 32-1, 7994.5 ft, xpl. Poikilotopic calcite replaced the feldspar crystals in this VRF. The calcite in the VRF goes extinct at same time as the poikilotopic calcite surrounding the grain, suggesting that calcite replaced feldspar and precipitated around the grain at the same time. (b) Well 42-1, 8015.5 ft, xpl. Dissolution porosity within the feldspar grain suggests that poikilotopic calcite replaced some feldspar, and later the feldspar partially dissolved, leaving intragranular porosity.

Ankerite

Ankerite is only present in samples from 13-10A, so it is not possible to determine its relationship to all diagenetic events. It formed after quartz overgrowths (Figure 52) and replaced feldspar in some places (Figure 53). Figure 52 shows ankerite that terminates against a euhedral quartz overgrowth, which indicates that the overgrowth precipitated first. Figure 53 shows that ankerite replaced some feldspar. There is porosity within the feldspar grain that is not filled with ankerite, which suggests that some feldspar dissolved after the ankerite replaced the feldspar.

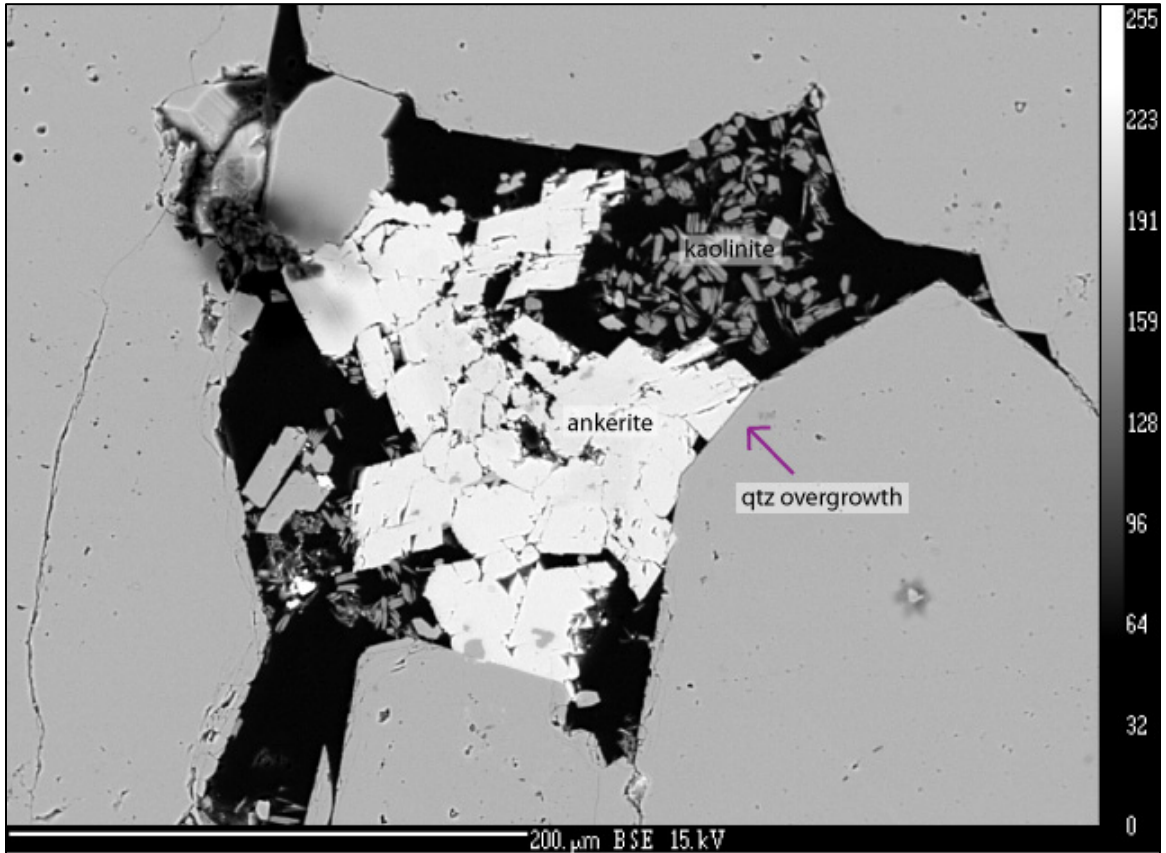


Figure 52. Well 13-10A, 7696.25 ft. A BSE image showing ankerite that formed on the outside of a euhedral quartz overgrowth, which indicates that ankerite precipitated after quartz cement.

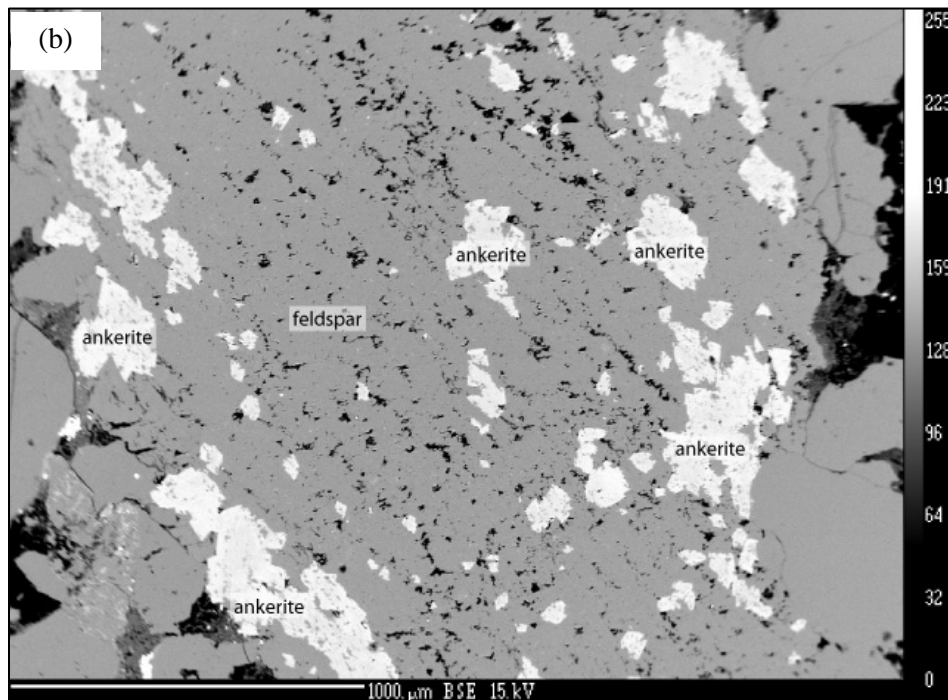
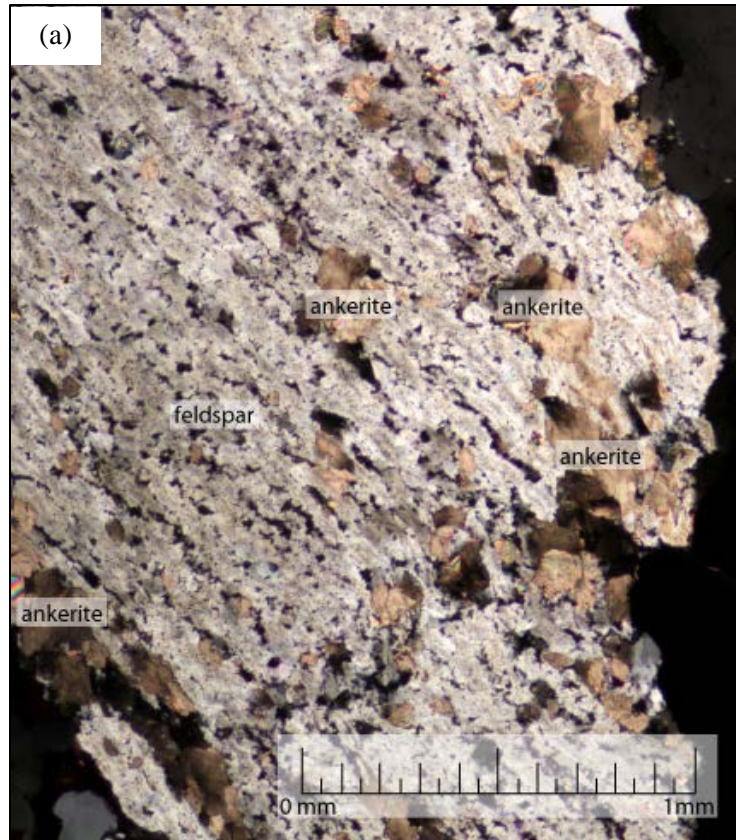


Figure 53. Sample E2, well 13-10A, 7684.75 ft. Ankerite replaced feldspar. Note that there are some micropores within the feldspar grain, and they are not filled with ankerite. This suggests that ankerite replaced feldspar, and some feldspar dissolution occurred later. (a) A photomicrograph, xpl. (b) A BSE image of the same feldspar grain.

Compaction

Compaction is variable in the Morrow B sandstone, which is evident from the IGV's and types of grain contacts. Types of grain contacts, in order of increasing amounts of compaction, are: floating grains (Figure 50a), point contacts (Figure 51a), long contacts (Figure 50b), concavo-convex contacts (Figure 54a), and sutured contacts (Figure 54b).

Both mechanical and chemical compaction occurred in the Morrow B sandstone. Evidence of significant mechanical compaction can be seen in samples that have low IGV's and long, concavo-convex, or sutured grain contacts. Stylolites are present in several slides, which is evidence of chemical compaction. Some stylolites contain carbonaceous material (Figure 45), whereas other stylolites contain clay seams (Figure 55).

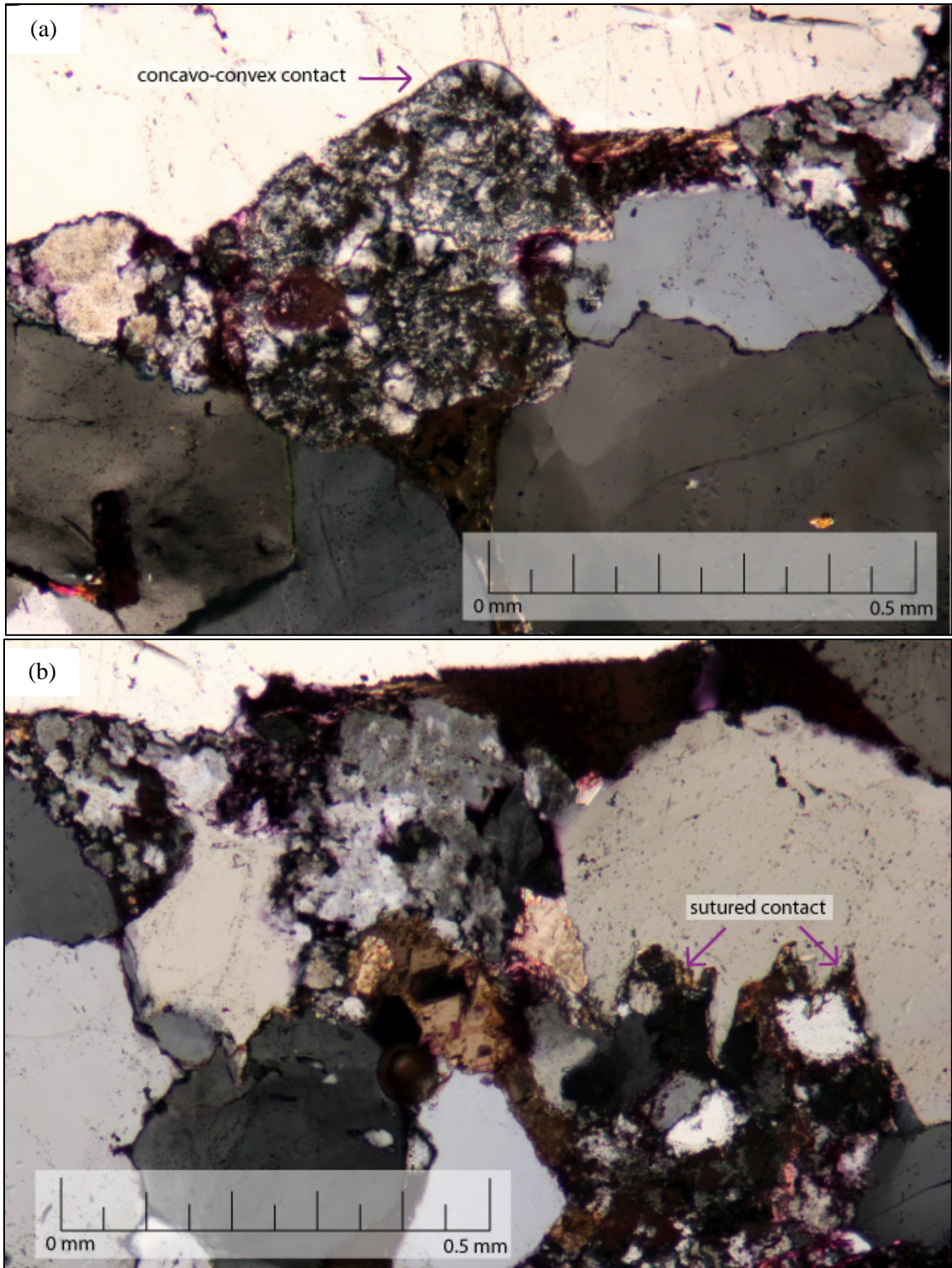


Figure 54. Well 13-10A, 7684.75 ft, xpl. Different types of grain contacts within the same sample indicate varying degrees of compaction. (a) Convo-convex grain contacts and (b) sutured grain contacts indicate high levels of compaction.

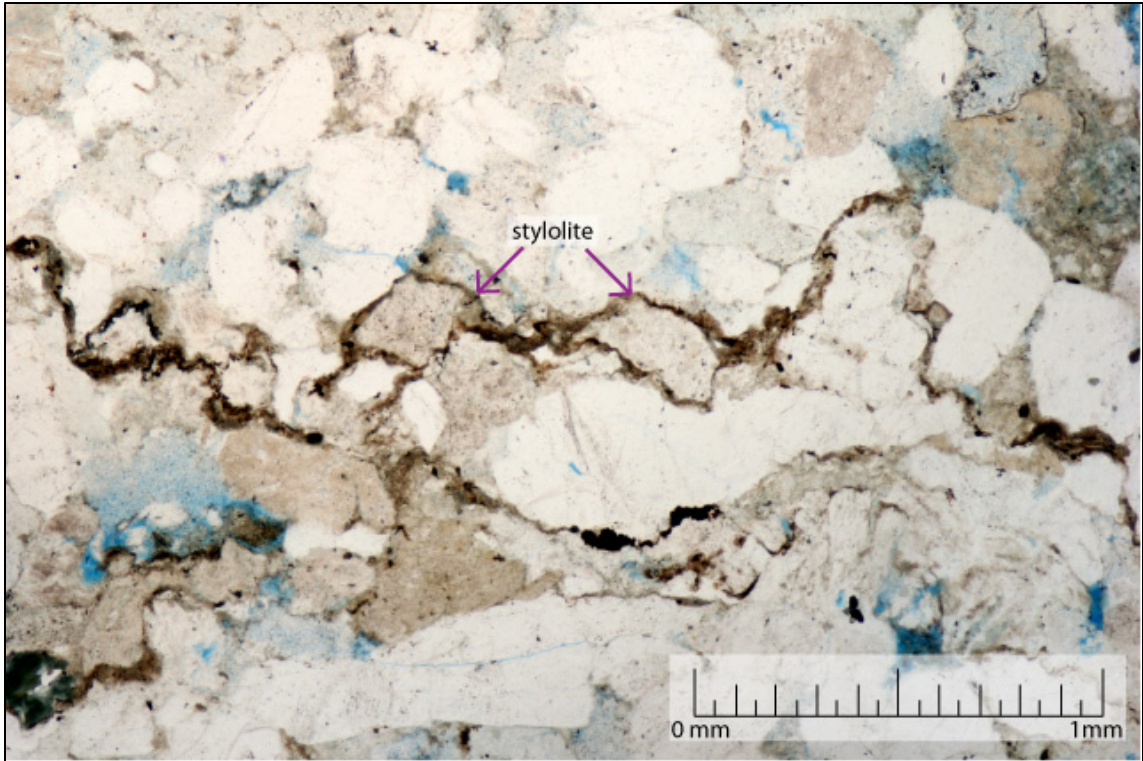


Figure 55. Well 9-8, 7693 ft, ppl. Stylolites are the result of pressure solution, which indicate significant chemical compaction.

Feldspar Dissolution

Feldspar dissolution occurred after calcite cementation (Figures 51b and 56b, c) and compaction. Some feldspar grains dissolved partially or completely, leaving intragranular micro- and macroporosity (Figures 51b, 56a, b, c). Evidence of complete feldspar grain dissolution comes from kaolinite “ghost grains,” which are grain-sized accumulations of kaolinite (Figure 57a). Some ghost grains have feldspar relicts (Figure 57b), which suggests that some ghost grains, even if they do not have feldspar relicts, may have originally been feldspar grains.

Feldspar dissolution occurred after compaction, which is evident from the presence of delicate skeletal feldspar in samples with a high degree of compaction. Figure 58 shows an example of such a grain: this sample is highly compacted, yet a delicate skeletal feldspar grain is preserved. If the feldspar grain had dissolved before compaction, the grain would have been crushed, and the intragranular porosity would have been destroyed.

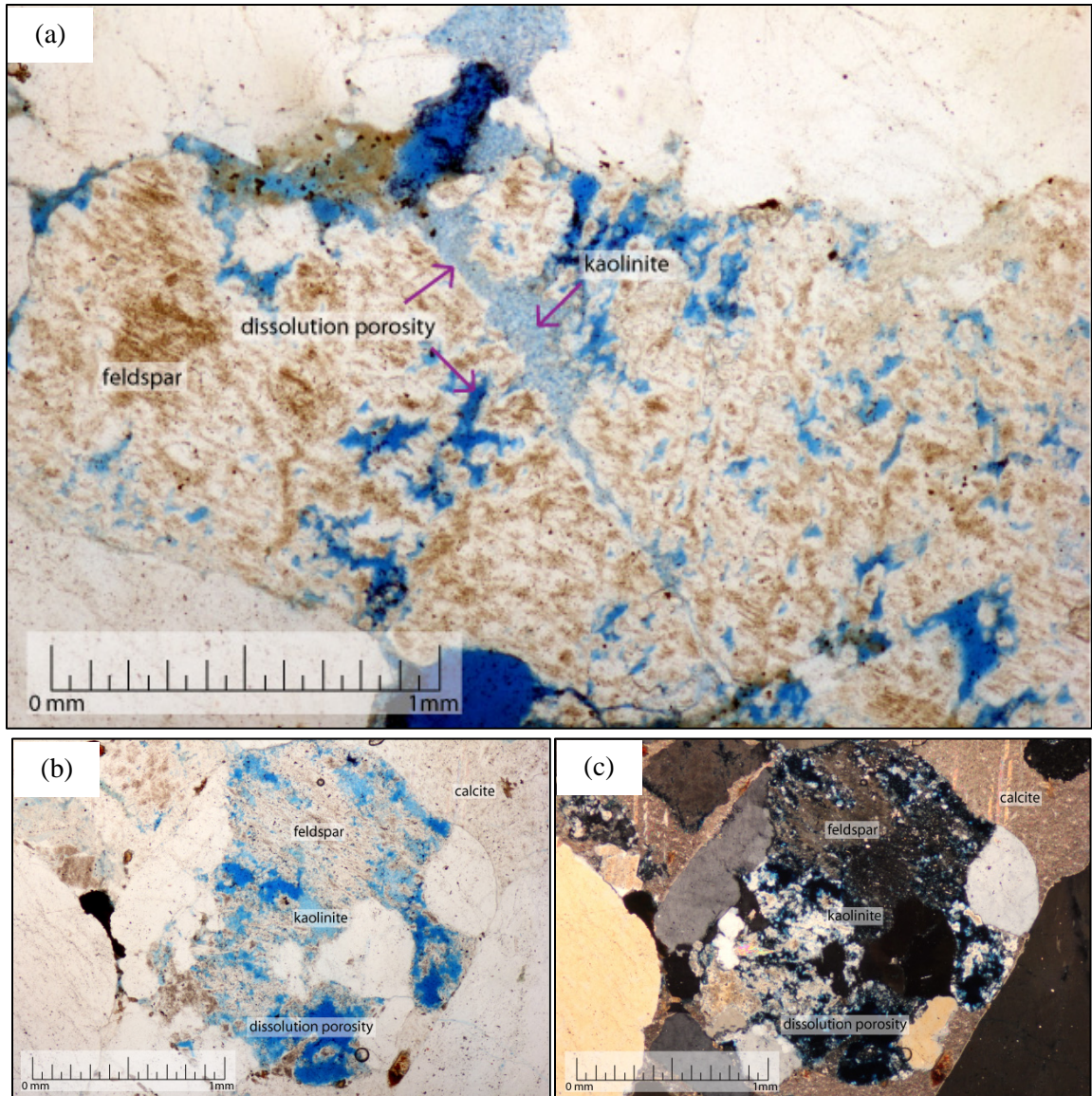


Figure 56. (a) Well 32-2, 7957 ft, ppl. Intragranular porosity in a feldspar grain from dissolution. Some intragranular porosity is filled with kaolinite. (b) Well 42-1, 8015.5 ft, ppl. Dissolution of feldspar in a GRF created intragranular porosity. Some intragranular porosity is filled with kaolinite. (c) xpl.

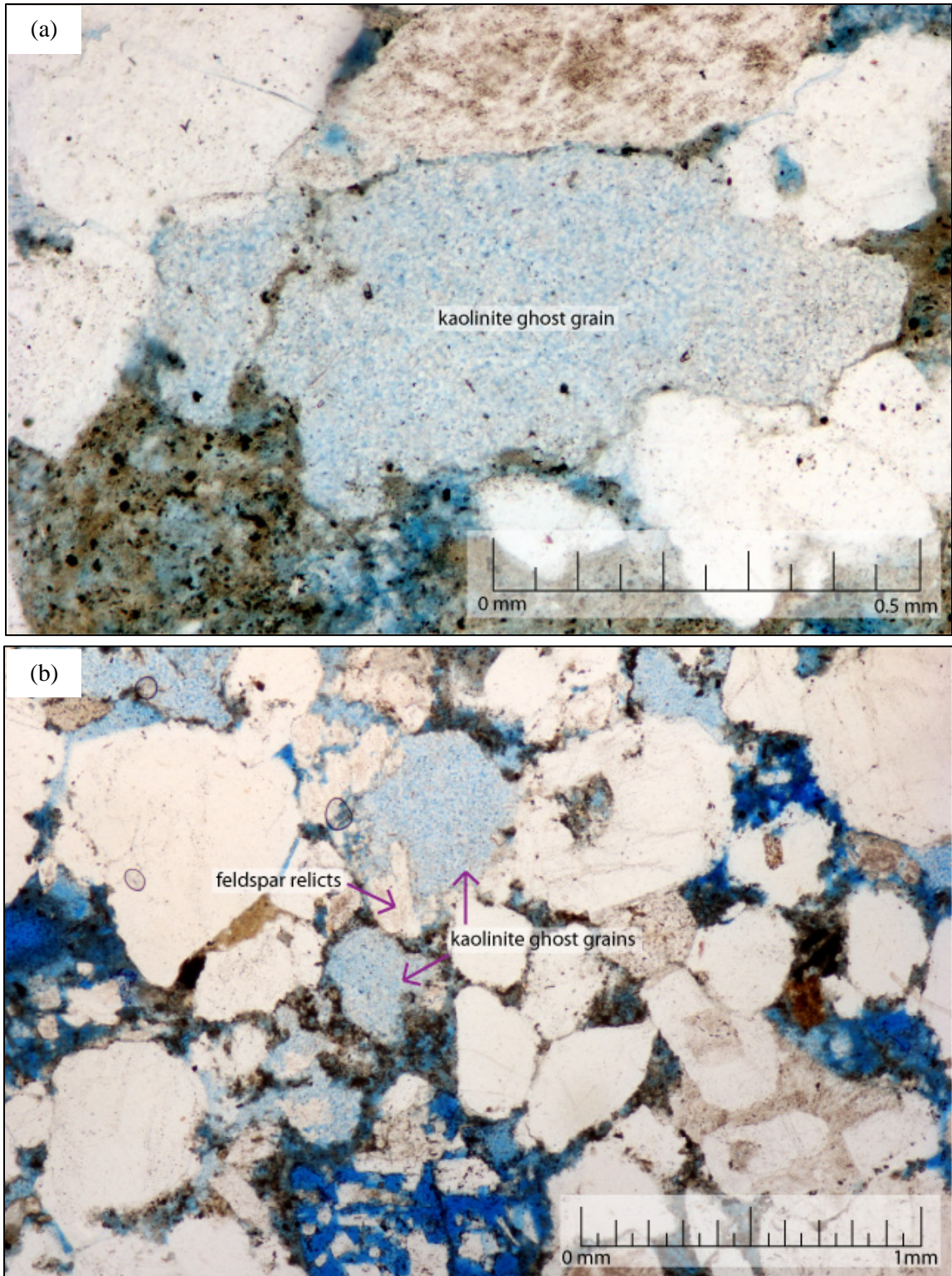


Figure 57. (a) Well 32-2, 7936 ft, ppl. Kaolinite “ghost grain.” (b) Well 32-1, 7970 ft, ppl. Kaolinite “ghost grains,” some with feldspar relicts. This suggests that other ghost grains may have originally been feldspar.

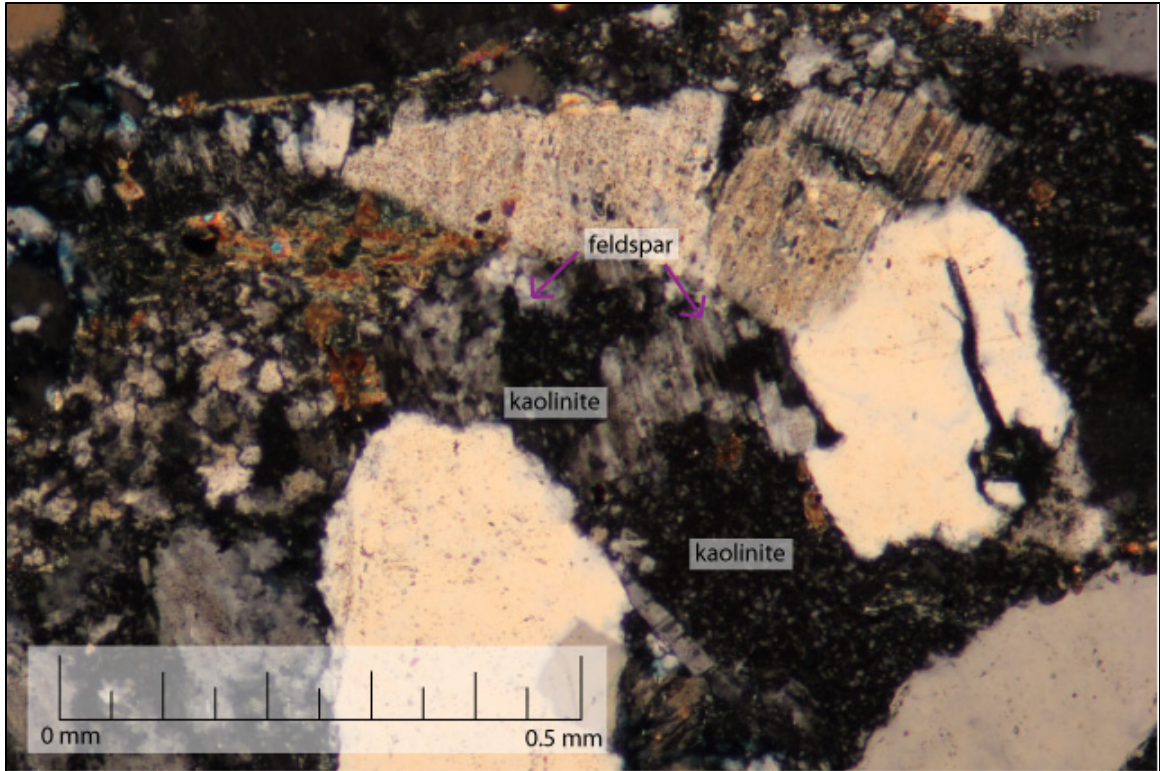


Figure 58. Well 9-8, 7693 ft, xpl. This sample is highly compacted, yet a delicate skeletal feldspar grain is preserved, which indicates that feldspar dissolution occurred after compaction. If the feldspar had dissolved before compaction occurred, it would have been crushed and the intragranular porosity would have been destroyed.

Authigenic Clay

The precipitation of authigenic clay occurred late in the diagenetic history. Kaolinite is the most easily recognizable clay from optical petrography alone. It was also identified in BSE images (Figures 59 and 60), by XRD (Tables 4 and 5), and by microprobe analysis (Table 9). Chlorite was not recognized optically, but was identified with BSE images (Figures 59 and 60) and XRD analysis (Tables 4 and 5). Kaolinite and chlorite fill pores and block pore throats, but it is unclear from the BSE images if chlorite precipitated before or after kaolinite (Figures 59 and 60). XRD analysis revealed that smectite and illite clay is also present in some samples (Tables 4 and 5), but it was not observed optically or in BSE images, so it is unknown if it is authigenic or detrital clay.

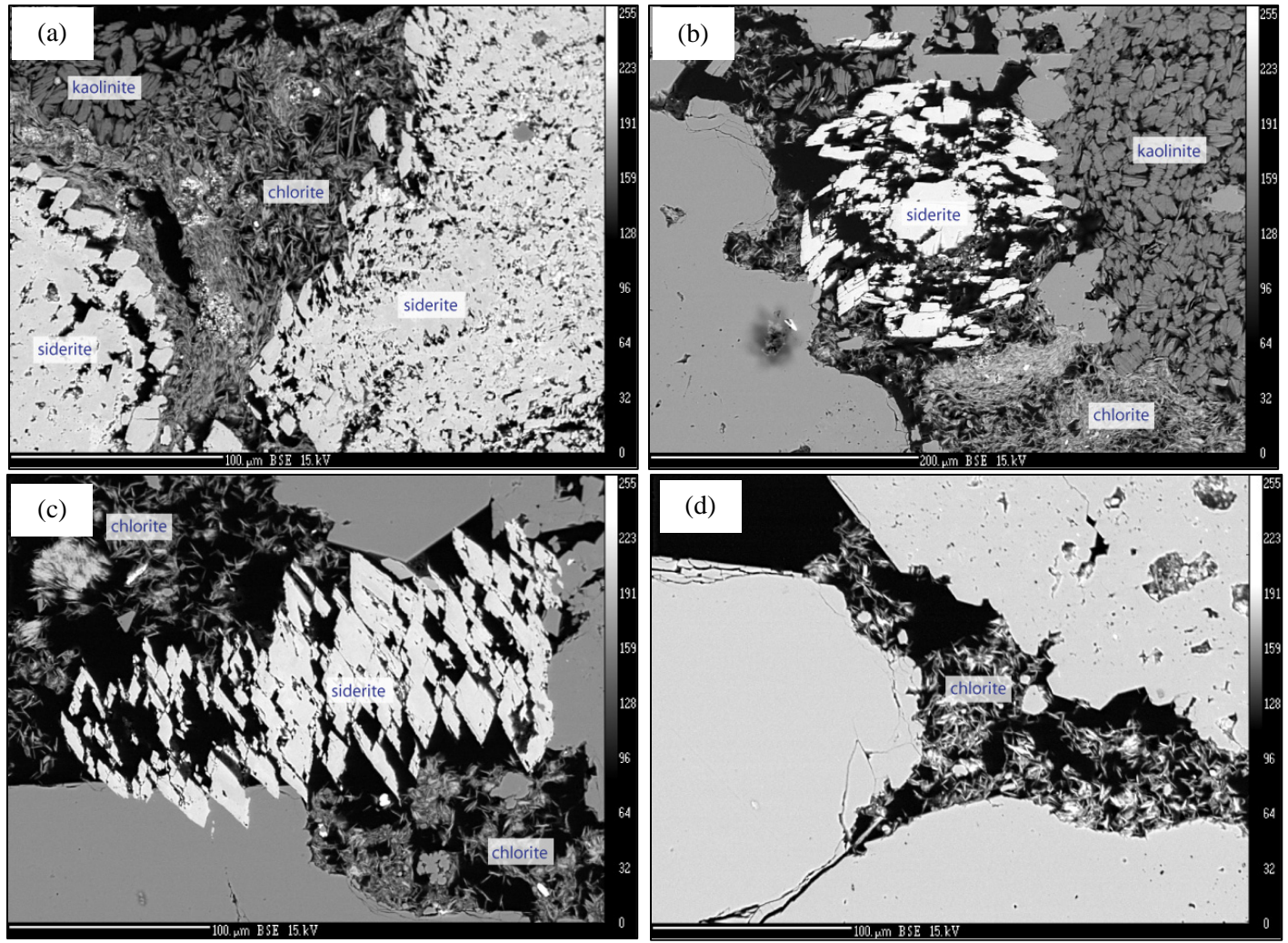


Figure 59. BSE images from sample E1, well 13-10A, 7675.90 ft. (a, b) Siderite, chlorite, and kaolinite filling a pore. (c) Siderite and chlorite blocking a pore throat. (d) Chlorite blocking a pore throat.

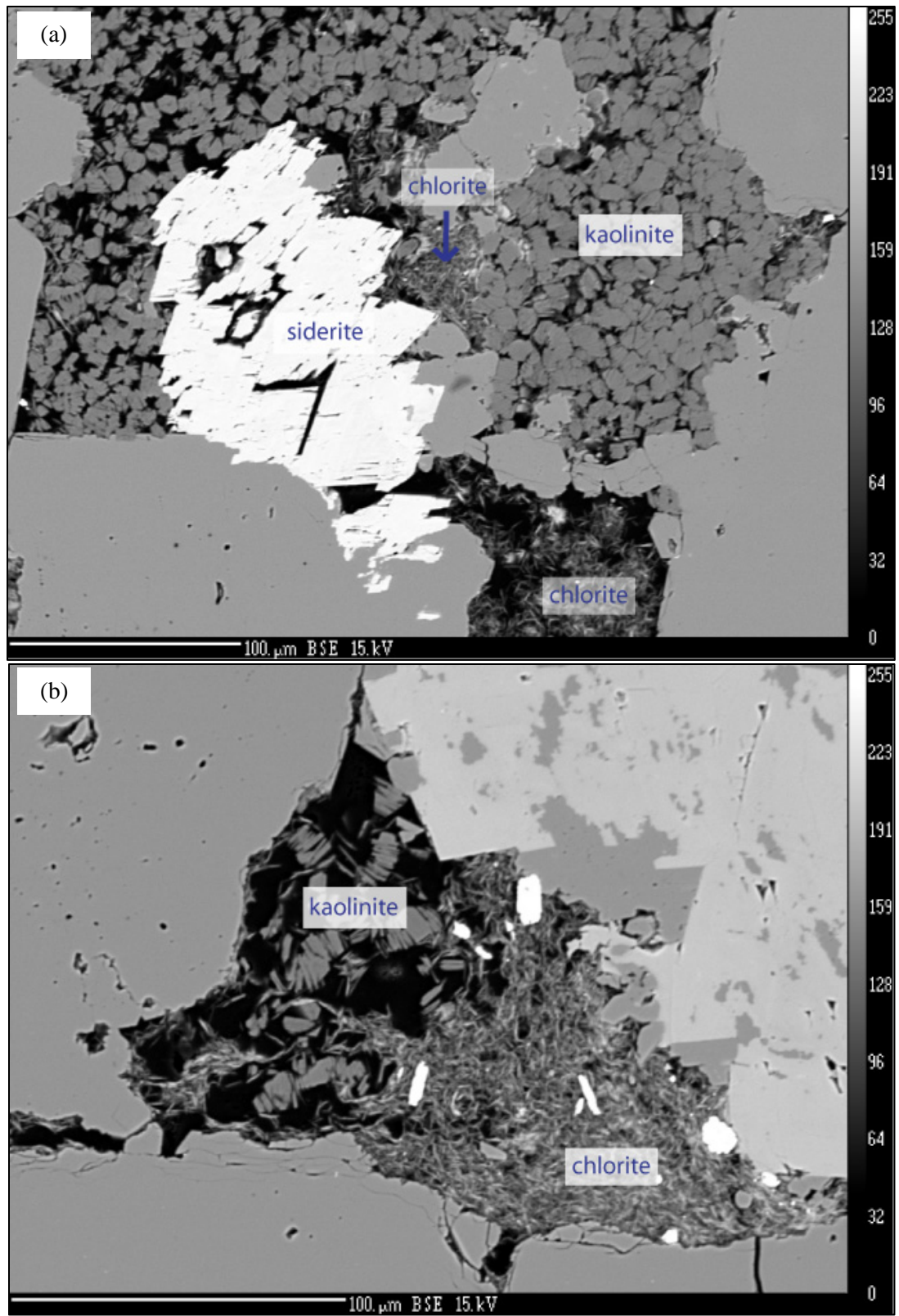


Figure 60. BSE images from well 13-10A. (a) Sample E2, 7684.75 ft. Siderite, chlorite, and kaolinite filling a pore. (b) Sample E3, 7686.4 ft. Kaolinite and chlorite filling a pore. The delicate booklets displayed by this kaolinite is indicative of authigenic clay.

Kaolinite

Kaolinite is abundant in the Morrow B sandstone, in the form of “ghost grains” and as pore-filling clay. It is possible for feldspar to be replaced by kaolinite in situ, either in the source rock or in soil. In the Morrow B sandstone, however, the kaolinite is thought to be authigenic for three reasons: (1) kaolinite ghost grains are too delicate and physically unstable to have survived transport; (2) the pore-filling kaolinite displays authigenic textures, such as booklets (Figures 59a, b and 60), that also would not have survived transport; and (3) the monomineralic nature of the kaolinite, which is seldom seen in detrital clays (Wilson and Pittman, 1977).

Kaolinite ghost grains are pseudomorphs of detrital feldspar and formed when feldspar grains were replaced by or dissolved and infilled by kaolinite, which holds the shape of the original grain (Wilson and Pittman, 1977; Figure 57). Kaolinite precipitation is thought to have occurred after feldspar dissolution for two reasons: (1) feldspar dissolution may have provided the aluminum necessary for kaolinite to precipitate (Curtis, 1983), and (2) some intragranular porosity within dissolved feldspar grains contains kaolinite (Figures 56a, b and 58). However, some partially dissolved feldspar grains that are surrounded by kaolinite do not have kaolinite within the intragranular pores (Figure 61), which suggests that some feldspar dissolution may have occurred after the kaolinite was in place. Alternatively, feldspar could have dissolved before kaolinite precipitation, and the kaolinite was not pervasive.

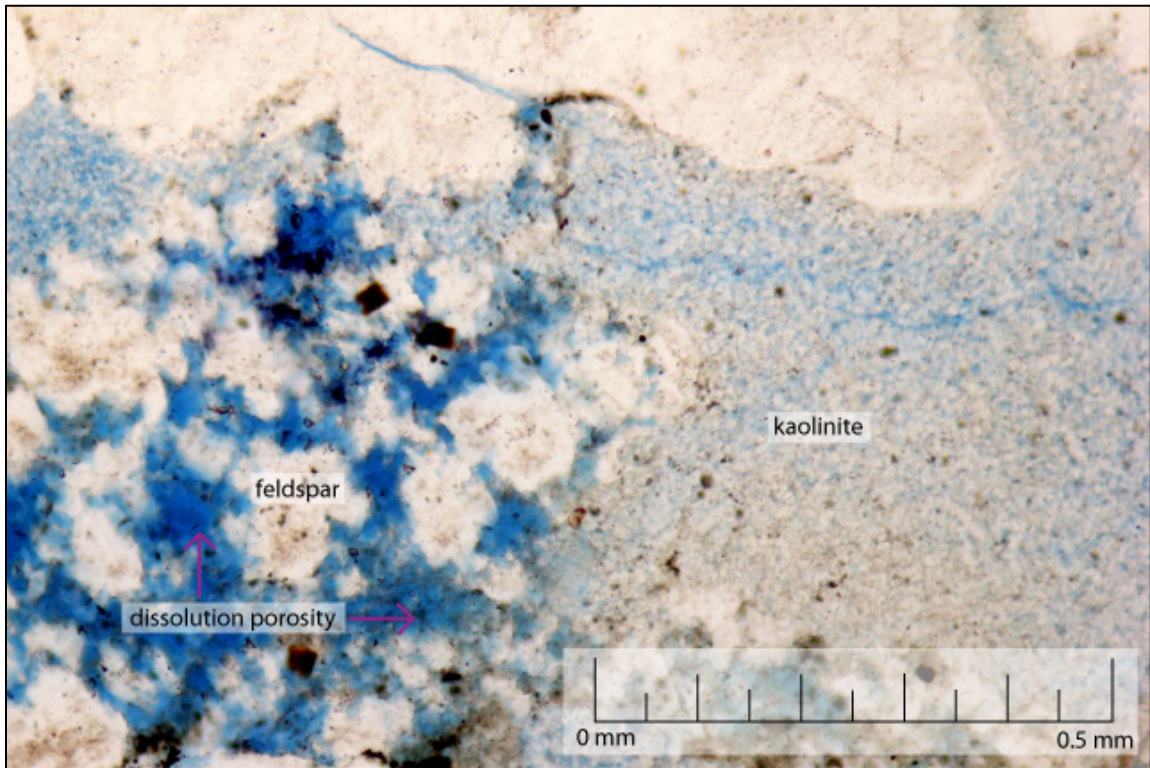


Figure 61. Well 32-3, 7983 ft, ppl. This partially dissolved feldspar grain is surrounded by kaolinite, but kaolinite is not present within the intragranular porosity. This suggests that some feldspar dissolution may have occurred after kaolinite precipitation.

Hydrocarbon Emplacement

Hydrocarbon emplacement occurred late in the diagenetic history of the Morrow B sandstone, after the precipitation of authigenic clay. The evidence for this is: (1) pore-filling authigenic clay would not have precipitated if the pores were already filled with oil and (2) the kaolinite in some locations appears to be oil-stained, which indicates that oil migration occurred after kaolinite was in place (Figure 62).



Figure 62. Well 13-10A, 7675.90 ft. This oil-stained kaolinite indicates that oil emplacement occurred after the precipitation of kaolinite. This kaolinite also displays authigenic textures in the form of delicate booklets.

Pore Types

Nine pore types were observed in thin sections of Morrow B sandstone: Intergranular Macroporosity, Intragranular Macroporosity, Grain Sized Macroporosity, Grain Sized Macroporosity in Poikilotopic calcite, Macro- and Microporosity in Carbonate Cement, Microporosity in Grains, Microporosity in Ghost Grains, Microporosity in Clay Matrix and Authigenic Clay, and Fracture Porosity (Table 10).

Intergranular Macroporosity

Intergranular macroporosity can either be primary (depositional) or secondary due to the dissolution of intergranular cement. There is no evidence of major cement dissolution in the Morrow B sandstone, so the intergranular macroporosity is thought to be primary porosity. Based on point-count data, intergranular macroporosity in the Morrow B sandstone is less abundant than microporosity but more abundant than dissolution porosity (Figure 38c). Macropores that are well interconnected (effective) may greatly contribute to permeability (Figure 63), however, abundant authigenic clay may have rendered some intergranular macroporosity less effective (Figure 64).

Intragranular Macroporosity

Intragranular macroporosity is less abundant than microporosity and intergranular macroporosity in the Morrow B sandstone (Figure 38c). It is primarily associated with feldspar dissolution, either within a feldspar grain (Figure 65) or from feldspar that dissolved within a GRF (Figure 66). However, in both instances, kaolinite often fills some or all of the intergranular macroporosity, leaving intergranular microporosity (Figure 65). The contribution to permeability may be high if the intragranular pores are connected to surrounding intergranular macroporosity (Figure 66). Intragranular pores might not be effective if they are completely isolated within the grain (Figure 65).

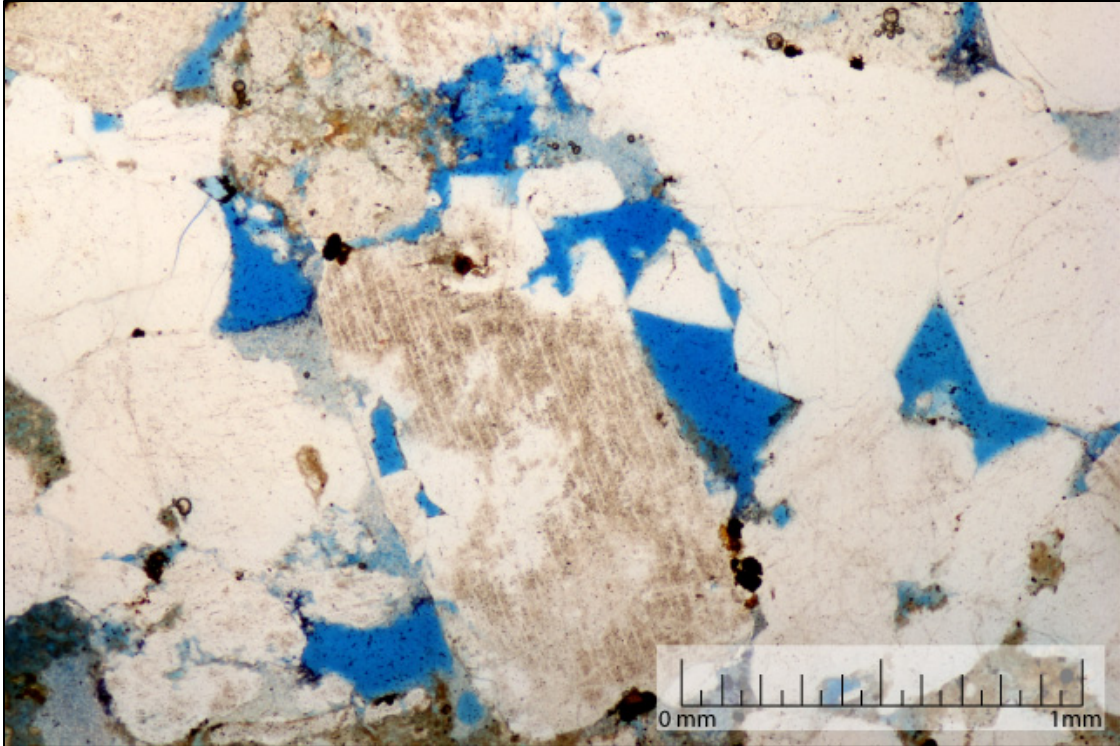


Figure 63. Well 9-8, 7704 ft, ppl. Photomicrograph showing abundant intergranular macroporosity. The feldspar grain in the middle contains feldspar cement and some quartz grains have quartz overgrowths.

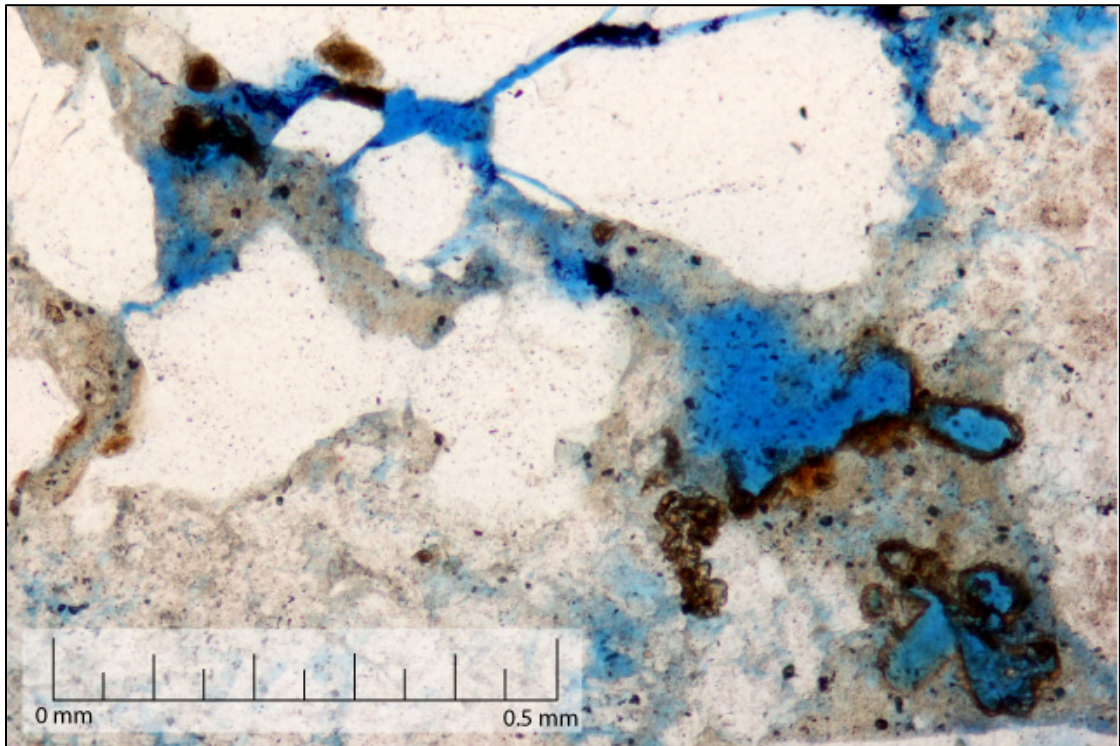


Figure 64. Well 32-2, 7936 ft, ppl. Macroporosity surrounded by authigenic clay and cement.

Table 10. Summary of porosity types observed in the Morrow B sandstone.

Porosity Type	Origin	Inferred Contribution to Sample Permeability	Common Adjacent Pore Types
Intergranular Macroporosity	Primary porosity	High	Intergranular macro- or microporosity
Intragranular Macroporosity	Grain dissolution (primarily feldspar)	High when connected to intergranular macroporosity, low when surrounded by microporosity, none when isolated in grain.	Isolated in large grains, or adjacent to intergranular macro- or microporosity
Grain-sized Macroporosity	Grain dissolution (primarily feldspar)	High when next to macroporosity, low when surrounded by microporosity.	Intergranular microporosity
Grain-sized Macroporosity in Poikilotopic Calcite	Grain dissolution (primarily feldspar)	None	None. Isolated pores
Macro- and Microporosity in Carbonate Cement	Partially cemented or dissolved siderite cement	High	Other pores in cement
Microporosity in Grains	Feldspar and Silica dissolution	Low	Intergranular microporosity or none (isolated in grains)
Microporosity in Ghost Grains	Kaolinite replacing dissolved feldspar grains	Low	Intergranular microporosity
Microporosity in Clay Matrix and Authigenic Clay	Kaolinite, other authigenic clay, detrital clay	Moderate	Intergranular macro- or microporosity
Fracture Porosity	Deformation	Very Low	Intergranular microporosity

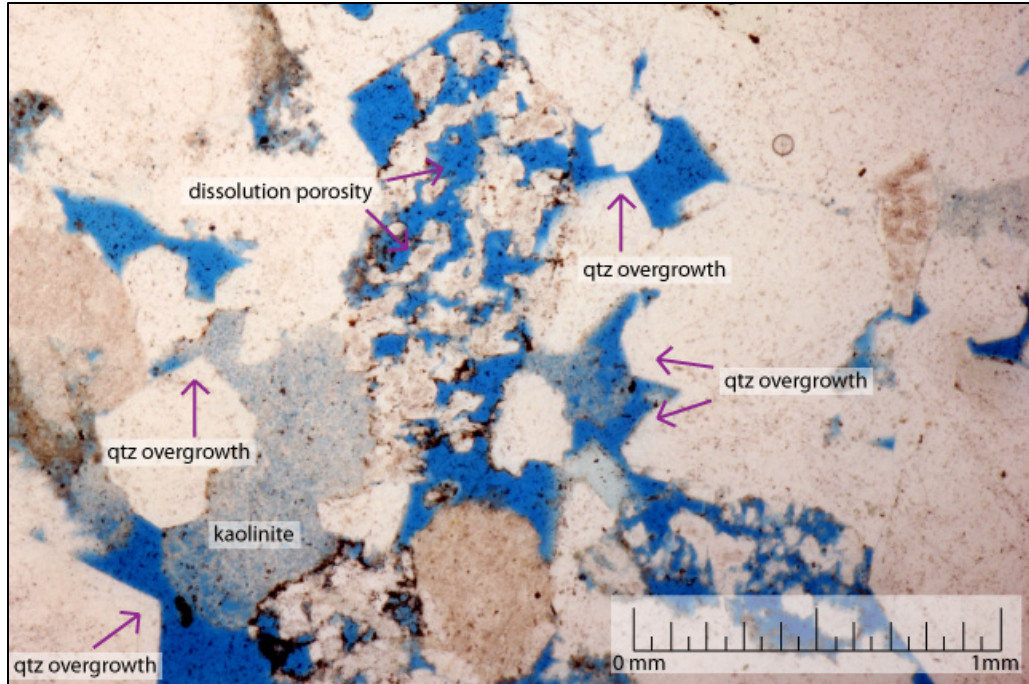


Figure 65. Well 32-1, 7980 ft, ppl. Intragranular macroporosity in a feldspar grain (center) appears to be connected to the surrounding intergranular macroporosity. In this example, the intragranular pores are effective. Elsewhere in the photo, the porosity has been reduced by quartz overgrowths and kaolinite.

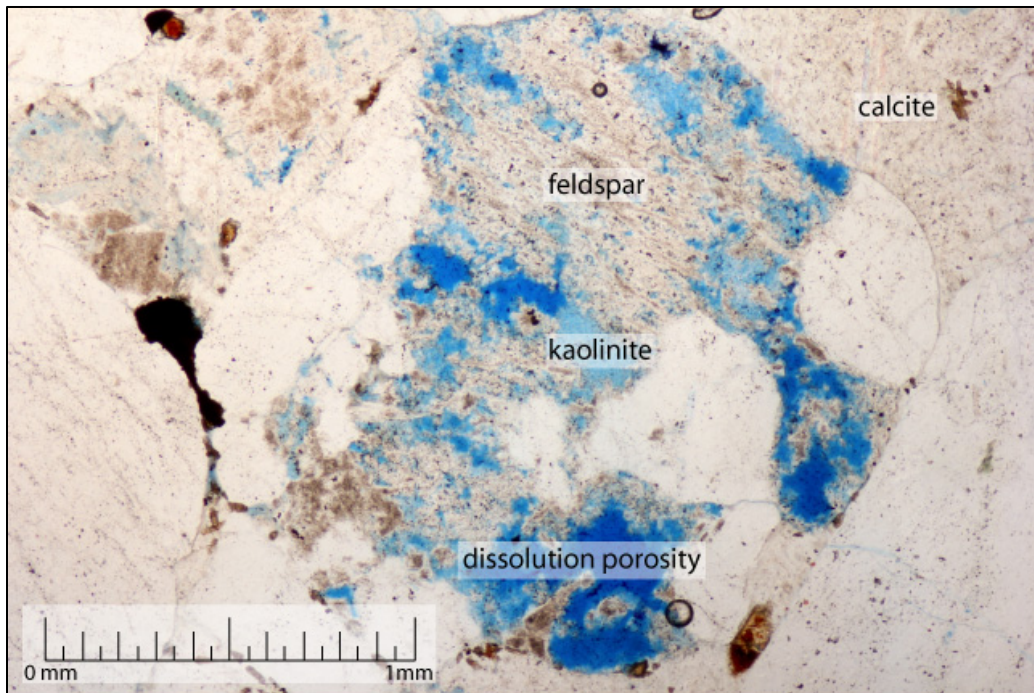


Figure 66. Well 42-1, 8015.5 ft, ppl. Feldspar dissolution in a GRF created intragranular macroporosity. Note that some porosity has been filled with kaolinite. This grain is encased in poikilotopic calcite, so the porosity is not effective.

Grain-Sized Macroporosity

Enlarged secondary porosity is generally the result of fracturing, shrinkage, dissolution of sedimentary material, or dissolution of authigenic cement or replacement (Schmidt and McDonald, 1979). In a few samples of the Morrow B sandstone, oversized pores are the same size and shape as surrounding grains, which indicates they are likely the result of grain dissolution, possibly feldspar or rock fragments (Figures 67-69).

Grain-sized macroporosity is only present in a few samples. One sample (E4, well 13-10A, 7696.25 ft) has abundant grain-sized pores and a high permeability. It is likely that the high permeability is the result of the grain-size pores because most of the intergranular porosity is filled with authigenic clay (Figure 67). Some grain-sized pores are surrounded by authigenic clay, which may cause these pores to be less effective (Figures 67 and 68). Another sample has grain-sized pores that are surrounded by poikilotopic calcite (Figure 69). This sample has very low porosity and permeability, likely because much of the IGV is filled with calcite, and the grain-sized pores are isolated by the cement.

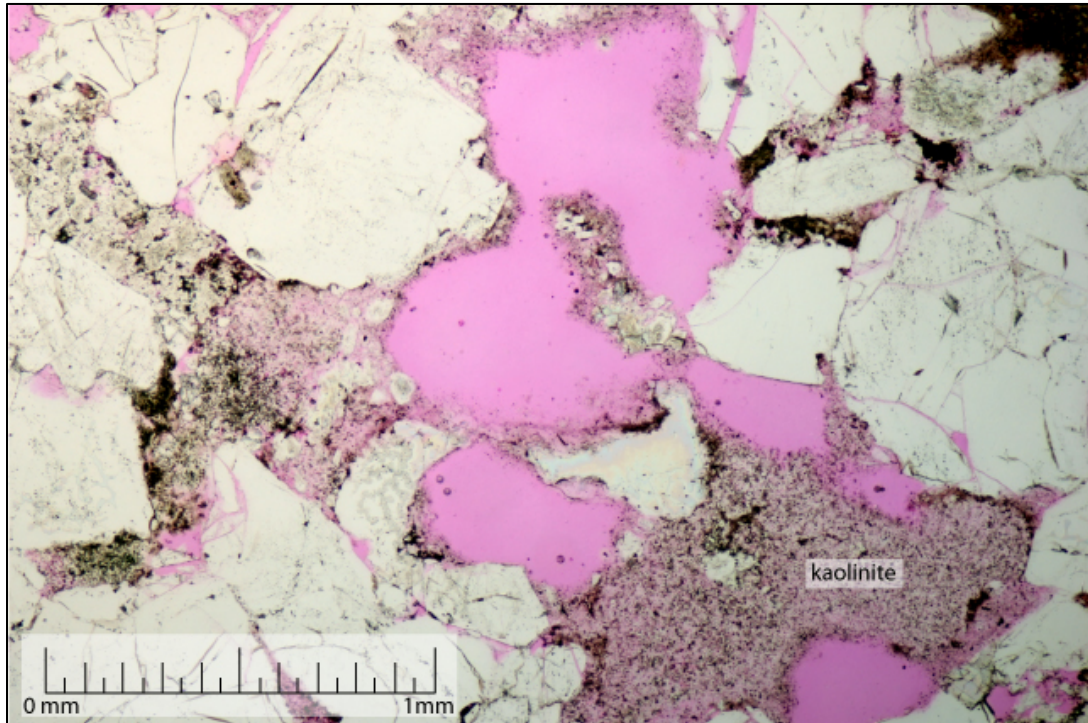


Figure 67. Well 13-10A, 7696.25 ft, ppl. These grain-sized pores are most likely the result of grain dissolution and appear to be interconnected. The high permeability of the sample is likely due to the presence of these grain-sized pores because most of intergranular porosity in this sample is filled with authigenic clay.

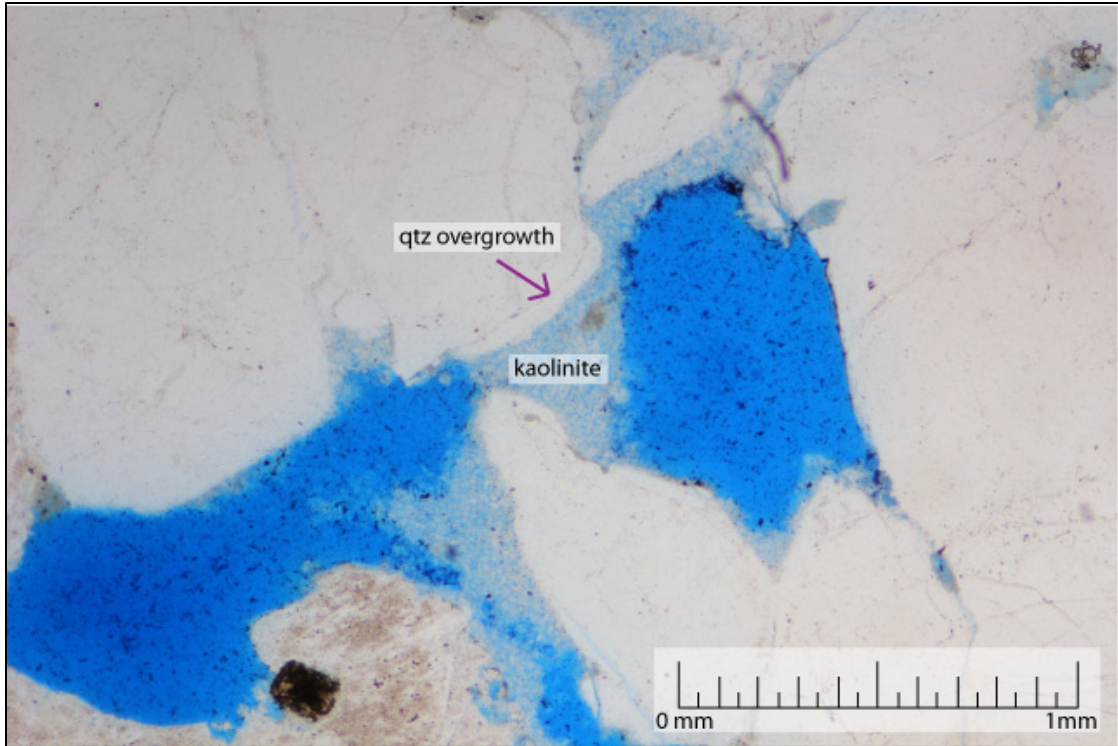


Figure 68. Well 32-2, 7957 ft, ppl. Kaolinite and quartz overgrowths blocking the throats of grain-sized pores. These pores are less effective because of the kaolinite.

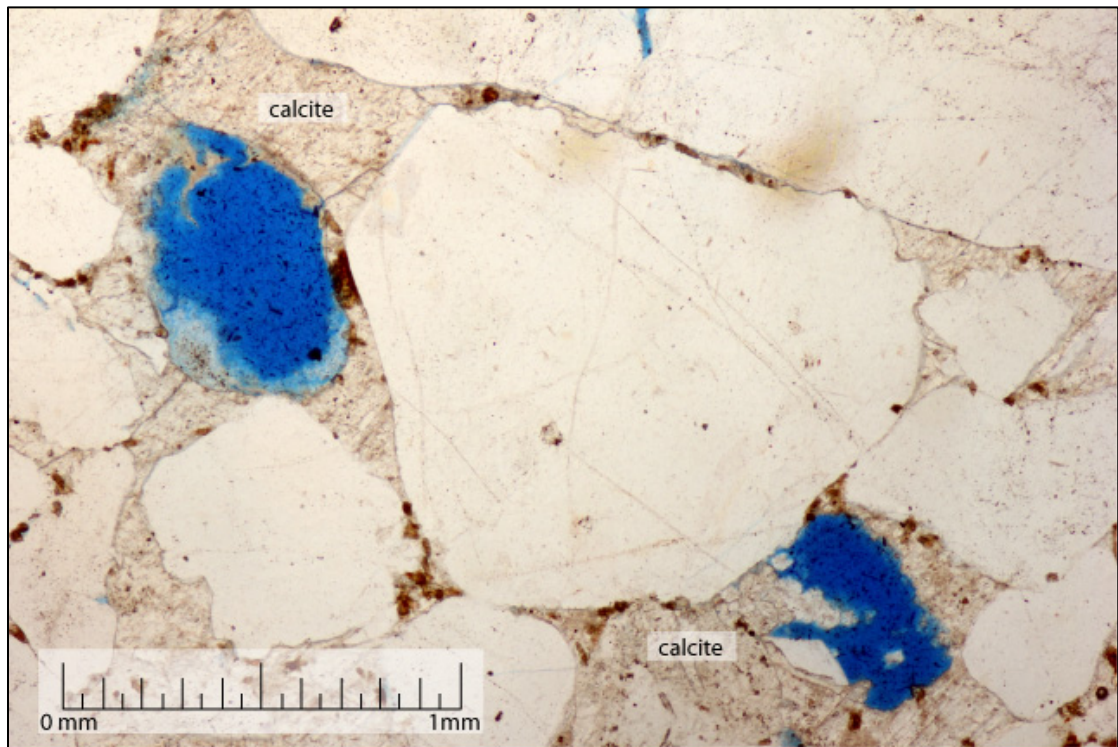


Figure 69. Well 42-1, 8015.5 ft, ppl. Grain-sized pores in poikilotopic calcite from the dissolution of feldspar or rock fragments. These pores are not effective because they are isolated in the cement.

Macro- and microporosity in Carbonate Cement

Porosity in carbonate cement formed in two ways: either from partial or full dissolution of grains surrounded by poikilotopic calcite (Figure 69) or partial cementation of siderite. In one sample (well 13-10A, 7675.9 ft), abundant siderite has either partially cemented the pore space or partially dissolved, leaving both macro- and microporosity (Figure 70).

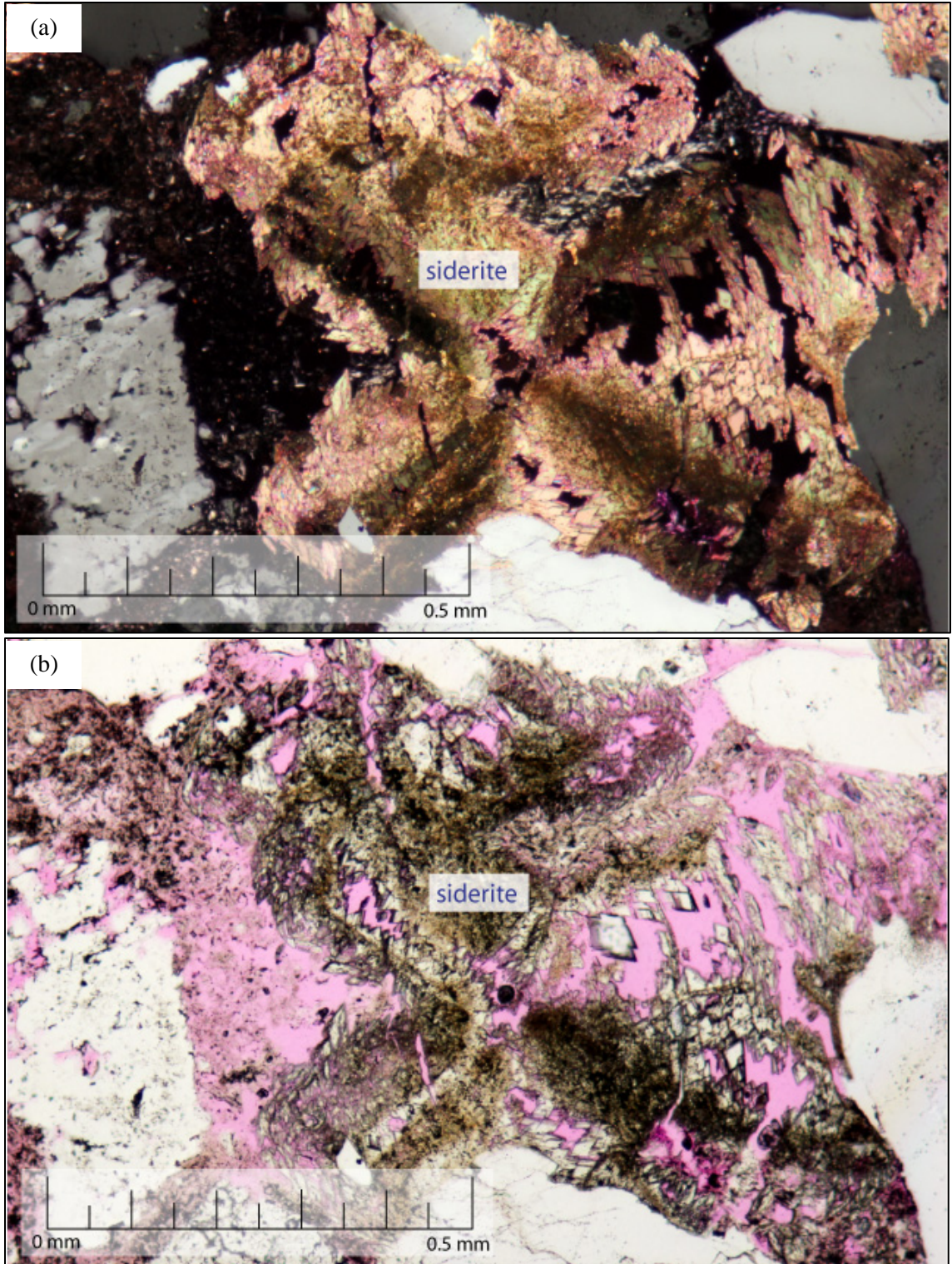


Figure 70. Well 13-10A, 7675.9 ft. Photomicrograph showing siderite and clay that fill an enlarged pore. The siderite is either partially cemented or partially dissolved, which created micro- and macroporosity. (a) xpl (b) ppl.

Microporosity in grains

Microporosity in grains is generally due to either dissolution of silica or feldspar, which created micropores (Figure 71), or intragranular macroporosity that has been filled by kaolinite (Figure 65, 72). Intragranular microporosity does not contribute much to permeability for two reasons: it is often isolated within grains, and the pores are too small to be effective. Micropores that are located at the edge of grains are more effective because they may connect to intergranular porosity (Figure 71).

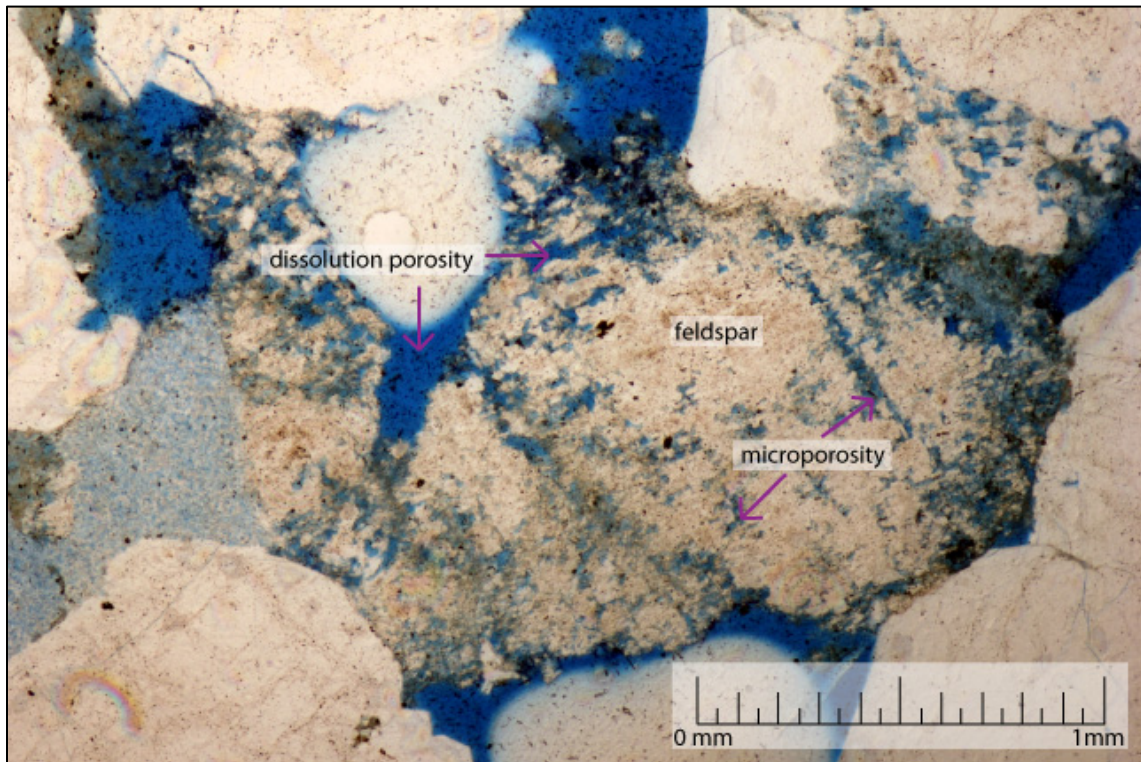


Figure 71. Well 42-1, 8028 ft, ppl. Microporosity and dissolution porosity in a feldspar grain. Some micropores are isolated within the grain, whereas others are connected to surrounding intergranular porosity.

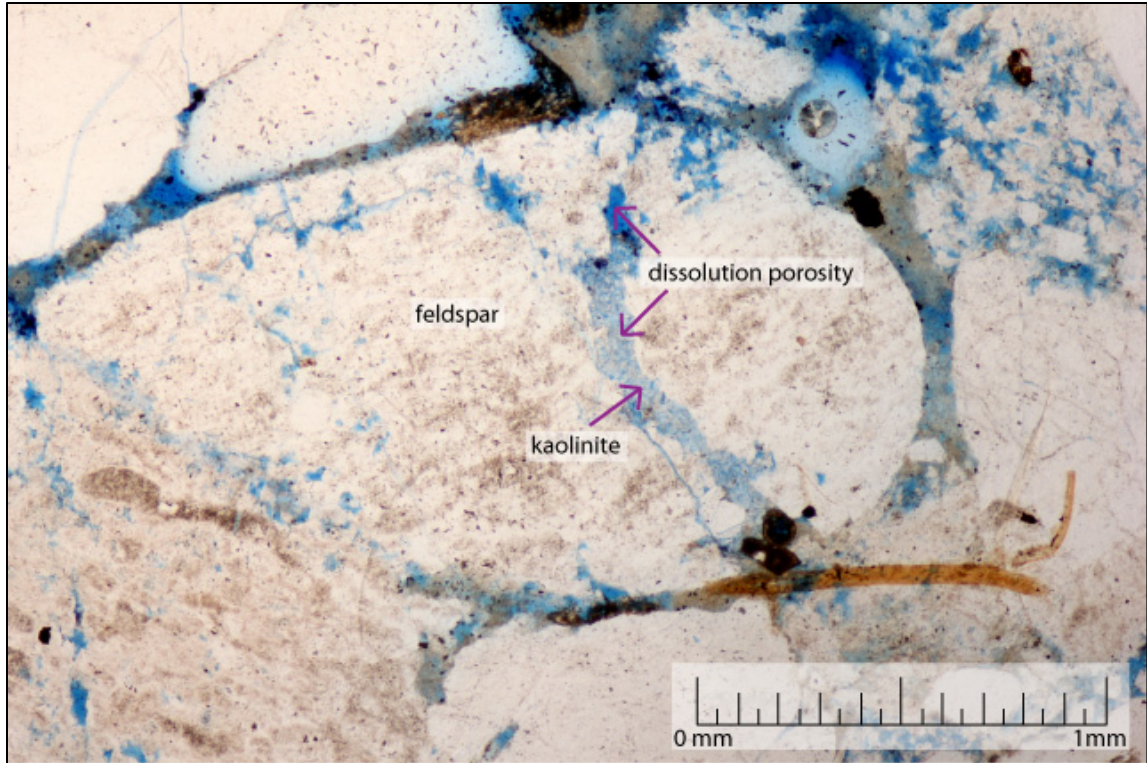


Figure 72. Well 42-1, 8028 ft, ppl. Photomicrograph showing dissolution porosity in a feldspar grain that is partially filled with kaolinite.

Microporosity in completely dissolved grains

Kaolinite “ghost grains” are present in all sampled wells. In contrast to kaolinite that fills intergranular porosity, kaolinite ghost grains fill the space once occupied by a feldspar grain, and sometime contain feldspar relicts (Figure 73). Some kaolinite “ghost grains” are rimmed by clay, and the original outline of the grain is apparent (Figure 73). In other cases, kaolinite fills both the space once held by feldspar and the surrounding intergranular porosity, making the former grain boundary indistinguishable (Figure 74). Kaolinite ghost grains are microporous and usually surrounded by microporous clay, so the contribution to permeability is low.

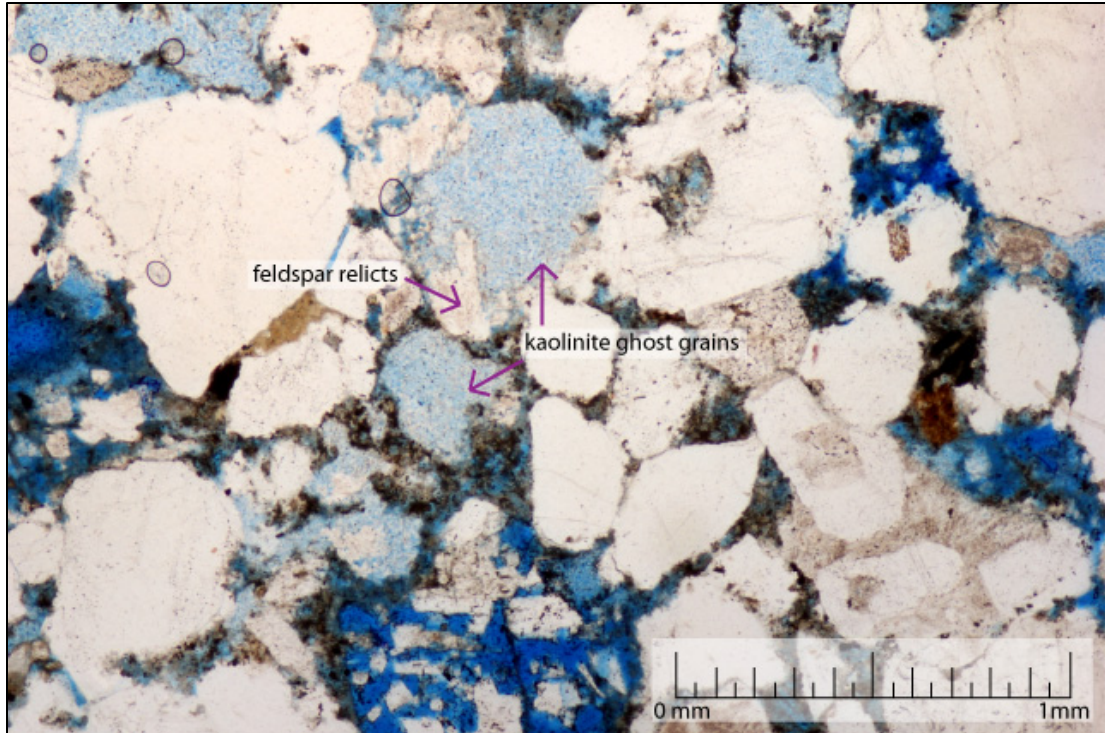


Figure 73. Well 32-1, 7970 ft, ppl. Photomicrograph showing microporous kaolinite ghost grains, some of which have feldspar relicts.

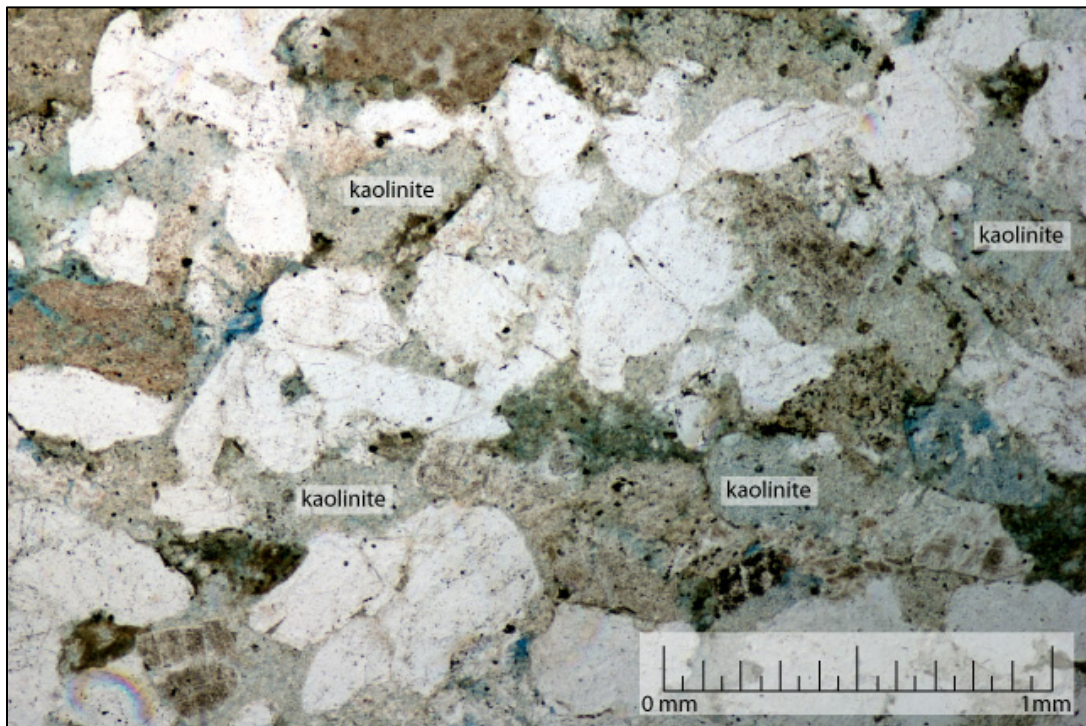


Figure 74. Well 9-8, 7694 ft, ppl. Kaolinite ghost grains and kaolinite filling pores. In some places, the outlines of the ghost grain are well defined; in other places they are indistinguishable.

Microporosity in Clay Matrix and Authigenic Clay

Microporosity in authigenic (primarily kaolinite) and detrital clay is the most abundant type of porosity in the Morrow B sandstone (Figures 64-65, 67-68, 72-74). These pores are technically effective, and because they are so abundant they must contribute somewhat to permeability. However, due to their small size, they are much less effective than intergranular macroporosity.

Fracture Porosity

Fracture porosity is negligible in the Morrow B sandstone. Fractures can either be artificial or natural. Artificial fractures can be caused by thin section preparation or pull-apart when a core is brought up from depth. It is unlikely that the fractures in the Morrow B sandstone were created during thin section preparation because they are filled with epoxy (Figure 75a, b). The fractures could be natural, generated during differential compaction, or artificial, from pull-apart. Mineralization is evidence of natural fractures, but no mineralized fractures were observed in any thin sections. As discussed previously, there is evidence for differential compaction in the Morrow B sandstone, so that is a likely cause of these fractures. Due to their small size and negligible quantity, fractures are not a significant source of permeability in the Morrow B sandstone.

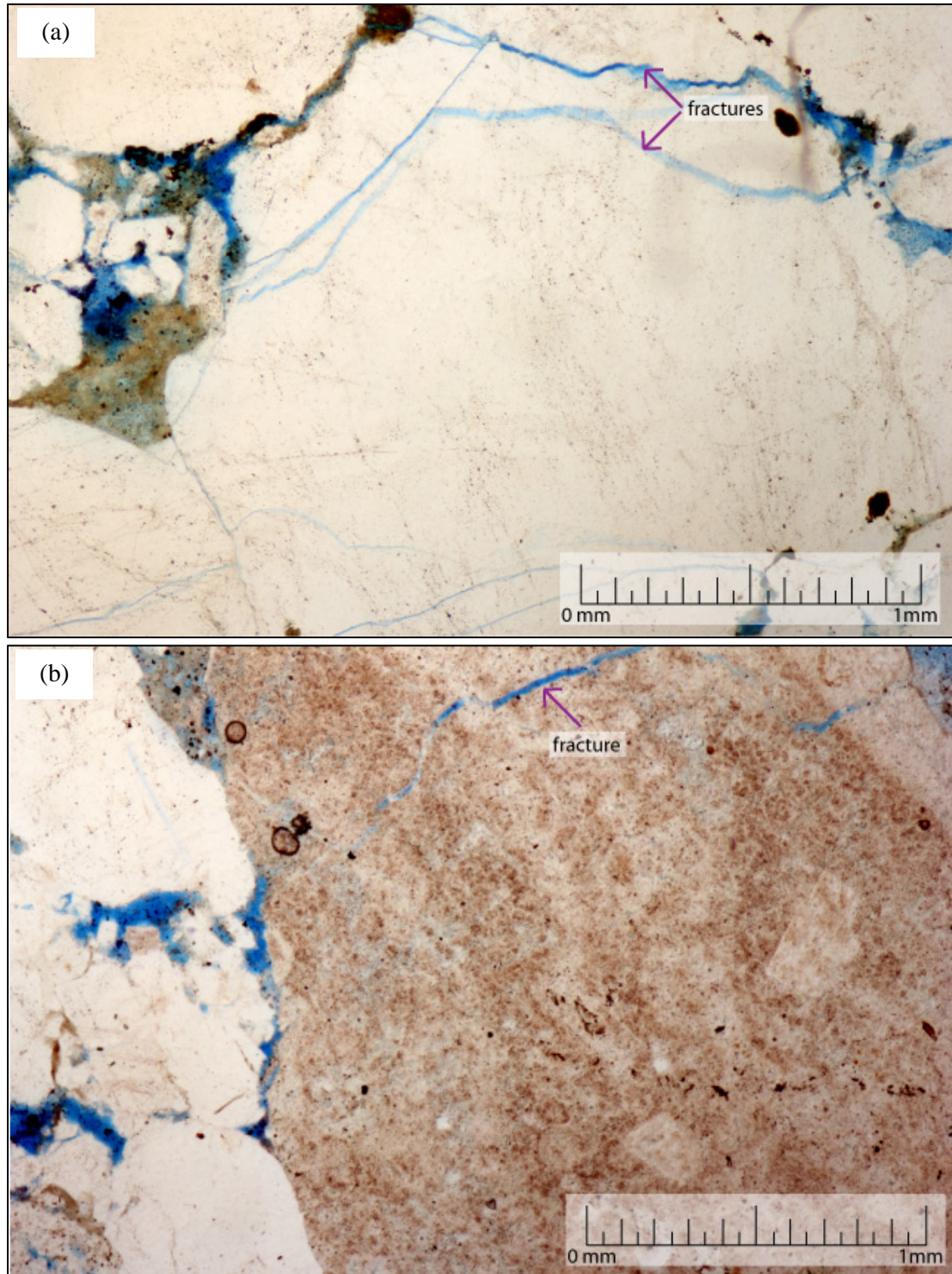


Figure 75. Photomicrographs showing fractures in the Morrow B sandstone. They are filled with epoxy so it is unlikely that they were caused by thin section preparation. The fractures may have been generated during differential compaction. (a) Well 32-3, 7983 ft, ppl. Microfractures in quartz grains. (b) Well 42-1, 8022 ft, ppl. Microfracture in a lithic fragment. The fracture is small and does not extend past the grain, so it probably does not contribute much to the permeability of the sample.

Porosity Facies

Samples from the Morrow B sandstone can be divided into five principle porosity facies and eight subfacies based on pore types, pore distribution, and principle controls on permeability (Table 11). Thin sections that have one dominant porosity facies were selected, and porosity versus permeability was plotted for each of the selected samples to assess the implications for reservoir quality (Figure 76). Table 12 shows how many samples from the western and eastern sides of the field were dominated by each porosity facies.

Table 11. Porosity facies of the Morrow B sandstone.

Porosity facies	Label	Sub facies	Pore types and distribution	Porosity and Permeability (P&P)	Found in samples from wells
Intergranular Macroporosity Dominated	A	"Clean" macroporosity	Little to no clay filling intergranular pores. Qtz overgrowths constrict some pores. Intergranular pores are well connected. Intragranular macroporosity is effective where it is in contact with intergranular porosity. Some ghost grains present.	High	32-1, 33-3
	B	Macroporosity dominated, with authigenic and detrital clay	Trace amounts of authigenic and detrital clay present in pores and pore throats. Some intergranular pores are connected. Intragranular porosity is less effective if the grain is surrounded by clay. Some kaolinite ghost grains.	Low-Moderate	9-8, 32-1, 32-2, 33-3, 42-1
Grain-sized Pore Dominated	C		Intergranular porosity is filled by microporous authigenic clay. Some grain-sized pores. Effective grain-sized pores create high permeability. Some grain-sized pores are surrounded by microporous clay, rendering them less effective.	High	13-10A
Microporous Authigenic Clay Dominated	D	Microporous authigenic clay dominated	Very little macroporosity. Intergranular pores are filled with kaolinite and some detrital clay, intragranular pores are also filled with kaolinite. Some slides have abundant kaolinite ghost grains.	Low-Moderate	9-8, 13-10A, 32-1, 32-2, 32-3, 42-1
	E	Low-IGV microporous authigenic clay dominated	Very little IGV due to compaction, and most is filled with microporous clay. Porosity is intragranular, due feldspar dissolution. Pores are found within partially dissolved feldspar grains and	Low	9-8
Carbonate Cement Dominated	F	Dissolution porosity in poikilotopic calcite	All IGV filled with calcite cement, so no intergranular porosity. Intragranular porosity is within grain-sized pores or partially dissolved feldspar grains. Some pores filled with kaolinite. Pores are not effective.	Low	9-8, 32-1, 42-1
	G	Intergranular porosity in siderite cement	Most porosity is in partially cemented siderite. Some authigenic and detrital clay present as well.	High	13-10A
Intragranular Porosity Dominated	H		Most porosity is intragranular and not effective. Very little intergranular porosity. No kaolinite ghost grains.	Low-Moderate	13-10A

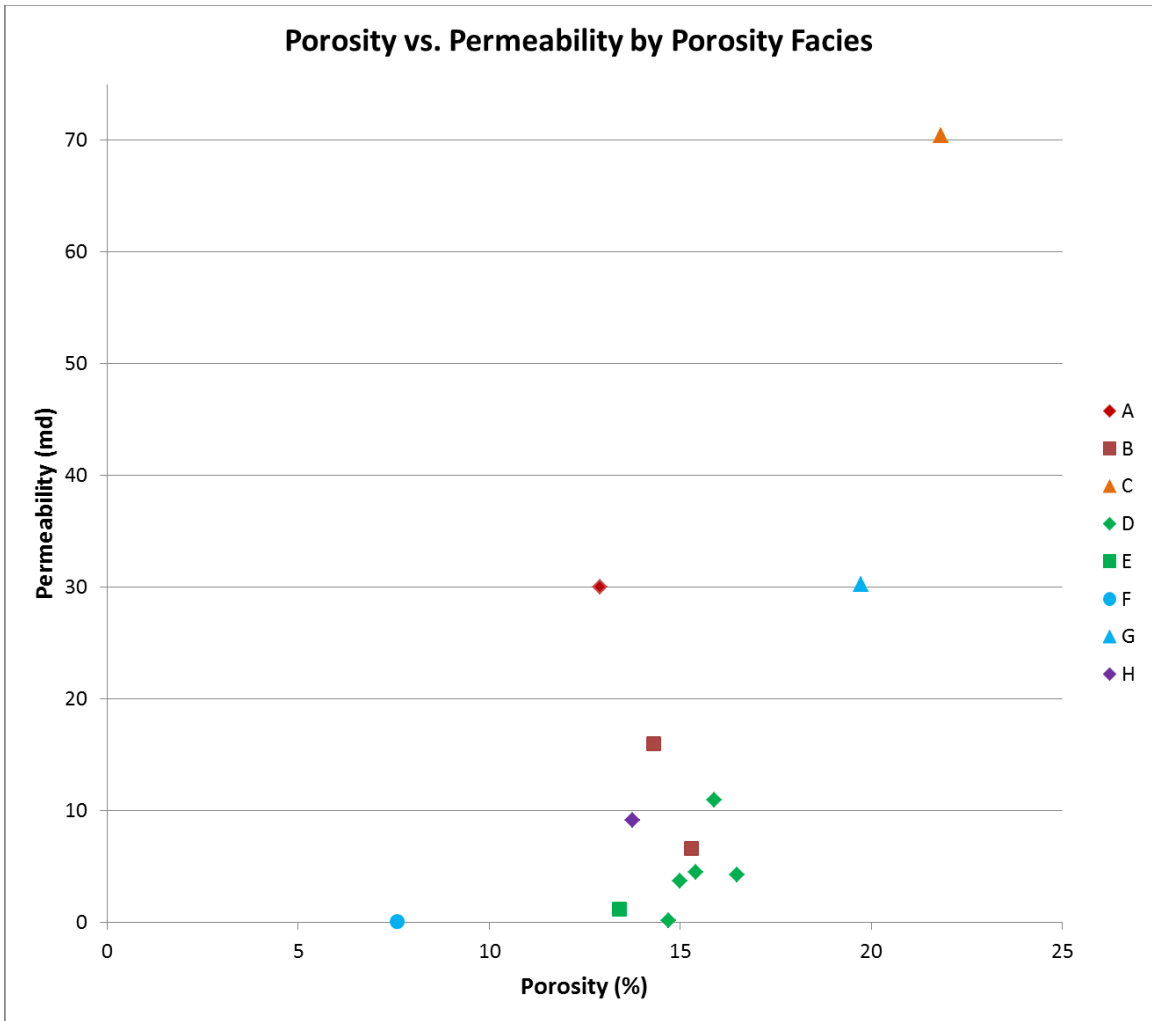


Figure 76. Porosity versus permeability by porosity facies. Porosity and permeability values are from thin sections that are dominated by a single porosity facies.

Table 12. Number of samples from the western and eastern sides of FWU that are dominated by each porosity facies.

West	Porosity facies	Description	P&P of facies	Count	Percent of samples
	A	"Clean" macroporosity	High	0	0%
	B	Macroporosity dominated, with authigenic and detrital clay	Low-Moderate	2	20%
	C	Grain-sized Pore Dominated	High	1	10%
	D	Microporous authigenic clay dominated	Low-Moderate	2	20%
	E	Low-IGV microporous authigenic clay dominated	Low	2	20%
	F	Dissolution porosity in poikilotopic calcite	Low	1	10%
	G	Intergranular porosity in siderite cement	High	1	10%
	H	Intragranular Porosity Dominated	Low-Moderate	1	10%
			Total	10	

East	Porosity facies	Description	P&P	Count	Percent of samples
	A	"Clean" macroporosity	High	2	11%
	B	Macroporosity dominated, with authigenic and detrital clay	Low-Moderate	7	39%
	C	Grain-sized Pore Dominated	High	0	0%
	D	Microporous authigenic clay dominated	Low-Moderate	6	33%
	E	Low-IGV microporous authigenic clay dominated	Low	0	0%
	F	Dissolution porosity in poikilotopic calcite	Low	3	17%
	G	Intergranular porosity in siderite cement	High	0	0%
	H	Intragranular Porosity Dominated	Low-Moderate	0	0%
			Total	18	

Intergranular Macroporosity Dominated

A. "Clean" macroporosity

In this facies, intergranular macroporosity is not obstructed by clay and has high porosity and permeability (Figures 76 and 77). In some areas, quartz overgrowths reduced porosity. With an absence of clay, intragranular macroporosity, particularly in dissolved feldspar grains, is effective where it is connected to intergranular porosity. Kaolinite ghost grains are present in some areas; however, because ghost grains are grain-shaped accumulations of kaolinite, the kaolinite fills the space once occupied by a feldspar grain and is not dispersed in pores or pore throats.

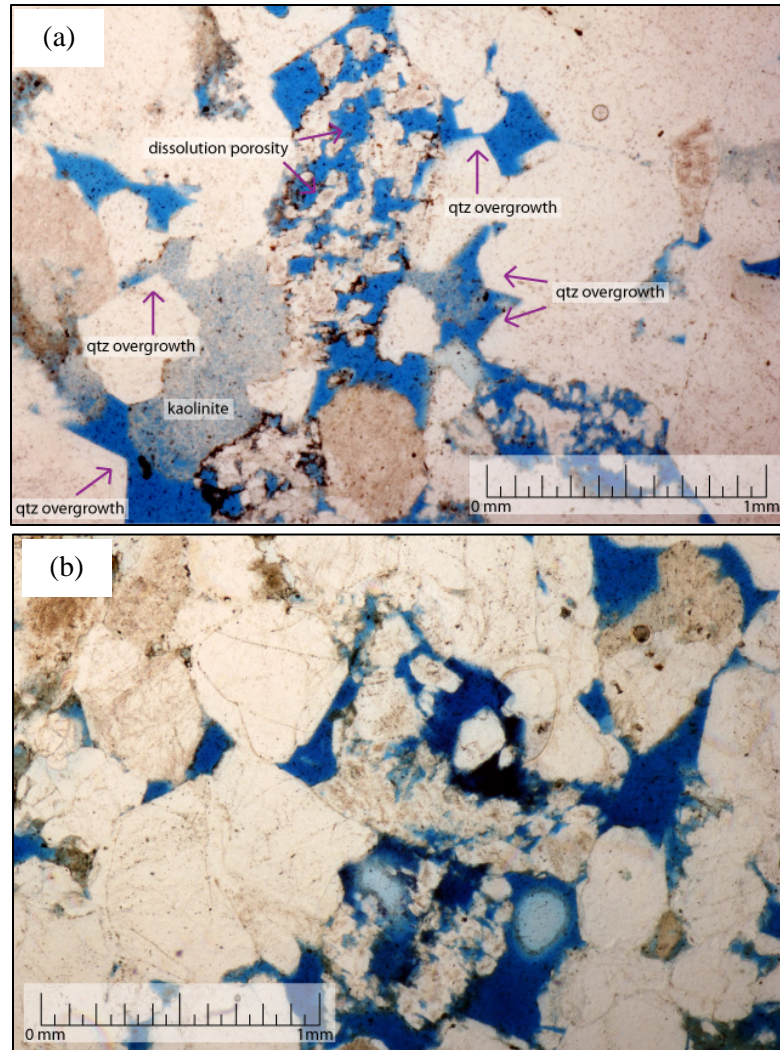


Figure 77. Representative thin sections from the “A” porosity facies. (a) Well 32-1, 7980 ft, ppl. Abundant intergranular macroporosity with very little authigenic clay. Quartz overgrowths have reduced porosity in some areas. (b) Well 32-1, 7983 ft, ppl. Abundant intergranular macroporosity with no authigenic clay.

B. Macroporosity dominated, with authigenic and detrital clay

This facies is similar to facies A, but has trace amounts clay reducing porosity and permeability (Figure 78). Facies B can have moderate to high porosity and permeability, depending on the amount and distribution of clay present (Figure 76). Clay in pore throats reduces permeability. Intragranular macroporosity is generally less effective if microporous clay surrounds the grains or is present within dissolved grains.

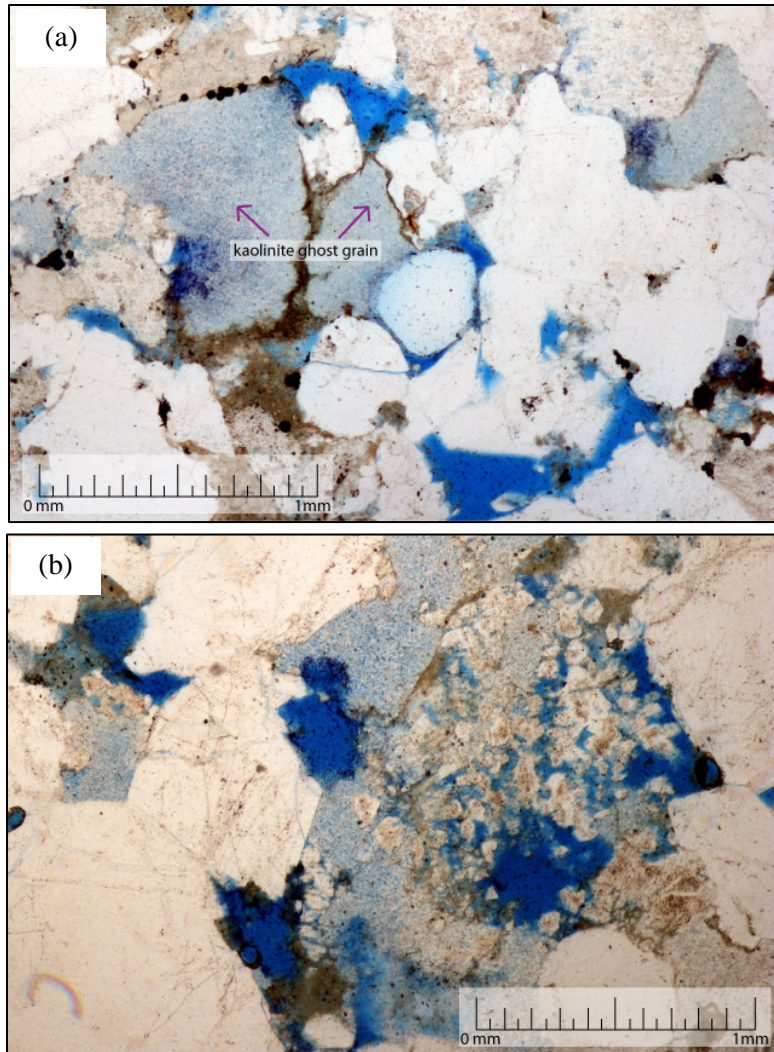


Figure 78. Representative thin sections from the “B” porosity facies. Intergranular macroporosity is abundant, but trace amounts of clay, particularly in pore throats, makes it less effective. (a) Well 9-8, 7704 ft, ppl. (b) Well 32-2, 7936 ft, ppl.

Grain-sized Pore Dominated

C. Grain-sized pore dominated

The permeability of this facies is dominated by grain-sized pores, which were created by the dissolution of feldspar or rock fragments. Authigenic clay is abundant, so most porosity, other than the grain-sized pores, is microporosity. Sample E4 is the only sample dominated by this subfacies, and it has the highest permeability (Figure 76). Effective grain-sized pores can create high permeability; however, some grain-sized pores are surrounded by microporous clay, which makes them less effective.

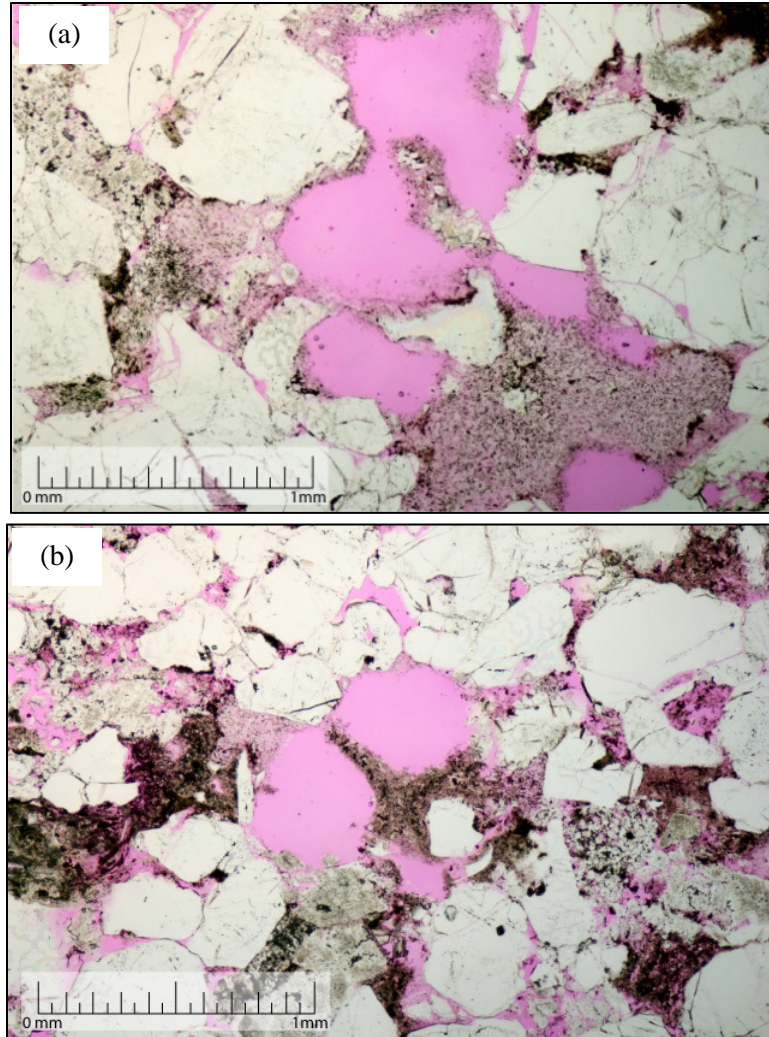


Figure 79. Well 13-10A, 7679.25 ft, ppl. Representative thin section from the “C” porosity facies. (a) Several grain-sized pores are interconnected, making them effective. (b) Two grain-sized pores are interconnected, but also surrounded by clay, which may make them less effective.

Microporous Authigenic Clay Dominated

D. Microporous Authigenic Clay Dominated

Most intergranular porosity is filled with microporous clay, leaving very little macroporosity (Figure 80). Most intragranular porosity is filled with microporous clay as well. Some slides have abundant kaolinite ghost grains. Porosity and permeability range from low – moderate (Figure 76).

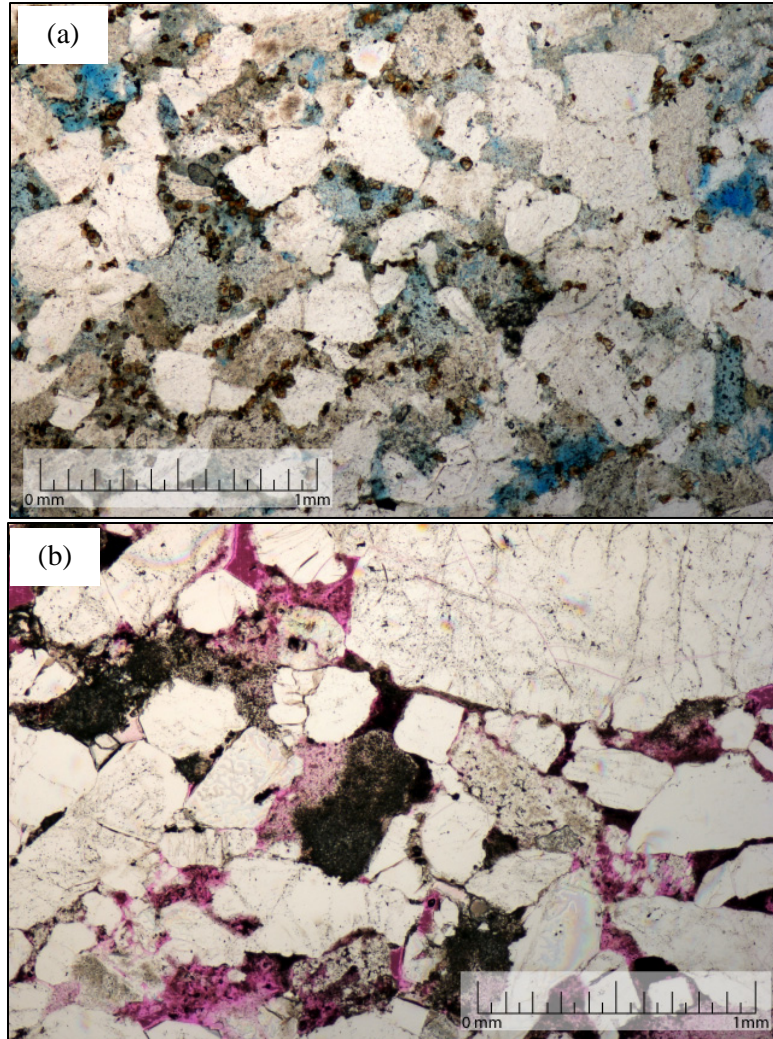


Figure 80. Representative thin sections from the “D” porosity facies. Most porosity is filled with authigenic clay and cement. (a) Well 42-1, 8005 ft, ppl. (b) Well 13-10A, 7684.74 ft, ppl.

E. Low-IGV Microporous Authigenic Clay Dominated

This facies is very similar to facies D but has lower IGV due to compaction, and therefore lower porosity and permeability (Figures 76 and 81). Microporosity is dominant, found within partially dissolved feldspar grains, kaolinite within dissolved feldspar grains, or kaolinite ghost grains. Intergranular macroporosity is rare.

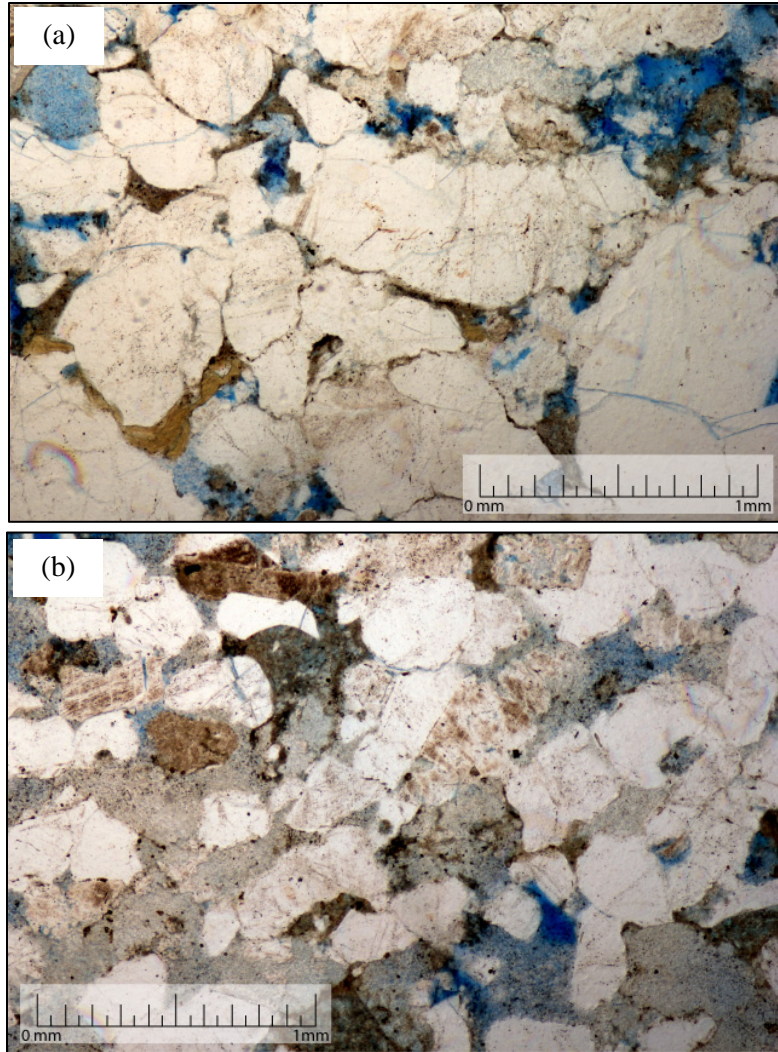


Figure 81. Representative thin sections from the “E” porosity facies. (a) Well 32-2, 7936 ft, ppl. Long grain contacts indicate significant compaction. (b) Well 9-8, 7694 ft, ppl. Abundant ghost grains.

Carbonate Cement Dominated

F. Dissolution porosity in poikilotopic calcite

In this subfacies, all IGV is filled with poikilotopic calcite cement, so there is no intergranular macroporosity (Figure 82). The porosity is intragranular, mostly due to feldspar dissolution. Pores are found within partially dissolved feldspar grains (macro), kaolinite within dissolved feldspar grains (micro), or kaolinite ghost grains (micro). Pores are not effective. This subfacies has the lowest porosity and permeability (Figure 76).

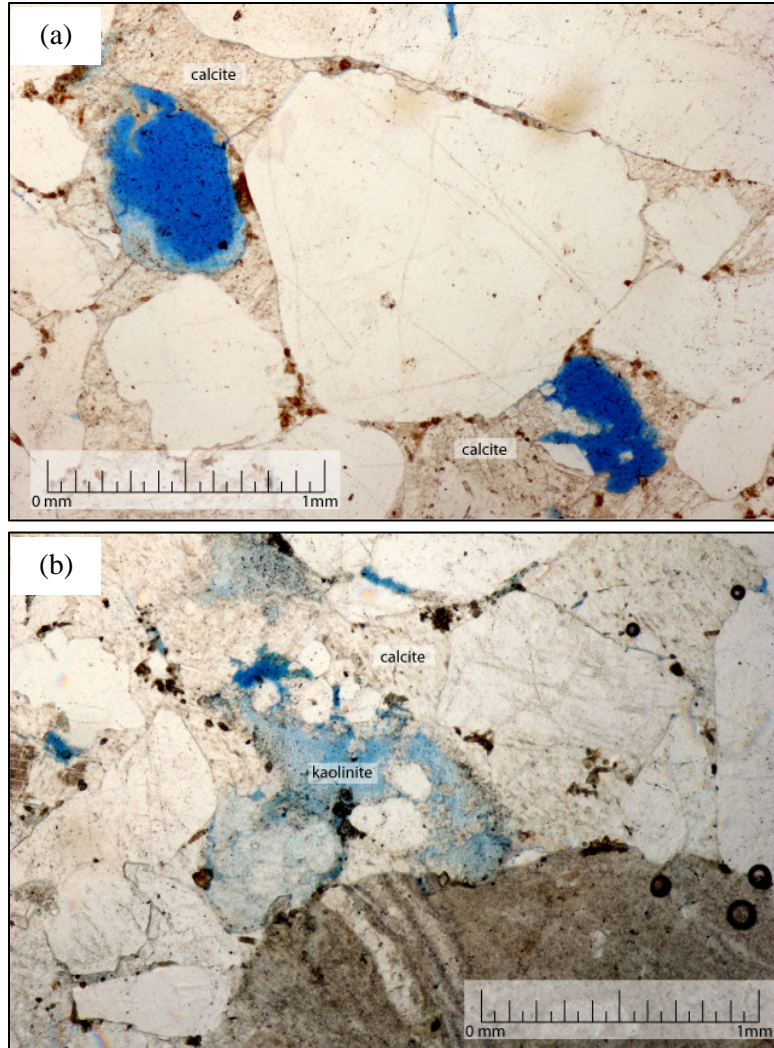


Figure 82. Well 42-1, 8015.5 ft, ppl. Representative thin section from the “F” porosity facies. (a) Two large pores are surrounded by poikilotopic calcite, and therefore are not effective. (b) Dissolution pores are filled with kaolinite and surrounded by poikilotopic calcite.

G. Intergranular porosity in siderite cement

Most porosity is found within partially cemented siderite (Figure 83). Trace amounts of authigenic and detrital clay is present as well. Intragranular porosity is present in some feldspar grains. Intragranular porosity is effective if it is connected to intergranular macroporosity. Intragranular porosity is not effective where it is isolated within a grain, or adjacent to cement or clay. Sample E1 is the only sample dominated by this subfacies, and it has high porosity and permeability (Figure 76).

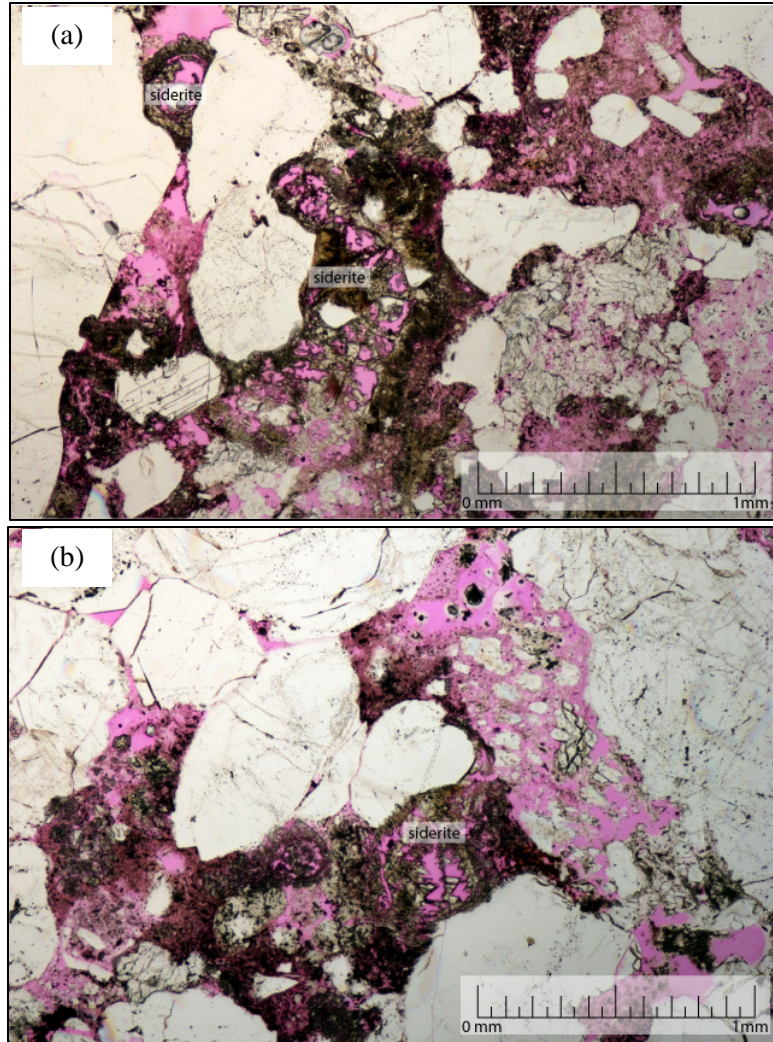


Figure 83. Well 13-10A, 7675.9 ft, ppl. Representative thin section from the “G” porosity facies. Siderite is abundant and occludes porosity.

Intragranular Porosity dominated

H. Low-IGV Intragranular Porosity Dominated

This subfacies is intragranular porosity dominated (Figure 84). Most porosity is from feldspar dissolution. There is little intergranular porosity due to compaction, and the remaining IGV is filled with microporous clay. Sample E3 is dominated by this facies has low porosity and permeability.

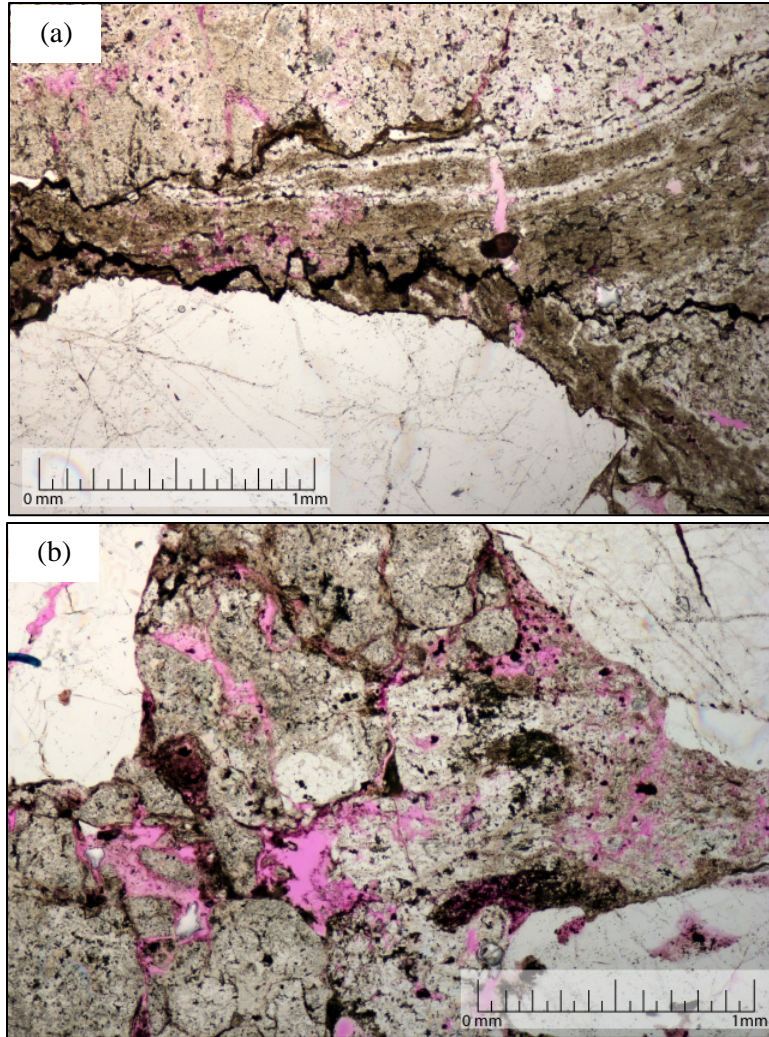


Figure 84. Well 13-10A, 7689.4 ft, ppl. Representative thin section from the “H” porosity facies. This facies is found in a sample that is highly compacted, with very little IGv. Most porosity is found within partially dissolved rock fragments. (a) Stylolites in this VRF indicate significant compaction. All porosity pictured is intragranular. (b) Intragranular porosity from dissolution of a rock fragment.

Mercury Injection Capillary Pressure (MICP)

Mercury Injection Capillary Pressure (MICP) data shows the pore-throat diameter distribution of samples E1- E4, which were taken from the Coarse-grained Sandstone facies from well 13-10A (Figures 85 and 86). The dominant pore-throat diameters of these samples are within the mesopore-throat domain (1 - 10 μm) and the macropore-throat domain (>10 μm , classification from Nelson, 2009; Table 13). See Appendix G for raw data.

Sample E1 is mesopore-throat dominated (Table 13, Figure 86a). It is slightly bimodal. The dominant pore-throat size is 7.36 microns, and the secondary pore-throat size is 3.25 microns. Sample E2 is mesopore-throat dominated and has the smallest dominant pore-throat size, which is 4.78 microns (Table 13, Figure 86b). It is not bimodal. Sample E3 is mesopore-throat dominated and has the second smallest dominant pore-throat size, which is 6.13 microns (Table 13, Figure 86c). It is slightly bimodal, with a secondary pore-throat size of 4.01 microns. Sample E4 is strongly bimodal. It has the largest dominant pore-throat size and smallest secondary pore-throat size (Table 13, Figure 86d). The dominant pore-throat size is 12.64 microns, which is in the macropore domain. The secondary pore-throat size is 1.92 microns, which is in the mesopore domain.

Pore-throat diameters were compared to plug permeability, grain size, and sorting to determine if any of these factors control pore-throat size distribution. There is a positive correlation between dominant pore-throat diameter and the plug permeability with an R^2 value of 0.986 (Figure 87a), and a negative correlation between secondary pore-throat size and permeability (Figure 87b), which suggests that permeability is controlled by the dominant pore-throat sizes, not the secondary pore-throat sizes. There is no relationship between average grain size and dominant pore-throat size; the finest grain size is associated with both the largest and smallest dominant pore-throat sizes (Table 13). However, grain size does correlate with the secondary pore-throat sizes. The best-sorted sample, E4, does have the largest dominant pore-throats. However, the pore-throat sizes could be attributed to the grain-sized pores rather than the sorting of the sample. Sorting does not correlate with secondary pore throat sizes.

Table 13. Porosity facies, plug porosity and permeability, grain size, and pore-throat size for samples E1 – E4 from the Coarse-grained Sandstone facies from well 13-10A.

Sample	Porosity Facies	Porosity (%)	Perm. (md)	Grain size	Sorting	Dominant pore-throat size (μm)		Secondary pore-throat size (μm)	
E1	G	19.73	30.25	vcL	VP	7.36	Meso	3.25	Meso
E2	D	16.49	4.25	cL	VP	4.78	Meso	-	-
E3	H	13.76	9.18	vcU	P	6.13	Meso	4.01	Meso
E4	C	21.83	70.40	cL	MW	12.64	Macro	1.92	Meso
	D	21.83	70.40	cL	MW	12.64	Macro	1.92	Meso

vcU= very coarse upper, vcL= very coarse lower, cL=coarse lower, VP= very poor, P= poor, MW= moderately well

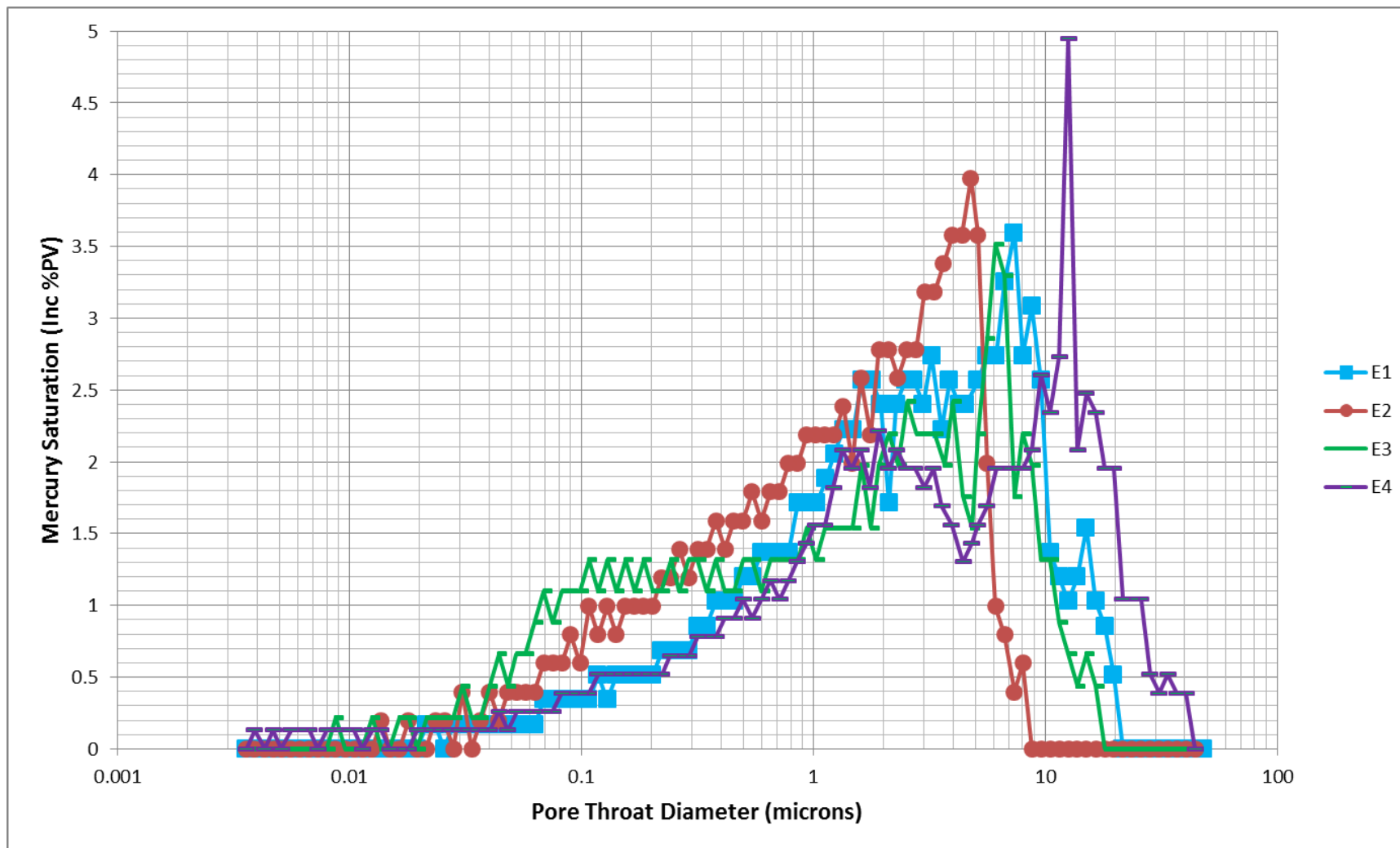


Figure 85. Comparison of pore throat diameter vs. mercury saturation for samples E1 – E4, well 13-10A. Mercury saturation is expressed in incremental percent of the pore volume.

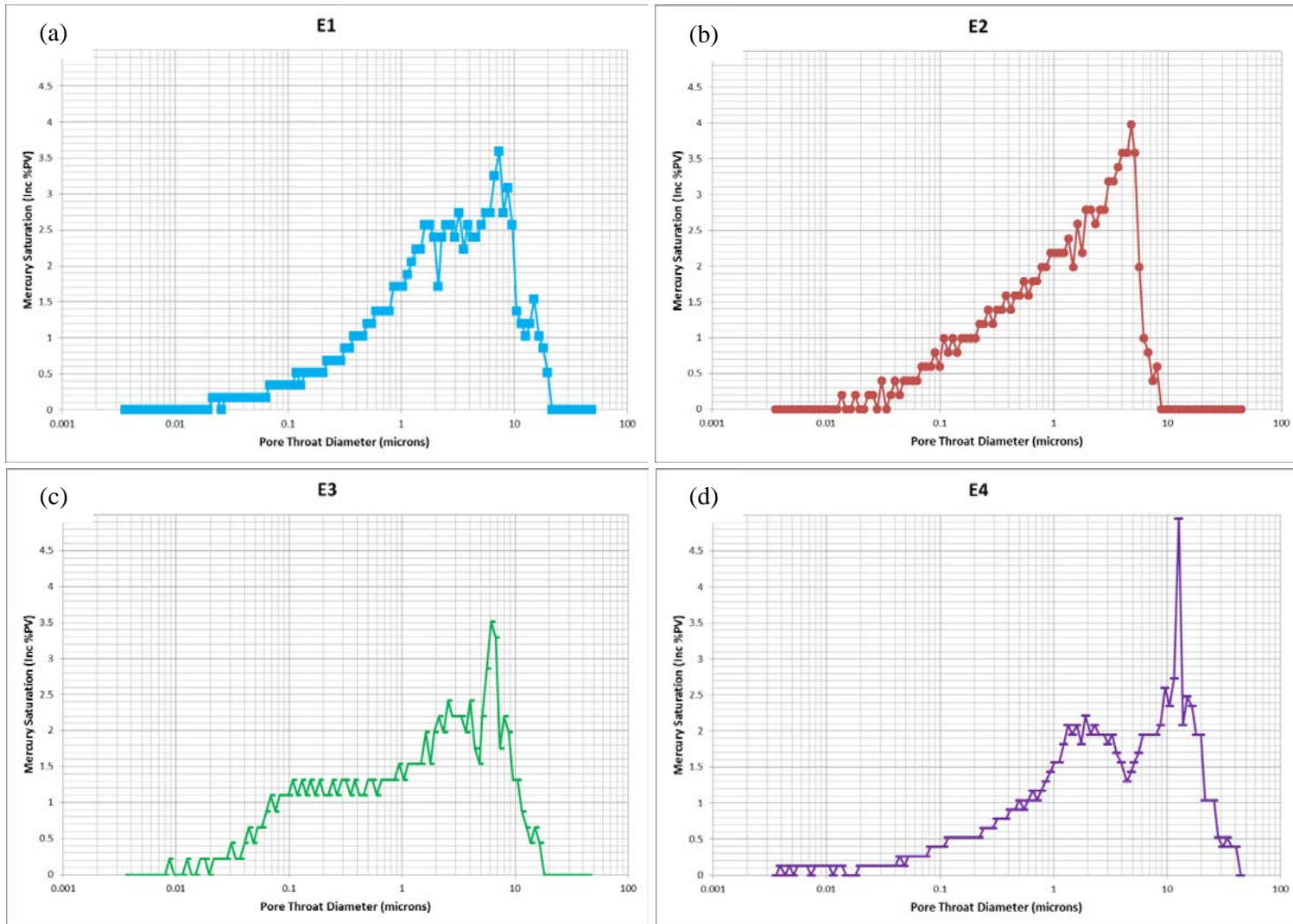


Figure 86. MICP data for samples E1 – E4 from well 13-10A. Mercury saturation is expressed in incremental percent of the pore volume. (a) Sample E1 (b) Sample E2 (c) Sample E3 (d) Sample E4.

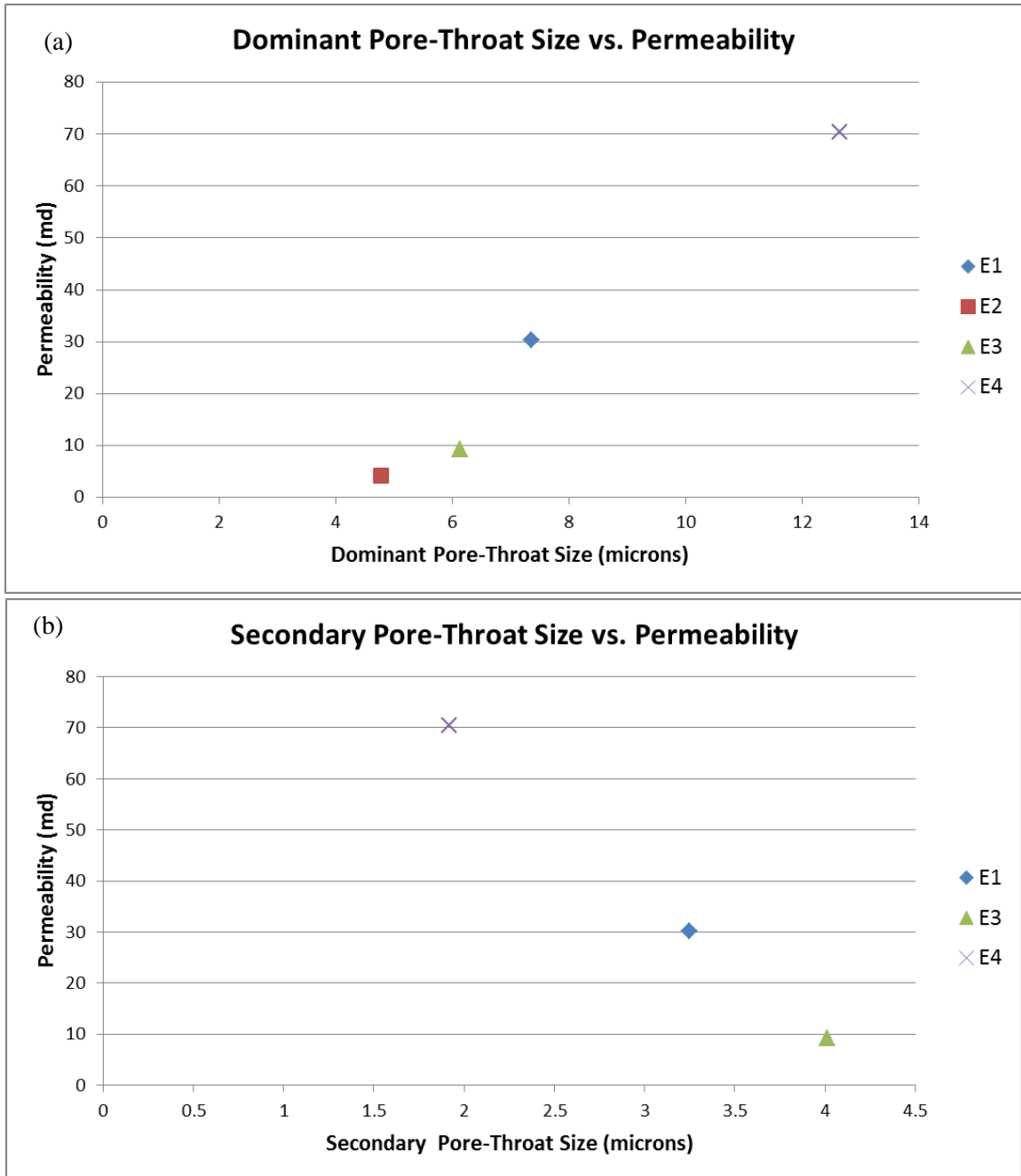


Figure 87. (a) Dominant pore-throat size versus plug permeability. There is a strong positive correlation, $R^2 = 0.986$. (b) Secondary pore-throat size versus plug permeability. There is a negative correlation. Note that sample E2 is not bimodal, and therefore does not have a secondary pore-throat size.

Image Analysis

Photomicrographs of the four samples from well 13-10A were analyzed with ImageJ to better understand pore size and distribution (Grove and Jerram, 2011; Appendix H). ImageJ was used to analyze discrete pores from a binarized image. It calculated the total porosity of each image, as well as the area and feret diameter of each pore. The feret diameter is defined as the longest direct distance between any two points on the boundary of the pore (Rasband, 2008). See Appendix E for detailed image analysis methods. This method has limitations because it analyzes a two-dimensional image of a three-dimensional pore system. If pores appear connected in a photomicrograph, ImageJ counts them as a single pore. For connected pores, the pore diameter as measured by ImageJ is artificially high.

For each photomicrograph, the area and feret diameter for all pores was averaged. It was observed that in some photomicrographs, particularly in sample E4, the largest pore accounts for a large percent of the total image porosity, so the area and feret diameter of the largest pore was recorded as well. The area of the largest pore was divided by the total image porosity to calculate the percent of the total image porosity from the largest pore. However, it should be noted that in some photomicrographs, the “largest pore” was actually several pores which appear connected.

The pore areas and feret diameters were averaged for each sample (Table 14). Samples E1 through E3 each have one main porosity facies, and five photomicrographs from each sample were analyzed. Sample E4 has two distinct porosity facies, C (grain-sized pore dominated) and D (microporous authigenic clay dominated). Four photomicrographs from each facies were analyzed, for a total of eight photomicrographs from sample E4. For sample E4, image analysis results for each facies were averaged separately to discern differences between the two facies.

Table 14. Summary of ImageJ data. Porosity and permeability values are from routine core (plug) analysis. Image porosity, areas, and feret diameters were calculated with ImageJ and averaged for each sample.

Sample	Facies	Porosity	Perm. (md)	Image porosity	Average for all pores		Largest pore		
					Area (μm^2)	Feret (μm)	Area (μm^2)	Feret (μm)	% of total image porosity
E1	G	19.7%	30.25	10.48%	238.81	12.59	120056.85	796.06	21%
E2	D	16.5%	4.25	8.60%	143.09	10.73	61644.52	591.07	13%
E3	H	13.8%	9.18	4.54%	204.81	12.01	39714.42	373.33	17%
E4	C	21.8%	70.40	21.40%	287.59	8.86	597257.18	1374.47	50%
	D	21.8%	70.40	19.74%	274.86	11.24	207358.84	1038.16	19%

The average image porosities were plotted against plug porosity, and there does appear to be a correlation between the two ($R^2 = 0.871$; Figure 88). Average pore area, average pore diameter, largest pore area, and largest pore diameter were plotted versus plug permeability to determine if those properties correlate to permeability (Figure 89). All of those values correlate with permeability ($R^2 = 0.617$ to 0.852), except for average

pore diameter ($R^2 = 0.257$). It appears that the average pore diameters from sample E4 do not correlate with permeability, but the largest pore sizes do correlate to permeability, which suggests that the permeability of that sample may be controlled by the largest pores, not the average-sized pores. It should be noted that for sample E4, the average pore sizes for the C (grain-sized pore dominated) and D (microporous authigenic clay dominated) facies are similar, but the largest pores from the C facies are much larger than those from the D facies.

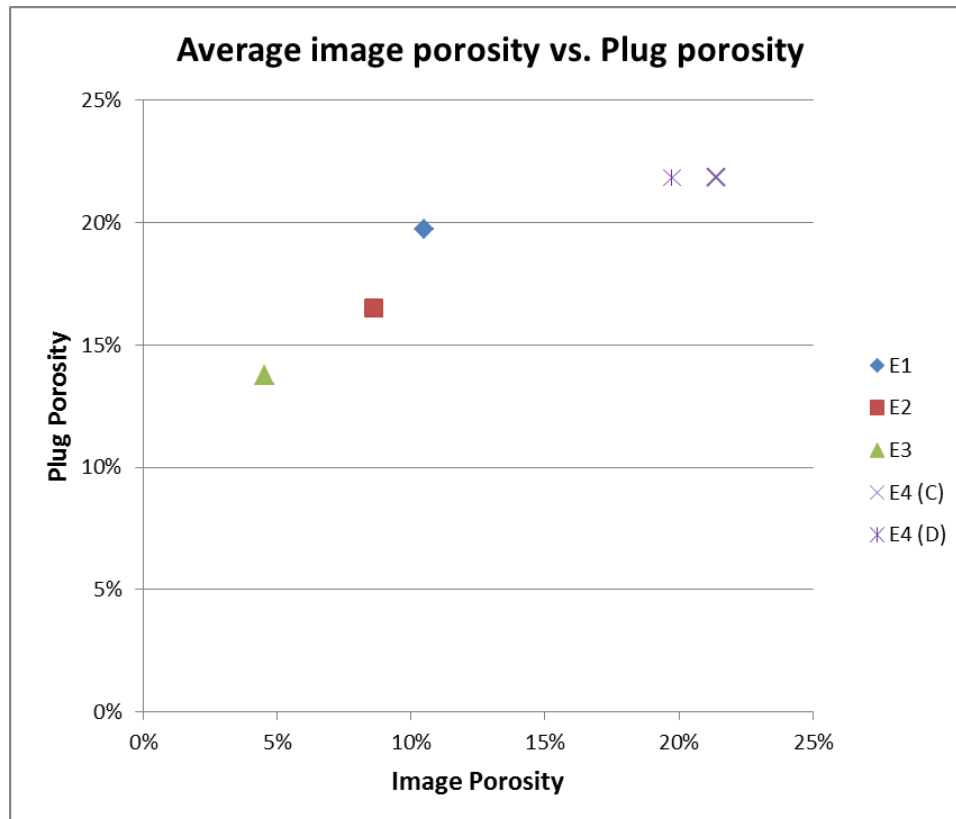


Figure 88. Average image porosity versus plug porosity. There is a correlation between average image porosity and plug porosity, $R^2 = 0.871$.

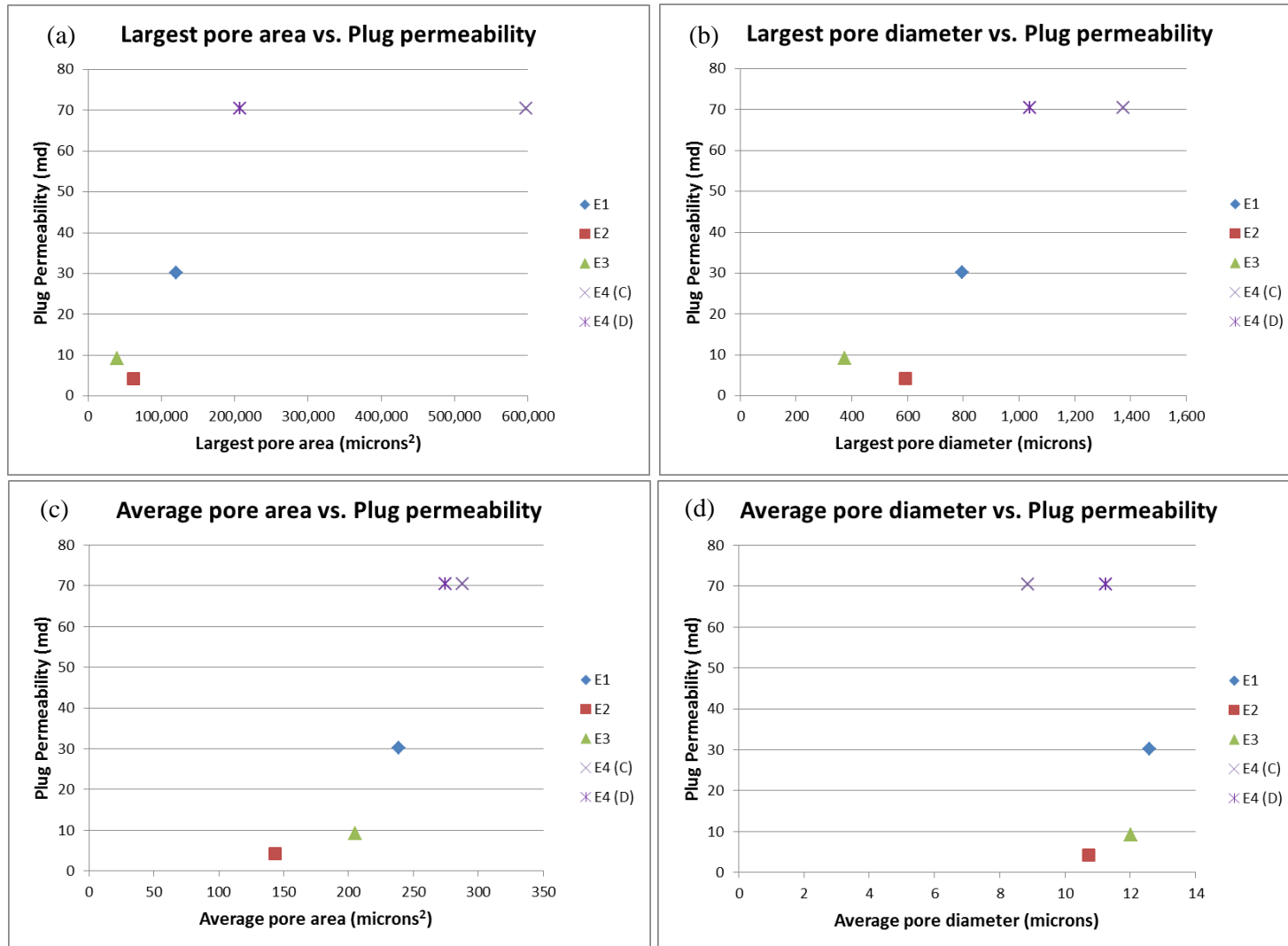


Figure 89. Pore size versus permeability. (a) Average pore area, $R^2=0.617$ (b) Average pore diameter, $R^2=0.843$ (c) Largest pore area, $R^2=0.852$ (d) Largest pore diameter, $R^2=0.257$.

CHAPTER 4: DISCUSSION

This chapter addresses the depositional environment of the upper Morrowan strata in the Farnsworth Unit and controls on reservoir quality and heterogeneity.

Depositional Environment

The upper Morrowan facies in FWU appear to be incised valley deposits, as described by Wheeler et al. (1990) and Puckette et al. (2008), and not fluvial-deltaic deposits as described by Munson (1988). The fluvial-deltaic interpretation was based upon sand-body geometry, petrographic log signatures, and grain size analysis methods that are probably unreliable (cf. Ehrlich, 1983). Puckette et al. (1996) caution against determining depositional environment solely on geometry, log signatures, or grain size, and suggest that all geological data must be considered and integrated with knowledge of sequence stratigraphy, and placed within the context of surrounding genetically related strata. New studies provide a greater context for the depositional environment and sequence stratigraphy of the Morrow B sandstone in FWU.

The lithofacies observed in core from FWU are similar to lithofacies described by Wheeler et al. (1990) and Puckette et al. (2008). Wheeler et al. (1990) focuses on Morrowan deposits in southeastern Colorado and southwestern Kansas. Puckette et al. (2008) studied the upper Morrow sandstone in southwestern Kansas and the Oklahoma Panhandle. The FWU lies south of these study areas and paleogeographically “downstream” (Figure 5). Because of this, the lithofacies of the FWU are somewhat different, but the same patterns of deposition are observed (Table 15). The general stratigraphy in FWU core, from deeper to shallower, is: marine mudstone, channel lag conglomerate, fluvial coarse-grained sandstone, estuarine fine-grained sandstone, and marine mudstone (Figure 90).

The Mudstone facies is divided into the Mudstone with Brachiopod Fossils, Dark Gray Mudstone, and Bioturbated Mudstone subfacies. No definitive evidence of depositional environment was observed in any of the mudstone subfacies; however, there is evidence to suggest a marine or marine-influenced depositional environment.

The Mudstone with Brachiopod Fossils subfacies is likely marine since brachiopods can only live in a marine environment. However, it is possible that the shells were transported by a storm. It may correspond to the M-1 facies from Puckette et al. (2008), which represents a low-energy marine environment.

The depositional environment of the Dark Gray Mudstone facies is ambiguous. What can be inferred is that it was deposited in a low-energy environment with anoxic

waters. This is evident from the coal intervals and preserved plant material. Siderite concretions can form in both fresh and marine waters, so without chemical analysis of the sample, the depositional environment cannot be determined. The coal and carbonaceous material indicate that the Dark Gray Mudstone may have been deposited in a swamp. This subfacies could correspond to facies #10, the Fluvial Flood-plain facies from Wheeler et al. (1990), which represents swamp or abandoned channel-fill deposits.

The upper Bioturbated Mudstone has a gradational contact with the estuarine Fine-grained Sandstone facies, so the lower part of upper mudstone could represent a transition between estuarine and marine during sea level transgression. Bioturbated intervals must have been oxygenated in order to support life. Layers of coal indicate anoxic water. The presence of both of these conditions in the same subfacies might indicate a transition from swamp to marine or estuarine. It may correspond to the M-1 facies from Puckette et al. (2008), which represents a low-energy marine environment.

The Conglomerate facies is also interpreted to be fluvial. The Paraconglomerate subfacies corresponds to the F-1 fluvial facies of Puckette et al. (2008). Because very similar deposits were described by Puckette et al. (2008) in core from Oklahoma and Kansas, it is a regional deposit. The clasts are very different from the Basal Lag Conglomerate, indicating that the sediment source may be different. The Basal Lag Conglomerate corresponds to facies #7, the Conglomerate to Conglomeratic Coarse-grained Sandstone, from Wheeler et al. (1990). It scoured the lower shelf mudstone and represents a sequence boundary.

The Coarse-grained Sandstone facies is interpreted to be fluvial. The large grain size, poor sorting, and lack of fines indicate a generally high-energy, fluvial or marine environment. The mudstone interbeds could be overbank deposits, which are found in fluvial environments. The possible rhythmites found in well 32-6 suggest tidal influence. However, Puckette et al. (2008) and Wheeler et al. (1990) describe tidally-influenced sandstones as having marine fossil fragments and glauconite, neither of which were observed in the Coarse-grained Sandstone facies of FWU.

Further evidence for the transition from fluvial deposition to marine deposition comes from the microprobe analysis. The Coarse-grained Sandstone facies contains siderite that formed in both fresh and marine pore-waters. Because it is unlikely that the pore waters could have started out marine and become fresh, the opposite is probably true. The Coarse-grained Sandstone was deposited in a freshwater, fluvial environment, at which time some fresh-water siderite formed, possibly on root-hairs or other carbonaceous material. Later, when the fluvial Coarse-grained Sandstone was buried by estuarine and marine deposits, the pore waters mixed and marine water infiltrated the Coarse-grained Sandstone. Then a second stage of siderite formed with a marine chemical composition.

The sedimentary structures of the Coarse-grained Sandstone facies differ among the wells, which suggest that a variety of fluvial processes influenced deposition within FWU. The Coarse-grained Sandstone facies in well 9-8 (west side) is finer grained than the sandstone in the other wells and it generally fines upward (Figure 11). It contains low-angle cross bedding (Figure 19), which is not present in other wells. The Coarse-grained Sandstone in core from wells 8-5, 13-10, and 13-10A (west side, Figures 10-12,

17) displays a sheet-like geometry. The sandstone in well 32-2 (east side) alternates from coarser- to finer-grained on a scale of several centimeters (Figure 13). It does not display significant cross bedding, but does display fining-upward sequences. Well 32-6 (east side) displays possible epsilon cross stratification (Figure 16). Cross bedding is not present throughout the entire sequence, but where present, it consistently dips in the same general direction, which may indicate lateral accretion. It locally contains very distinct cm-scale sets of coarser- and finer-grained sandstone (Figures 16 and 20). Overall, there does not appear to be a consistent spacial pattern in the types of sedimentary structures in the Coarse-grained Sandstone in the western and eastern sides of the field.

The Fine-grained Sandstone facies is interpreted to be estuarine. Estuaries receive sediment from fluvial and marine sources and are influenced by tide, wave, and fluvial processes (Dalrymple et al., 1992). The fining upward sequences could indicate fluvial processes, and the low-angle cross beds could be due to fluvial or tidal processes. Glauconite was observed in a thin section from this facies, which is indicative of marine influence. This facies could correspond to the E-1 estuary facies from Puckette et al. (2008) or to facies #6 from Wheeler et al. (1990), a tidally influenced fluvial channel.

The lithofacies within FWU are similar to incised valley deposits described elsewhere in the Anadarko Basin, so it is likely that they have the same sequence stratigraphy as reported by Wheeler et al. (1990). Incised valley deposits represent Lowstand Systems Tracts (LST) and Transgressive Systems Tracts (TST). The boundary between the top of the lower mudstone facies (Dark Gray Mudstone and lower Bioturbated Mudstone) and the Conglomerate facies represents the Lowstand Surface of Erosion (LSE). The Conglomerate facies in the Farnsworth Unit represents the Lowstand Systems Tract (LST). It scoured the shelf mudstone during a time of low sea-level, which is evident from the erosional contact with the mudstone facies and the mudstone rip-up clasts within the mudstone. During transgression, the Coarse-grained Sandstone was deposited by fluvial processes. As sea level continued to rise, the valley was flooded by an estuary and the Fine-grained Sandstone facies was deposited. During the Highstand Systems Tract, the sea flooded most of the Anadarko basin, and the sandstone deposits in FWU were covered by marine mudstone. The contact between the Fine-grained Sandstone and the upper Bioturbated Mudstone is gradational, which is evidence of transgression. In some areas of FWU, up to five pockets of coarse-grained sandstone are present, which suggests that this cycle of sea level rise and fall may have occurred several times in the area.

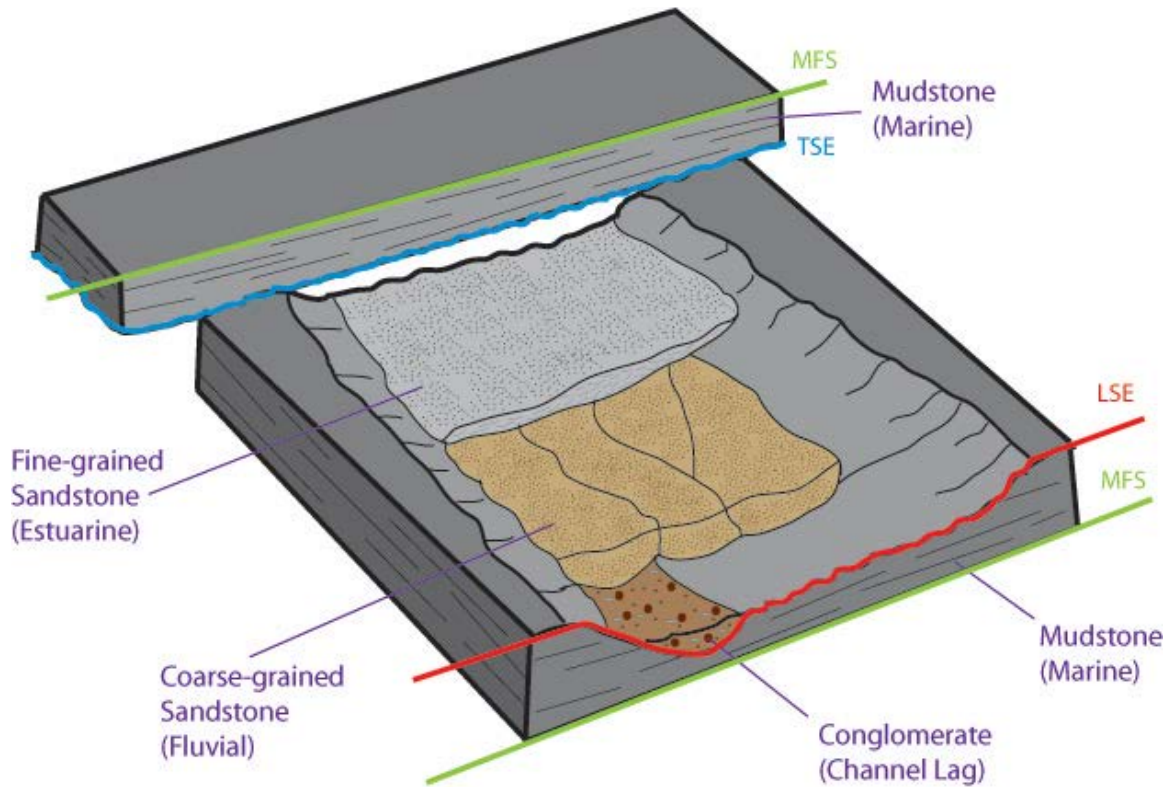


Figure 90. Depositional model for the Farnsworth Unit. Modified from Wheeler et al. (1990) and Puckette et al. (2008). MFS= Maximum Flooding Surface. LSE= Lowstand Surface of Erosion. TSE= Transgressive surface of Erosion.

FWU lithofacies and depositional environment interpretation			Corresponding Puckette et al. (2008) lithofacies and depositional environment interpretation			Corresponding Wheeler et al. (1990) lithofacies and depositional environment interpretation		
Lithofacies	Subfacies	Environmental Interpretation	Lithofacies	Description	Environmental Interpretation	Lithofacies	Description	Environmental Interpretation
Fine-grained Sandstone		Estuarine	E-2	Fine- to medium-grained sandstone and shale containing abundant trace fossils.	Estuarine: Upper estuary, tidally influenced with variable energy and possible fluvial input.	6	Cross-bedded sandstone with shale drapes: Gray to tan, fine- to coarse-grained quartz arenite or shaly sandstone; trough or tabular cross-bedded with incipient stylolites and shale drapes. Sparsely burrowed, glauconite and carbonaceous debris.	Fluvial or estuarine: Upper point-bar or flood-plain; tidally influenced fluvial channel
Coarse-grained Sandstone		Fluvial	F-2	Coarse-grained sandstone to conglomerate. Trough and planar cross-bedding and stacked fining upward sets.	Fluvial: High-energy braided stream of middle to lower channel sequence.	8	Coarse-grained, cross-bedded sandstone: medium- to very coarse-quartz arenite or subarkose to sublitharenite; trough or tabular cross-bedded in sets ranging from 3 in. to over 2 ft. thick; in many cases foreset laminae alternate between coarser and finer grain size fractions.	Fluvial Channel: Chute-modified point bar
Conglomerate	Paraconglomerate	Fluvial	F-1	Matrix supported paraconglomerate.	Fluvial: High current-energy stream.			
	Basal Lag Conglomerate	Fluvial				7	Conglomerate to conglomeratic sandstone: Gray to light brown, granules and pebbles of mudstone and composite quartz; matrix is fine- to very coarse-grained, poorly sorted, quartz arenite or sublitharenite to subarkose.	Fluvial channel: Braided stream, channel-bottom lag or lower point-bar
Mudstone	Mudstone with Brachiopod Fossils	Marine	M-1	Dark shale and/or claystone. Calcareous intervals contain abundant marine invertebrate fossils.	Marine: Low-energy marine environment. Disaerobic offshore shelf setting.			
	Dark Gray Mudstone	Swamp				11	Dark gray carbonaceous mudstone: generally planar- laminated; abundant carbonaceous debris including leaf and stick impressions; pyrite, root traces and slickensides common.	Fluvial flood-plain: Swamp or abandoned channel-fill
	Bioturbated Mudstone	Estuarine, swamp, marine	M-1	Dark shale and/or claystone. Calcareous intervals contain abundant marine invertebrate fossils.	Marine: Low-energy marine environment. Disaerobic offshore shelf setting.			

Table 15. Comparison of the lithofacies in FWU with lithofacies described in Puckette et al. (2008) and Wheeler et al. (1990).

Controls on reservoir quality and heterogeneity

The reservoir sandstone in the western side of FWU has a higher average (mean and median) permeability than the reservoir in eastern side of the field (Figure 35; Munson, 1988). One of the goals of this study is to determine whether this is due to depositional or diagenetic differences. Munson (1988) indicates that grain size decreases eastward in the field, and suggests that the lower permeability could be due to more authigenic clay, particularly kaolinite and smectite, in the eastern side of the field. Data from Munson (1988) was reevaluated and integrated with data from the newly-drilled 13-10A well.

Reservoir quality of the Morrow B sandstone in FWU does not appear to be controlled by depositional (primary) processes. The eastern side of the field is paleogeographically “downstream” (Figure 6) and may represent a transition from braided to meandering fluvial processes. However, there is no decrease in grain size or the degree of sorting across the field (Table 2, Figures 31, 32, 33), nor an increase in detrital clay (Table 6), that could account for the lower permeability in wells from the eastern side of the field.

No correlation was found between primary textural features (grain size and sorting) and reservoir quality (porosity and permeability; Figures 32 and 33). Munson (1988) indicated that average grain size decreases in an easterly direction; however, grain size data for that study was collected by disaggregating and sieving samples. When disaggregating samples, some grains, particularly altered feldspars and lithic fragments, may have broken apart, resulting in artificially smaller grain sizes. Conversely, several grains bound together by quartz or carbonate cement could be measured as a single large grain. For this study, grain sizes were visually estimated from core or thin sections. This is more qualitative than sieving, however it may provide more accurate mean grain sizes because there is no risk of breaking apart grains or measuring cemented grain aggregates. This study found that the eastern side of the field has a higher percent of coarser grain sizes and better sorting (Table 2). Typically, coarser grain size and better sorting corresponds to higher permeability (Nelson, 1994). Because grain size and sorting do not account for the lower permeability of the eastern side of the field, then it may be due to diagenetic factors.

Diagenetic (secondary) processes had a much greater effect on the reservoir quality of the Morrow B sandstone than depositional processes. The diagenetic processes that had the greatest effect on reservoir quality are: dissolution of grains, particularly feldspar and lithics; precipitation of authigenic clay; carbonate and quartz cementation; and compaction. Grain dissolution increased porosity in some places, and authigenic clay and compaction reduced the reservoir quality of the Morrow B sandstone. Dissolution of feldspar increased porosity and permeability by creating intragranular micro- and macroporosity. Some grains, possibly feldspar, dissolved completely, leaving grain-sized pores. Sample E4 has abundant grain-sized pores and also has the highest permeability of all samples examined in this study. This suggests that complete dissolution of grains contributes greatly to permeability. However, the dissolution of feldspar may have provided the aluminum for kaolinite to precipitate, which decreased reservoir quality. Authigenic clay, primarily kaolinite, is abundant in the Morrow B sandstone. Kaolinite was observed in every thin section from the reservoir facies, and it partially or completely

fills the pore space of many samples. XRD analysis revealed that smectite and illite are present in some samples. Authigenic forms of these clays have the potential to greatly reduce reservoir quality, but detrital clay in the form of clay seams or clay clasts does not have much effect on reservoir quality. Because smectite and illite were not observed by optical petrography or in BSE images, their distribution is unknown, and therefore their effect on reservoir quality is unclear. They appear to be present in very small amounts, so any effect is likely minimal. Carbonate cement also reduced porosity and permeability. Some of the lowest porosity and permeability values come from samples with abundant poikilotopic calcite. Poikilotopic calcite was observed in four samples from four different wells. Siderite cement reduced porosity and permeability, but not to the same degree as poikilotopic calcite because it only partially filled the pore space. Siderite is present in trace amounts in several samples, but only abundant in one sample from well 13-10A. This sample has fairly good reservoir quality. Compaction is variable among the samples, which is evident from the amount of IGV and type of grain contacts. Highly compacted samples generally have low porosity and permeability.

Munson (1988) found that the eastern side of FWU has higher average clay content than the western side; however, averages can be deceiving. The XRD data from Munson (1988) and from well 13-10A (this study) were plotted in box plots to determine if there is indeed more total clay, smectite, chlorite, and kaolinite in the eastern side of the field (Figure 91). Box plots of point count data from the western and eastern sides of the field were also created to discern any differences in composition or porosity types (Figures 92 and 93).

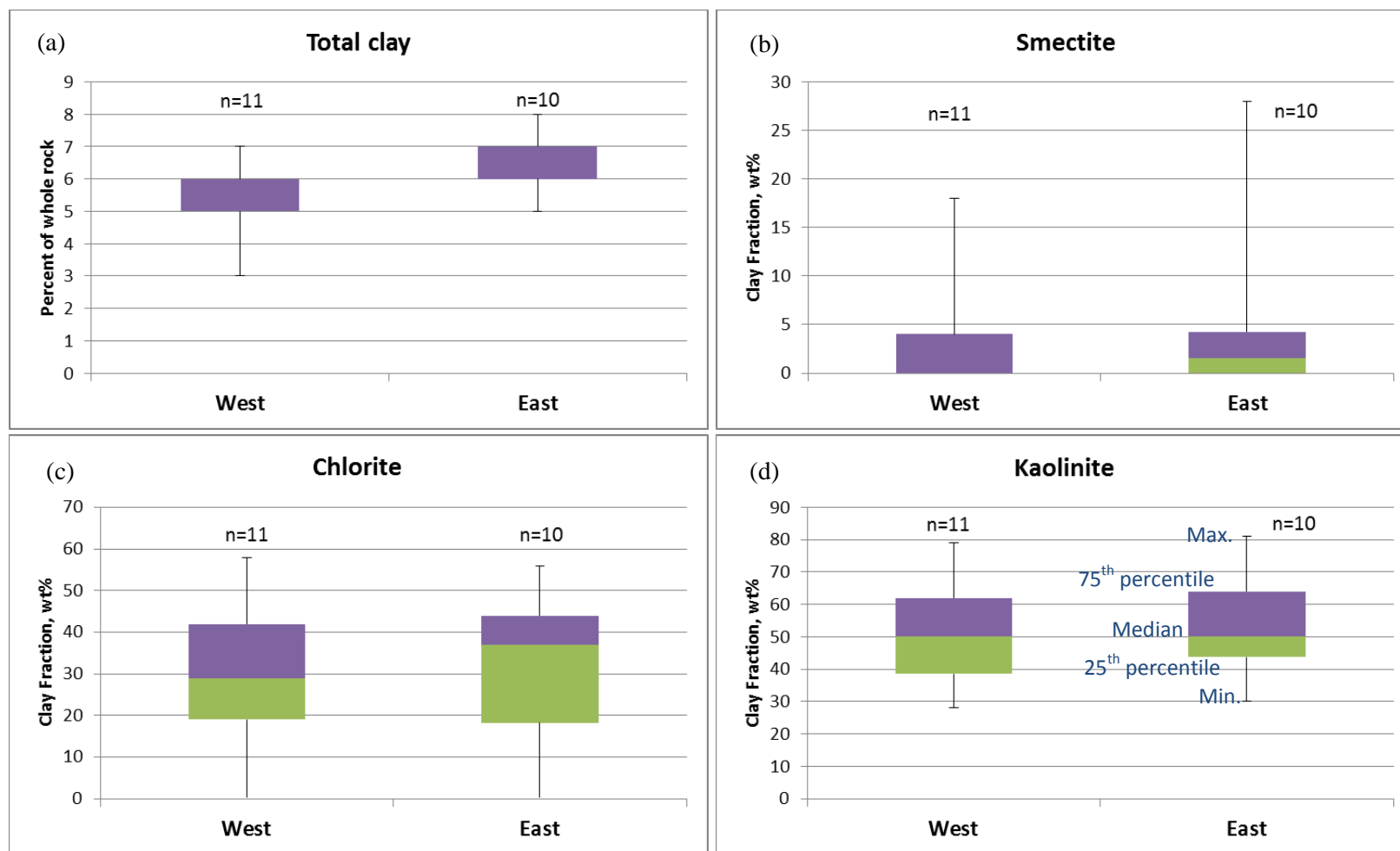


Figure 91. Box plots of XRD data from Munson (1988) and this study. (a) Total clay, in percent of whole rock. (b) Smectite clay fractionation, weight% (c) Chlorite clay fractionation, weight% (d) Kaolinite clay fractionation, weight%.

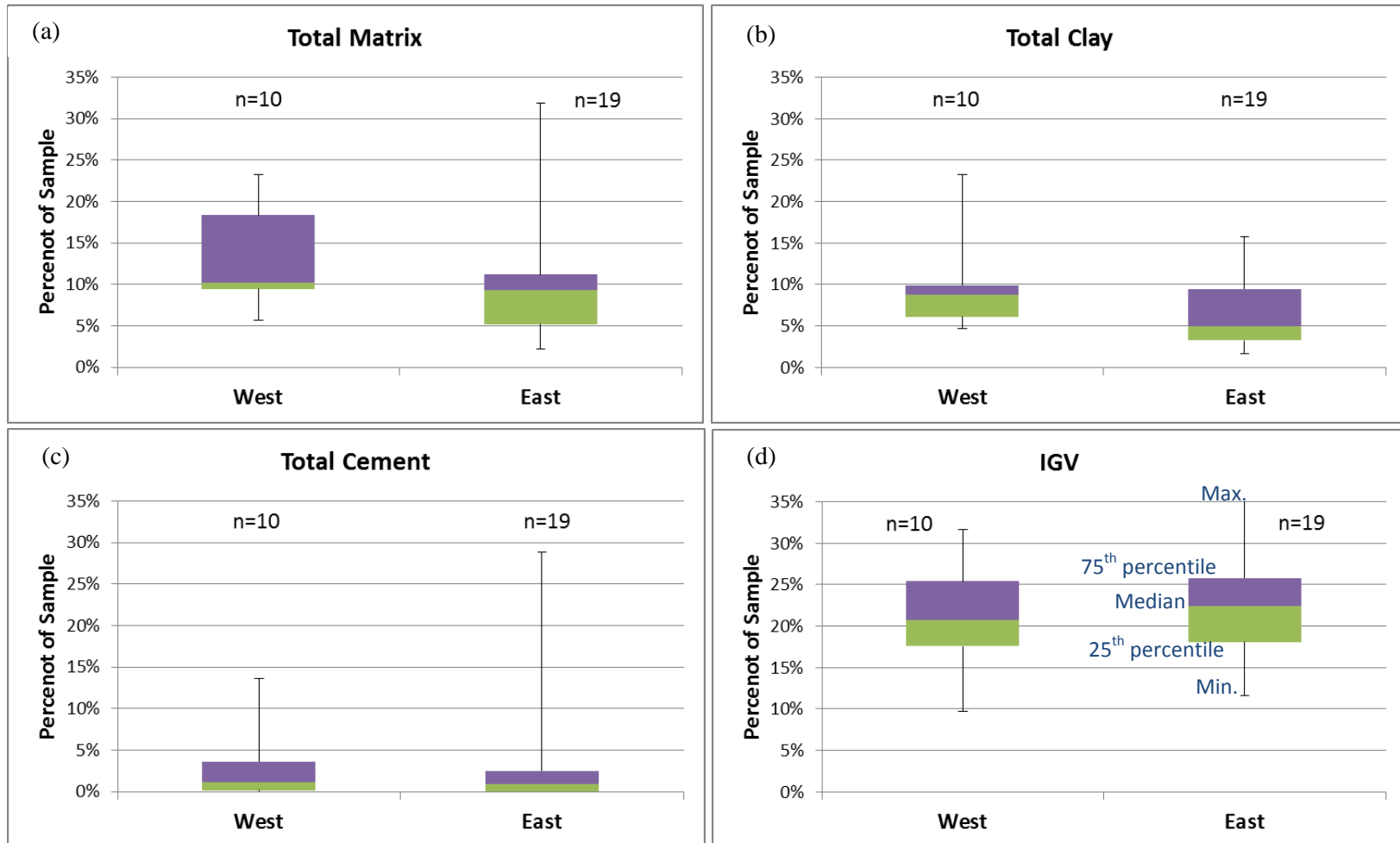


Figure 92. Box plots of select point counting data. (a) Total matrix, (b) Total clay, (c) Total cement, and (d) IGV.

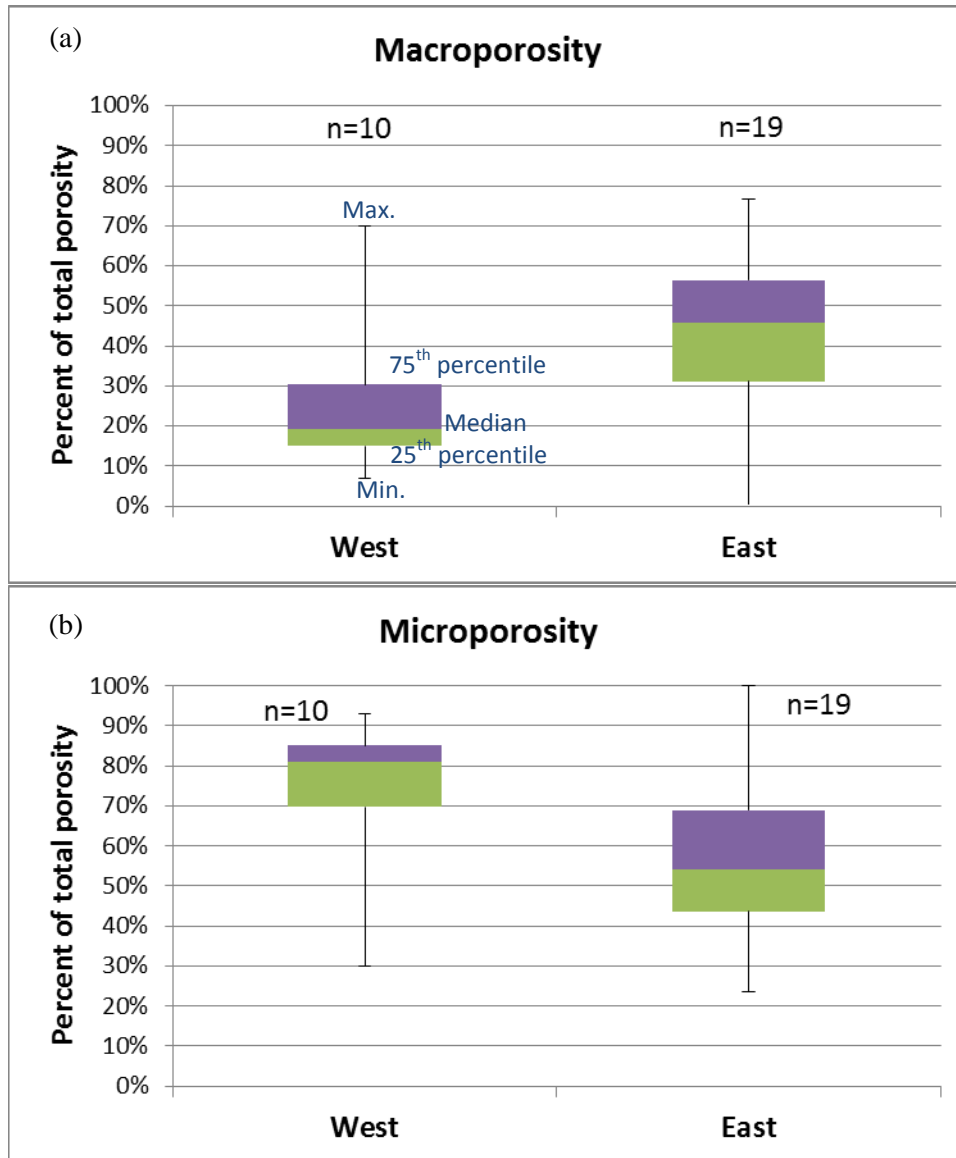


Figure 93. Box plots of porosity point count data. (a) Total macroporosity and (b) Total microporosity.

The box plots of XRD data reveal that there is very little difference in total clay content and clay fractionation of smectite and kaolinite in the eastern and western sides of the field, but slightly more chlorite on the eastern side of the field (Figure 91). The median total clay content for the eastern side of the field is only 1% higher, which is a very small difference. The clay fractionation of smectite and kaolinite is very similar in the western and eastern sides of the field. The median smectite content of the eastern side of the field is only 1.5% higher than the western side of the field, and the median kaolinite content is equal on both sides of the field. Median chlorite content is 8% higher in the eastern side of the field than the western side of the field.

Box plots of the point count data show that there is not much difference in total matrix (clay plus cement), total clay, total cement, or IGV for the western or eastern sides of the field (Figure 92). Median matrix content is 1% higher for samples from the western

side of the field than samples from the eastern side of the field, which is insignificant. The median cement content is equal in samples from both sides of the field. Median clay content is 4% higher in samples from the western side of the field. Median IGV is 1% higher in samples from the eastern side of the field, which is insignificant. Low IGV usually signifies a higher level of compaction, and because the IGV is essentially the same in samples from both sides of the field, it can be concluded that the samples from the eastern side of the field are not more compacted than samples from the western side of the field.

Based on XRD and point count data, the only significant compositional difference in clay, cement, or compaction in samples from the western and eastern sides is the amount of chlorite. The median clay fractionation of chlorite in samples from the eastern side of the field is 8% higher than samples from the western side of the field. The total clay content was measured from XRD analysis and point counting. XRD data indicates that the difference in clay between the two sides of the field is negligible. Point count data indicates that the total clay is 4% higher in samples from the western side of the field; however, that does this not explain why the permeability would be lower in samples from the eastern side of the field. Because XRD analysis is more accurate than point counting, the difference in total clay content between the eastern and western sides of the field is considered to be negligible.

Box plots of total microporosity and total macroporosity were created in order to discern any differences in the porosity types in the western and eastern sides of the field (Figure 93). Box plots of plug porosity indicate that the median plug porosity is only 1.5% higher in samples from the eastern side of the field (Figure 35a), which is insignificant. However, the median percent of macroporosity is 27% higher in sample from the eastern side of the field than the western side of the field (Figure 93a). Macroporosity is generally associated with better permeability than microporosity, so this does not explain why the permeability is lower in samples from the eastern side of the field.

If the total amount of clay, cement, compaction, or certain pore types cannot account for the difference in reservoir quality of the eastern or western sides, then the reason may lie in their distribution. In this study, observations of thin sections were used to create porosity facies based on pore types, pore distribution, and principle controls on permeability (Table 11). The porosities and permeabilities of samples dominated by a single porosity facies were plotted to determine the reservoir quality of each facies. Some facies are present in samples from all wells (B, D, F) whereas other facies are only dominant in samples from the western half of the field (C, E, G, H) or the eastern half (A). The facies found in both sides of the field have a range of reservoir qualities; it is not the case that the western side of the field has “better” porosity facies than the eastern side of the field. However, the fact that different porosity facies are observed in samples from different sides of FWU indicates that the pore types and distribution are heterogeneous across the field.

In summary, the lower permeability of the eastern side of the field is more likely due to a difference in diagenetic factors than depositional ones. This study did not find any differences in depositional processes across the field. The diagenetic processes that had the greatest impact on reducing reservoir quality were the precipitation of authigenic

clay, cementation, and compaction; however, the total amounts of these alterations are similar in both sides of the field. Total porosity is similar in both sides of the field, but samples from the eastern side have more macroporosity than samples from the western side. The porosity facies and distribution are heterogeneous, but this study was not able to quantify them in a way that would explain the lower permeability of the eastern side of the field.

Despite the lower permeability, the eastern side of FWU produced more oil than the western side early in the field's history (Munson, 1988). After waterflooding was implemented, the western side began producing more than the eastern side, which suggests that waterflooding was more successful in the western side of the field than the eastern side. Most of the thin sections examined for this study and porosity and permeability data are from pre-waterflooding samples. The thin sections and porosity and permeability data from well 13-10A, however, are from a newly drilled well, and represent post-waterflooding reservoir properties. Because kaolinite can dislodge and migrate during waterflooding, there is a possibility that waterflooding affected the distribution of the clay (Munson, 1988). At the time of this study, no post-waterflooding thin sections or porosity and permeability data were available from the eastern side of the field. If and when new wells are drilled on the eastern side of the field, new thin sections should be examined for evidence of clay migration and compared to pre-waterflooding samples from the eastern side of the field and pre- and post-waterflooding samples from the western side of the field. This may reveal whether waterflooding affected the two sides of the field differently.

Implications for residual trapping of CO₂

The most important properties of the pore network for residual trapping to occur are the pore-to-throat size ratio, the throat-to-pore coordination number, and the type and degree of nonrandom heterogeneity (Wardlaw and Cassan, 1978). The throat-to-pore coordination number is the number of throats connected to each pore. Because this is a three-dimensional property, and only two-dimensional views of the pore system were available for this study (thin sections, photomicrographs, BSE images), the coordination numbers could not be determined. Therefore, this study focused on the pore-to-throat ratios (PTRs) and heterogeneity of the pore network in order to assess residual trapping potential.

Wardlaw and Cassan (1978) used casts of pore networks to determine average pore size, and compared that to pore-throat data from MICP analysis. Pore casts were not available for this study, so image analysis was used to determine average pore sizes.

The PTRs were calculated for the following: average pore diameter and dominant pore-throat diameter, largest pore diameter and dominant pore-throat diameter, average pore diameter and secondary pore-throat diameter, and largest pore diameter and secondary pore-throat diameter (Table 16). It was not possible to determine the actual pore throat sizes that correspond to specific pores, so average values were compared. As mentioned previously, if pores appear connected in a photomicrograph, ImageJ counts them as a single pore. Because average pore diameters were used, and many of the "pores" measured by ImageJ are actually several connected pores, the pore-to-throat ratios are used only for relative comparison.

Table 16. Pore size-to-throat ratios of pore diameters and pore-throat diameters.

		Pore-to-Throat Ratio			
		Average pore: Dominant throat	Largest pore: Dominant throat	Average pore: Secondary throat	Largest pore: Secondary throat
Sample	Facies				
E1	G	1.71	108.16	3.87	244.94
E2	D	2.24	123.65	-	-
E3	H	1.96	60.90	3.00	93.10
E4	C	0.70	108.74	4.62	715.87
	D	0.89	82.13	5.86	540.71

For all samples, the largest pores have PTRs that are at least an order of magnitude larger than those of the average pore size; therefore, the largest pores may have a higher residual trapping potential than the average-sized pores. However, this is based on the assumption that the largest pores have a pore-throat size that is about the same as the dominant pore-throat size. If the largest pores have much larger pore-throats than the dominant pore-throat size, the PTRs will be smaller.

Based on the data summarized in Table 16, the porosity facies with the highest residual trapping potentials are the C (grain-sized pore dominated) and D (microporous clay dominated) facies. Sample E2, which is dominated by the D porosity facies, has the highest PTRs for both average-sized pores and the largest pore. Sample E2 is not bimodal, so PTRs were only calculated for the dominant pore-throat size.

Sample E4, which has two dominant porosity facies, C and D, has the largest dominant pore-throat diameters and smallest secondary pore-throat diameters. The dominant pore throat size is larger than the average pore size, causing the PTR of the average pores sizes and dominant pore throats to be less than one. As explained in the MICP data section, the pore-throat sizes for sample E4 are strongly bimodal, so the secondary pore-throat sizes probably correspond to the average pore sizes, and the dominant pore-throat sizes probably correspond to the grain-sized pores. Therefore, those are probably the most accurate PTRs for sample E4.

Based on the PTRs of four samples from well 13-10A, the porosity facies that may contribute the most to residual trapping are microporous clay-dominated and grain-sized pores surrounded by microporous clay. When more samples become available, these calculations should be repeated to determine the PTRs of other porosity facies.

The heterogeneity within the Morrow B sandstone will likely create a heterogeneous distribution of residual trapping potential. Saadatpoor et al. (2010) suggest that heterogeneity within capillary pressure controls the path taken by CO₂ within a reservoir. The Morrow B sandstone contains micro-scale heterogeneity within the pore network which controls the distribution of permeability and capillary pressure. Because only a few thin sections were available from each well, it was not possible to quantify this distribution.

CHAPTER 5. CONCLUSIONS

(1) The upper Morrow sandstone reservoir of Farnsworth Unit contains facies that are consistent with the incised valley model of deposition, with regionally extensive lithofacies that fit a basin-wide sequence stratigraphic model. The conglomerate facies was most likely deposited during a sea level lowstand, and the Morrow B sandstone by fluvial processes during transgression. The marine or marine-influenced mudstones above and below the fluvial facies likely represent highstand systems tracts.

(2) Reservoir quality is not controlled by primary textural characteristics, such as grain size and sorting. Rather, it is controlled by secondary, diagenetic processes. The diagenetic processes that had the greatest effect on reservoir quality are dissolution of feldspar and lithics, precipitation of authigenic clay, carbonate and quartz, and compaction.

(3) The paragenetic sequence of the Morrow B sandstone, in order from earliest to latest, is: siderite cementation, quartz overgrowths, feldspar overgrowths, calcite cementation, ankerite cementation, replacement of feldspar by calcite and ankerite, compaction (mechanical and chemical), feldspar dissolution, precipitation of authigenic clay, and hydrocarbon emplacement.

(4) This study did not find substantial geological evidence to explain why the eastern side of the field has a lower average permeability than the western side of the field. Average porosity is similar in both sides of the field, but the micro-scale spatial distribution of porosity is heterogeneous, which may be the reason for lower permeability on the eastern side.

(5) Samples from the Morrow B sandstone were divided into five principle porosity facies and eight subfacies based on pore types, pore distribution, and principle controls on permeability. The significant heterogeneity in pore geometry and size within the Morrow B sandstone will likely result in a heterogeneous distribution of residual trapping of CO₂ within the reservoir.

(6) The pore-to-throat ratios of four samples were calculated to assess their residual trapping potential. The porosity facies with the highest pore-to-throat ratios are microporous clay-dominated and grain-sized pore dominated.

SUGGESTIONS FOR FUTURE WORK

(1) The lithofacies in the FWU are typical of the incised valley model. Well logs and cross sections should be studied further to confirm that the sand body geometry also matches the incised valley model.

(2) The entire core for 13-10A was observed, but only six thin sections from that core were available at the time of this study. Many new thin sections are now available, and should be examined to determine how much porosity and permeability varies foot-by-foot in the core. The spatial distribution of porosity facies should be evaluated both within thin sections and throughout the cored interval of the Morrow B sandstone. Very high permeabilities (>700 md) have been measured in Morrow B core plugs, but no thin sections with permeabilities above 70 md were examined in this study. Understanding how reservoir quality is distributed throughout the Morrow B sandstone and what causes the highest permeabilities could be important for numerical flow modeling.

(3) If and when new wells are drilled on the eastern side of the field, the reservoir sandstone should be compared to pre-waterflooding samples to determine if kaolinite has migrated into pore throats due to EOR activities and could be the cause of the reduced production in the eastern side of the field.

(4) Further work can be done with the MICP data to assess residual trapping potential in a more quantitative manner. Specifically, calculations can be made from the imbibition and drainage curves to estimate the maximum residual nonwetting phase saturation.

REFERENCES

- Al-Shaieb, Z., Puckette, J., and Abdalla, A., 1995, Influence of sea-level fluctuation on reservoir quality of the upper Morrowan sandstones, northwestern shelf of the Anadarko Basin, *in* Hyne, N.J., ed., Sequence stratigraphy of the mid-continent: Tulsa Geological Society Special Publication, no. 4, p. 249-268.
- Al-Shaieb, Z., Puckette, J., 2001, Sequence stratigraphic control on reservoir quality in Morrow sandstone reservoirs, northwestern shelf, Anadarko Basin: Search and Discovery, AAPG/Datapages Inc. electronic journal, no. 10023, <http://www.searchanddiscovery.net/>.
- Blakeney, B.A., Krystinik, L.F., and Downey, A. A., 1990, Reservoir heterogeneity in Morrow valley fills, Stateline trend: Implications for reservoir management and field expansion, *in* Sonnenberg, S. A., et al., eds., Morrow sandstones of southeast Colorado and adjacent areas: Rocky Mountain Association of Geologists, Denver, Colorado, p. 131-142.
- Bachu, S., 2008, CO₂ storage in geological media: Role, means, status and barriers to deployment: Progress in Energy and Combustion Science, no. 34, p. 254-273.
- Cunningham, T. R., 1961, Stratigraphy Oklahoma-Texas Panhandles, p. 45-59 *in* Wagner, R.C., ed., Oil and Gas Fields of the Texas and Oklahoma Panhandles: Panhandle Geological Society, Amarillo, Texas, 264 p.
- Cooperative Research Centre for Greenhouse Gas Technologies (CO2CRC), 2011, Injection and Storage, <http://www.co2crc.com.au/> (accessed June, 2014).
- Curtis, C. D., 1983, A link between aluminum mobility and destruction of secondary porosity: American Association of Petroleum Geologists Bulletin, v. 67, p. 380-384.
- Dalrymple, R. W., Zaitlin, B. A., and Boyd, R., 1992, Estuarine facies models: conceptual basis and stratigraphic implications: Journal of Sedimentary Petrology, v. 62, no. 6, p. 1130-1146.

- DeVries, A., 2005, Sequence stratigraphy and micro-image analysis of the upper Morrow sandstone, Mustang East field, Morton County, Kansas, Master's thesis, Oklahoma State University, Stillwater, Oklahoma, 79 p.
- DOE (Department of Energy), 2012, DOE-sponsored project begins demonstrating CCUS technology in Alabama, <http://energy.gov/fe/articles/doe-sponsored-project-begins-demonstrating-ccus-technology> (accessed June, 2014).
- Ehrlich, R., 1983, Size analysis wears no clothes, or have movements come and gone?: *Journal of Sedimentary Research*, v. 53, no. 1.
- Folk, R. L., 1968, *The Petrology of Sedimentary Rocks*: Austin, Texas, Hemphill's Book Store, 170 p.
- Forgotson, J. M., Statler, A. T., and David, M., 1966, Influence of regional tectonics and local structure on deposition of Morrow Formation in western Anadarko Basin: *AAPG Bulletin*, v. 50, p. 518-532.
- Grove, C., and Jerram, D., 2011, jPOR: An ImageJ macro to quantify total optical porosity from blue-stained thin sections: *Computers & Geosciences*, v. 37, p. 1850-1859.
- Holtz, H.M., 2002, Residual gas saturation to aquifer influx: A calculation method for 3-D computer reservoir model construction. SPE Paper 75502 presented at SPE Gas Technology Symposium, Calgary, Alberta, Canada, 30 April–2 May, 2002.
- IPCC, 2005, IPCC special report on carbon dioxide capture and storage, prepared by Working Group III of the Intergovernmental Panel on Climate Change: Cambridge, United Kingdom and New York, NY, USA, Cambridge University Press, 442 p.
- Krystinik, L.F., and Blakeney, B.A., 1990, Sedimentology of the upper Morrow Formation in eastern Colorado and western Kansas, *in* Sonnenberg, S. A., et al., eds., *Morrow sandstones of southeast Colorado and adjacent areas*: Rocky Mountain Association of Geologists, Denver, Colorado, p. 37-50.
- Li, S., Dong, M., Li, Z., Huang, S., Qing, H., Nickel, E., 2005, Gas breakthrough pressure for hydrocarbon reservoir seal rocks: Implications for the security of long-term CO₂ storage in the Weyburn field: *Geofluids*, v. 5, p. 326–334.
- McKay, R. H., and Noah, J. T., 1996, Integrated perspective of the depositional environment and reservoir geometry, characterization, and performance of the Upper Morrow Buckhaults Sandstone in the Farnsworth Unit, Ochiltree County, Texas: *Oklahoma Geological Survey Circular*, no. 98, p. 101-114

- Mozley, P. S., 1989, Relation between depositional environment and the elemental composition of early diagenetic siderite: *GEOLOGY*, v. 17, p. 704-706.
- Munson, T. W., 1988, Depositional, diagenetic, and production history of the Upper Morrowan Buckhaults Sandstone, Farnsworth Field, Ochiltree County Texas, Master's Thesis, West Texas University, Canyon, Texas, 117 p.
- Munson, T. W., 1989, Depositional, diagenetic, and production history of the Upper Morrowan Buckhaults Sandstone, Farnsworth Field, Ochiltree County, Texas: *Oklahoma City Geological Society, Shale Shaker*, v. 40, no.13, p. 2-20.
- Nelson, P.H., 1994, Permeability-porosity relationships in sedimentary rocks: *The Log Analyst*, v. 35, no. 3, p. 38-62.
- Nelson, P.H., 2009, Pore-throat sizes in sandstones, tight sandstones, and shales: *AAPG Bulletin*, v. 93, no. 3, p. 329-340.
- Puckette, J., Abdalla, A., Rice, A., Al-Shaieb, Z., 1996, The upper Morrow reservoirs: Complex fluvio-deltaic depositional systems, *in* Johnson, K.S., ed., *Deltaic reservoirs in the southern midcontinent, 1993 symposium: Oklahoma Geological Survey Circular*, no. 98, p. 47-84.
- Puckette, J., Al-Shaieb, Z., and Van Evera, E., 2008, Sequence stratigraphy, lithofacies, and reservoir quality, upper Morrow sandstones, northwestern shelf, Anadarko Basin, *in* Andrews, R. D., ed., *Morrow and Springer in the southern midcontinent, 2005 symposium: Oklahoma Geological Survey Circular*, no. 111, p. 81-97.
- Rascoe, B., Jr., and Adler, F., 1983, Permo-Carboniferous hydrocarbon accumulations, Mid-Continent, USA: *AAPG Bulletin*, v. 67, p. 979-1001.
- Rasband, W.S., 2008, ImageJ, U.S. National Institutes of Health, Bethesda, Maryland, <http://rsb.info.nih.gov/ij/>
- Saadatpoor, E., Bryant, S. L., Sepehrnoori, K., 2010, New trapping mechanism in carbon sequestration: *Transport in Porous Media*, v. 82, p. 3-17.
- Schmidt, V., and McDonald, D., 1979, Texture and recognition of secondary porosity in sandstones: *SEPM Special Publication*, no. 26, p. 209-255.
- Sonnenberg, S.A., Shannon, L.T., Rader, K., and Von Drehle, W.F., 1990, Regional structure and stratigraphy of the Morrowan Series, southeastern Colorado and adjacent areas, *in* Sonnenberg, S. A., et al., eds., *Morrow sandstones of southeast Colorado and adjacent areas: Rocky Mountain Association of Geologists*, Denver, Colorado, p. 1-8.

- Southwestern Partnership for Carbon Sequestration, 2012, The 2012 carbon sequestration atlas of the United States and Canada, p. 82-91.
- Southwest Partnership, 2012, <http://www.southwestcarbonpartnership.org/> (accessed July, 2014).
- Swanson, D., 1979, Deltaic deposits in the Pennsylvanian upper Morrow Formation in the Anadarko Basin, *in* Pennsylvanian sandstones of the mid-continent: Tulsa Geological Society special publication, no. 1, p. 115-168.
- Wardlaw, N., and Cassan, J., 1978, Estimation of recovery efficiency by visual observation of pore systems in reservoir rocks: Bulletin of Canadian Petroleum Geology, v.26, no.4, p. 572-585.
- Washburn, E. W., 1921, The dynamics of capillary flow: Physical Review, v. 17, no. 3, p. 273-283.
- Wheeler, D., Scott, A., Coringrato, V., Devine, P., 1990, Stratigraphy and depositional history of the Morrow Formation, southeast Colorado and southwest Kansas *in* Sonnenberg, S. A., et al., eds., Morrow sandstones of southeast Colorado and adjacent areas: Rocky Mountain Association of Geologists, Denver, Colorado, p. 9-35.
- Wilson, M. D., and Pittman, E. D., 1977, Authigenic clays in sandstones: Recognition and influence on reservoir properties and paleoenvironmental analysis: Journal of Sedimentary Petrology, v. 47, no. 1, p. 3-31.

APPENDIX A. STRATIGRAPHIC COLUMNS

Legend

Symbols:

-  stylolite
-  minor stylolite
-  clay seam
-  mudstone intraclasts
-  fossil
-  plant fragment
-  fracture
-  siderite concretion
-  coal intraclast
-  pyrite
-  burrows
-  fossil hash
-  thin section sample location

Lithology:

- | | | | |
|--|-------------------------------|--|--------------------------|
|  | conglomerate |  | crossbedded conglomerate |
|  | massive sandstone |  | crossbedded sandstone |
|  | horizontally bedded sandstone |  | mudstone |
|  | calcareous siltstone |  | calcareous mudstone |
|  | coal |  | interval missing |

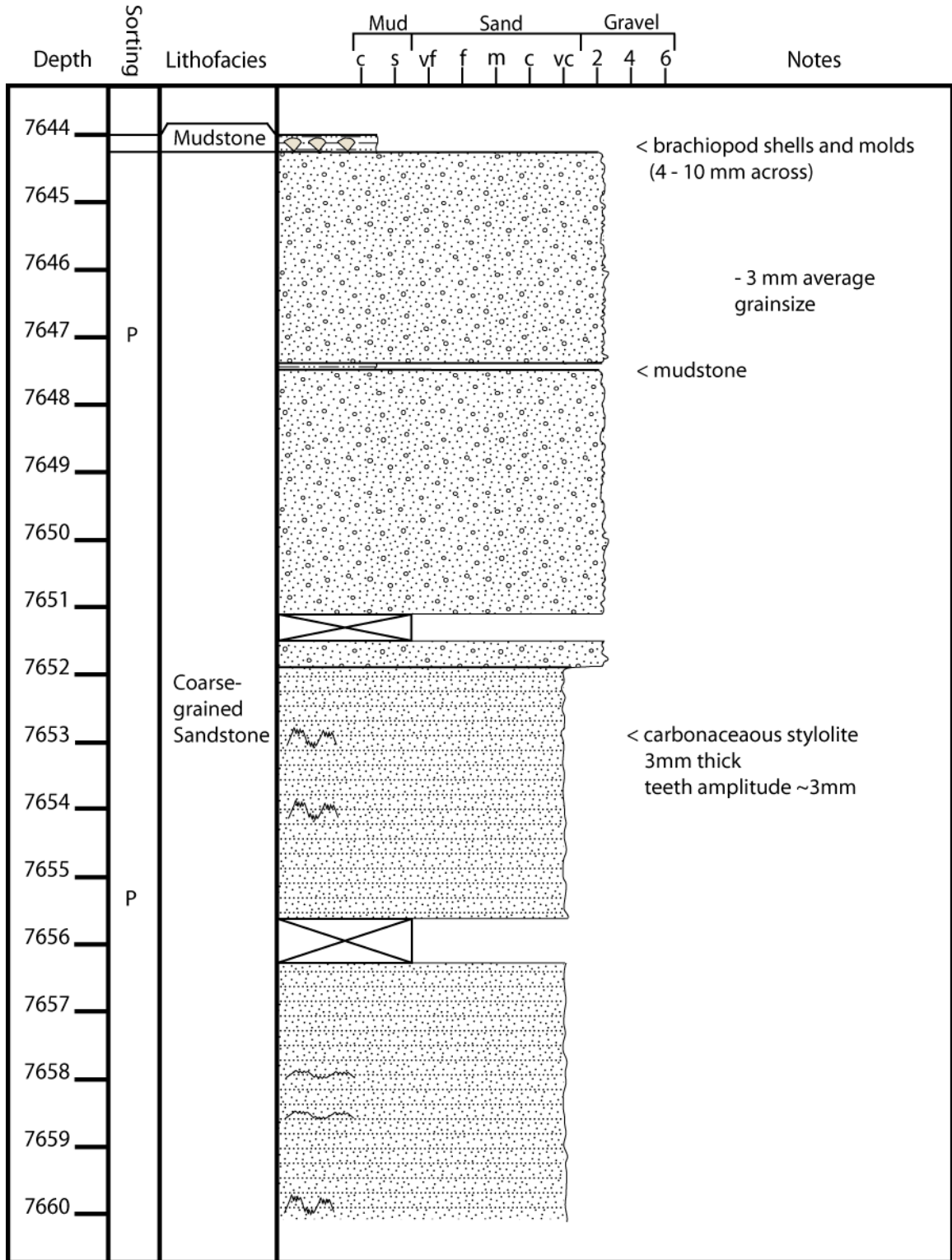
Sorting:

- W = Well
- M = Moderate
- P = Poor

Grain size:

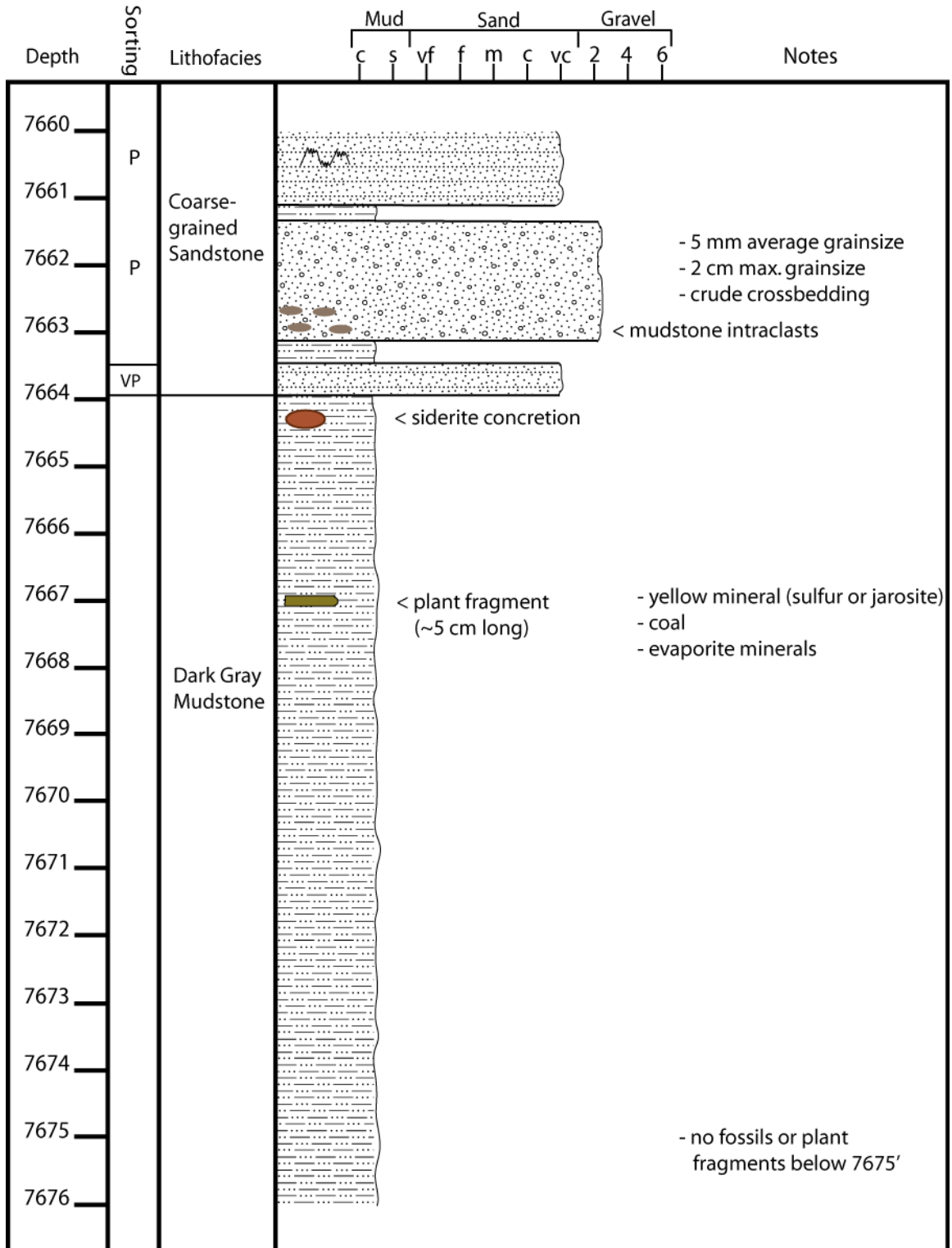
- | | |
|-------------------------|-------------------|
| vcL = very coarse lower | cL = coarse lower |
| vcU = very coarse upper | mL = medium lower |
| cU = coarse upper | fU = fine upper |

Well #8-5



Well #8-5

(Continued)

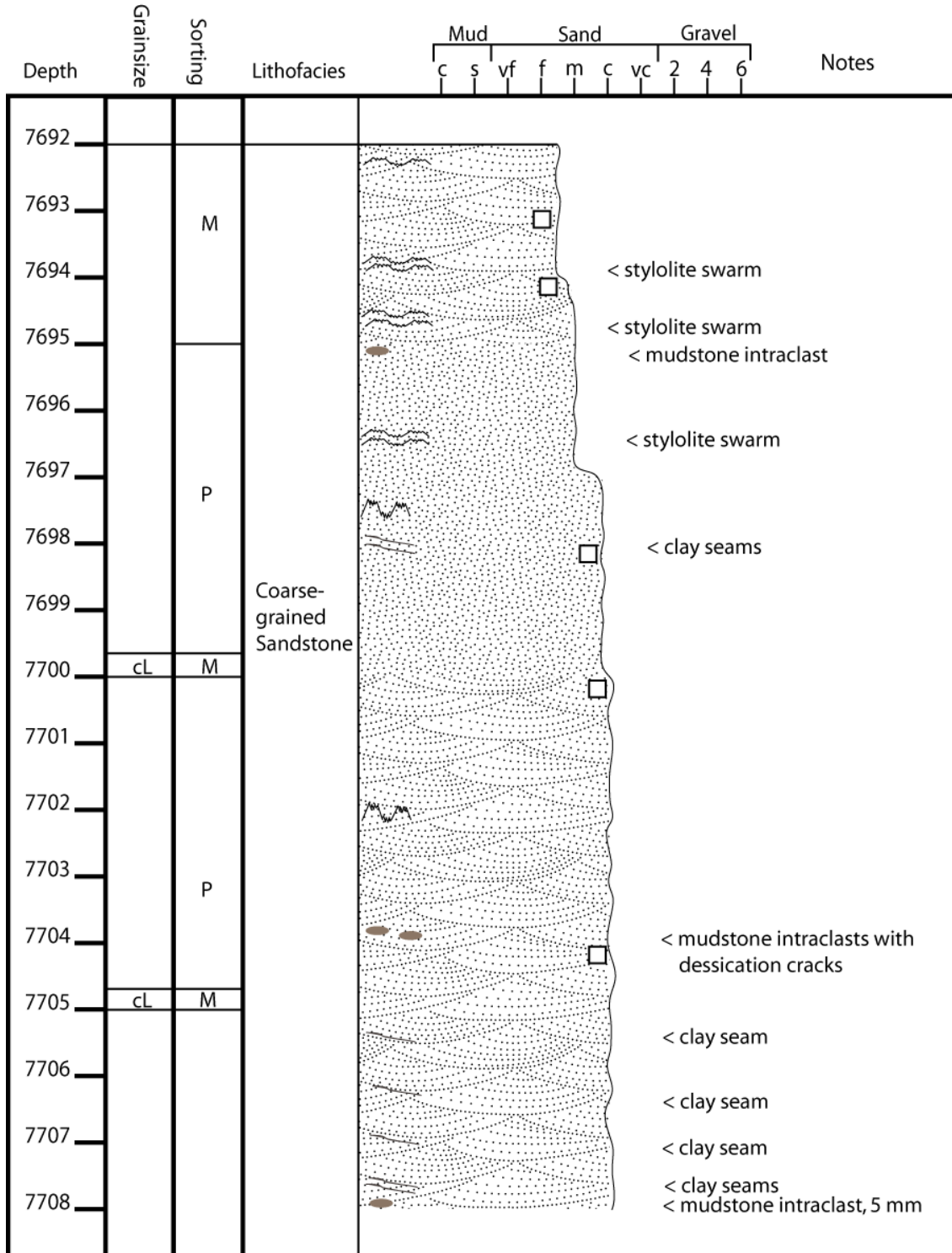


Well #8-5

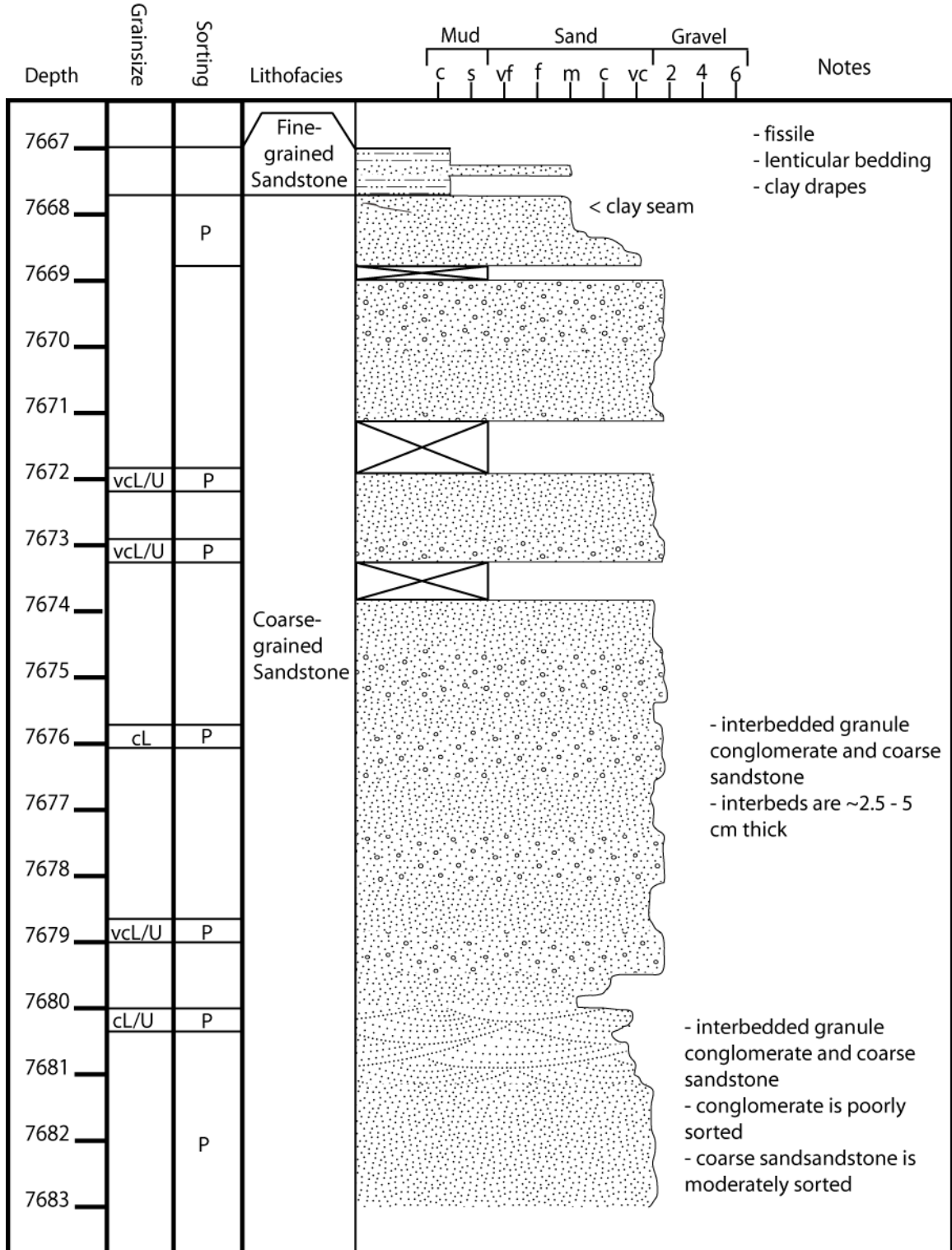
(Continued)

Depth	Sorting	Lithofacies	Mud			Sand			Gravel			Notes
			c	s	vf	f	m	c	vc	2	4	
7676												
7677												
7678												
7679												
7680												
7681												
7682												
7683												
7684		Dark Gray Mudstone										- homogenous - abundant slicken features
7685												
7686												
7687												
7688												
7689												
7690												
7691												
7692												

Well #9-8

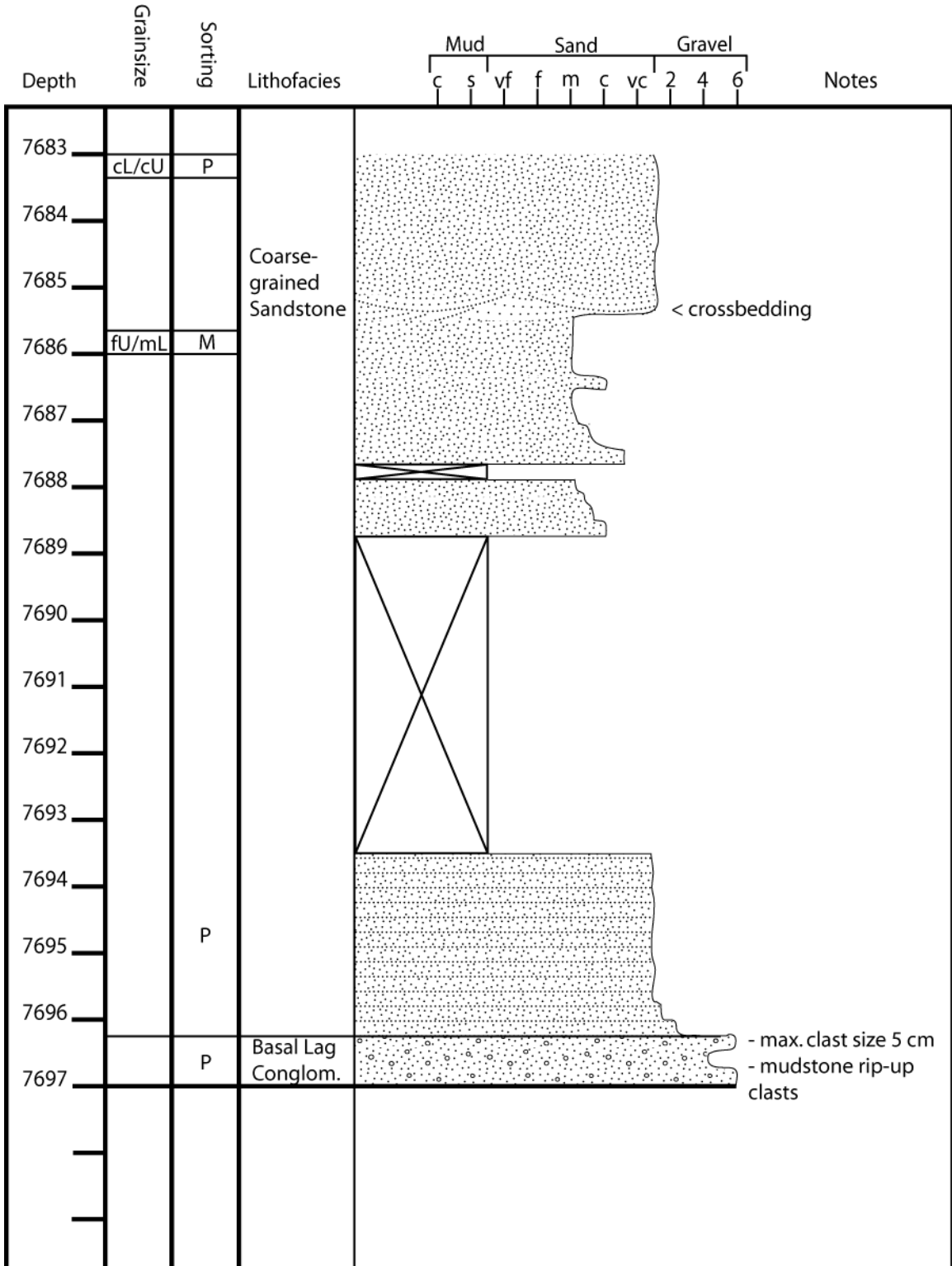


Well #13-10

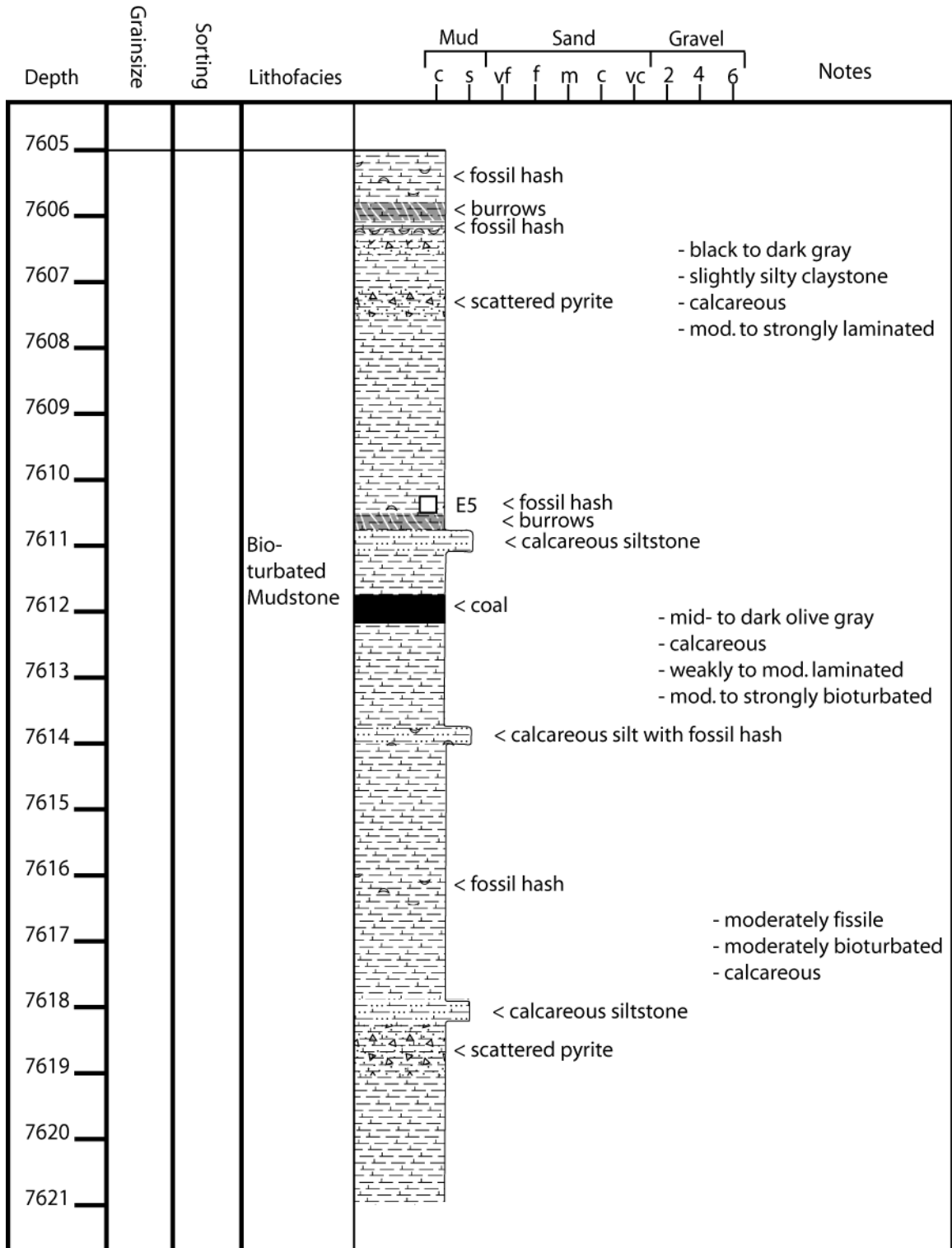


Well #13-10

(Continued)

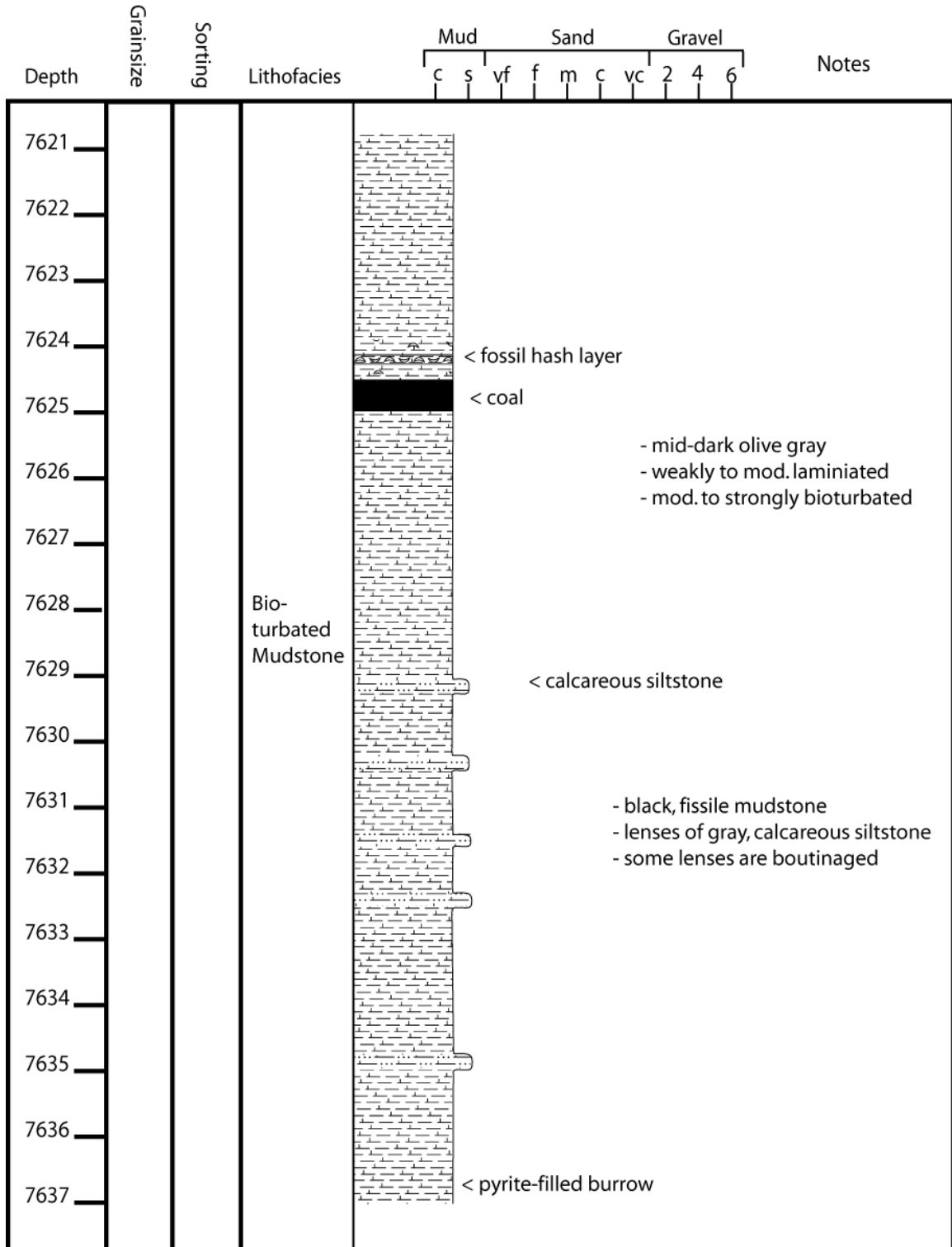


Well #13-10A



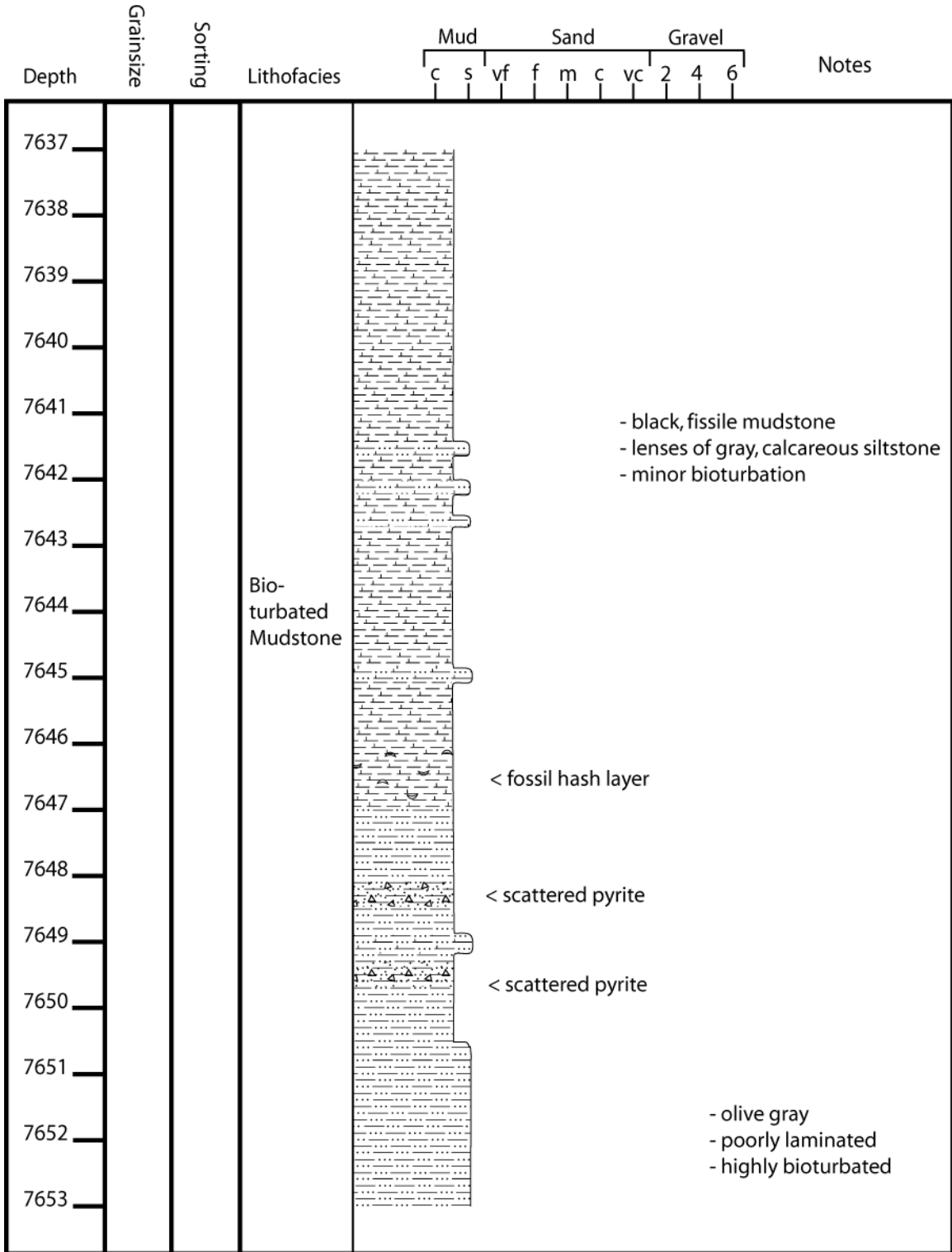
Well #13-10A

(Continued)



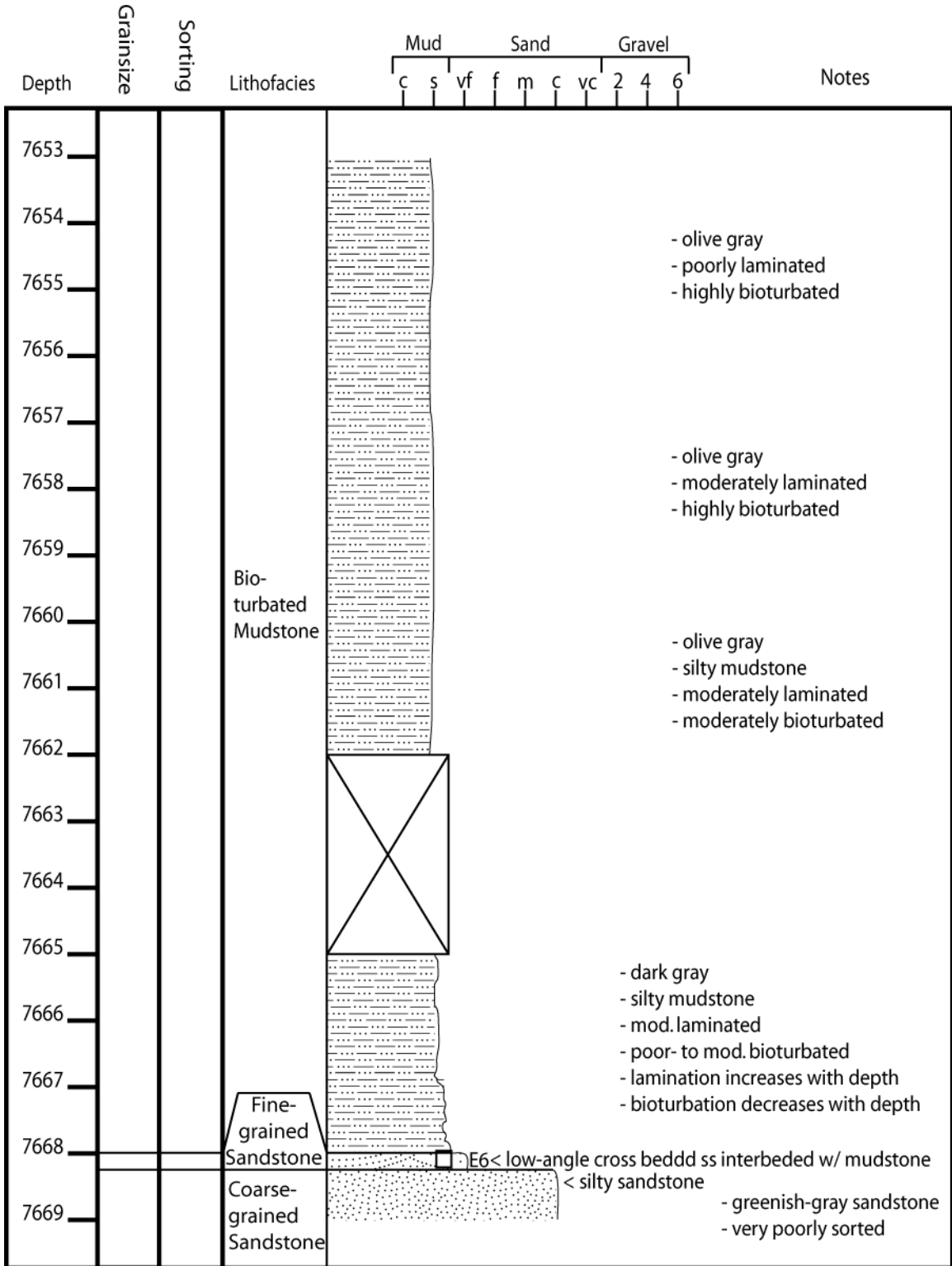
Well #13-10A

(Continued)



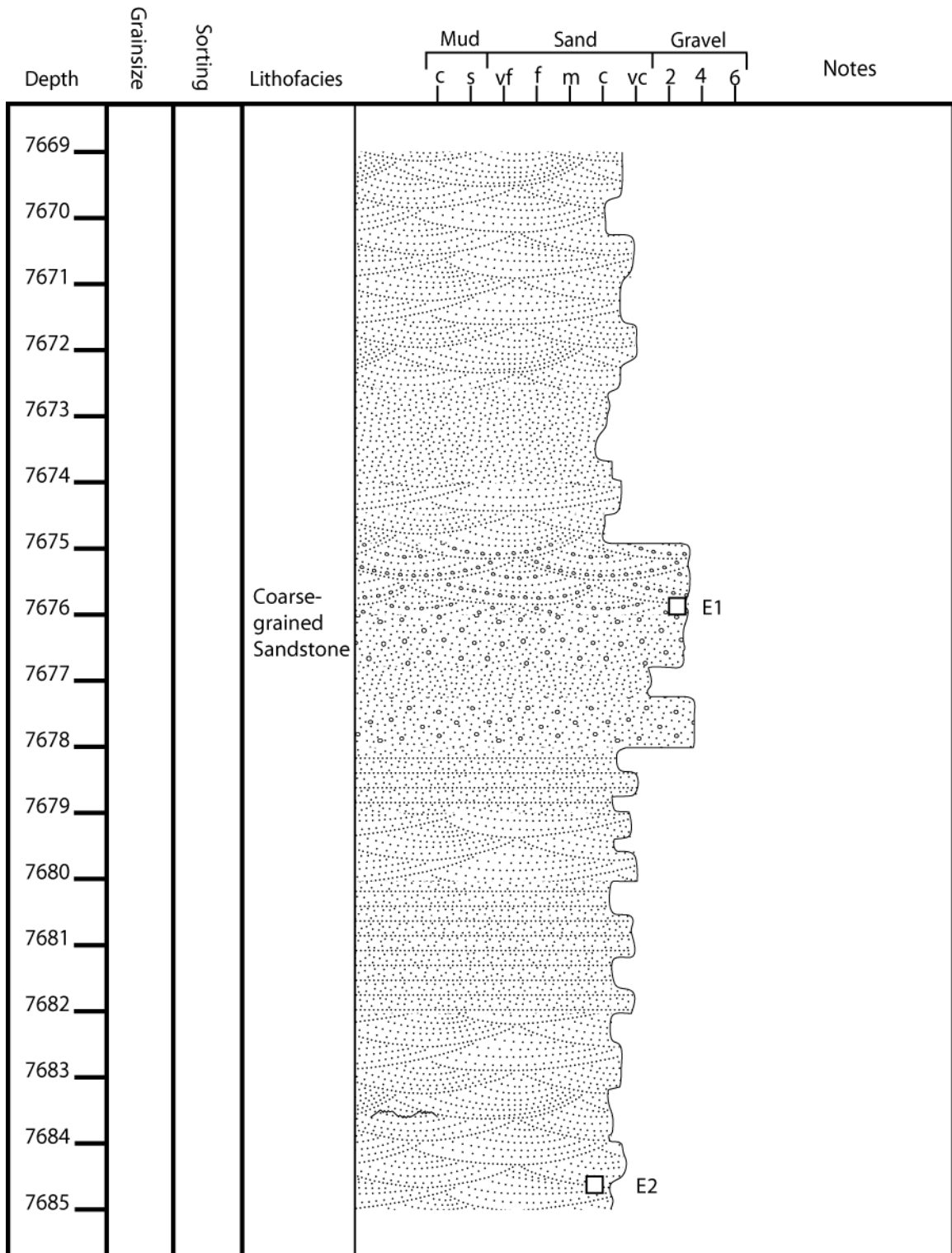
Well #13-10A

(Continued)



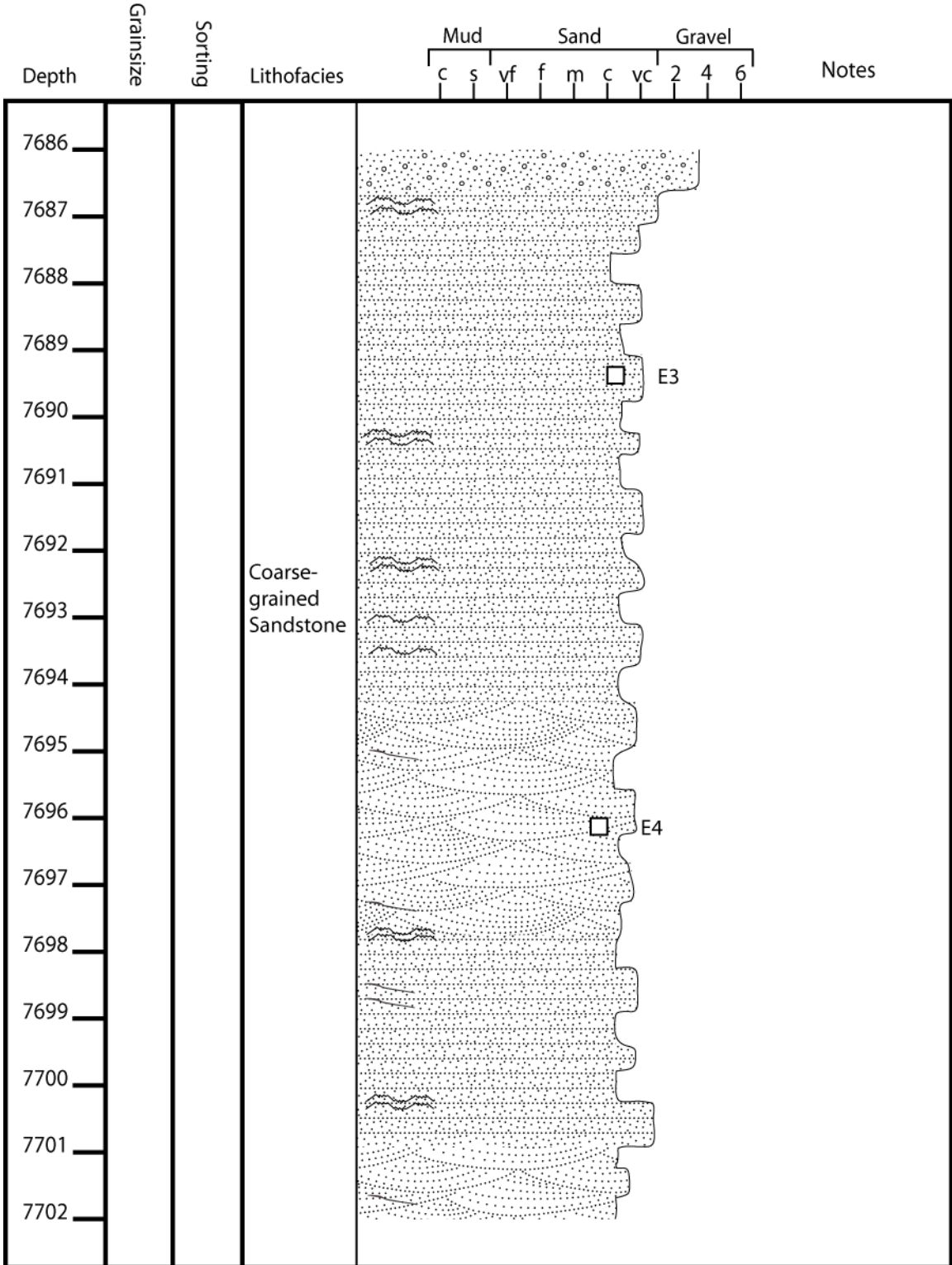
Well #13-10A

(Continued)



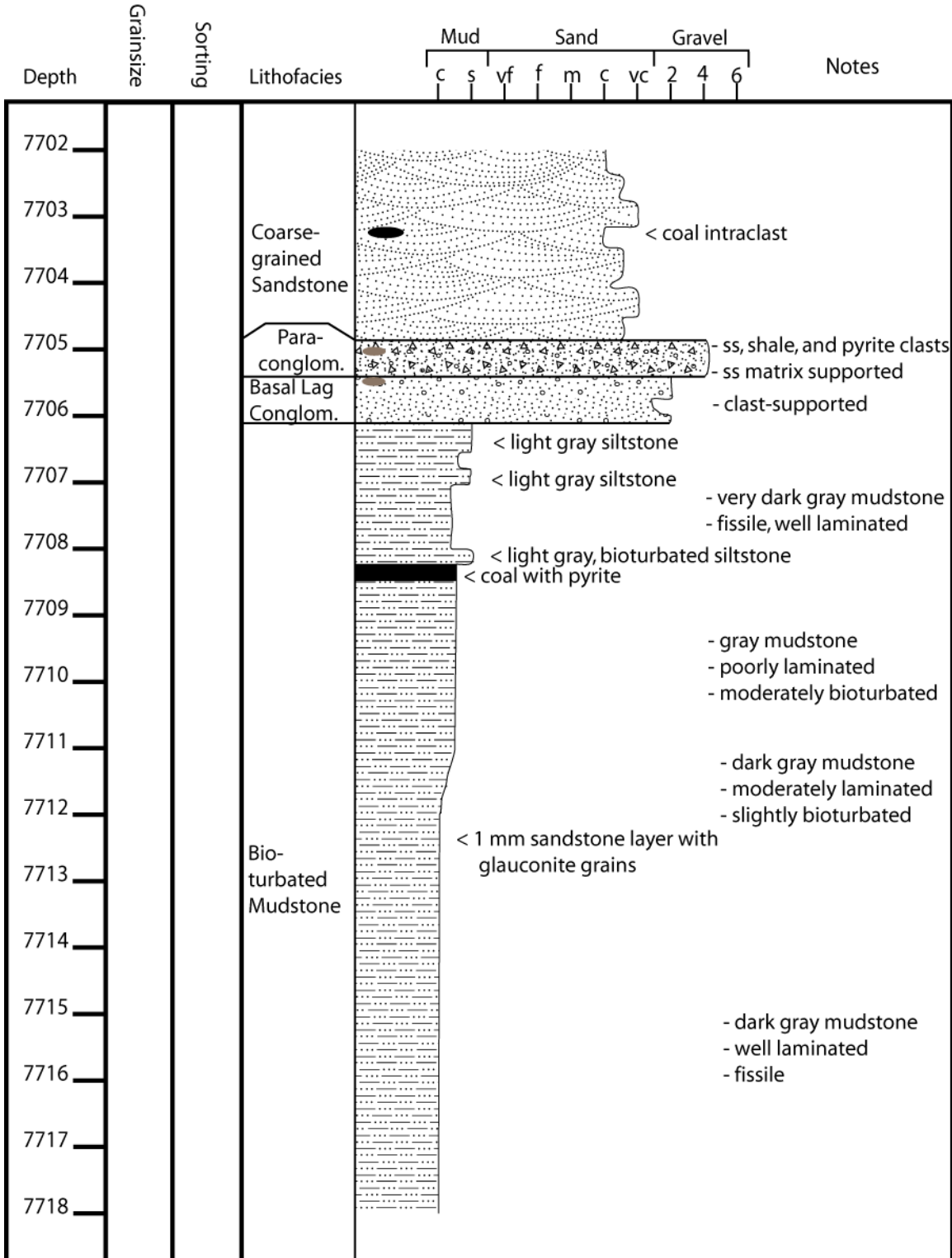
Well #13-10A

(Continued)



Well #13-10A

(Continued)

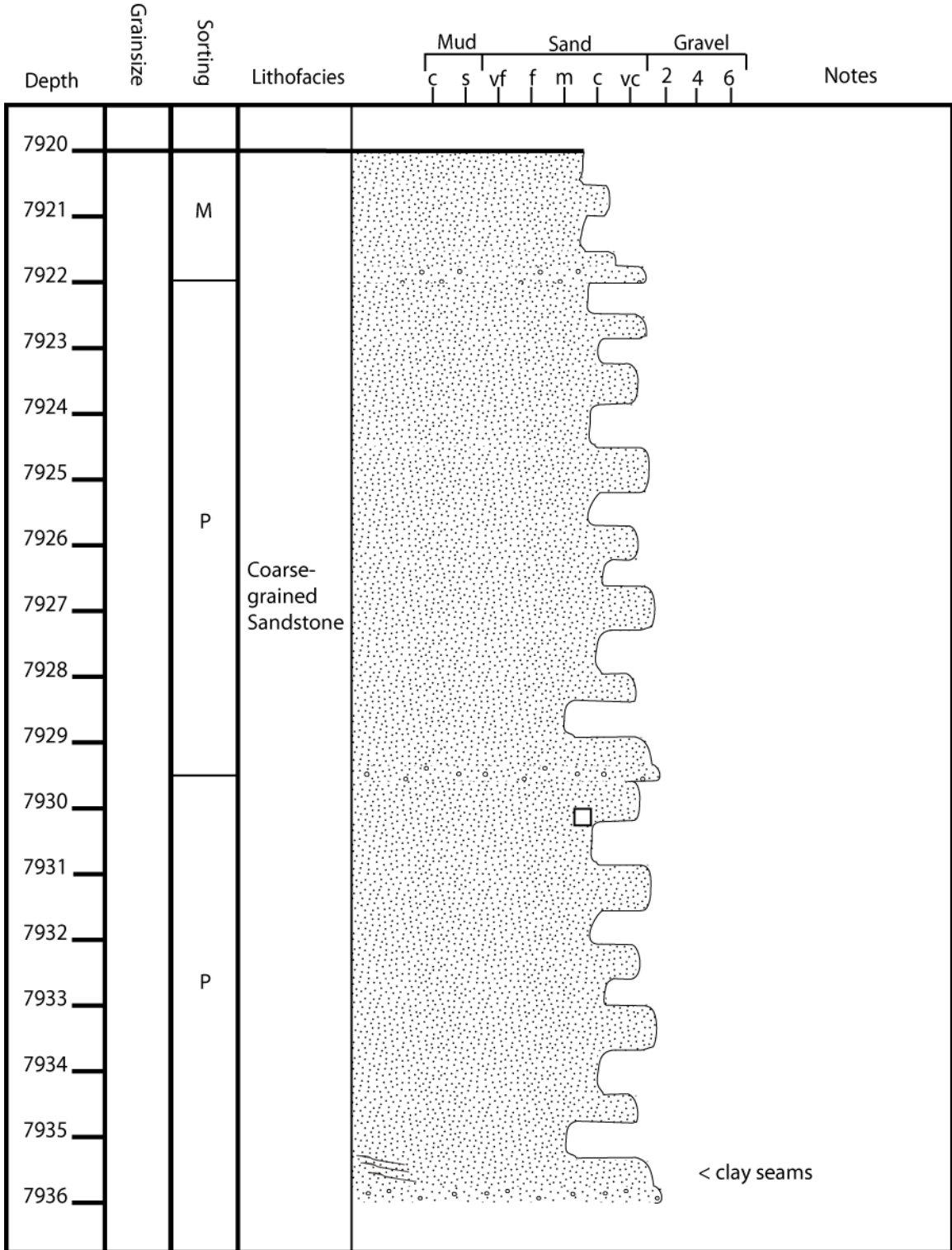


Well #13-10A

(Continued)

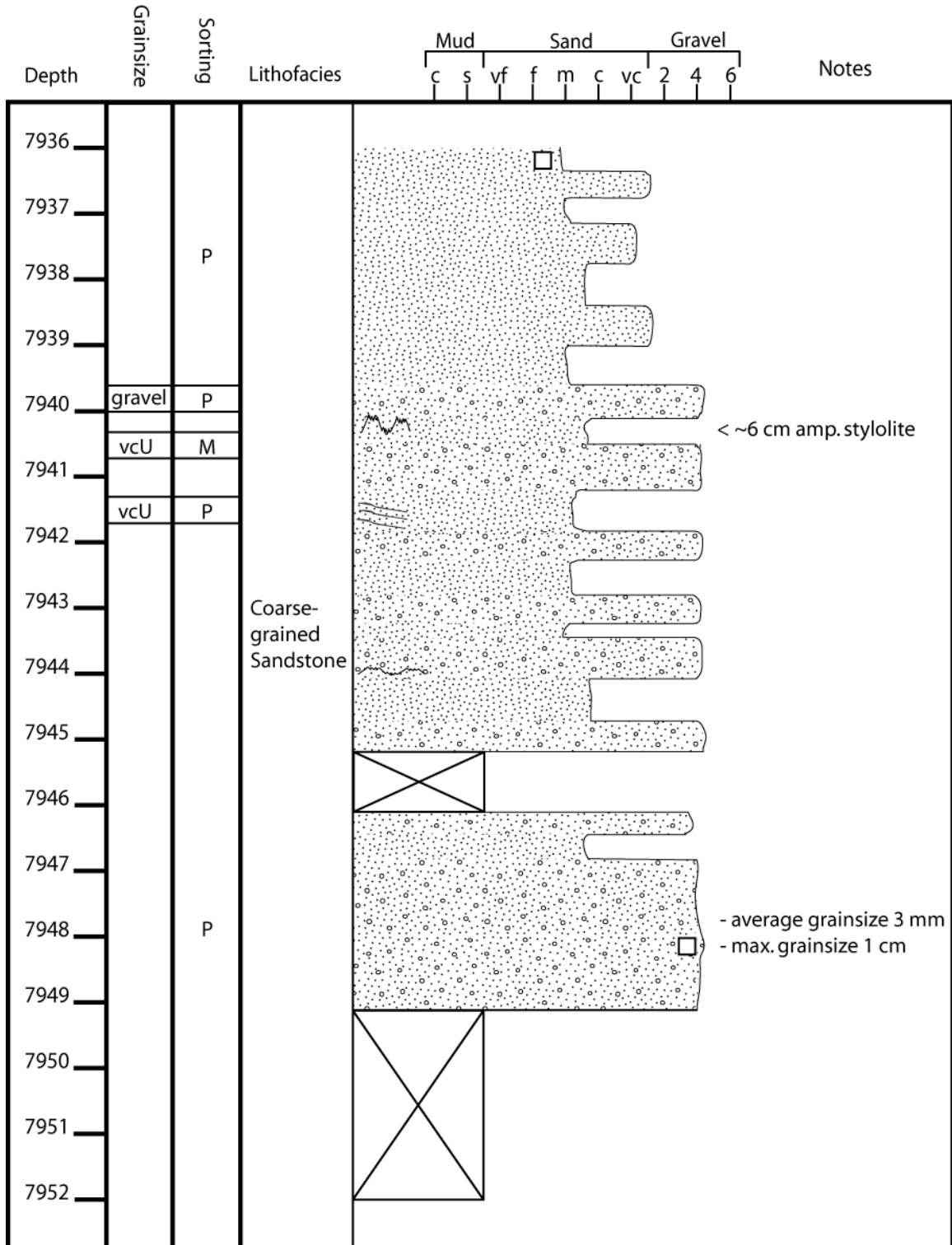
Depth	Grainsize	Sorting	Lithofacies	Mud			Sand			Gravel			Notes
				c	s	vf	f	m	c	vc	2	4	
7718													
7719													
7720													- dark gray mudstone - well laminated - fissile
7721													
7722			Bio-turbated Mudstone										
7723													- olive gray mudstone - poorly laminated - moderately bioturbated
7724													
7725													
7726													- dark gray mudstone - well laminated - fissile

Well #32-2

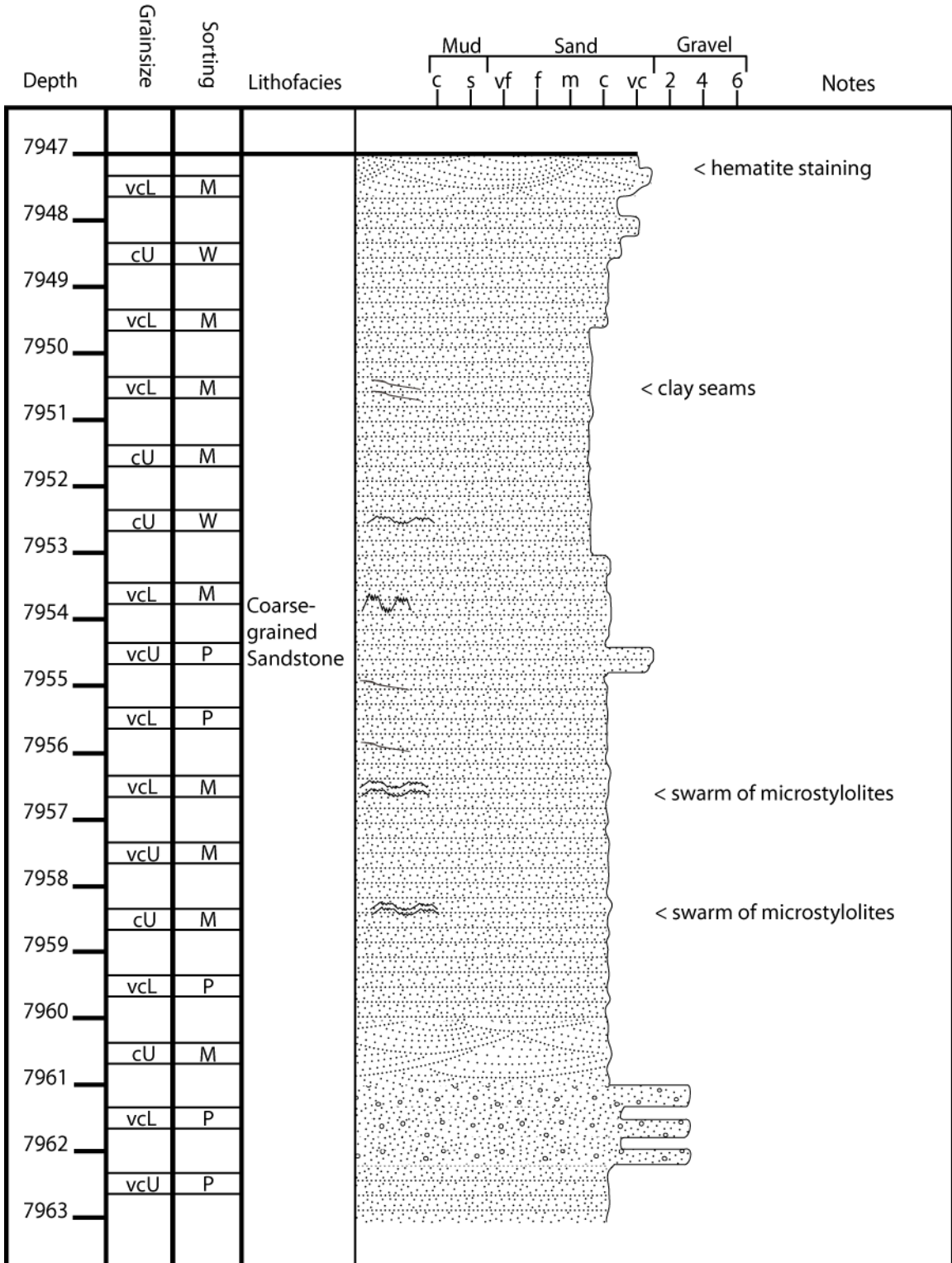


Well #32-2

(Continued)



Well #32-6



Well #32-6

(Continued)

Depth	Grainsize	Sorting	Lithofacies	Mud			Sand			Gravel			Notes			
				c	s	vf	f	m	c	vc	2	4		6		
7963			Coarse-grained Sandstone													
	vcU	P														
7964																
	cU	M														
7965																
	vcL	P														
7966																
	cL	W														< hematite staining
7967																
	cL	W														
7968																
	cL	W														
7969																
	vcL	M														< stylolite swarm
7970																
	vcU	P														
7971																
	vcU	P														
7972																
	cU	M														- cm-scale rhythmites, alternating coarser and finer grains
7973																
	gravel	P	- hematite cement mostly in finer-grained layers													
7974																
	cU	M	- finer-grained sets are thicker than coarser grained sets													
7975																
	cU	M														
7976																
	vcL	M	< well laminated, fissile mudstone													
7977																
	cL	P														
7978																
	vcL	P	< well laminated mudstone, fossil fragment (ostracod?)													
7979																

Well #32-6

(Continued)

Depth	Grainsize	Sorting	Lithofacies	Mud			Sand				Gravel			Notes
				c	s	vf	f	m	c	vc	2	4	6	
7979			Coarse-grained Sandstone											- over-steep crossbedding - cm-scale rhythmites
7980	vcL	P												< clay seams, parallel to crossbeds
7981	vcL	P												< stylolite swarm
7982	vcU	P												
7983	gravel	P												
7984	vcL	P												
7985	vcL	P												
7986	vcU	P												
7987	vcL	M												
7988	vcL	M												
7989	gravel	P												
7990	vcL	P												
7991	cU	M												
7992	vcL	P												
7993	vcL	P												
7994	vcU	P												
7995	vcL	P												

Well #32-6

(Continued)

Depth	Grainsize	Sorting	Lithofacies	Mud			Sand			Gravel			Notes
				c	s	vf	f	m	c	vc	2	4	
7995													
	vcL	P											
7996													
	vcU	P											
7997			Coarse-grained Sandstone										
	vcU	P											
7998													
	vcU	P											
7999		P	Conglom.										< mudstone intraclasts
8000			Dark Gray Mudstone										< siderite concretion - some slickensided surfaces
8001													

APPENDIX B. INVENTORY OF THIN SECTIONS AND SAMPLE ANALYSES

Well	Label	Depth	Rock Type	P&P	300-pt count	100-pt count	XRD	Microprobe	MICP
32-3	2-3-32	7987	Sandstone		X	VE			
32-3	1-3-32	7983	Sandstone		X	X			
32-2	4-B-2-3	7957	Sandstone		X	X			
32-2	3-B-2-3	7948	Sandstone	X	X	X			
32-2	2-B-2-3	7936	Sandstone	X	X	X			
32-2	1-B-2-3	7930	Sandstone	X	X	X			
42-1	5-1-56	8022	Sandstone	X	X	X			
42-1	4-1-56	8028	Sandstone	X	X	VE			
42-1	3-1-56	8015.5	Sandstone	X	X	VE			
42-1	2-1-56	8010	Sandstone	X	X	X			
42-1	1-1-56	8005	Sandstone	X	X	X			
32-1	4-C-1-32	7983	Sandstone	X	X	X			
32-1	3-C-1-32	7945.5	Sandstone		X	VE			
32-1	2-C-1-32	7980	Sandstone	X	X	VE			
32-1	1-C-1-32	7970	Sandstone	X	X	X			
9-8	6-9-8	7700	Sandstone	X	X	X			
9-8	5-9-8	7709	Sandstone	X	X	VE			
9-8	4-9-8	7704	Sandstone	X	X	X			
9-8	3-9-8	7698	Sandstone	X	X	X			
9-8	2-9-8	7694	Sandstone	X	X	VE			
9-8	1-9-8	7693	Sandstone	X	X	VE			
33-3	4-B-3-3	7943.2	Sandstone		X	X			
33-3	3-B-3-3	7958	Sandstone		X	VE			
33-3	2-B-3-3	7948.5	Sandstone		X	X			
33-3	1-B-3-3	7934	Sandstone		X	X			
13-10A	E1	7675.90	Sandstone	X	X	VE	X	X	X
13-10A	E2	7684.75	Sandstone	X	X	VE	X	X	X
13-10A	E3	7686.40	Sandstone	X	X	VE	X	X	X
13-10A	E4	7696.25	Sandstone	X	X	X	X	X	X
13-10A	E5	7610.40	Mudstone				X		X
13-10A	E6	7668.10	Sandstone	X	X		X		X
P&P = Porosity and Permeability Routine Plug Analysis									
VE = Visually Estimated									

APPENDIX C. X-RAY DIFFRACTION (XRD) METHODS



TerraTek X-ray Diffraction Lab, Salt Lake City, Utah USA

General X-ray Diffraction (XRD) Procedures (2013):

Semi-quantitative XRD Analysis of Bulk Samples: Representative splits of the selected bulk samples are ground using McCrone micronizing mills and loaded into aluminum sample holders. The powdered samples are analyzed with a Rigaku Ultima III or Bruker D8 Advance X-ray diffractometer from 2 to 66 degrees two-theta (2θ) using Cu K-alpha radiation and various slit and filter geometries. The raw data is interpreted using JADE software which identifies and quantifies the mineralogy based on Whole Pattern Fitting and Rietveld Refinement methods. This analysis yields semi-quantitative analysis of the whole rock and best characterizes overall mineralogy and amount of clay in the bulk sample.

The percent expandability is the total amount of swelling clay in the whole rock sample and is determined from amount of discrete smectite and interlayered smectite in mixed-layer clays and how much of these clays are in the whole rock sample. For example, a bulk sample with 25 percent mixed-layer illite-smectite which is composed of 20 percent interlayered smectite is approximately 5 percent expandable.

Semi-quantitative XRD Analysis of Clay Mineralogy: Bulk samples are crushed and disaggregated to obtain a sample less than 4 microns, decanted and centrifuged. Resulting slurries are mounted on glass slides as clay smears, and scanned after air-drying and vapor glycolation treatments. Clay minerals are identified and their approximate weight percentages are determined by comparison with mixtures of standard clay minerals in known percentages. XRD analysis of the clay size fraction yields the relative abundance of the clay minerals and determines the amount of expandability (amount of swelling clay) in the mixed-layer clays. The amount of interlayered smectite (swelling clay) in mixed-layer layers is used to determine the percent expandability of whole rock samples.

For more information, please contact:

*Susan Juch Lutz
TerraTek, A Schlumberger Company
1935 S. Fremont Drive
Salt Lake City, Utah 84104
801-584-2474
SLutz@slb.com*

APPENDIX D. ELECTRON MICROPROBE DATA

Carb20, wt% oxide																	
Formula	Comment	CO2	SiO2	SO2	MgO	CaO	MnO	FeO	SrO	BaO	Na2O	Total	X	Y	Z	Date	Geo Specie
9 / 1 .	CaCO3-01	40.04	0.03	0.01	0.01	59.79	0.08	0.02	0.00	0.02	0.00	100.00	7200	-3503	51	4/23/2014 12:46	Carbonate (on the basis of 6 O)
10 / 1 .	CaCO3-02	39.98	0.05	0.01	0.00	59.78	0.11	0.02	0.04	0.00	0.00	99.99	7209	-3487	52	4/23/2014 12:51	Carbonate (on the basis of 6 O)
11 / 1 .	CaCO3-03	40.48	0.03	0.01	0.03	59.37	0.08	0.00	0.00	0.00	0.00	100.00	7213	-3471	51	4/23/2014 12:55	Carbonate (on the basis of 6 O)
12 / 1 .	CaCO3-04	39.76	0.05	0.00	0.00	60.03	0.13	0.00	0.03	0.00	0.01	100.01	7220	-3452	52	4/23/2014 13:00	Carbonate (on the basis of 6 O)
13 / 1 .	FeCO3-01	38.42	0.06	0.00	0.12	0.01	3.12	58.23	0.02	0.00	0.01	99.99	9451	-5862	48	4/23/2014 13:05	Carbonate (on the basis of 6 O)
14 / 1 .	FeCO3-02	38.20	0.07	0.03	0.12	0.01	3.09	58.47	0.00	0.00	0.01	100.00	9468	-5838	48	4/23/2014 13:10	Carbonate (on the basis of 6 O)
15 / 1 .	FeCO3-03	38.67	0.08	0.00	0.13	0.02	3.13	57.95	0.01	0.00	0.00	99.99	9476	-5823	47	4/23/2014 13:15	Carbonate (on the basis of 6 O)
16 / 1 .	FeCO3-04	38.47	0.10	0.00	0.13	0.02	3.15	58.04	0.04	0.04	0.01	100.00	9494	-5810	48	4/23/2014 13:19	Carbonate (on the basis of 6 O)
17 / 1 .	MgCO3-01	46.51	0.05	0.01	22.49	30.84	0.02	0.04	0.02	0.00	0.01	99.99	5428	453	49	4/23/2014 13:24	Carbonate (on the basis of 6 O)
18 / 1 .	MgCO3-02	47.29	0.03	0.00	22.13	30.38	0.00	0.08	0.04	0.04	0.01	100.00	5447	470	49	4/23/2014 13:29	Carbonate (on the basis of 6 O)
19 / 1 .	MgCO3-03	46.85	0.03	0.00	22.36	30.62	0.00	0.09	0.04	0.00	0.00	99.99	5443	489	49	4/23/2014 13:34	Carbonate (on the basis of 6 O)
20 / 1 .	MgCO3-04	47.22	0.04	0.01	22.31	30.31	0.00	0.09	0.02	0.00	0.00	100.00	5440	507	49	4/23/2014 13:39	Carbonate (on the basis of 6 O)
21 / 1 .	E1-01	44.48	0.03	0.02	8.74	31.41	1.10	14.16	0.01	0.04	0.02	100.01	9950	27703	79	4/23/2014 13:43	Carbonate (on the basis of 6 O)
22 / 1 .	E1-02	44.56	0.07	0.01	10.32	32.89	0.65	11.40	0.09	0.00	0.01	100.00	9624	27079	79	4/23/2014 13:48	Carbonate (on the basis of 6 O)
23 / 1 .	E1-03	41.26	0.03	0.01	8.89	0.92	1.55	47.28	0.01	0.04	0.02	100.01	10070	27454	76	4/23/2014 13:53	Carbonate (on the basis of 6 O)
24 / 1 .	E1-04	41.07	0.03	0.01	9.35	0.70	1.38	47.38	0.06	0.00	0.03	100.01	10395	26922	79	4/23/2014 13:58	Carbonate (on the basis of 6 O)
25 / 1 .	E1-05	40.72	0.04	0.01	9.17	0.70	1.25	48.09	0.01	0.00	0.00	99.99	10447	26931	78	4/23/2014 14:03	Carbonate (on the basis of 6 O)
28 / 1 .	E1-08	43.33	0.02	0.00	8.80	31.82	1.11	14.81	0.04	0.03	0.02	99.98	9712	28273	80	4/23/2014 14:20	Carbonate (on the basis of 6 O)
31 / 1 .	E1-11	41.88	0.02	0.00	11.39	2.60	1.79	42.30	0.00	0.00	0.02	100.00	10333	28602	79	4/23/2014 14:34	Carbonate (on the basis of 6 O)
36 / 1 .	E1-16	0.08	99.39	0.01	0.00	0.00	0.00	0.47	0.02	0.01	0.01	99.99	3146	26150	72	4/23/2014 15:05	Carbonate (on the basis of 6 O)
39 / 1 .	E1-19	40.73	0.11	0.02	9.15	0.82	1.55	47.54	0.01	0.03	0.04	100.00	1002	24152	69	4/23/2014 15:21	Carbonate (on the basis of 6 O)
40 / 1 .	E1-20	41.27	0.12	0.01	8.89	1.48	0.76	47.33	0.01	0.09	0.03	99.99	873	24108	68	4/23/2014 15:26	Carbonate (on the basis of 6 O)
44 / 1 .	E1-24	40.71	0.02	0.00	9.44	0.61	1.21	48.01	0.00	0.00	0.00	100.00	-6462	25093	60	4/23/2014 15:50	Carbonate (on the basis of 6 O)
46 / 1 .	E1-26	40.47	0.59	0.00	5.49	1.69	1.05	50.58	0.02	0.05	0.07	100.01	-6421	25053	62	4/23/2014 16:00	Carbonate (on the basis of 6 O)
49 / 1 .	E1-29	40.21	0.05	0.01	2.22	1.96	0.93	54.55	0.02	0.00	0.05	100.00	-7144	29969	58	4/23/2014 16:18	Carbonate (on the basis of 6 O)
50 / 1 .	E1-30	40.73	0.04	0.02	2.74	2.18	0.94	53.20	0.00	0.02	0.13	100.00	-7216	29960	57	4/23/2014 16:23	Carbonate (on the basis of 6 O)
52 / 1 .	E1-32	44.34	0.01	0.00	10.24	33.27	0.61	11.43	0.03	0.06	0.00	99.99	-8324	30498	56	4/23/2014 16:33	Carbonate (on the basis of 6 O)
53 / 1 .	E1-33	40.80	1.47	0.04	5.96	1.97	0.59	49.04	0.06	0.00	0.07	100.00	-8242	30376	56	4/23/2014 16:38	Carbonate (on the basis of 6 O)
54 / 1 .	E1-34	40.50	0.04	0.01	8.96	0.66	1.03	48.75	0.00	0.02	0.04	100.01	-8214	30387	55	4/23/2014 16:43	Carbonate (on the basis of 6 O)
55 / 1 .	E1-35	40.81	0.03	0.01	8.92	0.47	1.12	48.62	0.00	0.00	0.01	99.99	-8119	30451	56	4/23/2014 16:48	Carbonate (on the basis of 6 O)
57 / 1 .	E1-37	38.85	0.04	0.00	1.26	1.52	1.06	57.17	0.02	0.01	0.06	99.99	-3028	29316	65	4/23/2014 16:59	Carbonate (on the basis of 6 O)
58 / 1 .	E1-38	40.68	0.04	0.00	8.92	0.50	0.88	48.90	0.02	0.02	0.04	100.00	-3061	29281	66	4/23/2014 17:04	Carbonate (on the basis of 6 O)
59 / 1 .	E1-39	40.30	0.03	0.00	8.89	0.55	0.97	49.23	0.02	0.00	0.01	100.00	-3027	29445	65	4/23/2014 17:09	Carbonate (on the basis of 6 O)
62 / 1 .	E1-42	44.08	0.00	0.00	9.20	31.26	0.68	14.77	0.00	0.02	0.00	100.01	-3879	33694	61	4/23/2014 17:26	Carbonate (on the basis of 6 O)

63 / 1 .	E1-43	40.26	0.04	0.02	9.16	0.55	1.03	48.89	0.01	0.03	0.00	99.99	-3358	33430	60	4/23/2014 17:31	Carbonate (on the basis of 6 O)
67 / 1 .	E2-01	40.72	0.21	0.00	9.58	1.04	1.51	46.93	0.00	0.00	0.02	100.01	6357	-38295	51	4/23/2014 17:51	Carbonate (on the basis of 6 O)
71 / 1 .	E2-05	40.16	0.04	0.02	10.54	0.78	2.84	45.60	0.00	0.00	0.01	99.99	-307	-37091	44	4/23/2014 18:14	Carbonate (on the basis of 6 O)
73 / 1 .	E2-07	40.51	0.01	0.02	11.00	1.04	1.57	45.82	0.02	0.00	0.00	99.99	-2549	-35430	41	4/23/2014 18:26	Carbonate (on the basis of 6 O)
74 / 1 .	E2-08	41.21	0.23	0.02	8.68	0.95	1.98	46.87	0.00	0.00	0.06	100.00	-2432	-35851	41	4/23/2014 18:31	Carbonate (on the basis of 6 O)
75 / 1 .	E2-09	39.90	0.03	0.00	8.06	1.26	1.92	48.81	0.01	0.02	0.00	100.01	-2149	-36314	40	4/23/2014 18:36	Carbonate (on the basis of 6 O)
76 / 1 .	E2-010	44.64	0.37	0.00	10.75	30.79	1.05	12.31	0.04	0.00	0.05	100.00	9636	-19466	89	4/23/2014 18:41	Carbonate (on the basis of 6 O)
78 / 1 .	E2-012	43.55	0.03	0.02	9.68	30.19	0.85	15.64	0.02	0.02	0.00	100.00	8181	-20636	86	4/23/2014 18:53	Carbonate (on the basis of 6 O)
83 / 1 .	CaCO3-05	40.20	0.08	0.00	0.02	59.58	0.11	0.01	0.00	0.00	0.00	100.00	7298	-3446	54	4/23/2014 19:21	Carbonate (on the basis of 6 O)
84 / 1 .	CaCO3-06	40.18	0.04	0.00	0.00	59.71	0.05	0.00	0.02	0.00	0.00	100.00	7338	-3450	54	4/23/2014 19:25	Carbonate (on the basis of 6 O)
85 / 1 .	FeCO3-05	37.69	0.07	0.01	0.12	0.01	3.12	58.95	0.02	0.00	0.00	99.99	9503	-5801	49	4/23/2014 19:30	Carbonate (on the basis of 6 O)
86 / 1 .	FeCO3-06	37.60	0.10	0.00	0.13	0.01	3.15	58.99	0.01	0.00	0.01	100.00	9492	-5783	50	4/23/2014 19:35	Carbonate (on the basis of 6 O)
87 / 1 .	MgCO3-05	47.58	0.04	0.01	22.26	29.91	0.03	0.09	0.06	0.00	0.01	99.99	5449	541	51	4/23/2014 19:40	Carbonate (on the basis of 6 O)
88 / 1 .	MgCO3-06	47.32	0.05	0.02	22.20	30.25	0.00	0.08	0.05	0.00	0.02	99.99	5457	564	52	4/23/2014 19:45	Carbonate (on the basis of 6 O)
5 / 1 .	CaCO3-01	42.86	0.05	0.00	0.00	56.92	0.12	0.00	0.03	0.01	0.01	100.00	7400	-3360	54	4/24/2014 17:59	Carbonate (on the basis of 6 O)
6 / 1 .	CaCO3-02	42.63	0.04	0.01	0.01	57.16	0.12	0.00	0.03	0.00	0.00	100.00	7419	-3365	54	4/24/2014 18:04	Carbonate (on the basis of 6 O)
7 / 1 .	CaCO3-03	42.91	0.04	0.00	0.00	56.93	0.09	0.03	0.00	0.01	0.00	100.01	7435	-3378	53	4/24/2014 18:08	Carbonate (on the basis of 6 O)
8 / 1 .	FeCO3-01	36.98	0.10	0.01	0.13	0.04	3.23	59.49	0.00	0.01	0.02	100.01	9495	-5819	50	4/24/2014 18:13	Carbonate (on the basis of 6 O)
9 / 1 .	FeCO3-02	36.97	0.08	0.01	0.13	0.00	3.20	59.60	0.00	0.01	0.01	100.01	9492	-5797	50	4/24/2014 18:18	Carbonate (on the basis of 6 O)
10 / 1 .	FeCO3-03	36.62	0.07	0.00	0.12	0.02	3.29	59.88	0.00	0.00	0.00	100.00	9491	-5768	50	4/24/2014 18:23	Carbonate (on the basis of 6 O)
11 / 1 .	MgCO3-01	46.92	0.04	0.01	22.15	30.75	0.04	0.06	0.00	0.02	0.00	99.99	5361	489	52	4/24/2014 18:28	Carbonate (on the basis of 6 O)
12 / 1 .	MgCO3-02	46.38	0.05	0.00	22.27	31.21	0.00	0.05	0.04	0.00	0.00	100.00	5339	488	52	4/24/2014 18:33	Carbonate (on the basis of 6 O)
13 / 1 .	MgCO3-03	46.70	0.04	0.01	22.17	30.86	0.05	0.09	0.08	0.00	0.01	100.01	5302	489	51	4/24/2014 18:38	Carbonate (on the basis of 6 O)
16 / 1 .	E3-03	43.12	0.66	0.02	9.96	30.82	1.36	13.91	0.03	0.00	0.12	100.00	8676	32869	80	4/24/2014 18:57	Carbonate (on the basis of 6 O)
18 / 1 .	E3-05	43.56	0.03	0.00	9.33	32.42	1.22	13.41	0.04	0.00	0.00	100.01	-6808	28139	67	4/24/2014 19:07	Carbonate (on the basis of 6 O)
22 / 1 .	E4-01	43.49	0.09	0.00	9.71	32.06	1.41	13.14	0.03	0.07	0.00	100.00	-7900	-33451	44	4/24/2014 19:32	Carbonate (on the basis of 6 O)
23 / 1 .	E4-02	43.27	0.03	0.00	9.01	31.87	1.20	14.51	0.05	0.04	0.02	100.00	-8235	-33078	41	4/24/2014 19:37	Carbonate (on the basis of 6 O)
32 / 1 .	E4-011	32.91	0.03	0.00	0.29	1.65	4.56	60.46	0.00	0.04	0.07	100.01	-4160	-26969	58	4/24/2014 20:24	Carbonate (on the basis of 6 O)
36 / 1 .	E4-015	42.40	0.48	0.00	10.56	1.13	1.70	43.70	0.01	0.00	0.02	100.00	-4182	-19814	63	4/24/2014 20:48	Carbonate (on the basis of 6 O)
37 / 1 .	E4-016	42.08	0.02	0.00	0.20	2.13	4.87	50.59	0.00	0.05	0.06	100.00	-4126	-19754	63	4/24/2014 20:53	Carbonate (on the basis of 6 O)
43 / 1 .	CaCO3-04	43.04	0.03	0.01	0.00	56.77	0.05	0.00	0.01	0.06	0.02	99.99	7457	-3394	53	4/24/2014 21:27	Carbonate (on the basis of 6 O)
44 / 1 .	CaCO3-05	42.91	0.03	0.01	0.00	56.91	0.09	0.01	0.02	0.02	0.01	100.01	7476	-3412	53	4/24/2014 21:32	Carbonate (on the basis of 6 O)
45 / 1 .	FeCO3-04	36.59	0.05	0.03	0.13	0.01	3.25	59.94	0.00	0.00	0.00	100.00	9541	-5803	49	4/24/2014 21:37	Carbonate (on the basis of 6 O)
46 / 1 .	FeCO3-05	36.47	0.07	0.00	0.14	0.01	3.22	60.08	0.00	0.00	0.02	100.01	9540	-5823	49	4/24/2014 21:42	Carbonate (on the basis of 6 O)
47 / 1 .	MgCO3-04	46.83	0.03	0.03	22.12	30.87	0.00	0.08	0.01	0.01	0.02	100.00	5228	512	51	4/24/2014 21:47	Carbonate (on the basis of 6 O)
48 / 1 .	MgCO3-05	46.75	0.04	0.01	22.09	30.97	0.04	0.07	0.01	0.02	0.00	100.00	5223	479	50	4/24/2014 21:52	Carbonate (on the basis of 6 O)

Carb10, wt% oxide																	
Formula	Comment	CO2	SiO2	SO2	MgO	CaO	MnO	FeO	SrO	BaO	Na2O	Total	X	Y	Z	Date	Geo Specie
29 / 1 .	E1-09	41.20	0.06	0.00	9.69	0.68	0.83	47.50	0.00	0.03	0.01	100.00	9270	28314	78	4/23/2014 14:24	Carbonate (on the basis of 6 O)
30 / 1 .	E1-10	41.11	0.05	0.02	6.83	0.59	0.62	50.74	0.00	0.03	0.00	99.99	9269	28301	80	4/23/2014 14:29	Carbonate (on the basis of 6 O)
35 / 1 .	E1-15	40.96	0.03	0.00	7.49	0.59	0.81	50.06	0.04	0.01	0.02	100.01	2621	26473	71	4/23/2014 15:00	Carbonate (on the basis of 6 O)
37 / 1 .	E1-17	40.75	0.03	0.00	8.63	0.50	0.81	49.27	0.01	0.00	0.00	100.00	3337	26068	72	4/23/2014 15:09	Carbonate (on the basis of 6 O)
43 / 1 .	E1-23	40.98	0.03	0.01	9.81	0.58	1.14	47.43	0.00	0.03	0.00	100.01	-5686	21527	58	4/23/2014 15:45	Carbonate (on the basis of 6 O)
45 / 1 .	E1-25	40.97	0.03	0.02	8.35	0.70	0.95	48.99	0.00	0.00	0.00	100.01	-6541	25005	61	4/23/2014 15:55	Carbonate (on the basis of 6 O)
51 / 1 .	E1-31	40.62	0.02	0.02	9.03	0.90	1.29	48.12	0.00	0.00	0.00	100.00	-7294	29949	57	4/23/2014 16:28	Carbonate (on the basis of 6 O)
60 / 1 .	E1-40	41.55	0.05	0.02	9.66	1.54	1.33	45.83	0.00	0.01	0.02	100.01	-3972	33951	62	4/23/2014 17:14	Carbonate (on the basis of 6 O)
64 / 1 .	E1-44	40.54	0.04	0.00	9.29	0.51	1.01	48.49	0.01	0.10	0.01	100.00	-3360	33354	59	4/23/2014 17:36	Carbonate (on the basis of 6 O)
65 / 1 .	E1-45	40.03	1.34	0.00	8.74	0.87	1.35	47.27	0.02	0.03	0.35	100.00	-3063	34160	62	4/23/2014 17:41	Carbonate (on the basis of 6 O)
66 / 1 .	E1-46	40.41	0.02	0.03	9.07	0.58	0.91	48.93	0.00	0.05	0.00	100.00	-3016	34162	62	4/23/2014 17:46	Carbonate (on the basis of 6 O)
68 / 1 .	E2-02	41.44	0.08	0.02	9.85	0.97	2.39	45.17	0.00	0.06	0.03	100.01	6341	-38119	54	4/23/2014 17:56	Carbonate (on the basis of 6 O)
17 / 1 .	E3-04	37.24	8.54	0.00	7.69	1.09	1.48	43.91	0.00	0.03	0.03	100.01	8318	32697	80	4/24/2014 19:02	Carbonate (on the basis of 6 O)
24 / 1 .	E4-03	38.84	0.70	0.00	0.21	1.56	4.11	54.50	0.01	0.02	0.05	100.00	-7145	-34222	43	4/24/2014 19:42	Carbonate (on the basis of 6 O)
25 / 1 .	E4-04	40.33	0.81	0.00	10.07	1.90	2.02	44.82	0.00	0.02	0.03	100.00	-7109	-34248	44	4/24/2014 19:47	Carbonate (on the basis of 6 O)
26 / 1 .	E4-05	43.45	0.12	0.00	9.19	31.72	1.28	14.20	0.03	0.00	0.01	100.00	-7162	-33984	44	4/24/2014 19:52	Carbonate (on the basis of 6 O)
27 / 1 .	E4-06	43.44	0.11	0.01	9.16	31.78	1.27	14.22	0.00	0.00	0.00	99.99	-7162	-33984	43	4/24/2014 19:57	Carbonate (on the basis of 6 O)
28 / 1 .	E4-07	39.72	1.49	0.02	9.82	2.03	1.97	44.93	0.00	0.00	0.02	100.00	-7115	-34254	45	4/24/2014 20:02	Carbonate (on the basis of 6 O)
29 / 1 .	E4-08	40.97	0.19	0.00	10.84	1.12	1.93	44.84	0.01	0.07	0.03	100.00	-7119	-33944	43	4/24/2014 20:07	Carbonate (on the basis of 6 O)
31 / 1 .	E4-010	40.00	2.54	0.01	7.84	1.45	2.61	45.38	0.00	0.00	0.18	100.01	-4218	-26947	57	4/24/2014 20:18	Carbonate (on the basis of 6 O)
34 / 1 .	E4-013	40.70	0.12	0.00	8.68	0.86	1.72	47.90	0.00	0.00	0.03	100.01	-4126	-26827	60	4/24/2014 20:35	Carbonate (on the basis of 6 O)

Carb5, wt% oxide																	
Formula	Comment	CO2	SiO2	SO2	MgO	CaO	MnO	FeO	SrO	BaO	Na2O	Total	X	Y	Z	Date	Geo Specie
26 / 1 .	E1-06	42.09	0.09	0.02	5.76	2.79	0.52	48.56	0.02	0.06	0.08	99.99	10704	26667	80	4/23/2014 14:08	Carbonate (on the basis of 6 O)

Glass20, wt% oxide																			
Formula	Comment	P2O5	SiO2	SO2	TiO2	Al2O3	MgO	CaO	MnO	FeO	Na2O	K2O	F	Cl	Total	X	Y	Z	Date
27 / 1 .	E1-07	0.10	39.63	0.04	0.37	20.42	1.68	0.80	0.01	4.80	1.39	4.53	0.39	1.94	76.11	10217	26871	80	4/23/2014 14:13
32 / 1 .	E1-12	0.04	22.70	0.03	0.53	17.61	3.79	0.43	0.01	19.97	0.08	0.70	0.13	0.62	66.63	8385	29335	72	4/23/2014 14:39
33 / 1 .	E1-13	0.00	41.31	0.03	0.00	33.99	0.01	0.06	0.00	0.01	0.07	0.01	0.05	0.42	75.95	8363	29750	75	4/23/2014 14:46
34 / 1 .	E1-14	0.08	23.60	0.01	0.34	17.37	3.18	0.23	0.00	16.27	0.15	1.05	0.10	0.98	63.35	2592	26644	73	4/23/2014 14:53
41 / 1 .	E1-21	0.97	23.16	0.05	0.11	17.51	3.07	1.01	0.03	13.88	0.09	1.47	0.00	1.06	62.40	1122	24138	73	4/23/2014 15:31
56 / 1 .	E1-36	0.04	36.67	0.05	0.57	22.02	2.44	0.36	0.00	9.17	0.28	3.82	0.02	0.60	76.05	-8141	30158	59	4/23/2014 16:53
61 / 1 .	E1-41	0.03	41.04	0.04	0.02	33.66	0.00	0.08	0.00	0.00	0.07	0.03	0.08	0.44	75.51	-4079	33950	60	4/23/2014 17:19
69 / 1 .	E2-03	0.00	44.54	0.02	0.03	36.86	0.01	0.04	0.00	0.12	0.08	0.04	0.01	0.09	81.82	6411	-38282	51	4/23/2014 18:00
72 / 1 .	E2-06	0.57	23.69	0.02	0.21	18.85	4.87	0.24	0.02	21.32	0.20	0.49	0.13	0.53	71.13	-1028	-37103	38	4/23/2014 18:19
77 / 1 .	E2-11	0.17	20.78	0.07	0.01	15.32	2.58	0.40	0.04	12.62	0.22	1.10	0.00	1.12	54.43	8239	-20953	86	4/23/2014 18:46
14 / 1 .	E3-01	0.00	42.69	0.00	0.00	36.53	0.00	0.05	0.02	0.03	0.06	0.00	0.00	0.28	79.67	334	28140	75	4/24/2014 18:43
15 / 1 .	E3-02	0.03	18.18	0.07	0.07	15.75	3.63	0.24	0.00	17.88	0.15	0.37	0.00	0.92	57.26	633	28140	71	4/24/2014 18:50
19 / 1 .	E3-06	0.06	21.53	0.07	0.08	16.71	3.87	0.15	0.00	18.00	0.18	0.57	0.04	0.32	61.58	-6971	27593	71	4/24/2014 19:11
20 / 1 .	E3-07	0.05	21.79	6.30	0.09	18.01	4.28	0.17	0.01	21.52	0.30	0.62	0.08	0.38	73.60	-5926	27419	74	4/24/2014 19:18
21 / 1 .	E3-08	0.00	26.18	0.00	0.02	21.88	3.75	0.08	0.73	30.95	0.20	0.13	0.03	0.10	84.05	-5939	27566	72	4/24/2014 19:25
30 / 1 .	E4-09	0.04	41.74	0.02	0.00	35.52	0.19	0.14	0.01	0.91	0.11	0.42	0.13	0.30	79.54	-7058	-33911	42	4/24/2014 20:12
35 / 1 .	E4-014	0.07	21.10	0.00	0.07	19.81	4.84	0.28	0.04	24.64	0.03	0.09	0.00	0.58	71.56	3837	-29288	76	4/24/2014 20:41
38 / 1 .	E4-017	0.00	27.22	0.03	0.11	18.17	3.25	0.25	0.03	15.19	0.49	1.59	0.09	0.67	67.08	-4337	-19787	62	4/24/2014 20:58

Glass10, wt% oxide																			
Formula	Comment	P2O5	SiO2	SO2	TiO2	Al2O3	MgO	CaO	MnO	FeO	Na2O	K2O	F	Cl	Total	X	Y	Z	Date
38 / 1 .	E1-18	0.00	23.82	0.04	0.03	20.72	5.24	0.17	0.09	27.30	0.13	0.19	0.06	0.38	78.17	3125	25929	75	4/23/2014 15:14
42 / 1 .	E1-22	0.00	39.69	0.00	0.00	31.66	0.00	0.06	0.00	0.09	0.05	0.00	0.00	0.58	72.12	1103	24270	69	4/23/2014 15:38
47 / 1 .	E1-27	0.00	24.93	0.06	0.08	16.78	3.18	0.54	0.00	15.26	0.10	1.22	0.03	0.89	63.07	-6427	24936	64	4/23/2014 16:04
48 / 1 .	E1-28	0.97	27.09	0.02	1.09	17.68	8.65	1.13	0.09	27.08	0.15	0.19	0.63	0.13	84.89	-7142	30028	60	4/23/2014 16:11
70 / 1 .	E2-04	0.03	19.11	0.03	0.03	14.54	2.64	0.20	0.00	13.27	0.20	0.77	0.08	1.09	52.00	-268	-37031	42	4/23/2014 18:07
33 / 1 .	E4-012	0.00	19.19	0.04	0.01	16.21	3.62	0.27	0.00	17.75	0.28	0.44	0.01	1.20	59.03	-4220	-26917	61	4/24/2014 20:28

APPENDIX E. IMAGEJ METHODS

ImageJ and the jPOR plug-in (v1.1) were used for image analysis. This document was written as instructions to re-create the methods used in this study. Begin by downloading ImageJ (<http://rsbweb.nih.gov/ij/download.html>) and the jPOR plug-in (<http://www.geoanalysis.org/jPOR.html>), and follow the set-up instructions.

Pre-processing the image

For photos with blue epoxy:

1. Open a photomicrograph in Adobe Photoshop.
2. Touch up the photo if needed.

When the photo is thresholded, anything blue will turn black and everything else will turn white. Keep this in mind when you pre-process your photo. If there is a bubble in the epoxy, it will need to be filled in with blue coloring or it will not register as porosity. If there are any blemishes in the photo that will be counted as porosity, paint over them as needed. White is the best color to use when covering up anything that is not porosity.

3. Image>mode>Indexed Color
 - Set 'Palette' to 'Custom' and you will be presented with a new window- click load and navigate to the custom JPOR palette (JPOR_60) and click load- OK this operation.
 - Set dither to none under Indexed Color options and click OK. The image will now be an 8-bit paletted file.
 - This will only need to be set the first time. Next time, for step 3, when you select "Indexed Color" it will automatically be set to "Previous." Select OK.
4. Save the processed image as a .bmp (Windows bitmap).

For photos with pink epoxy:

1. Open photomicrograph in Adobe Photoshop.
2. Touch up the photo if needed.

When the photo is eventually thresholded, porosity will turn black and everything else will turn white. Keep this in mind when you pre-process your photo. If there is a bubble in the epoxy, it will need to be filled in with pink coloring or it will not register as porosity. If there are any other blemishes in the photo that will be counted as porosity, paint over them as needed. White is the best color to use when covering up anything that is not porosity.

3. Image>adjustments>replace color
 - The jPOR pallet was created for thin sections with blue epoxy. Therefore, all pink epoxy must be turned blue.
 - With the eye-dropper, select a spot that best represents the epoxy color.
 - Click on the colored box in the lower right corner that says "result." Select a target color that turns the porosity blue. This can also be done using the Hue, Saturation, and Lightness sliders. The closer to true blue the better, if it is too green or too purple it might not threshold correctly.
 - Once the porosity looks blue, click "OK."
4. Image>mode>Indexed Color

- Set 'Palette' to 'Custom' and you will be presented with a new window- click load and navigate to the custom JPOR palette (JPOR_60) and click load- OK this operation.
 - Set dither to none under Indexed Color options and click OK. The image will now be an 8-bit paletted file.
 - This will only need to be set the first time. Next time, for step 3, when you select "Indexed Color" it will automatically be set to "Previous." Select OK.
5. Save the processed image as a .bmp (Windows bitmap).

Thresholding Photos using jPOR plug-in

1. Open ImageJ
2. Plugins>jPORv1.1
3. Select a photo that you have pre-processed. It should be in a .bmp file format
4. Press F1
 - Threshold for maximum porosity.
 - During this step, it is helpful to have the original image open to ensure that it is thresholding correctly.
 - If it is not thresholding correctly, then pre-process the photo again to correct it.
5. When the thresholding looks correct, press "Apply."
6. On ImageJ tool bar, click File>Save As>Tiff
7. Once the thresholded photo is saved, click out of jPOR windows, but leave thresholded photo open.

Image Analysis of ImageJ

1. Open a thresholded photo, or skip to step 2 if one is open already.
2. Process>noise>despeckle
 - Repeat this six times
3. Analyze>Set Scale.
 - *Distance in Pixels:* If analyzing the entire photo, look in upper left corner of the photo window. Enter the width of the photo in pixels
 - *Known distance:* You must determine the actual length of the photo. In this study, it was determined by taking a photo of a scale bar with each power of the microscope, and the photo width was measured. Enter the width of the photo, in microns.
 - *Unit of length:* um (if using microns)
 - Click OK
4. Save the photo. It will ask if you want to replace existing photo, click "Yes." Next time you open the thresholded photo, it will already be "despeckled" and have the scale set. This is important if you need to re-analyze your photo.
5. Analyze>Measure
 - This gives you the image porosity.
 - File>Save As. Save the results, preferably with the image name because no identifying info will be saved, only the results.
6. Analyze>Set measurements
 - Select measurements to be analyzed.
 - For this study, the following were selected:

- area
- bounding rectangle
- shape descriptors
- area fraction
- perimeter
- fit ellipse
- Feret's diameter
- Display label

7. Analyze>Analyze particles

- *Size*: 0-Infinity
- *Show*: outlines
- Check “Display results” and “clear results”
- Click OK

8. Results box will appear.

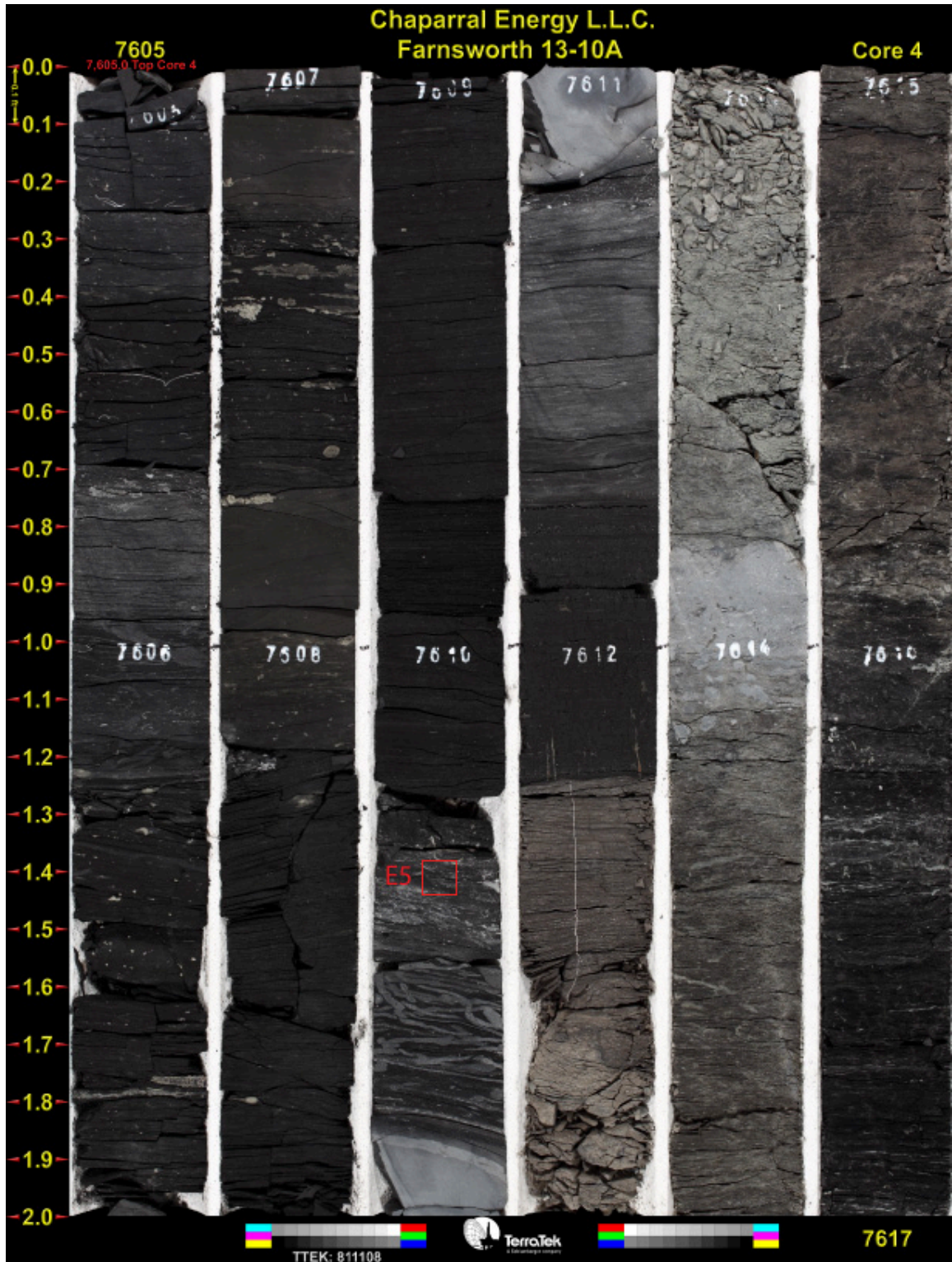
- File>Save As.
- Save file, preferably with the image name because no identifying info will be saved, only the results.

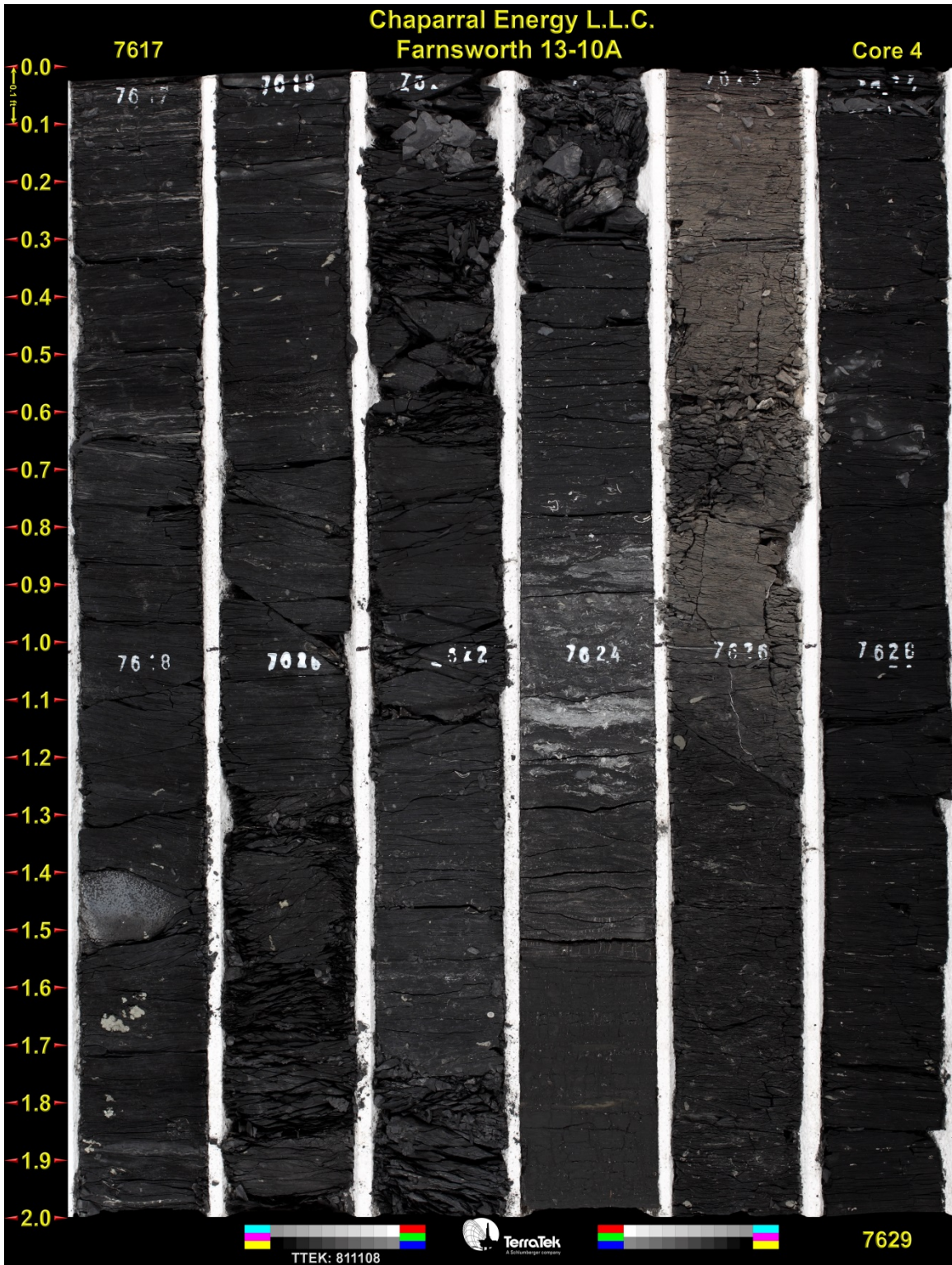
Data

The “measure” spreadsheet will show “% Area.” This is the percent of the photo that is black, which is the image porosity.

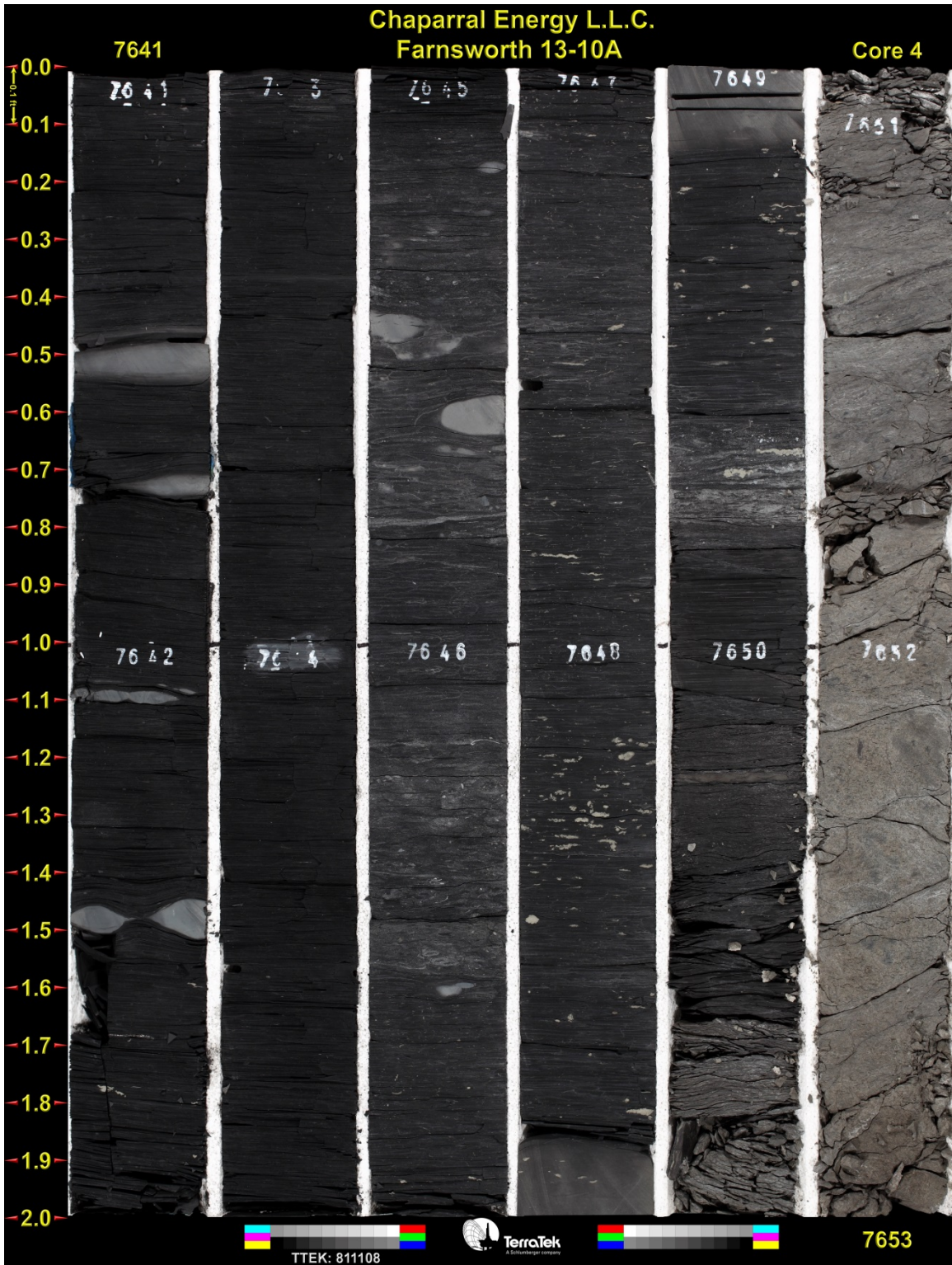
The “results” spreadsheet has measurements of each individual pore. “Area” is the area of a pore in μm^2 , feret is the longest diameter (in microns), and minferet is the shortest diameter (in microns). If another unit was used when “setting the scale” in ImageJ, then those will be the units in the results.

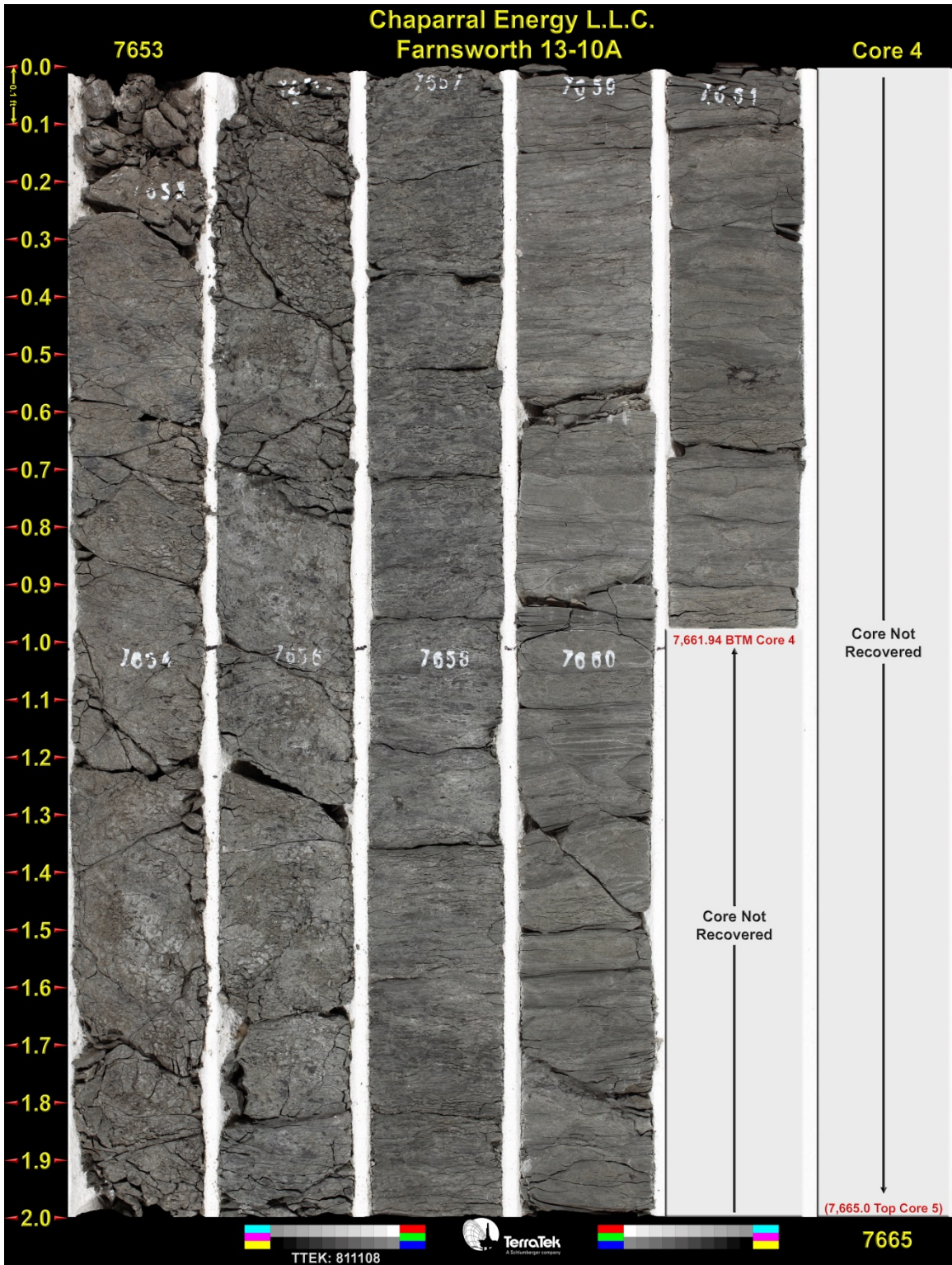
APPENDIX F. PHOTOS OF CORE FROM WELL 13-10A

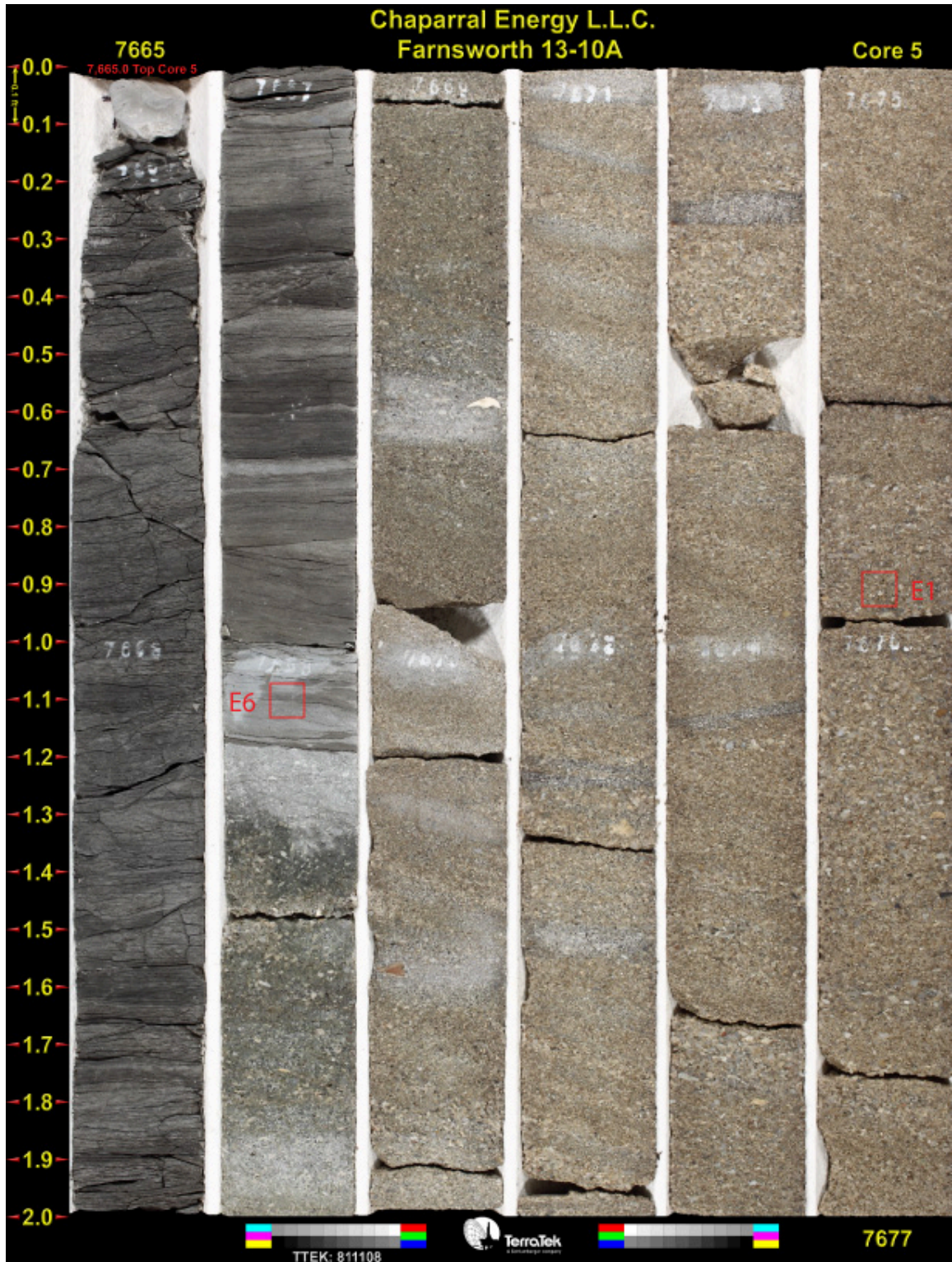


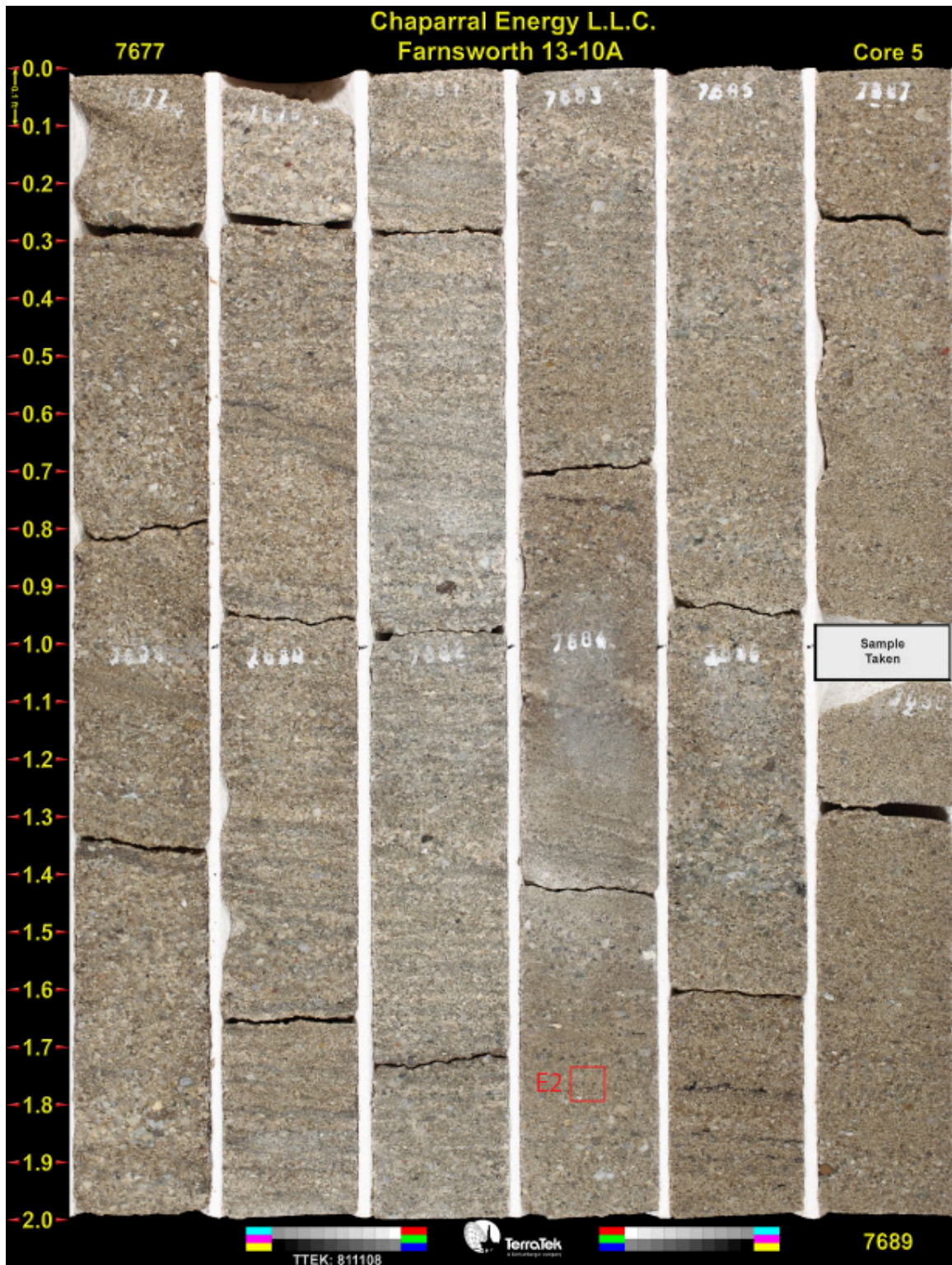


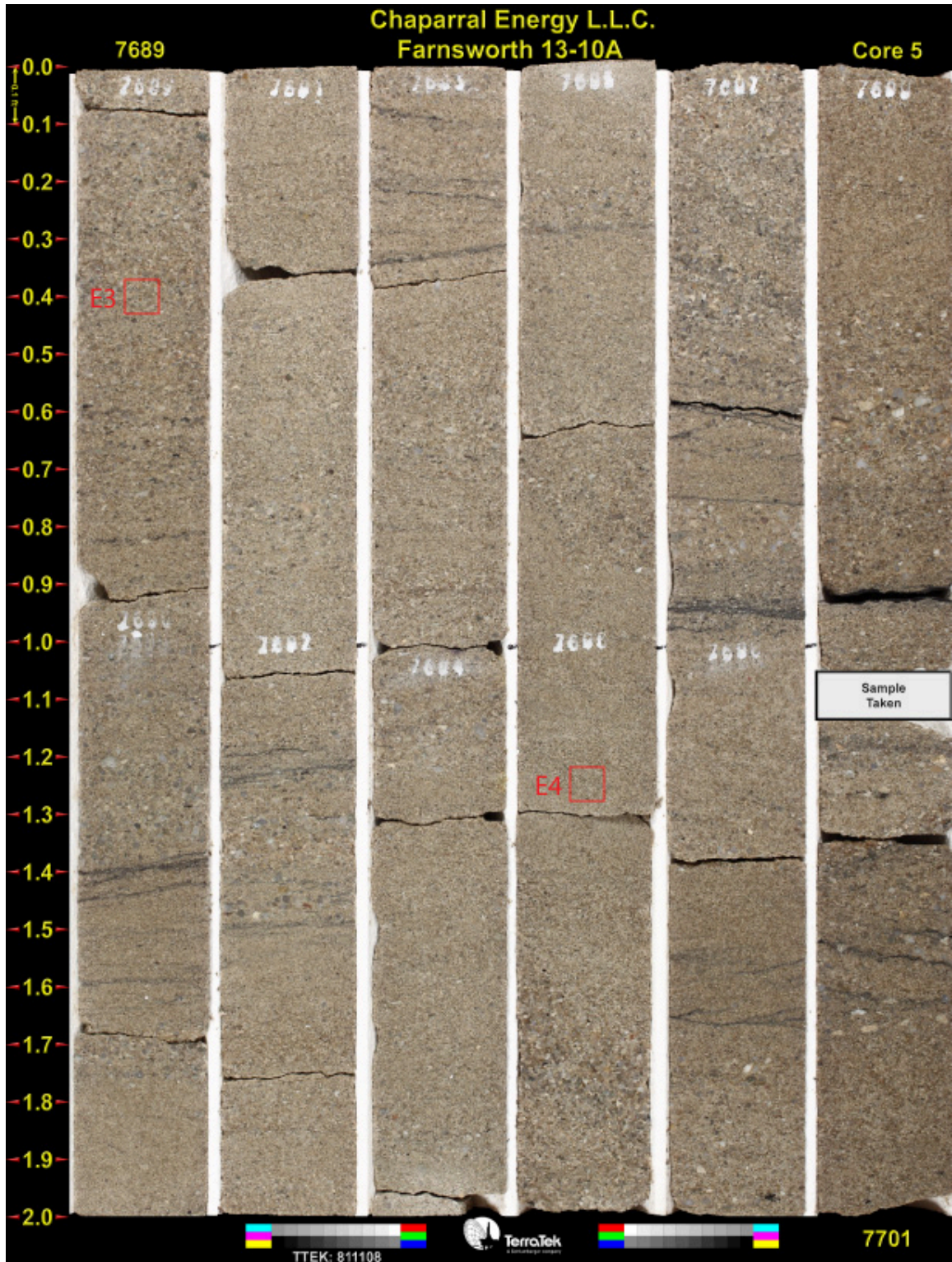


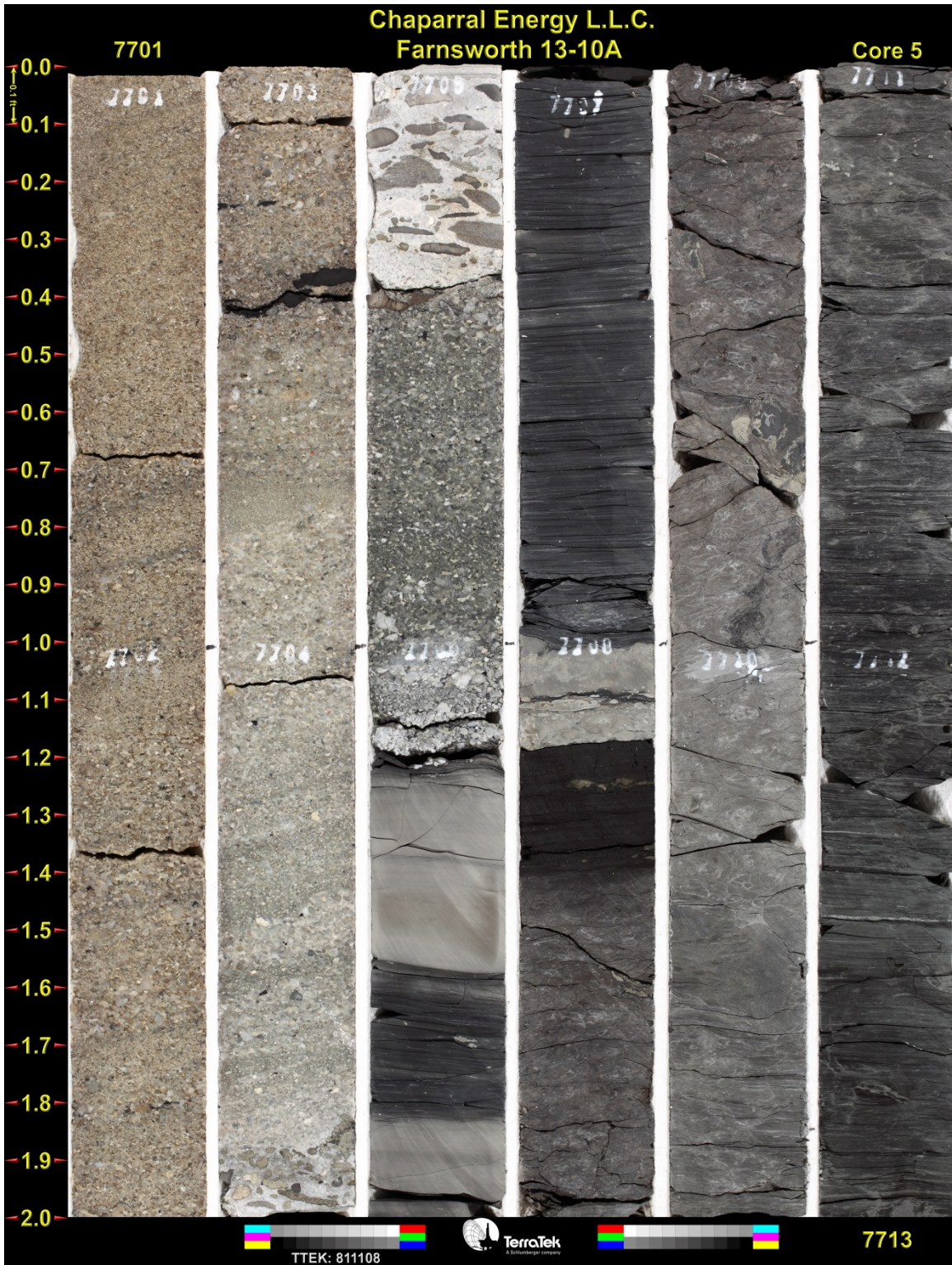


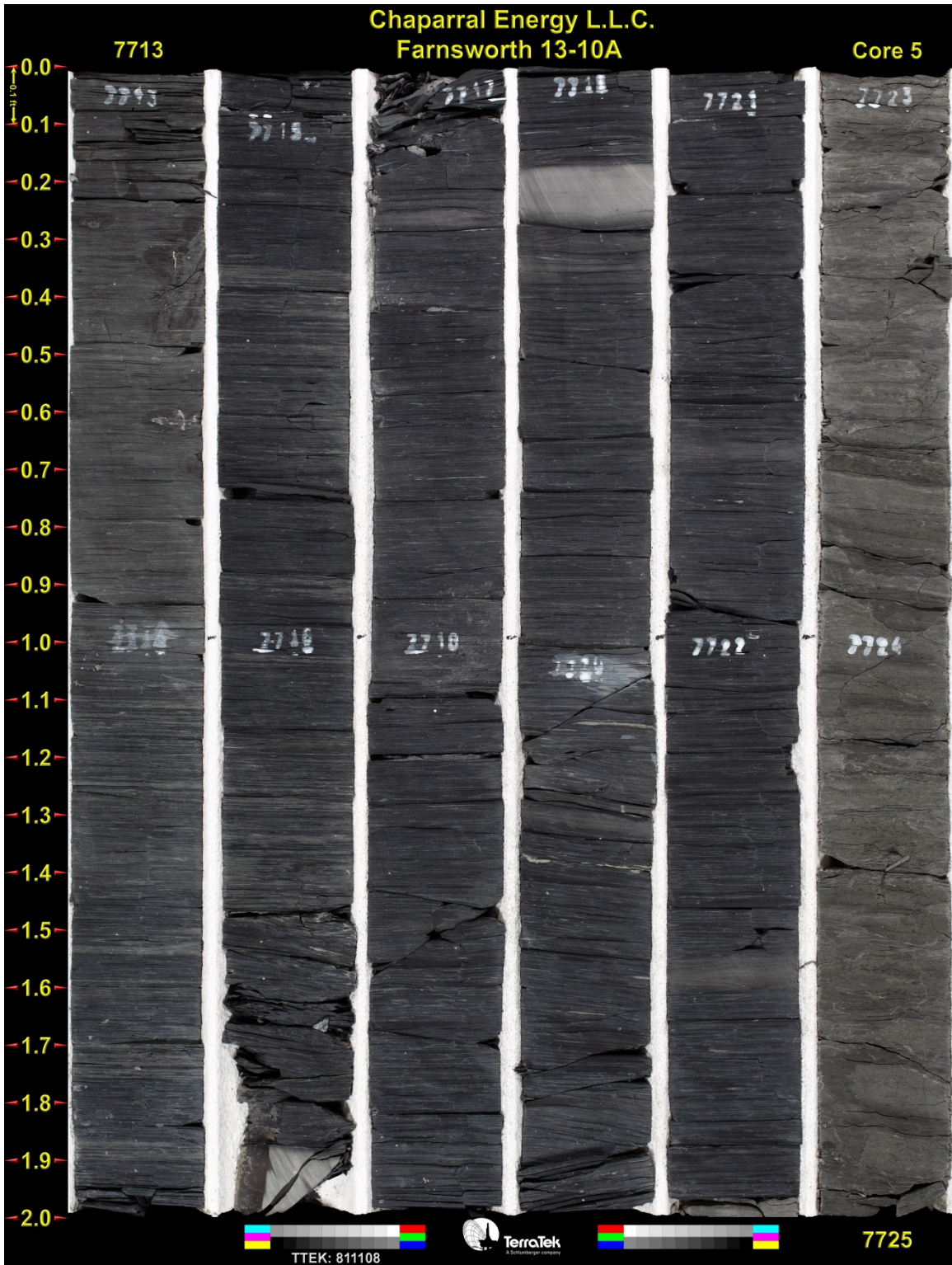








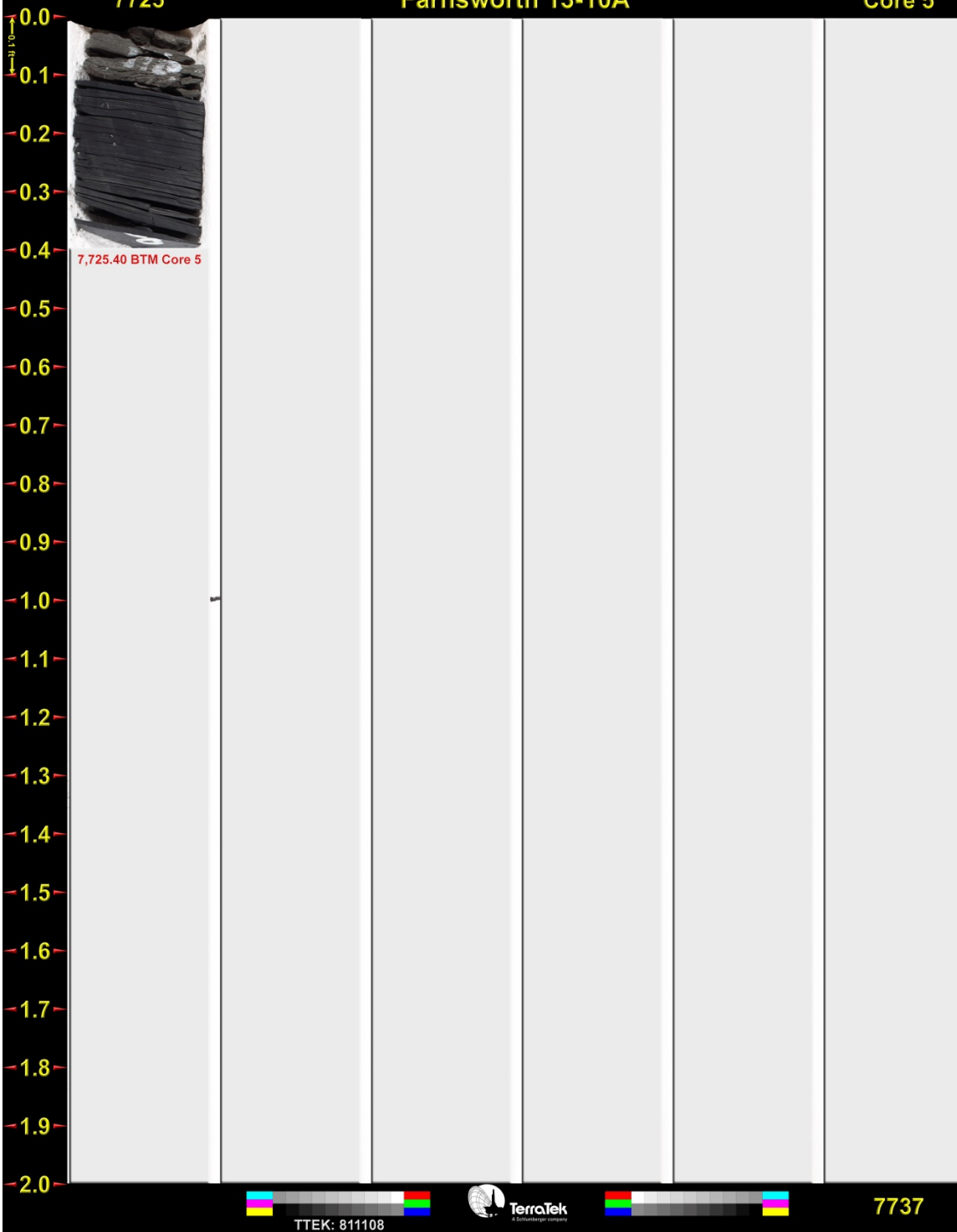




Chaparral Energy L.L.C.
Farnsworth 13-10A

Core 5

7725



APPENDIX G. MICP DATA

AIRMERCURY CAPILLARY PRESSURE DATA : BY PoroTechnology

**Spl #E1 @ 7675.9 ft.
Farnsworth Unit 13-10A**

MICP Closure(psia) = 9.88

MICP Porosity = 13.80%

MICP Gr. Den.(gm/cc) = 2.662

MICP Bulk Density(gm/cc) = 2.294

MICP-Calc. Air Perm = 9.12 md

Median Pore Aperture Dia.(microns) = 2.666

Injection Pressure (psia)	Pore Diameter (microns)	Hg (nwp) Saturation cum%PV	100-Hg(wp) Saturation cum%PV	Leverett "J" Function	Gas/Brine Pc (psia)	Gas/Oil Pc (psia)	Oil/Brine Pc (psia)	Ht. Above Free	Ht. Above Free Water
								Water (ft.) Gas/Brine	(ft.) Oil/Brine
4.40	48.44	0.0	100.0	0.02	0.60	0.29	0.36	1.5	3.2
4.81	44.30	0.0	100.0	0.02	0.65	0.31	0.39	1.7	3.5
5.26	40.53	0.0	100.0	0.02	0.72	0.34	0.43	1.8	3.8
5.76	37.02	0.0	100.0	0.02	0.78	0.37	0.47	2.0	4.2
6.30	33.85	0.0	100.0	0.02	0.86	0.41	0.52	2.2	4.6
6.89	30.95	0.0	100.0	0.03	0.94	0.45	0.56	2.4	5.0
7.54	28.28	0.0	100.0	0.03	1.03	0.49	0.62	2.6	5.5
8.25	25.85	0.0	100.0	0.03	1.12	0.54	0.68	2.8	6.0
9.03	23.62	0.0	100.0	0.03	1.23	0.59	0.74	3.1	6.6
9.88	21.59	0.0	100.0	0.04	1.34	0.64	0.81	3.4	7.2
10.79	19.77	0.5	99.5	0.04	1.47	0.70	0.88	3.7	7.9
11.79	18.10	1.4	98.6	0.04	1.60	0.77	0.97	4.1	8.6
12.89	16.55	2.4	97.6	0.05	1.75	0.84	1.06	4.4	9.4
14.19	15.03	3.9	96.1	0.05	1.93	0.92	1.16	4.9	10.3
15.49	13.77	5.1	94.9	0.06	2.11	1.01	1.27	5.3	11.3
16.89	12.63	6.2	93.8	0.06	2.30	1.10	1.38	5.8	12.3
18.49	11.54	7.4	92.6	0.07	2.51	1.20	1.52	6.4	13.5
20.29	10.52	8.7	91.3	0.07	2.76	1.32	1.66	7.0	14.8
22.19	9.62	11.3	88.7	0.08	3.02	1.44	1.82	7.7	16.2
24.29	8.78	14.4	85.6	0.09	3.30	1.58	1.99	8.4	17.7
26.58	8.02	17.1	82.9	0.10	3.61	1.73	2.18	9.2	19.4
28.98	7.36	20.7	79.3	0.11	3.94	1.88	2.38	10.0	21.1
31.78	6.71	24.0	76.0	0.12	4.32	2.07	2.61	11.0	23.1
34.78	6.13	26.7	73.3	0.13	4.73	2.26	2.85	12.0	25.3
37.98	5.62	29.5	70.5	0.14	5.17	2.47	3.11	13.1	27.6
41.58	5.13	32.0	68.0	0.15	5.65	2.70	3.41	14.3	30.3
46.91	4.55	34.4	65.6	0.17	6.38	3.05	3.85	16.2	34.2
50.07	4.26	36.8	63.2	0.18	6.81	3.25	4.11	17.3	36.5
55.11	3.871	39.4	60.6	0.20	7.49	3.58	4.52	19.0	40.1
59.53	3.594	41.6	58.4	0.22	8.10	3.87	4.88	20.5	43.3
65.57	3.254	44.3	55.7	0.24	8.92	4.26	5.38	22.6	47.7
71.63	2.978	46.7	53.3	0.26	9.74	4.66	5.87	24.7	52.1
78.20	2.728	49.3	50.7	0.29	10.64	5.08	6.41	27.0	56.9
85.37	2.499	51.9	48.1	0.31	11.61	5.55	7.00	29.5	62.1
93.52	2.281	54.3	45.7	0.34	12.72	6.08	7.67	32.3	68.1
100.20	2.129	56.0	44.0	0.37	13.63	6.51	8.22	34.6	72.9

AIRMERCURY CAPILLARY PRESSURE DATA : BY PoroTechnology

(Continued)

**Spl #E1 @ 7675.9 ft.
Farnsworth Unit 13-10A**

Injection Pressure (psia)	Pore Diameter (microns)	Hg (nwp) Saturation cum%PV	100-Hg(wp) Saturation cum%PV	Leverett "J" Function	Gas/Brine Pc (psia)	Gas/Oil Pc (psia)	Oil/Brine Pc (psia)	Ht. Above Free	Ht. Above Free Water
								Water (ft.) Gas/Brine	(ft.) Oil/Brine
109.11	1.955	58.4	41.6	0.40	14.84	7.09	8.95	37.6	79.4
119.28	1.789	61.0	39.0	0.44	16.22	7.75	9.78	41.2	86.8
131.68	1.620	63.5	36.5	0.48	17.91	8.56	10.80	45.4	95.9
143.38	1.488	65.8	34.2	0.53	19.50	9.32	11.76	49.5	104.4
157.49	1.355	68.0	32.0	0.58	21.42	10.24	12.91	54.3	114.7
172.30	1.238	70.0	30.0	0.63	23.43	11.20	14.13	59.4	125.4
188.31	1.133	71.9	28.1	0.69	25.61	12.24	15.44	65.0	137.1
206.25	1.034	73.6	26.4	0.76	28.05	13.41	16.91	71.2	150.2
225.92	0.944	75.3	24.7	0.83	30.73	14.68	18.53	77.9	164.5
248.31	0.859	77.1	22.9	0.91	33.77	16.14	20.36	85.7	180.8
271.28	0.786	78.4	21.6	1.00	36.89	17.63	22.24	93.6	197.5
296.79	0.719	79.8	20.2	1.09	40.36	19.29	24.34	102.4	216.1
324.97	0.656	81.2	18.8	1.19	44.20	21.12	26.65	112.1	236.6
355.94	0.599	82.5	17.5	1.31	48.41	23.14	29.19	122.8	259.1
390.11	0.547	83.7	16.3	1.43	53.05	25.36	31.99	134.6	284.0
427.54	0.499	84.9	15.1	1.57	58.15	27.79	35.06	147.5	311
467.61	0.456	86.0	14.0	1.72	63.59	30.39	38.34	161.3	340
511.03	0.417	87.0	13.0	1.87	69.50	33.22	41.90	176.3	372
560.22	0.381	88.0	12.0	2.06	76.19	36.41	45.94	193.3	408
612.10	0.349	88.9	11.1	2.25	83.25	39.79	50.19	211.2	446
670.74	0.318	89.7	10.3	2.46	91.22	43.60	55.00	231	488
733.39	0.291	90.4	9.6	2.69	99.74	47.67	60.14	253	534
803.86	0.265	91.1	8.9	2.95	109.32	52.25	65.92	277	585
879.26	0.243	91.8	8.2	3.23	119.58	57.15	72.10	303	640
961.72	0.222	92.5	7.5	3.53	130.79	62.51	78.86	332	700
1047.68	0.204	93.0	7.0	3.84	142.48	68.10	85.91	361	763
1147.61	0.186	93.5	6.5	4.21	156.07	74.59	94.10	396	835
1257.40	0.170	94.0	6.0	4.61	171.01	81.73	103.11	434	915
1377.14	0.155	94.5	5.5	5.05	187.29	89.51	112.93	475	1003
1506.90	0.142	95.0	5.0	5.53	204.94	97.95	123.57	520	1097
1647.11	0.130	95.4	4.6	6.04	224.01	107.06	135.06	568	1199
1806.19	0.118	95.9	4.1	6.63	245.64	117.40	148.11	623	1315
1975.07	0.108	96.2	3.8	7.25	268.61	128.38	161.96	681	1438
2155.91	0.099	96.6	3.4	7.91	293.20	140.13	176.78	744	1570
2365.23	0.090	96.9	3.1	8.68	321.67	153.74	193.95	816	1722
2584.68	0.083	97.3	2.7	9.48	351.52	168.00	211.94	892	1882
2824.85	0.076	97.6	2.4	10.36	384.18	183.62	231.64	975	2056
3094.29	0.069	97.9	2.1	11.35	420.82	201.13	253.73	1068	2253
3382.85	0.063	98.1	1.9	12.41	460.07	219.89	277.39	1167	2463
3703.21	0.058	98.3	1.7	13.58	503.64	240.71	303.66	1278	2696
4052.91	0.053	98.5	1.5	14.87	551.20	263.44	332.34	1398	2951
4425.29	0.048	98.6	1.4	16.23	601.84	287.64	362.87	1527	3222
4834.51	0.044	98.8	1.2	17.73	657.49	314.24	396.43	1668	3520
5291.79	0.0403	99.0	1.0	19.41	719.68	343.97	433.93	1826	3852

AIRMERCURY CAPILLARY PRESSURE DATA : BY PoroTechnology

(Continued)

**Spl #E1 @ 7675.9 ft.
Farnsworth Unit 13-10A**

Injection Pressure (psia)	Pore Diameter (microns)	Hg (nwp) Saturation cum%PV	100-Hg(wp) Saturation cum%PV	Leverett "J" Function	Gas/Brine Pc (psia)	Gas/Oil Pc (psia)	Oil/Brine Pc (psia)	Ht. Above Free Water (ft.) Gas/Brine	Ht. Above Free Water (ft.) Oil/Brine
5790.12	0.0368	99.1	0.9	21.24	787.46	376.36	474.79	1998	4215
6336.47	0.0337	99.3	0.7	23.24	861.76	411.87	519.59	2186	4613
6927.24	0.0308	99.5	0.5	25.41	942.10	450.27	568.03	2390	5043
7589.57	0.0281	99.7	0.3	27.84	1032.18	493.32	622.34	2618	5525
8295.45	0.0257	99.7	0.3	30.43	1128.18	539.20	680.23	2862	6039
9077.04	0.0235	99.8	0.2	33.30	1234.48	590.01	744.32	3132	6608
9936.36	0.0215	100.0	0.0	36.45	1351.34	645.86	814.78	3428	7234
10877.78	0.0196	100.0	0.0	39.90	1479.38	707.06	891.98	3753	7919
11877.53	0.0180	100.0	0.0	43.57	1615.34	772.04	973.96	4098	8647
12977.57	0.0164	100.0	0.0	47.61	1764.95	843.54	1064.16	4477	9448
14276.90	0.0149	100.0	0.0	52.37	1941.66	928.00	1170.71	4926	10394
15574.40	0.0137	100.0	0.0	57.13	2118.12	1012.34	1277.10	5373	11338
17074.66	0.0125	100.0	0.0	62.64	2322.15	1109.85	1400.12	5891	12430
18673.55	0.0114	100.0	0.0	68.50	2539.60	1213.78	1531.23	6442	13594
20373.10	0.0105	100.0	0.0	74.74	2770.74	1324.25	1670.59	7029	14832
22286.43	0.0096	100.0	0.0	81.76	3030.95	1448.62	1827.49	7689	16225
24390.22	0.0087	100.0	0.0	89.47	3317.07	1585.36	2000.00	8415	17756
26691.44	0.0080	100.0	0.0	97.91	3630.04	1734.94	2188.70	9209	19431
29293.39	0.0073	100.0	0.0	107.46	3983.90	1904.07	2402.06	10106	21326
31993.93	0.0067	100.0	0.0	117.37	4351.17	2079.61	2623.50	11038	23292
34993.20	0.0061	100.0	0.0	128.37	4759.08	2274.56	2869.44	12073	25475
38294.49	0.0056	100.0	0.0	140.48	5208.05	2489.14	3140.15	13212	27878
41892.62	0.0051	100.0	0.0	153.68	5697.40	2723.02	3435.19	14453	30498
45783.20	0.0047	100.0	0.0	167.95	6226.52	2975.91	3754.22	15795	33330
50066.13	0.0043	100.0	0.0	183.66	6808.99	3254.30	4105.42	17273	36448
54765.67	0.0039	100.0	0.0	200.90	7448.13	3559.77	4490.78	18894	39869
59968.58	0.0036	100.0	0.0	219.99	8155.73	3897.96	4917.42	20689	43657
50098.27	0.0036	100.0	0.0						
41900.01	0.0043	100.0	0.0						
32004.22	0.0056	100.0	0.0						
22309.74	0.0080	100.0	0.0						
15615.01	0.0115	100.0	0.0						
10912.79	0.0164	100.0	0.0						
7628.48	0.0235	100.0	0.0						
5322.07	0.0336	100.0	0.0						
3712.37	0.0482	100.0	0.0						
2591.41	0.0691	100.0	0.0						
1811.20	0.0988	100.0	0.0						
1510.63	0.1185	100.0	0.0						
1261.44	0.1419	100.0	0.0						
1051.85	0.1702	99.8	0.2						
882.07	0.2029	99.3	0.7						
737.12	0.2428	98.8	1.2						

AIRMERCURY CAPILLARY PRESSURE DATA : BY PoroTechnology

(Continued)

**Spl #E1 @ 7675.9 ft.
Farnsworth Unit 13-10A**

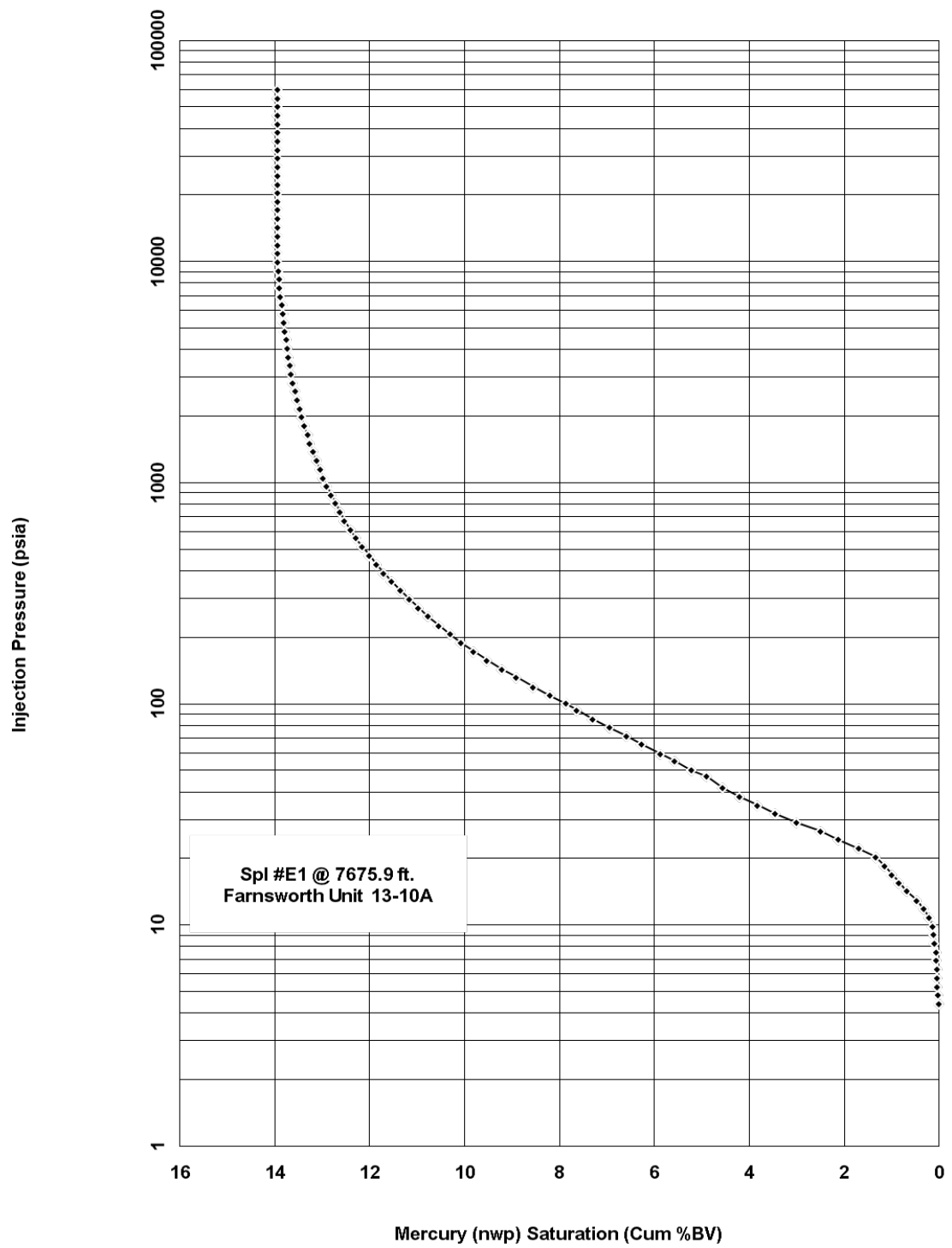
Injection Pressure (psia)	Pore Diameter (microns)	Hg (nwp) Saturation cum%PV	100-Hg(wp) Saturation cum%PV	Leverett "J" Function	Gas/Brine Pc (psia)	Gas/Oil Pc (psia)	Oil/Brine Pc (psia)	Ht. Above Free Water (ft.) Gas/Brine	Ht. Above Free Water (ft.) Oil/Brine
616.61	0.2903	98.3	1.7						
515.82	0.3470	97.6	2.4						
431.91	0.4144	96.9	3.1						
360.76	0.4962	96.1	3.9						
301.97	0.5928	95.2	4.8						
252.47	0.7090	94.2	5.8						
211.02	0.8482	93.0	7.0						
177.35	1.0093	91.6	8.4						
148.56	1.2049	90.1	9.9						
124.50	1.4378	88.5	11.5						
103.80	1.7244	86.6	13.4						
88.00	2.0340	84.8	15.2						
74.02	2.4183	82.5	17.5						
63.48	2.8196	80.3	19.7						
53.49	3.3467	77.7	22.3						
44.95	3.9820	75.0	25.0						
38.18	4.6883	72.3	27.7						
30.48	5.8724	67.0	33.0						
25.89	6.9130	64.0	36.0						
21.95	8.1564	61.0	39.0						

AIRMERCURY CAPILLARY PRESSURE DATA : BY Porotechnology

(Continued)

**Spl #E1 @ 7675.9 ft.
Farnsworth Unit 13-10A**

Injection Pressure (psia)	Pore Diameter (microns)	Hg (nwp) Saturation cum%PV	100-Hg(wp) Saturation cum%PV	Leverett "J" Function	Gas/Brine Pc (psia)	Gas/Oil Pc (psia)	Oil/Brine Pc (psia)	Ht. Above Free Water (ft.) Gas/Brine	Ht. Above Free Water (ft.) Oil/Brine
616.61	0.2903	98.3	1.7						
515.82	0.3470	97.6	2.4						
431.91	0.4144	96.9	3.1						
360.76	0.4962	96.1	3.9						
301.97	0.5928	95.2	4.8						
252.47	0.7090	94.2	5.8						
211.02	0.8482	93.0	7.0						
177.35	1.0093	91.6	8.4						
148.56	1.2049	90.1	9.9						
124.50	1.4378	88.5	11.5						
103.80	1.7244	86.6	13.4						
88.00	2.0340	84.8	15.2						
74.02	2.4183	82.5	17.5						
63.48	2.8196	80.3	19.7						
53.49	3.3467	77.7	22.3						
44.95	3.9820	75.0	25.0						
38.18	4.6883	72.3	27.7						
30.48	5.8724	67.0	33.0						
25.89	6.9130	64.0	36.0						
21.95	8.1564	61.0	39.0						



AIRMERCURY CAPILLARY PRESSURE DATA : BY Porotechnology

**Spl #E2 @ 7684.75 ft.
Farnsworth Unit 13-10A**

MICP Closure(psia) = 24.3

MICP Porosity = 12.04%

MICP Gr. Den.(gm/cc) = 2.650

MICP Bulk Density(gm/cc) = 2.331

MICP-Calc. Air Perm = 2.54 md

Median Pore Aperture Dia.(microns) = 1.457

Injection Pressure (psia)	Pore Diameter (microns)	Hg (nwp) Saturation cum%PV	100-Hg(wp) Saturation cum%PV	Leverett "J" Function	Gas/Brine Pc (psia)	Gas/Oil Pc (psia)	Oil/Brine Pc (psia)	Ht. Above	Ht. Above
								Free Water (ft.) Gas/Brine	Free Water (ft.) Oil/Brine
4.81	44.32	0.0	100.0	0.01	0.65	0.31	0.39	1.7	3.5
5.26	40.53	0.0	100.0	0.01	0.72	0.34	0.43	1.8	3.8
5.76	37.02	0.0	100.0	0.01	0.78	0.37	0.47	2.0	4.2
6.30	33.85	0.0	100.0	0.01	0.86	0.41	0.52	2.2	4.6
6.89	30.95	0.0	100.0	0.01	0.94	0.45	0.56	2.4	5.0
7.54	28.29	0.0	100.0	0.02	1.03	0.49	0.62	2.6	5.5
8.25	25.85	0.0	100.0	0.02	1.12	0.54	0.68	2.8	6.0
9.03	23.62	0.0	100.0	0.02	1.23	0.59	0.74	3.1	6.6
9.88	21.59	0.0	100.0	0.02	1.34	0.64	0.81	3.4	7.2
10.79	19.77	0.0	100.0	0.02	1.47	0.70	0.88	3.7	7.9
11.79	18.09	0.0	100.0	0.02	1.60	0.77	0.97	4.1	8.6
12.89	16.55	0.0	100.0	0.03	1.75	0.84	1.06	4.4	9.4
14.19	15.03	0.0	100.0	0.03	1.93	0.92	1.16	4.9	10.3
15.49	13.77	0.0	100.0	0.03	2.11	1.01	1.27	5.3	11.3
16.89	12.63	0.0	100.0	0.04	2.30	1.10	1.38	5.8	12.3
18.49	11.54	0.0	100.0	0.04	2.51	1.20	1.52	6.4	13.5
20.29	10.52	0.0	100.0	0.04	2.76	1.32	1.66	7.0	14.8
22.19	9.62	0.0	100.0	0.05	3.02	1.44	1.82	7.7	16.2
24.29	8.78	0.0	100.0	0.05	3.30	1.58	1.99	8.4	17.7
26.58	8.02	0.6	99.4	0.06	3.61	1.73	2.18	9.2	19.4
28.98	7.36	1.0	99.0	0.06	3.94	1.88	2.38	10.0	21.1
31.78	6.71	1.8	98.2	0.07	4.32	2.07	2.61	11.0	23.1
34.78	6.13	2.8	97.2	0.07	4.73	2.26	2.85	12.0	25.3
37.98	5.62	4.8	95.2	0.08	5.17	2.47	3.11	13.1	27.6
41.58	5.13	8.3	91.7	0.09	5.65	2.70	3.41	14.3	30.3
44.62	4.78	12.3	87.7	0.09	6.07	2.90	3.66	15.4	32.5
48.66	4.38	15.9	84.1	0.10	6.62	3.16	3.99	16.8	35.4
53.55	3.98	19.5	80.5	0.11	7.28	3.48	4.39	18.5	39.0
58.44	3.651	22.9	77.1	0.12	7.95	3.80	4.79	20.2	42.5
64.07	3.330	26.0	74.0	0.13	8.71	4.16	5.25	22.1	46.6
70.64	3.020	29.2	70.8	0.15	9.61	4.59	5.79	24.4	51.4
76.73	2.780	32.0	68.0	0.16	10.44	4.99	6.29	26.5	55.9
83.97	2.540	34.8	65.2	0.17	11.42	5.46	6.89	29.0	61.1
92.16	2.315	37.4	62.6	0.19	12.53	5.99	7.56	31.8	67.1
100.96	2.113	40.2	59.8	0.21	13.73	6.56	8.28	34.8	73.5
111.14	1.919	42.9	57.1	0.23	15.12	7.22	9.11	38.3	80.9

AIRMERCURY CAPILLARY PRESSURE DATA : BY PoroTechnology

(Continued)

**Spl #E2 @ 7684.75 ft.
Farnsworth Unit 13-10A**

Injection Pressure (psia)	Pore Diameter (microns)	Hg (nwp) Saturation cum%PV	100-Hg(wp) Saturation cum%PV	Leverett "J" Function	Gas/Brine Pc (psia)	Gas/Oil Pc (psia)	Ht. Above		
							Oil/Brine Pc (psia)	Free Water (ft.)	Free Oil/Brine (ft.)
120.50	1.770	45.1	54.9	0.25	16.39	7.83	9.88	41.6	87.7
132.61	1.609	47.7	52.3	0.27	18.03	8.62	10.87	45.8	96.5
144.79	1.473	49.7	50.3	0.30	19.69	9.41	11.87	50.0	105.4
158.73	1.344	52.1	47.9	0.33	21.59	10.32	13.02	54.8	115.6
173.83	1.227	54.3	45.7	0.36	23.64	11.30	14.25	60.0	126.5
189.54	1.126	56.5	43.5	0.39	25.78	12.32	15.54	65.4	138.0
207.51	1.028	58.6	41.4	0.43	28.22	13.49	17.02	71.6	151.1
227.44	0.938	60.8	39.2	0.47	30.93	14.78	18.65	78.5	165.6
249.61	0.855	62.8	37.2	0.52	33.95	16.22	20.47	86.1	181.7
272.50	0.783	64.8	35.2	0.56	37.06	17.71	22.35	94.0	198.4
298.32	0.715	66.6	33.4	0.62	40.57	19.39	24.46	102.9	217.2
326.20	0.654	68.4	31.6	0.68	44.36	21.20	26.75	112.5	237.5
356.74	0.598	70.0	30.0	0.74	48.52	23.19	29.25	123.1	259.7
390.91	0.546	71.8	28.2	0.81	53.16	25.41	32.05	134.9	284.6
428.07	0.498	73.4	26.6	0.89	58.22	27.82	35.10	147.7	311.6
469.01	0.455	75.0	25.0	0.97	63.79	30.49	38.46	161.8	341
511.32	0.417	76.3	23.7	1.06	69.54	33.24	41.93	176.4	372
560.96	0.380	77.9	22.1	1.16	76.29	36.46	46.00	193.5	408
613.26	0.348	79.3	20.7	1.27	83.40	39.86	50.29	211.6	446
671.38	0.318	80.7	19.3	1.39	91.31	43.64	55.05	231.6	489
734.10	0.291	81.9	18.1	1.52	99.84	47.72	60.20	253	534
804.00	0.265	83.3	16.7	1.67	109.34	52.26	65.93	277	585
878.83	0.243	84.5	15.5	1.82	119.52	57.12	72.06	303	640
963.05	0.222	85.7	14.3	2.00	130.97	62.60	78.97	332	701
1048.48	0.204	86.7	13.3	2.17	142.59	68.15	85.98	362	763
1148.44	0.186	87.7	12.3	2.38	156.19	74.65	94.17	396	836
1258.25	0.170	88.7	11.3	2.61	171.12	81.79	103.18	434	916
1378.66	0.155	89.7	10.3	2.86	187.50	89.61	113.05	476	1004
1508.46	0.141	90.5	9.5	3.13	205.15	98.05	123.69	520	1098
1647.95	0.129	91.5	8.5	3.42	224.12	107.12	135.13	569	1200
1808.50	0.118	92.2	7.8	3.75	245.96	117.55	148.30	624	1317
1977.89	0.108	93.2	6.8	4.10	268.99	128.56	162.19	682	1440
2158.72	0.099	93.8	6.2	4.47	293.59	140.32	177.02	745	1572
2367.21	0.090	94.6	5.4	4.91	321.94	153.87	194.11	817	1723
2587.77	0.082	95.2	4.8	5.36	351.94	168.21	212.20	893	1884
2829.04	0.075	95.8	4.2	5.86	384.75	183.89	231.98	976	2060
3096.70	0.069	96.4	3.6	6.42	421.15	201.29	253.93	1068	2254
3388.00	0.063	96.8	3.2	7.02	460.77	220.22	277.82	1169	2466
3706.38	0.058	97.2	2.8	7.68	504.07	240.91	303.92	1279	2698
4056.93	0.053	97.6	2.4	8.41	551.74	263.70	332.67	1400	2953
4430.88	0.048	98.0	2.0	9.18	602.60	288.01	363.33	1529	3226
4838.55	0.044	98.2	1.8	10.03	658.04	314.51	396.76	1669	3522
5299.60	0.040	98.6	1.4	10.98	720.75	344.47	434.57	1828	3858
5796.94	0.0368	98.8	1.2	12.01	788.38	376.80	475.35	2000	4220

AIRMERCURY CAPILLARY PRESSURE DATA : BY PoroTechnology

(Continued)

**Spl #E2 @ 7684.75 ft.
Farnsworth Unit 13-10A**

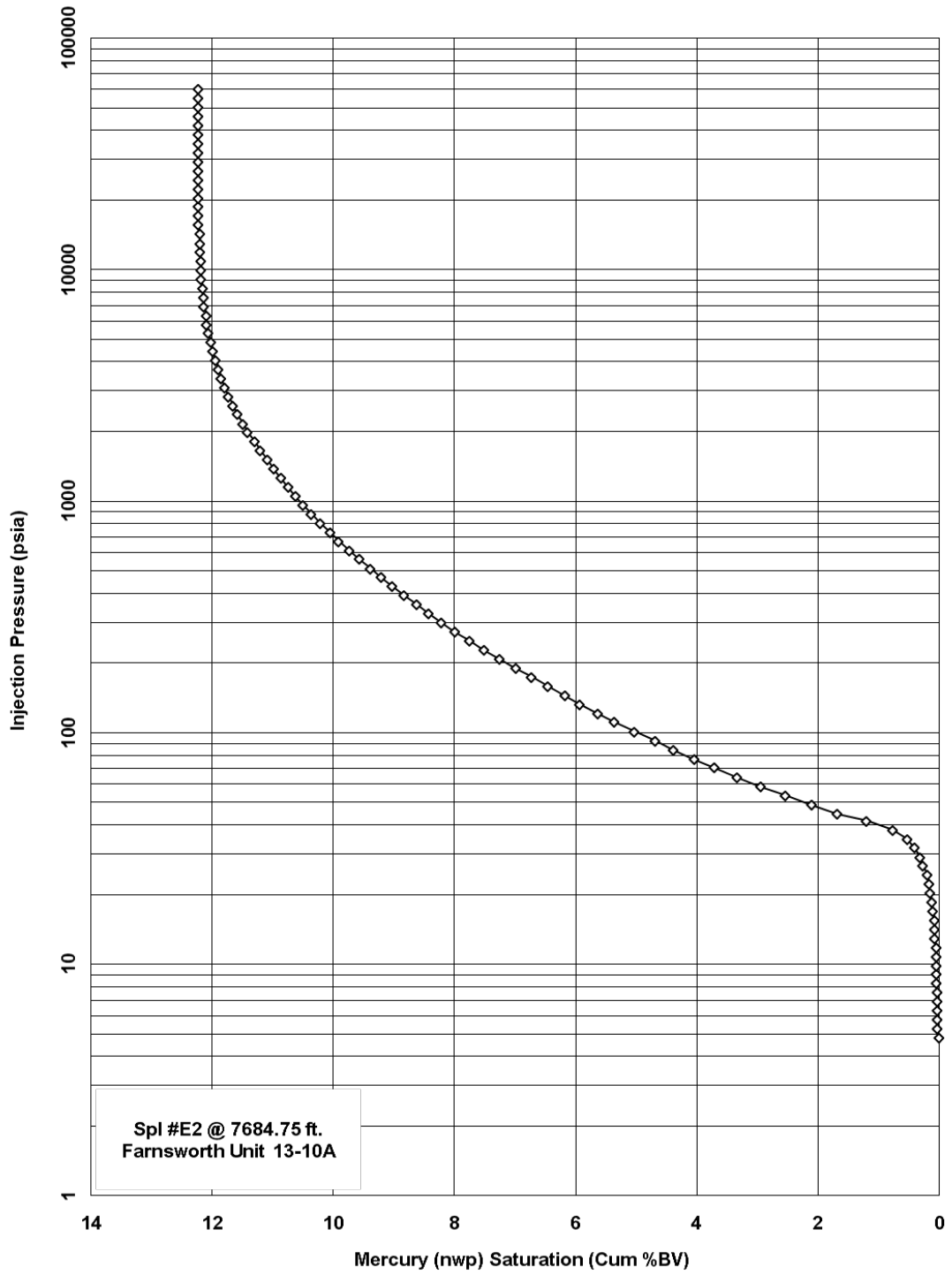
Injection Pressure (psia)	Pore Diameter (microns)	Hg (nwp) Saturation cum%PV	100-Hg(wp) Saturation cum%PV	Leverett "J" Function	Gas/Brine Pc (psia)	Gas/Oil Pc (psia)	Oil/Brine Pc (psia)	Ht. Above Free	Ht. Above Free
								Water (ft.) Gas/Brine	Water (ft.) Oil/Brine
6337.46	0.0337	98.8	1.2	13.14	861.89	411.93	519.67	2186	4614
6939.66	0.0307	99.2	0.8	14.38	943.79	451.08	569.05	2394	5052
7592.51	0.0281	99.2	0.8	15.74	1032.58	493.51	622.59	2619	5527
8308.14	0.0257	99.4	0.6	17.22	1129.91	540.03	681.27	2866	6048
9081.42	0.0235	99.6	0.4	18.82	1235.07	590.29	744.68	3133	6611
9945.57	0.0214	99.6	0.4	20.61	1352.60	646.46	815.54	3431	7240
10874.74	0.0196	99.6	0.4	22.54	1478.96	706.86	891.73	3752	7917
11876.17	0.0180	99.8	0.2	24.61	1615.16	771.95	973.85	4097	8646
12977.48	0.0164	99.8	0.2	26.90	1764.94	843.54	1064.15	4477	9448
14275.89	0.0149	99.8	0.2	29.59	1941.52	927.93	1170.62	4925	10393
15576.45	0.0137	100.0	0.0	32.28	2118.40	1012.47	1277.27	5374	11340
17077.68	0.0125	100.0	0.0	35.40	2322.56	1110.05	1400.37	5892	12433
18673.92	0.0114	100.0	0.0	38.70	2539.65	1213.80	1531.26	6443	13595
20376.04	0.0105	100.0	0.0	42.23	2771.14	1324.44	1670.84	7030	14834
22286.79	0.0096	100.0	0.0	46.19	3031.00	1448.64	1827.52	7689	16225
24390.43	0.0087	100.0	0.0	50.55	3317.10	1585.38	2000.02	8415	17756
26693.47	0.0080	100.0	0.0	55.33	3630.31	1735.08	2188.86	9209	19433
29294.31	0.0073	100.0	0.0	60.72	3984.03	1904.13	2402.13	10107	21326
31992.90	0.0067	100.0	0.0	66.31	4351.03	2079.54	2623.42	11038	23291
34994.15	0.0061	100.0	0.0	72.53	4759.20	2274.62	2869.52	12073	25476
38293.21	0.0056	100.0	0.0	79.37	5207.88	2489.06	3140.04	13211	27877
41893.29	0.0051	100.0	0.0	86.83	5697.49	2723.06	3435.25	14453	30498
45786.34	0.0047	100.0	0.0	94.90	6226.94	2976.11	3754.48	15796	33332
50067.96	0.0043	100.0	0.0	103.77	6809.24	3254.42	4105.57	17273	36449
54766.48	0.0039	100.0	0.0	113.51	7448.24	3559.82	4490.85	18894	39870
59972.90	0.0036	100.0	0.0	124.30	8156.31	3898.24	4917.78	20691	43660
50099.68	0.0036	100.0	0.0						
41899.24	0.0043	100.0	0.0						
32004.55	0.0056	100.0	0.0						
22311.31	0.0080	100.0	0.0						
15616.80	0.0115	100.0	0.0						
10916.27	0.0164	100.0	0.0						
7626.64	0.0235	100.0	0.0						
5321.59	0.0336	100.0	0.0						
3713.43	0.0482	100.0	0.0						
2591.74	0.0691	100.0	0.0						
1813.55	0.0987	100.0	0.0						
1511.06	0.1185	100.0	0.0						
1261.25	0.1419	100.0	0.0						
1050.66	0.1704	99.8	0.2						
881.80	0.2030	99.4	0.6						
737.56	0.2427	98.8	1.2						
616.06	0.2906	98.0	2.0						

AIRMERCURY CAPILLARY PRESSURE DATA : BY PoroTechnology

(Continued)

**Spl #E2 @ 7684.75 ft.
Farnsworth Unit 13-10A**

Injection Pressure (psia)	Pore Diameter (microns)	Hg (nwp) Saturation cum%PV	100-Hg(wp) Saturation cum%PV	Leverett "J" Function	Gas/Brine Pc (psia)	Gas/Oil Pc (psia)	Oil/Brine Pc (psia)	Ht. Above Free Water (ft.) Gas/Brine	Ht. Above Free Water (ft.) Oil/Brine
515.80	0.3470	97.4	2.6						
430.78	0.4155	96.6	3.4						
359.91	0.4973	95.6	4.4						
301.00	0.5947	94.6	5.4						
251.05	0.7130	93.6	6.4						
210.94	0.8486	92.2	7.8						
176.39	1.0148	91.1	8.9						
147.77	1.2113	89.5	10.5						
123.44	1.4501	87.9	12.1						
103.21	1.7344	86.1	13.9						
86.92	2.0594	84.3	15.7						
72.33	2.4746	82.1	17.9						
60.44	2.9817	80.1	19.9						
50.49	3.5455	78.1	21.9						
42.99	4.1640	75.9	24.1						
35.87	4.9901	73.8	26.2						
30.09	5.9497	71.6	28.4						
25.39	7.0494	69.4	30.6						
21.05	8.5045	67.2	32.8						



AIRMERCURY CAPILLARY PRESSURE DATA : BY PoroTechnology

**Spl #E3 @ 7686.4 ft.
Farnsworth Unit 13-10A**

MICP Closure(psia) = 11.8

MICP Porosity = 11.02%

MICP gr. Den.(gm/cc) = 2.643

MICP Bulk Density(gm/cc) = 2.352

MICP-Calc. Air Perm = 3.670 md

Median Pore Aperture Dia.(microns) = 1.606

Injection Pressure (psia)	Pore Diameter (microns)	Hg (nwp) Saturation cum%PV	100-Hg(wp) Saturation cum%PV	Leverett "J" Function	Gas/Brine Pc (psia)	Gas/Oil Pc (psia)	Oil/Brine Pc (psia)	Ht. Above Free	Ht. Above Free Water
								Water (ft.) Gas/Brine	(ft.) Oil/Brine
4.81	44.32	0.0	100.0	0.01	0.65	0.31	0.39	1.7	3.5
5.26	40.53	0.0	100.0	0.01	0.72	0.34	0.43	1.8	3.8
5.76	37.02	0.0	100.0	0.01	0.78	0.37	0.47	2.0	4.2
6.30	33.85	0.0	100.0	0.02	0.86	0.41	0.52	2.2	4.6
6.89	30.95	0.0	100.0	0.02	0.94	0.45	0.56	2.4	5.0
7.54	28.29	0.0	100.0	0.02	1.03	0.49	0.62	2.6	5.5
8.25	25.85	0.0	100.0	0.02	1.12	0.54	0.68	2.8	6.0
9.03	23.62	0.0	100.0	0.02	1.23	0.59	0.74	3.1	6.6
9.88	21.59	0.0	100.0	0.03	1.34	0.64	0.81	3.4	7.2
10.79	19.77	0.0	100.0	0.03	1.47	0.70	0.88	3.7	7.9
11.79	18.09	0.0	100.0	0.03	1.60	0.77	0.97	4.1	8.6
12.89	16.55	0.4	99.6	0.03	1.75	0.84	1.06	4.4	9.4
14.19	15.03	1.1	98.9	0.04	1.93	0.92	1.16	4.9	10.3
15.49	13.77	1.5	98.5	0.04	2.11	1.01	1.27	5.3	11.3
16.89	12.63	2.2	97.8	0.04	2.30	1.10	1.38	5.8	12.3
18.49	11.54	3.1	96.9	0.05	2.51	1.20	1.52	6.4	13.5
20.29	10.52	4.4	95.6	0.05	2.76	1.32	1.66	7.0	14.8
22.19	9.62	5.7	94.3	0.06	3.02	1.44	1.82	7.7	16.2
24.29	8.78	7.7	92.3	0.06	3.30	1.58	1.99	8.4	17.7
26.58	8.02	9.9	90.1	0.07	3.61	1.73	2.18	9.2	19.4
28.98	7.36	11.6	88.4	0.08	3.94	1.88	2.38	10.0	21.1
31.78	6.71	14.9	85.1	0.08	4.32	2.07	2.61	11.0	23.1
34.78	6.13	18.5	81.5	0.09	4.73	2.26	2.85	12.0	25.3
37.98	5.62	21.3	78.7	0.10	5.17	2.47	3.11	13.1	27.6
41.58	5.13	23.5	76.5	0.11	5.65	2.70	3.41	14.3	30.3
44.15	4.83	25.1	74.9	0.11	6.00	2.87	3.62	15.2	32.1
48.21	4.43	28.8	73.2	0.13	6.56	3.13	3.95	16.6	35.1
53.10	4.02	29.2	70.8	0.14	7.22	3.45	4.35	18.3	38.7
57.99	3.679	31.2	68.8	0.15	7.89	3.77	4.76	20.0	42.2
63.62	3.353	33.4	66.6	0.17	8.65	4.14	5.22	21.9	46.3
70.19	3.039	35.6	64.4	0.18	9.55	4.56	5.76	24.2	51.1
76.26	2.797	37.8	62.2	0.20	10.37	4.96	6.25	26.3	55.5
83.49	2.555	40.2	59.8	0.22	11.35	5.43	6.85	28.8	60.8
91.67	2.327	42.2	57.8	0.24	12.47	5.96	7.52	31.6	66.7
100.46	2.123	44.4	55.6	0.26	13.66	6.53	8.24	34.7	73.1
110.64	1.928	46.4	53.6	0.29	15.05	7.19	9.07	38.2	80.5

AIRMERCURY CAPILLARY PRESSURE DATA : BY PoroTechnology

(Continued)

**Spl #E3 @ 7686.4 ft.
Farnsworth Unit 13-10A**

Injection Pressure (psia)	Pore Diameter (microns)	Hg (nwp) Saturation cum%PV	100-Hg(wp) Saturation cum%PV	Leverett "J" Function	Gas/Brine Pc (psia)	Gas/Oil Pc (psia)	Oil/Brine Pc (psia)	Ht. Above Free Water (ft.)	Ht. Above Free Water (ft.)
119.99	1.778	47.9	52.1	0.31	16.32	7.80	9.84	41.4	87.4
132.10	1.615	49.9	50.1	0.34	17.97	8.59	10.83	45.6	96.2
144.27	1.479	51.4	48.6	0.38	19.62	9.38	11.83	49.8	105.0
158.21	1.348	53.0	47.0	0.41	21.52	10.28	12.97	54.6	115.2
173.30	1.231	54.5	45.5	0.45	23.57	11.26	14.21	59.8	126.2
189.01	1.129	56.0	44.0	0.49	25.71	12.29	15.50	65.2	137.6
206.94	1.031	57.4	42.6	0.54	28.14	13.45	16.97	71.4	150.7
226.91	0.940	58.9	41.1	0.59	30.86	14.75	18.61	78.3	165.2
249.08	0.856	60.2	39.8	0.65	33.87	16.19	20.42	85.9	181.3
271.96	0.784	61.5	38.5	0.71	36.99	17.68	22.30	93.8	198.0
297.79	0.716	62.9	37.1	0.78	40.50	19.36	24.42	102.7	216.8
325.66	0.655	64.2	35.8	0.85	44.29	21.17	26.70	112.4	237.1
356.20	0.599	65.3	34.7	0.93	48.44	23.15	29.21	122.9	259.3
390.36	0.547	66.6	33.4	1.02	53.09	25.37	32.01	134.7	284.2
427.52	0.499	67.9	32.1	1.11	58.14	27.79	35.06	147.5	311.2
468.46	0.455	69.0	31.0	1.22	63.71	30.45	38.41	161.6	341
510.76	0.418	70.1	29.9	1.33	69.46	33.20	41.88	176.2	372
560.40	0.381	71.4	28.6	1.46	76.21	36.43	45.95	193.3	408
612.69	0.348	72.5	27.5	1.60	83.33	39.82	50.24	211.4	446
670.79	0.318	73.8	26.2	1.75	91.23	43.60	55.00	231.4	488
733.50	0.291	75.2	24.8	1.91	99.76	47.88	60.15	253	534
803.39	0.266	76.3	23.7	2.09	109.26	52.22	65.88	277	585
878.22	0.243	77.6	22.4	2.29	119.44	57.08	72.01	303	639
962.42	0.222	78.7	21.3	2.51	130.89	62.56	78.92	332	701
1047.84	0.204	79.8	20.2	2.73	142.51	68.11	85.92	362	763
1147.79	0.186	81.1	18.9	2.99	156.10	74.61	94.12	396	836
1257.57	0.170	82.2	17.8	3.27	171.03	81.74	103.12	434	916
1377.97	0.155	83.5	16.5	3.59	187.40	89.57	112.99	475	1003
1507.75	0.142	84.6	15.4	3.93	205.05	98.00	123.64	520	1098
1647.22	0.130	85.9	14.1	4.29	224.02	107.07	135.07	568	1199
1807.76	0.118	87.0	13.0	4.71	245.86	117.50	148.24	624	1316
1977.13	0.108	88.4	11.6	5.15	268.89	128.51	162.12	682	1439
2157.94	0.099	89.5	10.5	5.62	293.48	140.27	176.95	744	1571
2366.41	0.090	90.5	9.5	6.16	321.83	153.82	194.05	816	1723
2586.95	0.083	91.6	8.4	6.74	351.83	168.15	212.13	892	1883
2828.17	0.075	92.5	7.5	7.36	384.63	183.83	231.91	976	2059
3095.85	0.069	93.6	6.4	8.06	421.04	201.23	253.86	1068	2254
3387.13	0.063	94.5	5.5	8.82	460.65	220.16	277.74	1169	2466
3705.50	0.058	95.2	4.8	9.65	503.95	240.86	303.85	1278	2698
4056.04	0.053	95.8	4.2	10.56	551.62	263.64	332.60	1399	2953
4429.98	0.048	96.3	3.7	11.54	602.48	287.95	363.26	1528	3225
4837.64	0.044	96.9	3.1	12.60	657.92	314.45	396.89	1669	3522
5298.69	0.040	97.4	2.6	13.80	720.62	344.41	434.49	1828	3857
5796.02	0.0368	97.6	2.4	15.09	788.26	376.74	475.27	2000	4220

AIRMERCURY CAPILLARY PRESSURE DATA : BY PoroTechnology

(Continued)

**Spl #E3 @ 7686.4 ft.
Farnsworth Unit 13-10A**

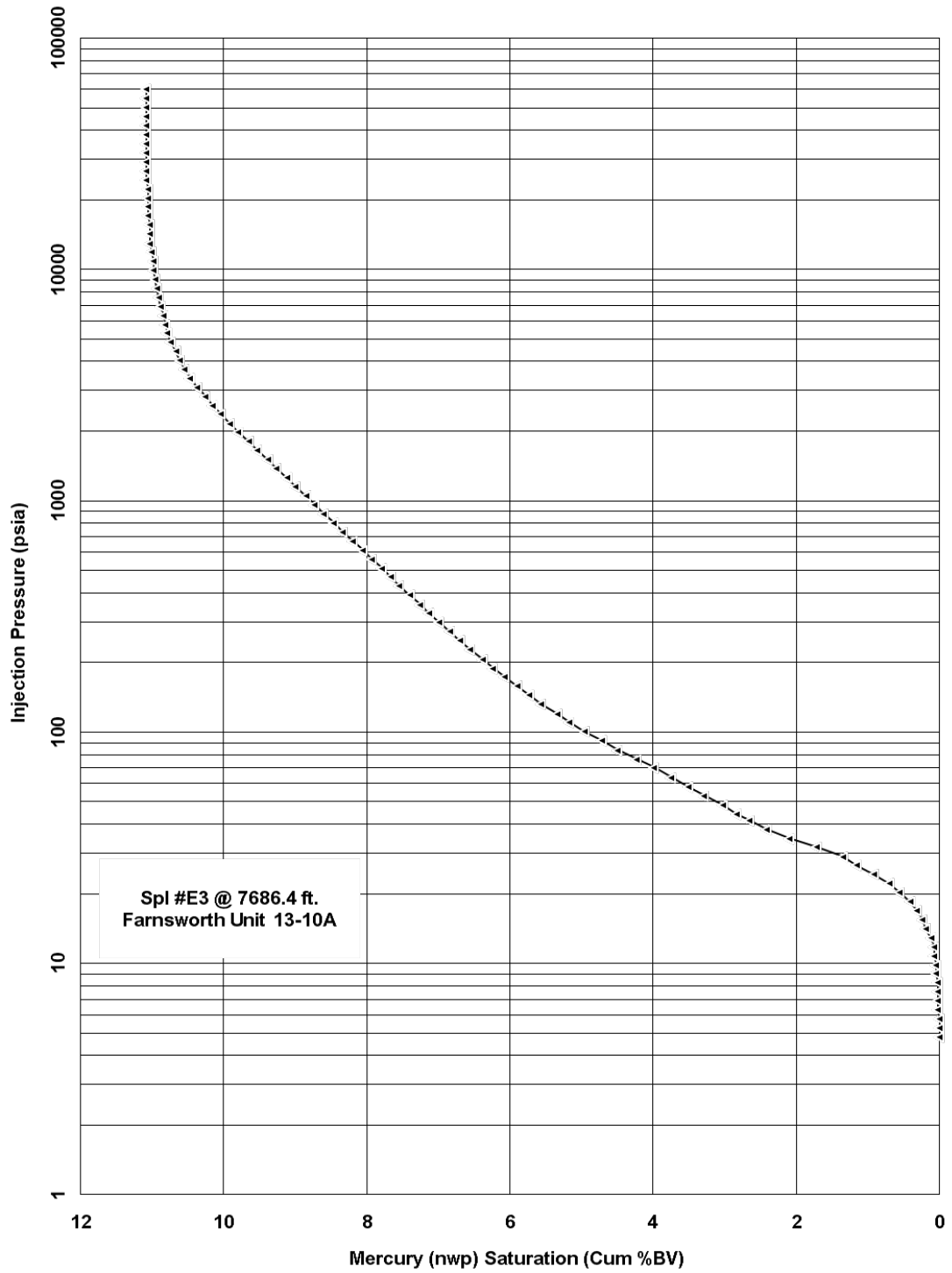
Injection Pressure (psia)	Pore Diameter (microns)	Hg (nwp) Saturation cum%PV	100-Hg(wp) Saturation cum%PV	Leverett "J" Function	Gas/Brine Pc (psia)	Gas/Oil Pc (psia)	Oil/Brine Pc (psia)	Ht. Above Free Water (ft.) Gas/Brine	Ht. Above Free Water (ft.) Oil/Brine
6336.53	0.0337	97.8	2.2	16.50	861.77	411.87	519.60	2186	4613
6938.73	0.0307	98.2	1.8	18.07	943.67	451.02	568.98	2394	5051
7591.58	0.0281	98.5	1.5	19.77	1032.45	493.45	622.51	2619	5527
8307.20	0.0257	98.7	1.3	21.63	1129.78	539.97	681.19	2866	6048
9080.48	0.0235	98.9	1.1	23.65	1234.95	590.23	744.60	3133	6611
9944.63	0.0215	99.1	0.9	25.90	1352.47	646.40	815.46	3431	7240
10873.80	0.0196	99.1	0.9	28.32	1478.84	706.80	891.65	3751	7916
11875.22	0.0180	99.3	0.7	30.92	1615.03	771.89	973.77	4097	8645
12976.52	0.0164	99.6	0.4	33.79	1764.81	843.47	1064.07	4477	9447
14274.94	0.0149	99.6	0.4	37.17	1941.39	927.87	1170.55	4925	10392
15575.50	0.0137	99.6	0.4	40.56	2118.27	1012.41	1277.19	5374	11339
17076.72	0.0125	99.8	0.2	44.47	2322.43	1109.99	1400.29	5891	12432
18672.96	0.0114	99.8	0.2	48.63	2539.52	1213.74	1531.18	6442	13594
20375.08	0.0105	99.8	0.2	53.06	2771.01	1324.38	1670.76	7029	14833
22285.83	0.0096	99.8	0.2	58.03	3030.87	1448.58	1827.44	7689	16224
24389.47	0.0087	100.0	0.0	63.51	3316.97	1585.32	1999.94	8414	17756
26692.51	0.0080	100.0	0.0	69.51	3630.18	1735.01	2188.79	9209	19432
29293.35	0.0073	100.0	0.0	76.28	3983.90	1904.07	2402.05	10106	21326
31991.94	0.0067	100.0	0.0	83.31	4350.90	2079.48	2623.34	11037	23290
34993.19	0.0061	100.0	0.0	91.13	4759.07	2274.56	2869.44	12073	25475
38292.25	0.0056	100.0	0.0	99.72	5207.75	2489.00	3139.96	13211	27877
41892.34	0.0051	100.0	0.0	109.09	5697.36	2723.00	3435.17	14453	30498
45785.38	0.0047	100.0	0.0	119.23	6226.81	2976.05	3754.40	15796	33332
50067.01	0.0043	100.0	0.0	130.38	6809.11	3254.36	4105.49	17273	36449
54765.52	0.0039	100.0	0.0	142.62	7448.11	3559.76	4490.77	18894	39869
59971.95	0.0036	100.0	0.0	156.17	8156.19	3898.18	4917.70	20690	43660
50098.72	0.0036	100.0	0.0						
41898.27	0.0043	100.0	0.0						
32003.57	0.0056	100.0	0.0						
22310.33	0.0080	100.0	0.0						
15615.82	0.0115	100.0	0.0						
10915.29	0.0164	100.0	0.0						
7625.65	0.0235	100.0	0.0						
5320.61	0.0336	100.0	0.0						
3712.46	0.0482	100.0	0.0						
2590.77	0.0691	100.0	0.0						
1812.60	0.0988	100.0	0.0						
1510.12	0.1185	99.8	0.2						
1260.31	0.1420	99.1	0.9						
1049.73	0.1705	98.7	1.3						
880.88	0.2032	97.8	2.2						
736.66	0.2430	97.1	2.9						
615.16	0.2910	96.0	4.0						

AIRMERCURY CAPILLARY PRESSURE DATA : BY Porotechnology

(Continued)

**Spl #E3 @ 7686.4 ft.
Farnsworth Unit 13-10A**

Injection Pressure (psia)	Pore Diameter (microns)	Hg (nwp) Saturation cum%PV	100-Hg(wp) Saturation cum%PV	Leverett "J" Function	Gas/Brine Pc (psia)	Gas/Oil Pc (psia)	Oil/Brine Pc (psia)	Ht. Above Free Water (ft.) Gas/Brine	Ht. Above Free Water (ft.) Oil/Brine
514.93	0.3476	95.2	4.8						
429.92	0.4164	94.1	5.9						
359.02	0.4986	92.7	7.3						
300.19	0.5963	91.4	8.6						
250.25	0.7153	89.9	10.1						
210.16	0.8517	88.4	11.6						
175.63	1.0192	86.8	13.2						
147.03	1.2174	85.1	14.9						
122.72	1.4567	83.3	16.7						
102.50	1.7463	81.8	18.2						
86.23	2.0759	80.0	20.0						
71.66	2.4980	78.2	21.8						
59.77	2.9946	76.3	23.7						
49.84	3.5916	74.5	25.5						
42.36	4.2261	72.5	27.5						
35.26	5.0767	70.3	29.7						
29.50	6.0686	68.1	31.9						
24.84	7.2065	65.7	34.3						
20.51	8.7261	63.3	36.7						



AIRMERCURY CAPILLARY PRESSURE DATA : BY PoroTechnology

**Spl #E4 @ 7696.25 ft.
Farnsworth Unit 13-10A**

MICP Closure(psia) = 4.80

MICP Porosity = 17.49%

MICP Gr. Den.(gm/cc) = 2.669

MICP Bulk Density(gm/cc) = 2.202

MICP-Calc. Air Perm = 32.5 md

Median Pore Aperture Dia.(microns) = 3.278

Injection Pressure (psia)	Pore Diameter (microns)	Hg (nwp) Saturation cum%PV	100-Hg(wp) Saturation cum%PV	Leverett "J" Function	Gas/Brine Pc (psia)	Gas/Oil Pc (psia)	Oil/Brine Pc (psia)	Ht. Above Free	Ht. Above Free
								Water (ft.) Gas/Brine	Water (ft.) Oil/Brine
4.80	44.41	0.0	100.0	0.03	0.65	0.31	0.39	1.7	3.5
5.25	40.60	0.4	99.6	0.03	0.71	0.34	0.43	1.8	3.8
5.75	37.08	0.8	99.2	0.04	0.78	0.37	0.47	2.0	4.2
6.29	33.90	1.3	98.7	0.04	0.86	0.41	0.52	2.2	4.6
6.89	30.98	1.7	98.3	0.04	0.94	0.45	0.56	2.4	5.0
7.53	28.32	2.2	97.8	0.05	1.02	0.49	0.62	2.6	5.5
8.24	25.88	3.3	96.7	0.05	1.12	0.54	0.68	2.8	6.0
9.02	23.64	4.3	95.7	0.06	1.23	0.59	0.74	3.1	6.6
9.87	21.61	5.3	94.7	0.06	1.34	0.64	0.81	3.4	7.2
10.78	19.79	7.3	92.7	0.07	1.47	0.70	0.88	3.7	7.8
11.78	18.11	9.2	90.8	0.07	1.60	0.77	0.97	4.1	8.6
12.88	16.56	11.6	88.4	0.08	1.75	0.84	1.06	4.4	9.4
14.18	15.05	14.1	85.9	0.09	1.93	0.92	1.16	4.9	10.3
15.48	13.78	16.1	83.9	0.10	2.11	1.01	1.27	5.3	11.3
16.88	12.64	21.1	78.9	0.10	2.30	1.10	1.38	5.8	12.3
18.48	11.55	23.8	76.2	0.11	2.51	1.20	1.52	6.4	13.5
20.28	10.52	26.2	73.8	0.12	2.76	1.32	1.66	7.0	14.8
22.18	9.62	28.8	71.2	0.14	3.02	1.44	1.82	7.7	16.1
24.28	8.79	30.9	69.1	0.15	3.30	1.58	1.99	8.4	17.7
26.58	8.03	32.8	67.2	0.16	3.61	1.73	2.18	9.2	19.4
28.98	7.36	34.8	65.2	0.18	3.94	1.88	2.38	10.0	21.1
31.77	6.71	36.7	63.3	0.20	4.32	2.07	2.61	11.0	23.1
34.78	6.13	38.7	61.3	0.21	4.73	2.26	2.85	12.0	25.3
37.97	5.62	40.4	59.6	0.23	5.16	2.47	3.11	13.1	27.6
41.57	5.13	41.9	58.1	0.26	5.65	2.70	3.41	14.3	30.3
44.15	4.83	43.4	56.6	0.27	6.00	2.87	3.62	15.2	32.1
48.21	4.43	44.7	55.3	0.30	6.56	3.13	3.95	16.6	35.1
53.96	3.95	46.2	53.8	0.33	7.34	3.51	4.42	18.6	39.3
59.48	3.586	47.9	52.1	0.37	8.09	3.87	4.88	20.5	43.3
64.77	3.294	49.9	50.1	0.40	8.81	4.21	5.31	22.3	47.2
70.84	3.011	51.7	48.3	0.44	9.63	4.60	5.81	24.4	51.6
77.44	2.755	53.6	46.4	0.48	10.53	5.03	6.35	26.7	56.4
84.64	2.520	55.6	44.4	0.52	11.51	5.50	6.94	29.2	61.6
93.22	2.288	57.7	42.3	0.57	12.68	6.06	7.64	32.2	67.9
100.99	2.112	59.6	40.4	0.62	13.73	6.56	8.28	34.8	73.5
111.37	1.915	61.8	38.2	0.68	15.15	7.24	9.13	38.4	81.1

AIRMERCURY CAPILLARY PRESSURE DATA : BY PoroTechnology

(Continued)

**Spl #E4 @ 7696.25 ft.
Farnsworth Unit 13-10A**

Injection Pressure (psia)	Pore Diameter (microns)	Hg (nwp) Saturation cum%PV	100-Hg(wp) Saturation cum%PV	Leverett "J" Function	Gas/Brine Pc (psia)	Gas/Oil Pc (psia)	Ht. Above Free		
							Oil/Brine Pc (psia)	Water (ft.) Gas/Brine	Water (ft.) Oil/Brine
121.16	1.761	63.7	36.3	0.75	16.48	7.88	9.94	41.8	88.2
132.95	1.605	65.8	34.2	0.82	18.08	8.64	10.90	45.9	96.8
145.42	1.467	67.7	32.3	0.89	19.78	9.45	11.92	50.2	105.9
158.91	1.342	69.8	30.2	0.98	21.61	10.33	13.03	54.8	115.7
173.96	1.226	71.6	28.4	1.07	23.66	11.31	14.26	60.0	126.6
189.86	1.124	73.2	26.8	1.17	25.82	12.34	15.57	65.5	138.2
208.53	1.023	74.7	25.3	1.28	28.36	13.55	17.10	71.9	151.8
228.17	0.935	76.2	23.8	1.40	31.03	14.83	18.71	78.7	166.1
250.29	0.852	77.5	22.5	1.54	34.04	16.27	20.52	86.4	182.2
273.13	0.781	78.6	21.4	1.68	37.15	17.75	22.40	94.2	198.8
297.38	0.717	79.7	20.3	1.83	40.44	19.33	24.39	102.6	216.5
325.73	0.655	80.9	19.1	2.00	44.30	21.17	26.71	112.4	237.1
355.77	0.600	81.9	18.1	2.19	48.38	23.13	29.17	122.7	259.0
389.64	0.548	82.8	17.2	2.40	52.99	25.33	31.95	134.4	283.7
427.46	0.499	83.9	16.1	2.63	58.13	27.78	35.05	147.5	311.2
467.58	0.456	84.8	15.2	2.88	63.59	30.39	38.34	161.3	340
513.63	0.415	85.7	14.3	3.16	69.85	33.39	42.12	177.2	374
559.52	0.381	86.5	13.5	3.44	76.09	36.37	45.88	193.0	407
612.89	0.348	87.2	12.8	3.77	83.35	39.84	50.26	211.4	446
671.31	0.318	88.0	12.0	4.13	91.30	43.64	55.05	231.6	489
732.92	0.291	88.7	11.3	4.51	99.88	47.64	60.10	253	534
803.74	0.265	89.3	10.7	4.94	109.31	52.24	65.91	277	585
879.06	0.243	90.0	10.0	5.41	119.55	57.14	72.08	303	640
961.50	0.222	90.5	9.5	5.91	130.76	62.50	78.84	332	700
1048.16	0.204	91.0	9.0	6.45	142.55	68.13	85.95	362	763
1148.23	0.186	91.5	8.5	7.06	156.16	74.63	94.15	396	836
1257.59	0.170	92.1	7.9	7.73	171.03	81.74	103.12	434	916
1378.31	0.155	92.6	7.4	8.48	187.45	89.59	113.02	476	1003
1507.49	0.142	93.1	6.9	9.27	205.02	97.99	123.61	520	1097
1648.15	0.129	93.6	6.4	10.14	224.15	107.13	135.15	569	1200
1806.15	0.118	94.1	5.9	11.11	245.64	117.40	148.10	623	1315
1976.26	0.108	94.5	5.5	12.15	268.77	128.46	162.05	682	1439
2156.26	0.099	94.9	5.1	13.26	293.25	140.16	176.81	744	1570
2365.77	0.090	95.3	4.7	14.55	321.74	153.78	193.99	816	1722
2585.24	0.083	95.7	4.3	15.90	351.59	168.04	211.99	892	1882
2824.36	0.076	96.0	4.0	17.37	384.11	183.58	231.60	974	2056
3094.59	0.069	96.2	3.8	19.03	420.86	201.15	253.76	1068	2253
3383.01	0.063	96.5	3.5	20.80	460.09	219.90	277.41	1167	2463
3702.61	0.058	96.7	3.3	22.77	503.55	240.67	303.61	1277	2696
4048.66	0.053	97.0	3.0	24.90	550.62	263.16	331.99	1397	2947
4421.70	0.048	97.1	2.9	27.19	601.35	287.41	362.58	1525	3219
4830.84	0.044	97.4	2.6	29.71	656.99	314.00	396.13	1667	3517
5288.17	0.040	97.5	2.5	32.52	719.19	343.73	433.63	1824	3850
5789.38	0.0368	97.7	2.3	35.60	787.36	376.31	474.73	1997	4215

AIRMERCURY CAPILLARY PRESSURE DATA : BY PoroTechnology

(Continued)

**Spl #E4 @ 7696.25 ft.
Farnsworth Unit 13-10A**

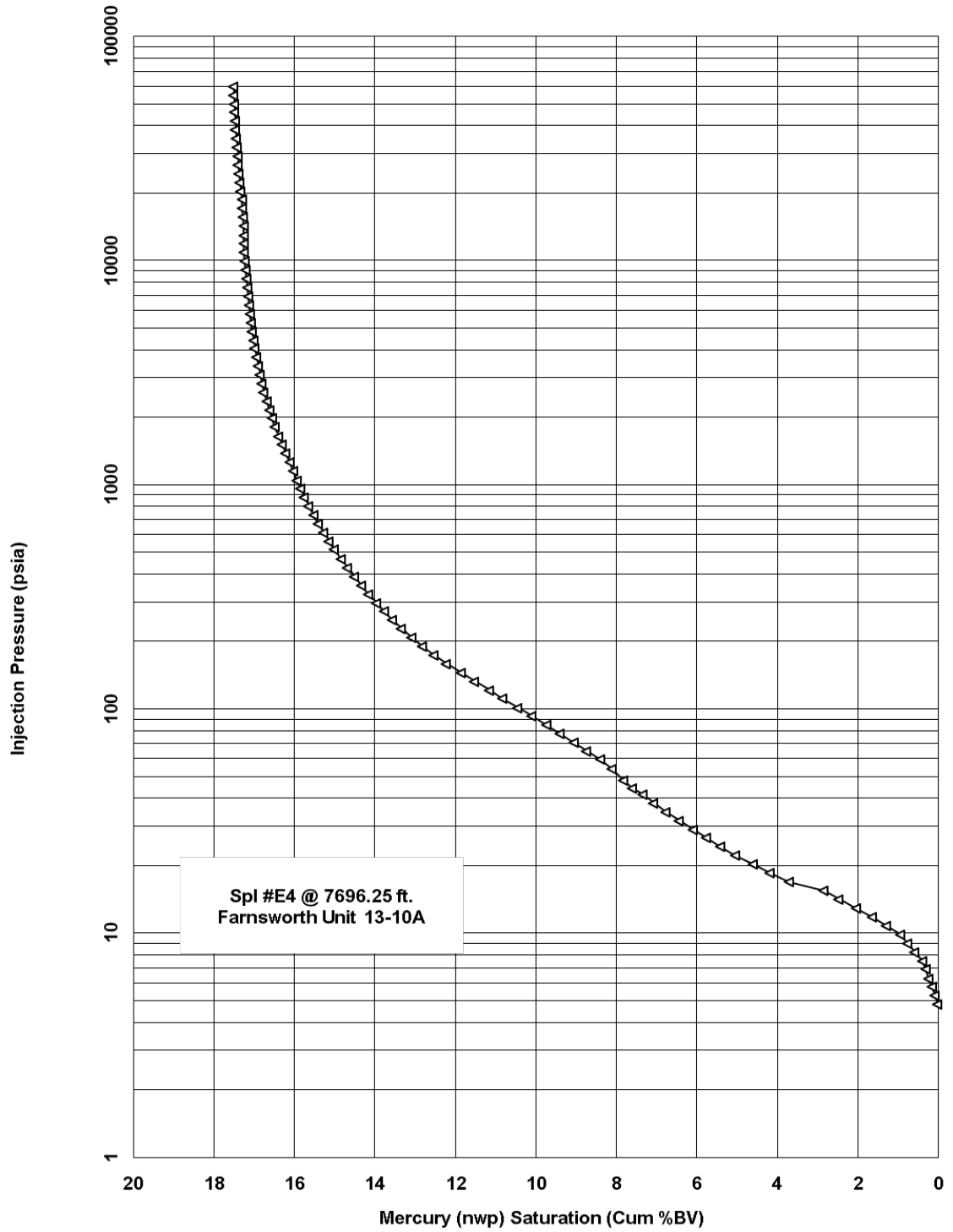
Injection Pressure (psia)	Pore Diameter (microns)	Hg (nwp) Saturation cum%PV	100-Hg(wp) Saturation cum%PV	Leverett "J" Function	Gas/Brine e Pc (psia)	Gas/Oil Pc (psia)	Ht. Above Free		
							Oil/Brine Pc (psia)	Water (ft.) Gas/Brine	Water (ft.) Oil/Brine
6340.22	0.0336	97.8	2.2	38.99	862.27	412.11	519.90	2187	4616
6932.71	0.0308	97.9	2.1	42.63	942.85	450.63	568.48	2392	5047
7590.39	0.0281	98.0	2.0	46.68	1032.29	493.38	622.41	2619	5526
8300.51	0.0257	98.2	1.8	51.04	1128.87	539.53	680.64	2864	6043
9078.90	0.0235	98.3	1.7	55.83	1234.73	590.13	744.47	3132	6609
9943.95	0.0215	98.4	1.6	61.15	1352.38	646.36	815.40	3431	7239
10879.98	0.0196	98.6	1.4	66.90	1479.68	707.20	892.16	3754	7921
11880.71	0.0180	98.6	1.4	73.06	1615.78	772.25	974.22	4099	8649
12983.18	0.0164	98.6	1.4	79.84	1765.71	843.91	1064.62	4479	9452
14279.56	0.0149	98.6	1.4	87.81	1942.02	928.17	1170.92	4926	10396
15578.87	0.0137	98.7	1.3	95.80	2118.73	1012.63	1277.47	5375	11341
17077.21	0.0125	98.8	1.2	105.01	2322.50	1110.02	1400.33	5892	12432
18682.09	0.0114	98.8	1.2	114.88	2540.76	1214.34	1531.93	6445	13601
20378.56	0.0105	99.0	1.0	125.32	2771.48	1324.61	1671.04	7031	14836
22287.88	0.0096	99.1	0.9	137.06	3031.15	1448.71	1827.61	7689	16226
24392.03	0.0087	99.2	0.8	150.00	3317.32	1585.48	2000.15	8415	17757
26693.22	0.0080	99.3	0.7	164.15	3630.28	1735.06	2188.84	9209	19433
29294.53	0.0073	99.3	0.7	180.14	3984.06	1904.14	2402.15	10107	21326
31996.05	0.0067	99.5	0.5	196.76	4351.46	2079.74	2623.68	11039	23293
34994.63	0.0061	99.6	0.4	215.19	4759.27	2274.65	2869.56	12073	25476
38296.84	0.0056	99.7	0.3	235.50	5208.37	2489.29	3140.34	13212	27880
41882.25	0.0051	99.7	0.3	257.55	5695.99	2722.35	3434.34	14449	30490
45759.74	0.0047	99.9	0.1	281.39	6223.32	2974.38	3752.30	15787	33313
50057.97	0.0043	99.9	0.1	307.82	6807.88	3253.77	4104.75	17270	36442
54766.20	0.0039	100.0	0.0	336.78	7448.20	3559.80	4490.83	18894	39870
59954.77	0.0036	100.0	0.0	368.68	8153.85	3897.06	4916.29	20684	43647
50103.15	0.0036	100.0	0.0						
41901.48	0.0043	100.0	0.0						
32004.51	0.0056	100.0	0.0						
22307.03	0.0080	100.0	0.0						
15613.28	0.0115	100.0	0.0						
10913.65	0.0164	100.0	0.0						
7627.19	0.0235	100.0	0.0						
5322.52	0.0336	100.0	0.0						
3714.11	0.0482	100.0	0.0						
2590.03	0.0691	99.0	1.0						
1811.45	0.0988	98.7	1.3						
1510.40	0.1185	98.4	1.6						
1263.18	0.1417	98.2	1.8						
1050.79	0.1703	97.9	2.1						
881.91	0.2030	97.5	2.5						
737.14	0.2428	97.1	2.9						
617.56	0.2898	96.7	3.3						

AIRMERCURY CAPILLARY PRESSURE DATA : BY PoroTechnology

(Continued)

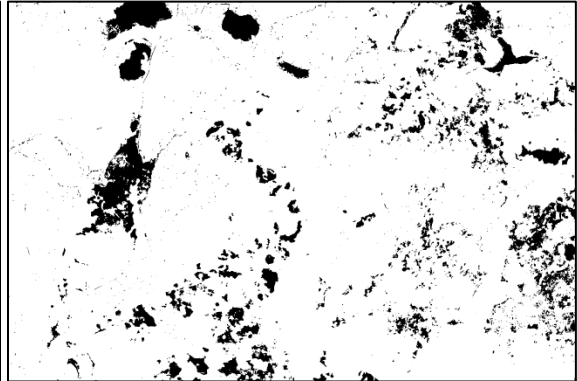
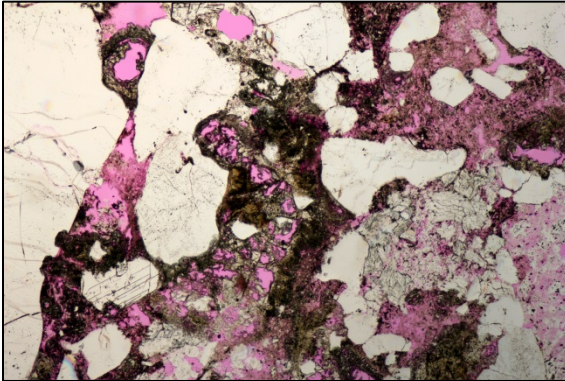
**Spl #E4 @ 7696.25 ft.
Farnsworth Unit 13-10A**

Injection Pressure (psia)	Pore Diameter (microns)	Hg (nwp) Saturation cum%PV	100-Hg(wp) Saturation cum%PV	Leverett "J" Function	Gas/Brine Pc (psia)	Gas/Oil Pc (psia)	Ht. Above Free	
							Oil/Brine Pc (psia)	Water (ft.) Gas/Brine
512.95	0.3490	96.4	3.6					
430.00	0.4163	95.8	4.2					
361.60	0.4950	95.2	4.8					
302.24	0.5922	94.5	5.5					
253.78	0.7053	93.8	6.2					
211.01	0.8483	92.8	7.2					
177.83	1.0066	91.9	8.1					
149.98	1.1935	90.9	9.1					
125.31	1.4284	89.7	10.3					
103.34	1.7321	87.9	12.1					
86.96	2.0583	86.5	13.5					
72.50	2.4690	84.9	15.1					
60.39	2.9643	83.2	16.8					
51.06	3.5054	81.4	18.6					
42.31	4.2309	79.2	20.8					
35.66	5.0193	77.0	23.0					
29.64	6.0396	74.3	25.7					
24.96	7.1718	72.1	27.9					
21.06	8.4975	69.9	30.1					

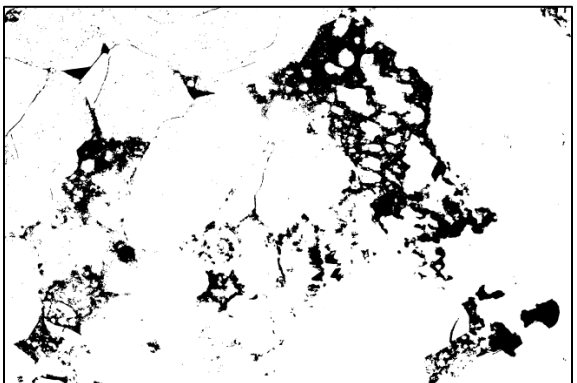
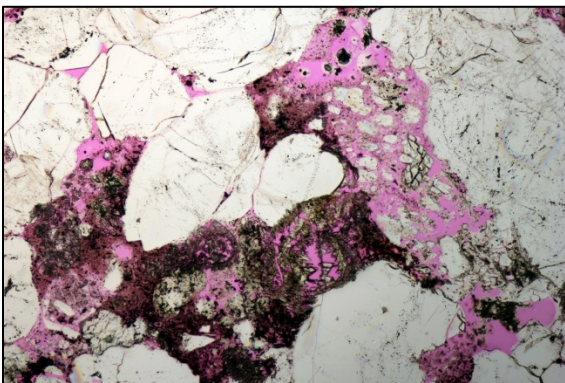


APPENDIX H. PHOTOMICROGRAPHS ANALYZED WITH IMAGEJ

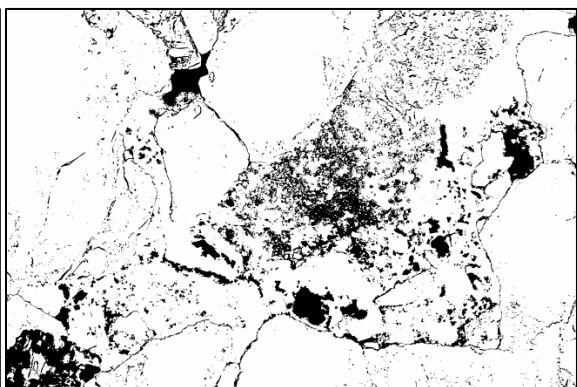
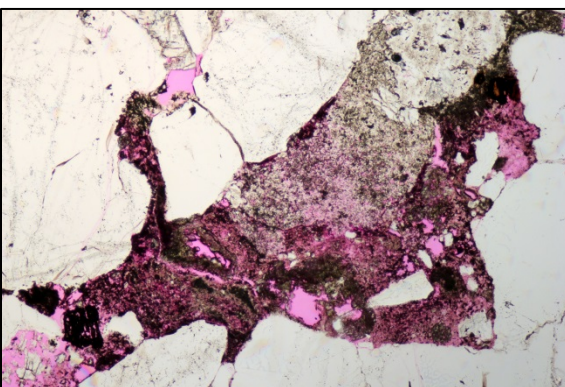
Sample E1, G Facies



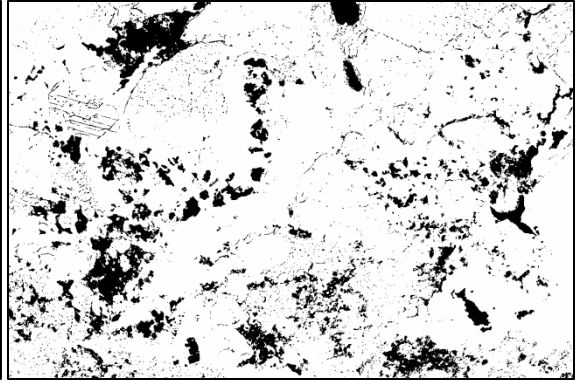
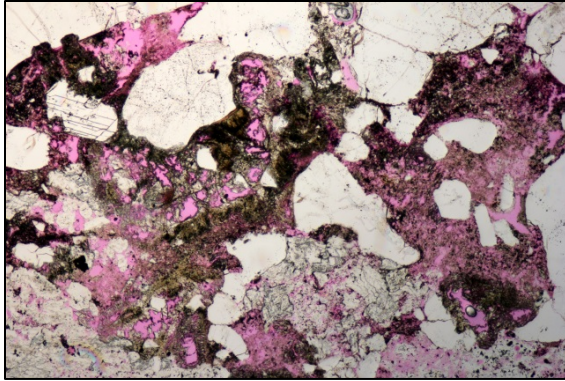
IMG_0108. Image Porosity: 9.61%



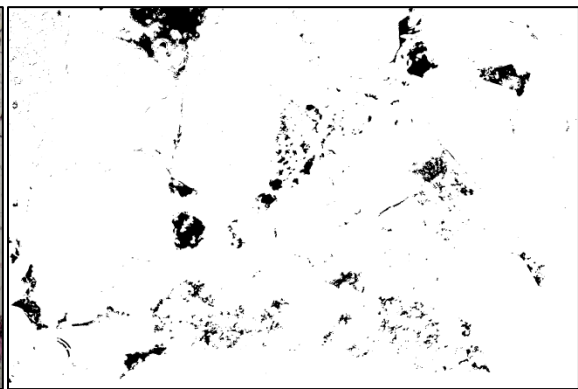
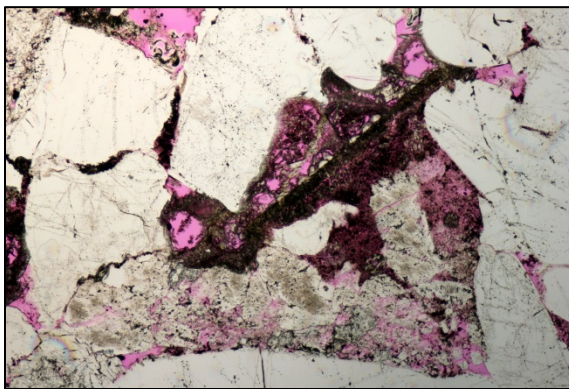
IMG_0107. Image Porosity: 12.18%



IMG_0117. Image Porosity: 12.71%

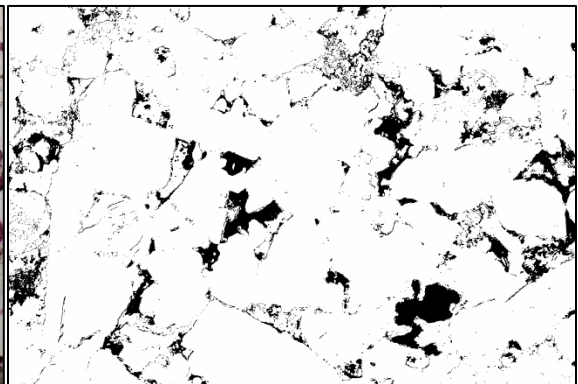
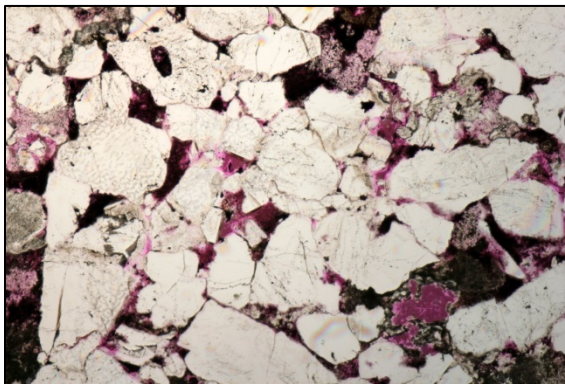


IMG_0133. Image Porosity: 13.72%

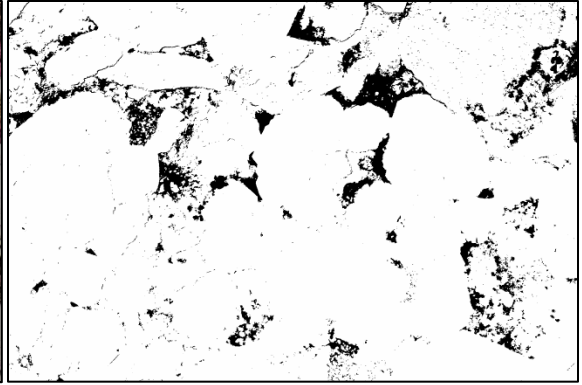
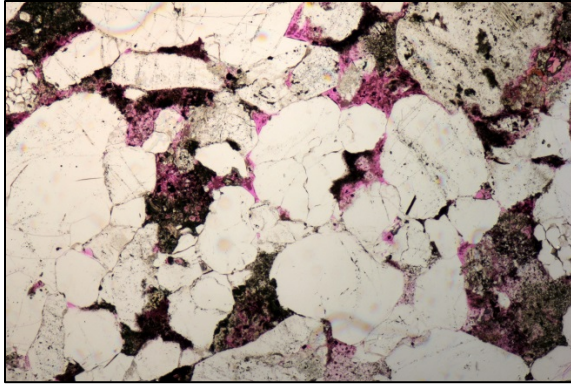


IMG_0110. Image Porosity: 4.18%

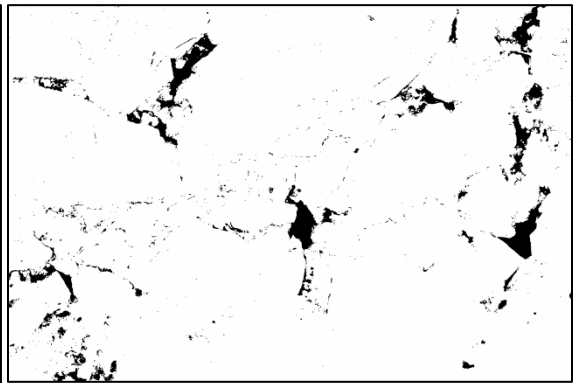
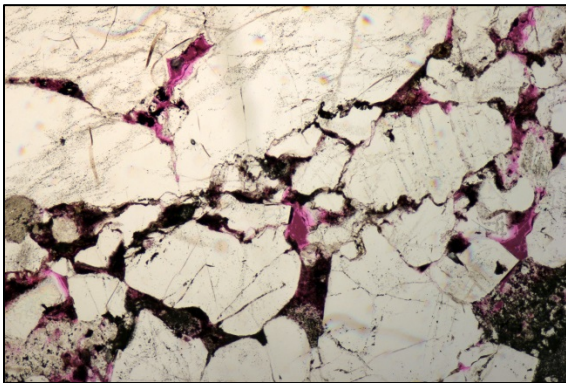
Sample E2, D Facies



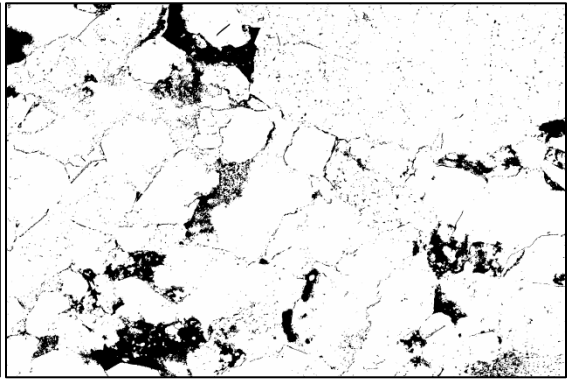
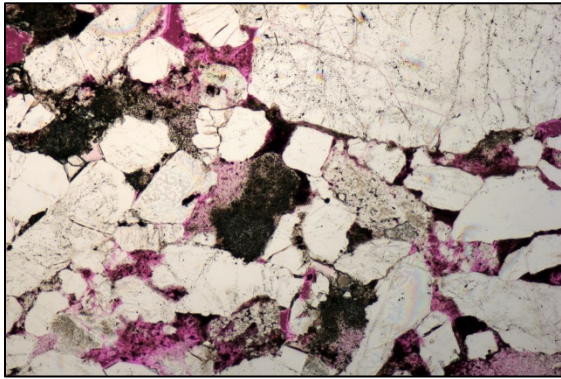
IMG_0088. Image Porosity: 9.16%



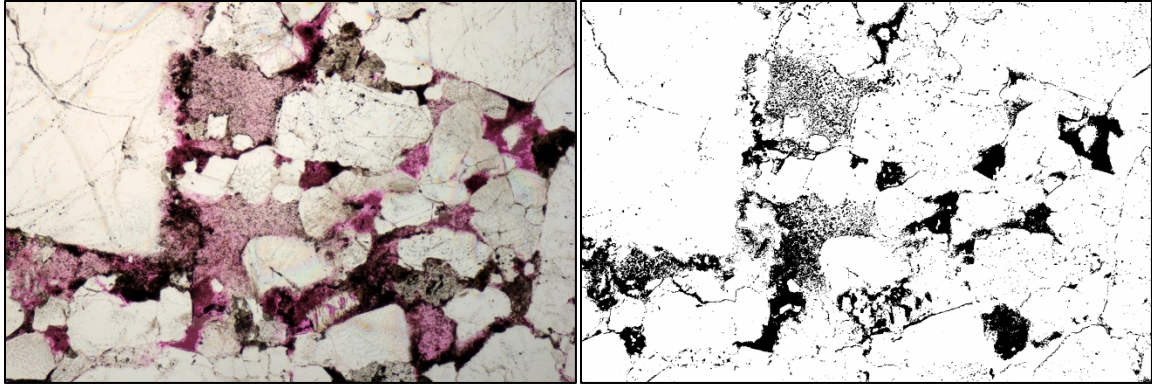
IMG_0091. Image Porosity: 7.21%



IMG_0092: Image Porosity: 4.11%

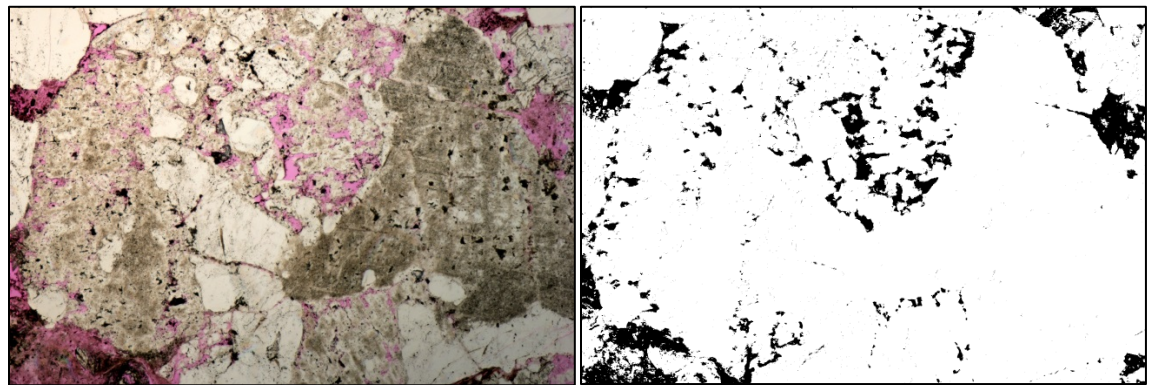


IMG_0093. Image Porosity: 9.81%

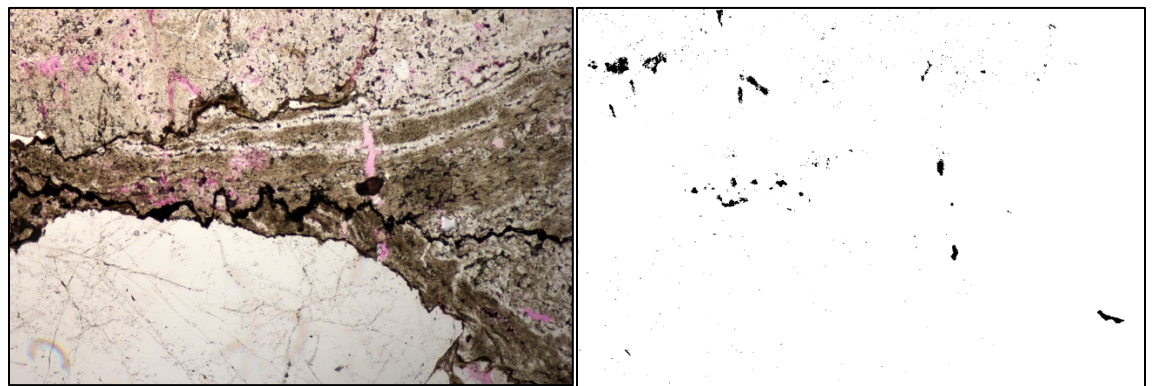


IMG_0094. Image Porosity: 12.72%

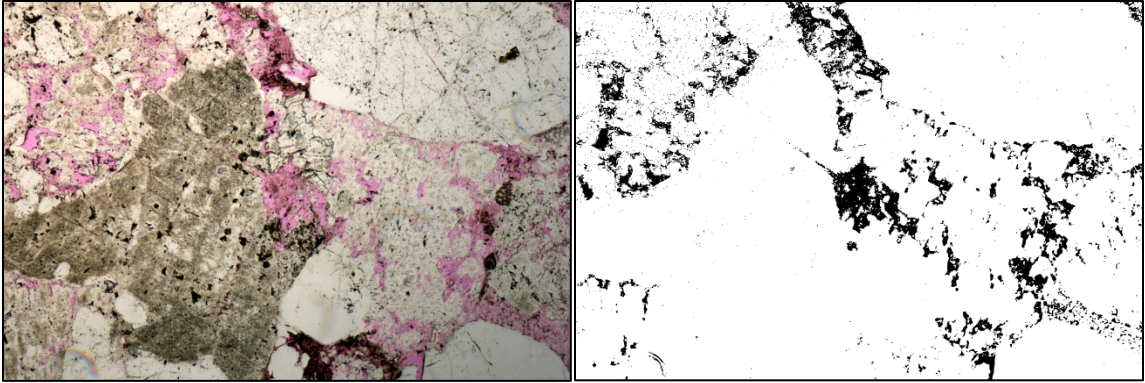
Sample E3, H Facies



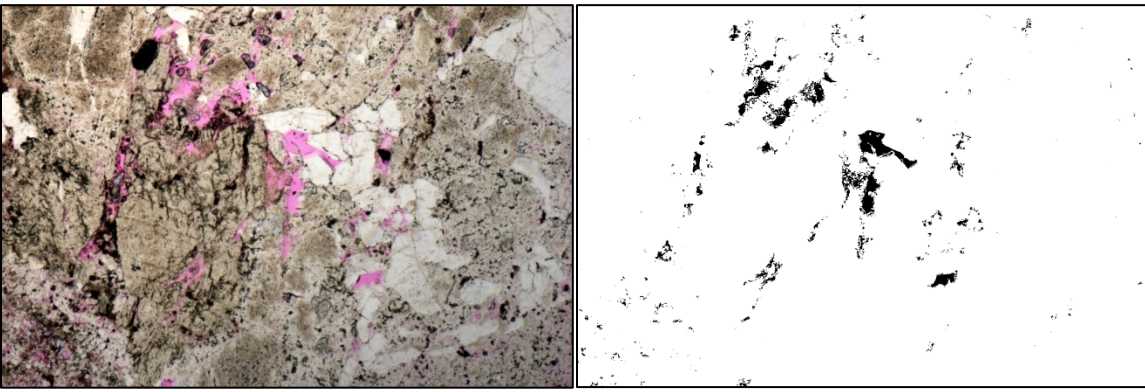
IMG_0104. Image Porosity: 9.10%



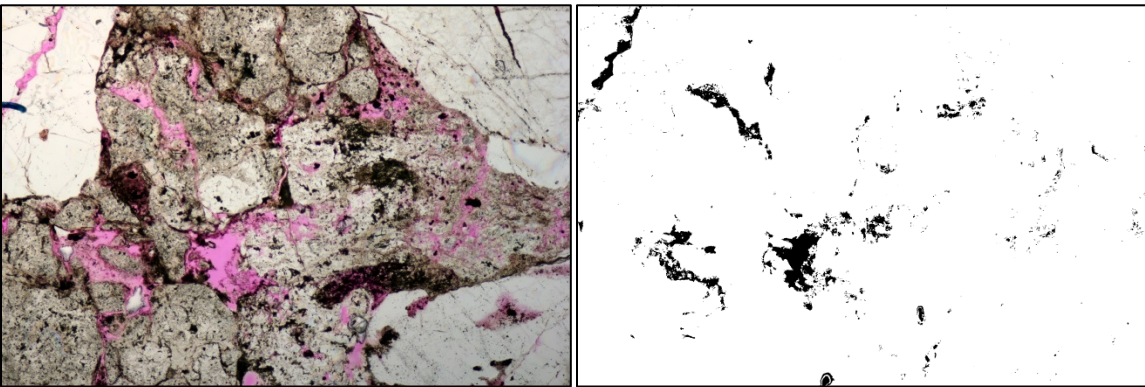
IMG_0102. Image Porosity: 0.75%



IMG_0126. Image Porosity: 7.93%



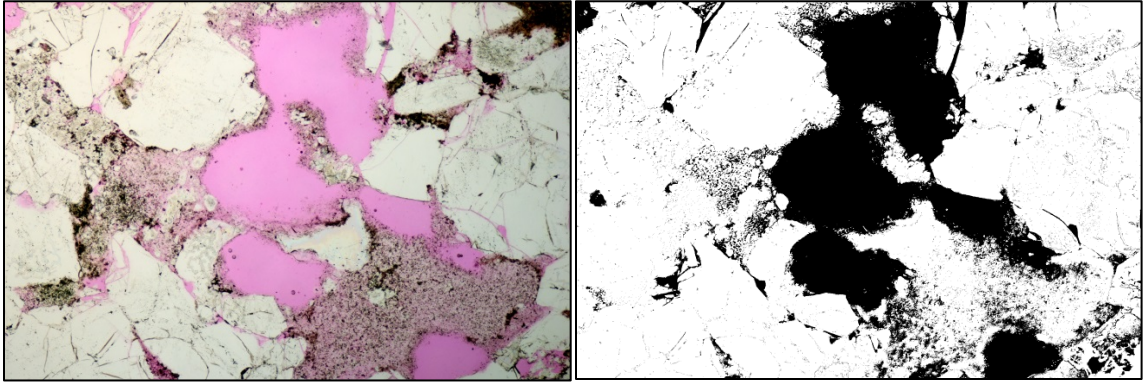
IMG_0153. Image Porosity: 2.13%



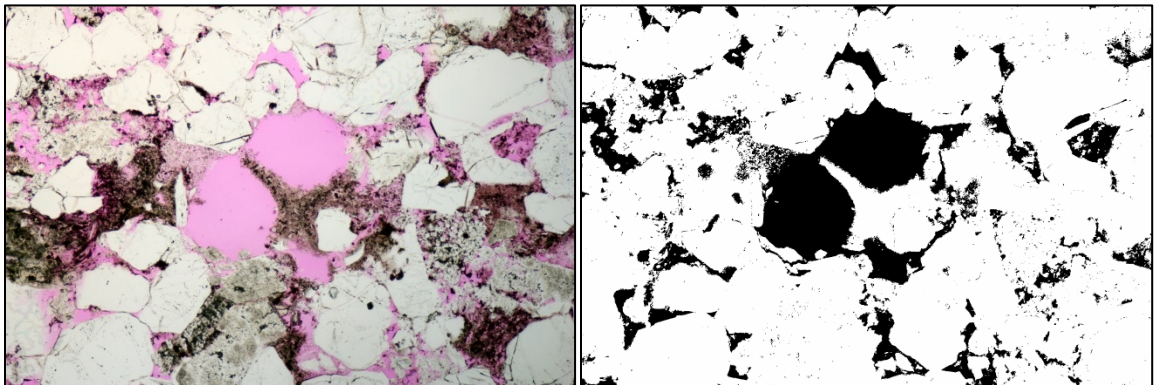
IMG_0166. Image Porosity: 2.86%

Sample E4

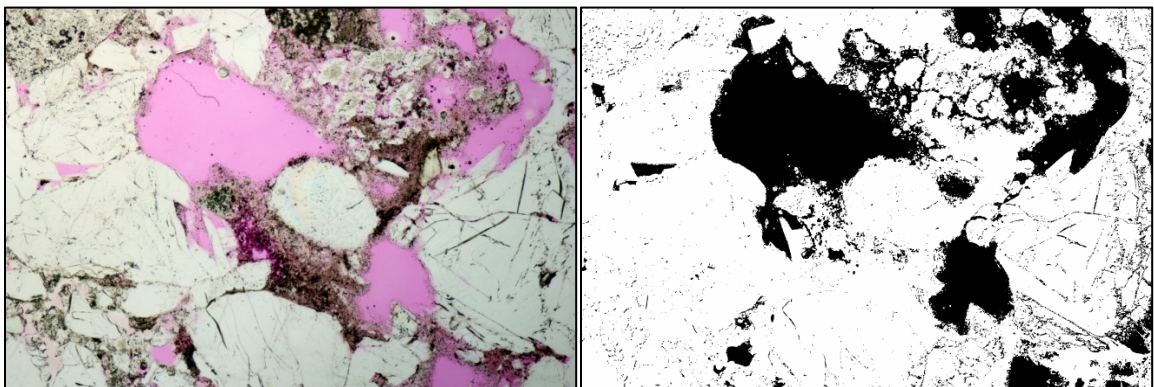
C Facies



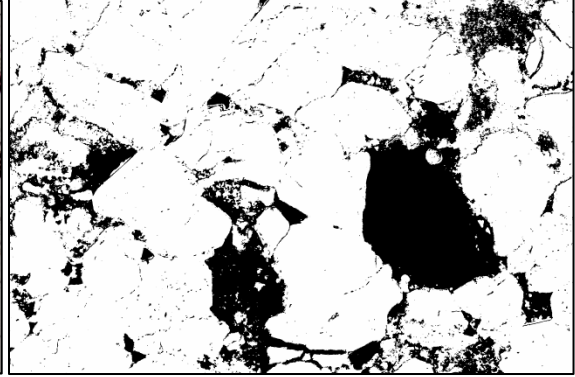
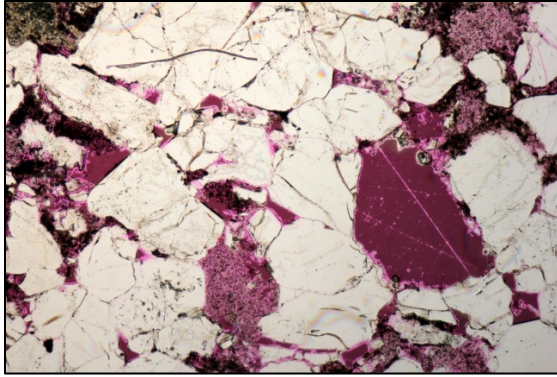
IMG_0080. Image Porosity: 22.30%



IMG_0082. Image Porosity: 17.38%

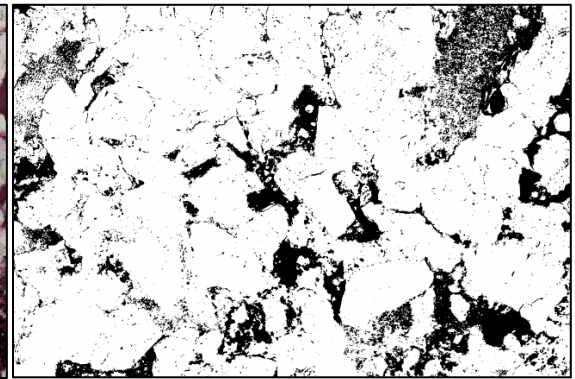
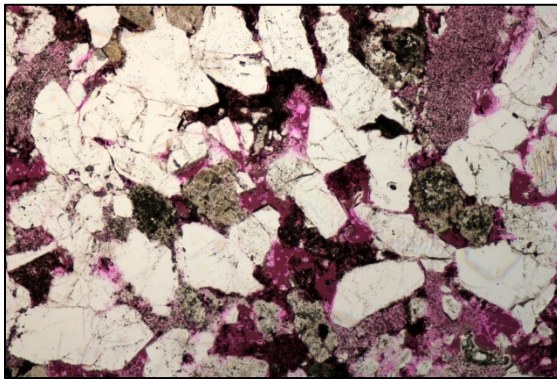


IMG_0081. Image Porosity: 25.08%

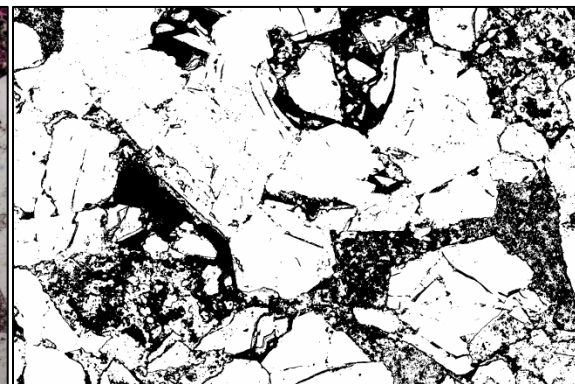
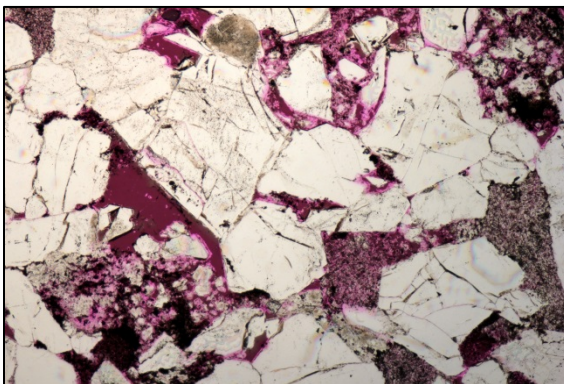


IMG_0086. Image Porosity: 20.84%

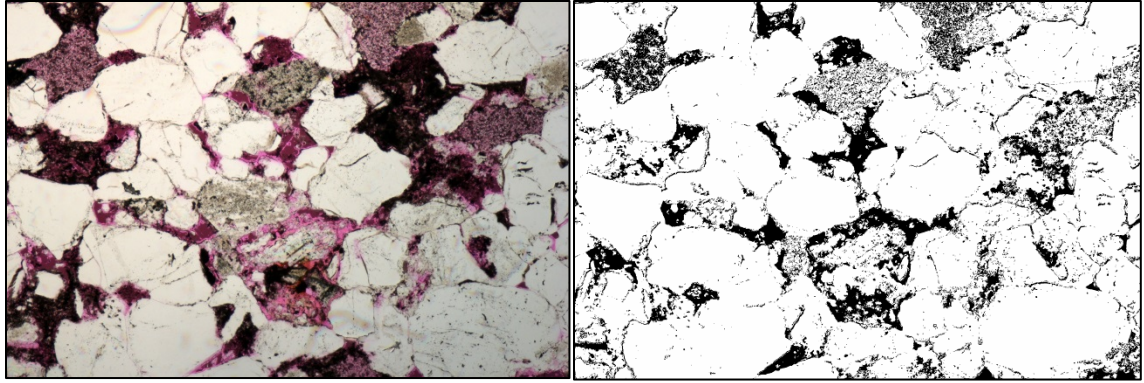
D Facies



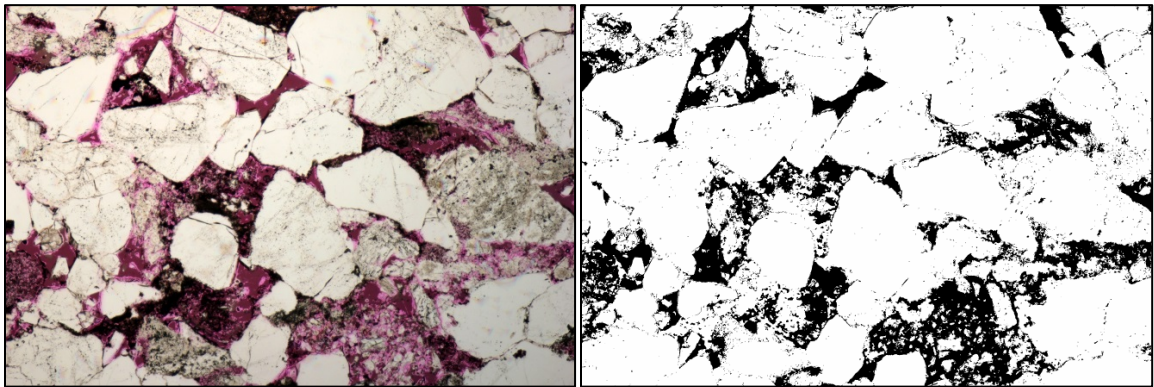
IMG_0081. Image Porosity: 17.26%



IMG_0082. Image Porosity: 27.50%



IMG_0083. Image Porosity: 15.34%



IMG_0087. Image Porosity: 18.84%

Depositional and Diagenetic Controls on Reservoir Heterogeneity:
Upper Morrow Sandstone, Farnsworth Unit, Ochiltree County, Texas

By Sara R. Gallagher

Permission to make digital or hard copies of all or part of this work for personal or classroom use is granted without fee provided that copies are not made or distributed for profit or commercial advantage and that copies bear this notice and the full citation on the last page. To copy otherwise, to republish, to post on servers or to redistribute to lists, requires prior specific permission and may require a fee. |